UNIVERSITY OF TRENTO

Doctoral School in Civil, Environmental and Mechanical Engineering

Curriculum 3. Modelling and Simulation

Alessandro Cazzolli

Snapping and Fluttering of Elastic Rods

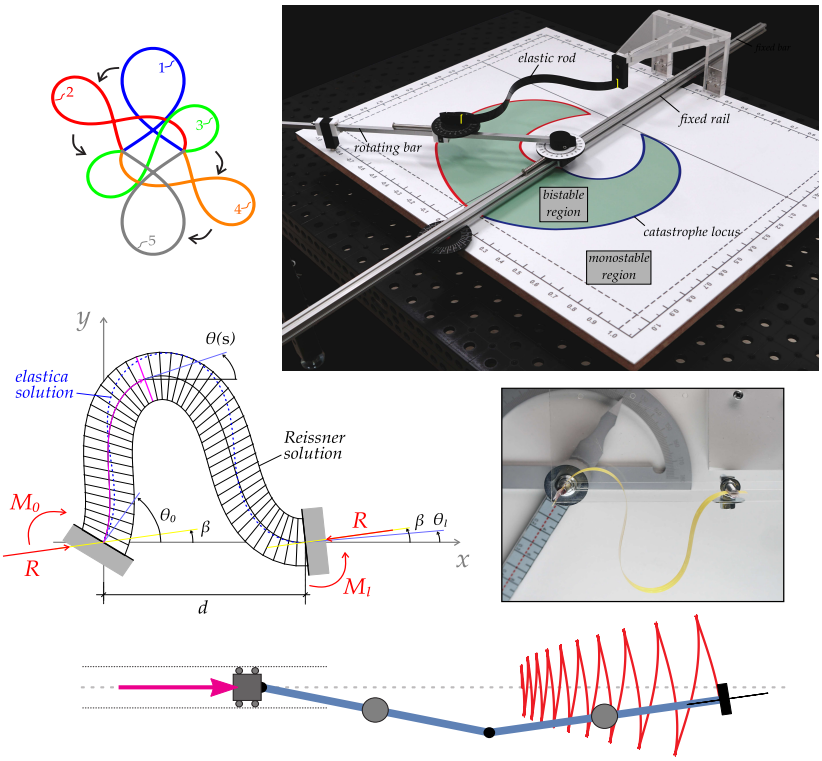

2020 - Doctoral thesis

The exact solutions for planar rods undergoing large rotations and subject to kinematically controlled ends are presented in the first part of the thesis. In particular, the equilibrium equations for a rod subject to Dirichlet boundary conditions and to isoperimetric constraints are derived through variational principles for both the Euler's elastica and the Reissner beam, while the related closed-form solutions are obtained in terms of the Jacobi elliptic functions. The study of stability of the Euler's elastica is addressed in the second part of the thesis through a modified version of the conjugate points method, thus disclosing the existence of a universal snap surface that represents the whole set of "saddle points" of the total potential energy, and therefore corresponding to snapping configurations. These theoretical findings allow for the prediction of snapping instabilities along any equilibrium path involving variations in the boundary conditions and are confirmed by numerical and experimental data. The universal snap surface is also exploited towards the realization of the elastica catastrophe machine, as the first extension of the classical Zeeman's machine to continuous elastic elements. Two families of the elastica catastrophe machine are presented and the theoretical model is fully validated through a prototype designed and tested at the Instability Lab of the University of Trento. Finally, the equations of motion of a pre-stressed planar rod and of its discretized counterpart subject to non-holonomic constraints are obtained in the last part. The analysis of the linearized stability surprisingly proves the existence of flutter instabilities despite the conservative nature of the considered systems. Moreover, Hopf bifurcations and destabilization paradoxes in the presence of dissipative forces are found. The non-linear equations of the proposed discretized model are also numerically solved, thus confirming the predicted stability properties and revealing the birth of periodic stable solutions.

UNIVERSITY OF TRENTO

Doctoral School in Civil, Environmental and Mechanical Engineering - Modelling and Simulation
XXXII cycle 2016/2019

Doctoral Thesis

Alessandro Cazzolli

Snapping and Fluttering of Elastic Rods

Advisors:

Prof. Davide Bigoni	University of Trento
Prof. Francesco Dal Corso	University of Trento

Trento, April 2020

University of Trento
Doctoral School in Civil, Environmental and Mechanical Engineering
http://web.unitn.it/en/dricam
Via Mesiano 77, I-38123 Trento
Tel. +39 0461 282670 / 2611 - *dicamphd@unitn.it*

"Without haste, but without respite"
Lev Nikolayevich Tolstoy
Anna Karenina

Acknowledgements

First and foremost, I express my sincere and profound gratitude to my supervisors Prof. Davide Bigoni and Prof. Francesco Dal Corso for their fundamental inspirations, suggestions and remarks they have provided me during my PhD. Their faith and consideration in my work and capabilities have been crucial for the development of my work. My thanks goes also to Dr. Diego Misseroni for his advice and his invaluable work in the experimental activity, which has been of great importance for my research. I'm also grateful to Prof. John H. Maddocks for his useful explanations regarding the stability of rods.

I would also like to express my deep esteem and gratitude to my colleague Giovanni Bordiga, who has been sharing with me the same office and his friendship for the last three years. I wish him the best for his PhD final examination and for his future academic career. A special greeting goes also to all my colleagues Gabriel, Marco, my flatmate Riccardo, Luca, Andrea, Gian, Dominik, Gabriele, Diana, Costanza, Mirko, Piotr, L.K., Moritz, Matteo, Mattia, Ilaria and Dr. C.d. Daniele Veber. I am also deeply grateful to my parents and my brother Guido for their unfailing support and encouragements, which have been fundamental during my academic studies.

A very special thanks goes to my beloved Chiara for being my safe haven and the person who most of all is able to understand and support me even in hard times, and to my dear grandpa Placido, whose memory will be a constant font of inspiration to me. This thesis is dedicated to them.

Support from the ERC Advanced Grant "Instabilities and non-local multiscale modelling of materials" 340561-FP7-PEOPLE- IDEAS-ERC-2013-AdG (2014-2019) is gratefully acknowledged.

Published papers

The main results presented in this thesis have been summarized in the following papers:

1. Cazzolli, A., Dal Corso, F. (2019). Snapping of elastic strips with controlled ends. *International Journal of Solids and Structures*. 162, 285-303

2. Cazzolli, A., Misseroni, D., Dal Corso, F. (2019). Elastica catastrophe machine: theory, design and experiments. *Journal of the Mechanics and Physics of Solids*, 103735.

3. Cazzolli, A., Dal Corso, F., Bigoni, D. (2020). Non-holonomic constraints inducing flutter instability in structures under conservative loadings. *Submitted*.

Contents

1 Introduction

During the last decades, many scientists and engineers have been focusing on the behaviour of natural and biological systems, which can often be analyzed with structural models characterized by a strongly non-linear behaviour involving large deformations. With the purpose to solve complex real life problems, a large variety of innovative biomimetic technologies has been developed to achieve superior mechanical performances. For instance, transitions to periodic solutions for self-oscillating natural systems, which may be modelled through Hopf bifurcations [1, 60], have inspired the design of new devices which can be exploited for energy harvesting and locomotion [8, 88]. A very special attention is also dedicated to the so called 'soft-robotics' [72, 101, 106, 116], which is devoted to the development of machines made up of compliant components. This new branch of robotics has found appplications in several fields, such as limbless locomotion [39] (for instance via snapping instabilities [82, 112, 115]), energy harvesting [54, 61] and medical rehabilitation [92]. Within this framework, compliant structural systems are analysed through non-linear mechanical modelling, numerical simulations and experiments towards the design of a new generation of efficient devices and actuators, with special attention to snapping instabilities and Hopf bifurcations of mechanical systems.

The first part of the present work is devoted to the development of closed-form solutions for non-linear elastic rods deforming in a plane where large rotations may arise. Particular attention is given to the problem of a rod with kinematically controlled ends, namely whose rotations and displacements at both

ends are specified by imposing Dirichlet boundary conditions and isoperimetric contraints, respectively. It is worth underlining that, due to the generality of the proposed closed-form solutions, the presented mathematical framework can be easily extended to the study of different boundary value problems (for instance with Dirichlet-Neumann or Neumann-Neumann boundary conditions).

In Chapter 2, the closed-form solution for the inextensible Euler's elastica is obtained by means of the Jacobi's elliptic functions. Such exact formulation allows to reduce the problem to the evaluation of two real parameters only, which can be calculated by exploiting the set of imposed isoperimetric constraints. Multiple solutions for the aforementioned parameters, which correspond to the multiple equilibrium configurations of the Euler's elastica, can therefore be numerically obtained through the resolution for a non-linear algebraic system.

In Chapter 3 the closed-form solution for the Reissner beam [97] is developed. In particular, differently from the Euler's elastica, this rod is characterized by finite axial and shear deformations, while the generic cross-section is still constrained to remain undeformed. The exact solution, obtained through the Jacobi's elliptic functions, represents a generalization of the analogous solution holding for the Euler's elastica. In analogy with the latter case, the solution for the Reissner beam is a function of a few unknown parameters, which can be obtained by exploiting the imposed constraints' equations arranged into a non-linear algebraic system of which the roots are to be evaluated.

Some examples of the obtained deformed shapes for both the Euler's elastica and the Reissner beam are shown in Fig.1.1, where the fundamental distinction is made between the 'inflectional' and 'non-inflectional' solutions.

The second part of the thesis is devoted to applications of the closed-form solution for the Euler's elastica presented in Chapter 2.

In Chapter 5, snapping mechanisms are investigated for an elastic rod with both ends prescribed to move and rotate. By means of the stability criterion (presented in Chapter 4) based on the study of the sign second variation of the total potential energy, the number of stable equilibrium configurations for every combination of the boundary conditions is obtained. This result leads to the definition of a *universal snap surface*, collecting the sets of critical boundary conditions for which the system snaps. The elastic energy release at snapping is also investigated, providing useful insights for the optimization of impulsive motion devices[112]. The theoretical predictions are finally validated through comparisons with experimental results and finite element simulations, both fully confirming the reliability of the introduced universal surface. The presented analysis may find applications in a wide range of technological fields, as for instance energy harvesting and jumping robots.

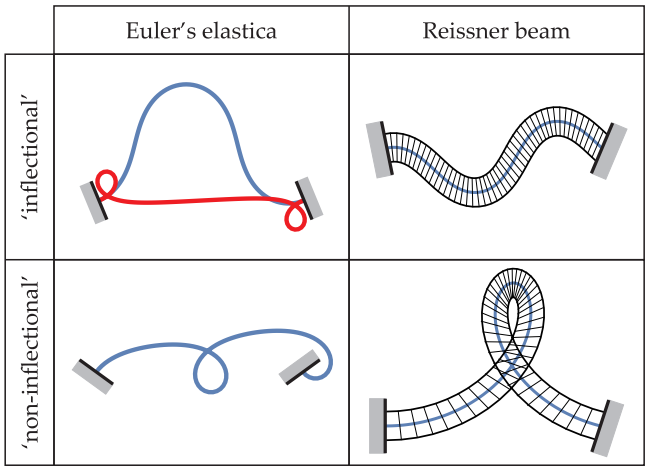

Figure 1.1: Examples of deformed configurations for the Euler's elastica (left) and the Reissner beam (right) subject to controlled rotations and displacements at both ends. Solutions are discriminated into two fundamental cases of presence (upper part) and absence (lower part) of inflection points within the span of the rods. The effects of shear deformations for the Reissner beam are immediately evidenced by the fact that cross-sections (black lines) do not in general remain orthogonal to the centerline (blue). Moreover, the extensibility effect is clearly indicated by the variable distance between successive cross-sections.

The theory, design, and experimental validation of a catastrophe machine based on a flexible element are addressed in Chapter 6. A general theoretical framework is developed through an extension of the classical catastrophe machines, which are made up of discrete elastic elements [114, 118]. The new formulation, based on the non-linear solution for the Euler's elastica, is enhanced by considering the concept of the universal snap surface. Among the infinite set of *elastica catastrophe machines*, two families are proposed and investigated to explicitly assess their features. The related catastrophe locus (representing the border of the bistability domain of the structure) is disclosed to encompass a large variety of shapes, very different from those generated by the classical counterpart. Substantial changes in the catastrophe locus properties, such as convexity and number of bifurcation points, can be obtained by tuning the design parameters of the proposed machines towards the design of very efficient snapping devices. Experiments performed on the physical realization of the proposed catastrophe machine fully validate the theoretical framework. The de-

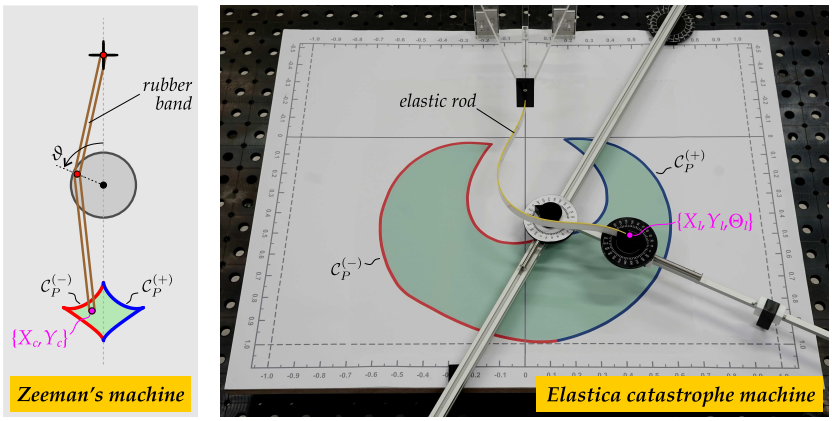

Figure 1.2: Comparison between the classical Zeeman's catastrophe machine (left) and a photo of the prototype realized for the proposed *elastica catastrophe machine* (right). Both machines are characterized by bistability when the rubber's end coordinates X_c, Y_c for the classical machine (left) and the final end of the elastica (right, coordinates X_l, Y_l) lie inside of the respective green area. The catastrophe locus, denoted by $\mathcal{C}$, therefore represents the the border between bistable and monostable domains (gray background) and corresponds to snapping configurations.

veloped model can find applications in mechanics at different scales, for instance, in the design of new devices for actuation or of hysteresis loop mechanisms to achieve energy harvesting, locomotion, and wave mitigation. The classical Zeeman's machine and the proposed elastica catastrophe machine are compared in Fig.1.2.

In the third and last part of the present work, the equations of motion and the stability of visco-elastic devices subject to non-holonomic constraints are studied in detail. In particular, it is shown that dynamic instabilities, including Hopf bifurcations, flutter, divergence, and destabilizing effects connected to dissipation phenomena, can be obtained in structural systems loaded by conservative forces, as a consequence of the application of non-holonomic constraints. Such feature is in contrast with the fact that non-conservative loads (as those of the follower type) are usually believed to be the only possible source of such dynamic instabilities [2]. Non-holonomic constraints may be realized through a 'perfect skate' (or a non-sliding wheel), or, more in general, through the slipless contact between two circular rigid cylinders, one of which is free of rotating about its axis.

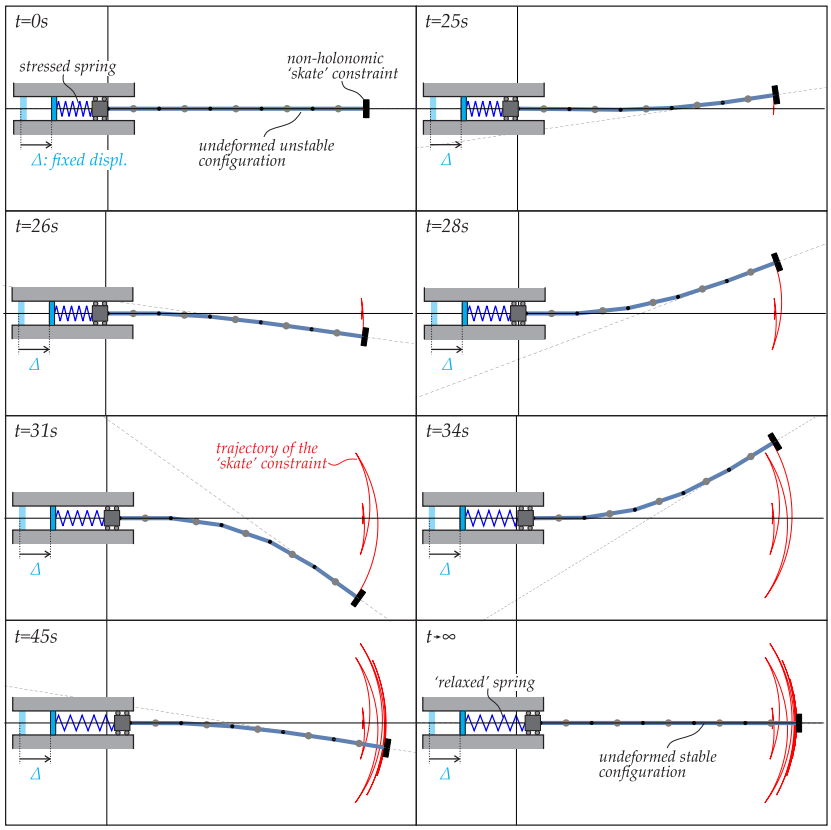

Figure 1.3: Time evolution for the dynamics of a discrete chain subject to a 'skate' non-holonomic constraint (which may be realized through a skate or a wheel) applied at its final end and loaded through an horizontal compressed spring (highlighted in blue). The system is made up of $N = 5$ rigid bars connected through visco-elastic hinges, and exhibits a flutter instability as the compression of the spring overcomes a critical load. The induced horizontal motion causes a relaxation of the spring, so that the system eventually reaches a stable straight configuration. Differently, a steady horizontal motion can be triggered by substituting the elastic spring with a dead load acting on the initial end.

Chapter 7 is devoted to the study of a visco-elastic non-holonomic chain made up of an arbitrary number N of rigid bars. In particular, special attention is devoted to the study of a double-pendulum subject to both the introduced

non-holonomic constraints and stressed through two different, but conservative, loading conditions. The study of the linearized stability, that also includes the discovery of a new type of Ziegler's destabilization paradox, is complemented by the stability analysis of the Hopf bifurcations that the system may undergo and by the numerical analysis of the post-critical behaviour. The motion of the structure produced by these dynamic instabilities may also reach a limit cycle, a feature that can be exploited for soft-robotics applications, especially for the realization of limbless locomotion. A numerical solution showing flutter instability for the aforementioned discretized system subject to viscous forces and a conservative loading is shown in Fig.1.3.

Finally, the non-linear equations of motion for a continuous rod subject to a 'skate' non-holonomic constraint is presented in Chapter 8. The analysis of the linearized stability is also performed, leading to conclusions which are very similar to those holding for the discretized system. Finally, the flutter load for the discretized model (with homogenized parameters) reveals a behaviour which tends to that calculated for the continuous system when the number N of its constitutive rigid bars is increased.

Part I

Exact solutions for the Euler's elastica and the Reissner beam

2

The exact solution for the Euler's elastica

An inextensible elastic rod of length l is considered to be deformed within a plane orthogonal to the axis of minimum momenta of inertia of the rod's cross section. The rod has a uniform cross section and is initially flat, so that its centerline is described by a straight line in the undeformed configuration. Moreover, no further constraints induced by self-contact phenomena are considered. Neglecting the effects of self weight and disregarding rigid body motions, the mechanical fields along the generic curvilinear coordinate $\mathsf{s} \in [0, l]$ can be represented in a 'local' reference system $x - y$ (Fig. 2.1), with origin at one rod's end ($\mathsf{s} = 0$), and x-axis passing by the other one ($\mathsf{s} = l$), so that $x(0) = y(0) = y(l) = 0$, and pointing from the initial to the final curvilinear coordinate. The primary kinematic field is the rotation angle $\theta(\mathsf{s})$, which measures the rotation of the structure's centerline with respect to the x-axis, from which, by considering the inextensibility constraint

$$x'(\mathsf{s}) = \cos\theta(\mathsf{s}), \qquad y'(\mathsf{s}) = \sin\theta(\mathsf{s}), \tag{2.1}$$

the position fields can be obtained as

$$x(\mathsf{s}) = \int_0^{\mathsf{s}} \cos\theta(\varsigma)\,\mathrm{d}\varsigma, \qquad y(\mathsf{s}) = \int_0^{\mathsf{s}} \sin\theta(\varsigma)\,\mathrm{d}\varsigma. \tag{2.2}$$

The rod is considered subject to kinematic boundary conditions in terms of position and rotation at both ends, which slowly move in time along *quasi-static evolutions*. By considering the $x - y$ reference system allows for the rational interpretation of the boundary conditions imposed at the two rod's ends. Indeed, the six kinematic boundary conditions (two positions and one rotation at each end) affect the rod configuration by means of the following three primary kinematical quantities

$$x(l) = d, \qquad \theta(0) = \theta_0, \qquad \theta(l) = \theta_l, \tag{2.3}$$

being d the distance between the two clamps, $d \in [0, l]$ where the lower bound is given by the definition of the x-axis direction while the upper bound is related to the inextensibility assumption (although extensibility may affect the mechanical response even in the proximity of the limit condition, $d \simeq l$).

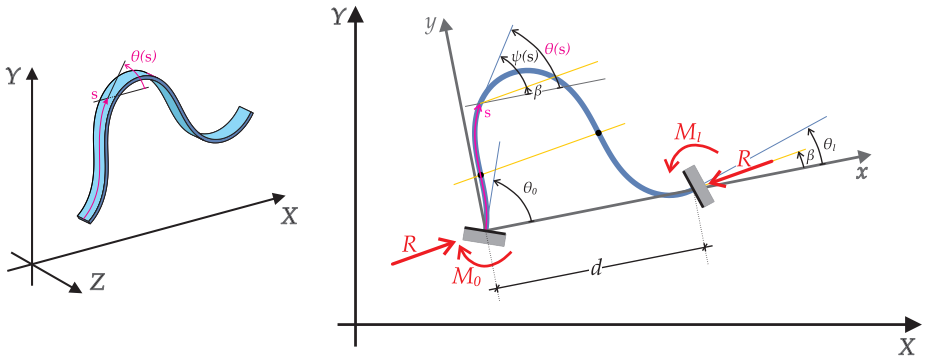

Figure 2.1: Generic deformed configuration for a rod of length l with kinematically controlled ends within the 'global' reference system $X - Y$ and the 'local' reference system $x - y$. Neglecting rigid-body motions, the equilibrium configuration is dependent only on the three independent kinematic quantities d, θ_0, and θ_l. Reaction forces and moments at the two controlled ends are also reported.

The planar behaviour of the considered rod is modelled as the Euler's elastica, so that a linear elastic constitutive law is introduced for the bending moment M, which is given by $M(\mathsf{s}) = B\theta'(\mathsf{s})$ where the symbol $'$ stands for the derivative with respect to the curvilinear coordinate s and B is the bending stiffness, constant because the rod's cross section is uniform. The total potential energy $\mathcal{V}$ expressing the energy of the system under *quasi-static conditions* is

given by

$$\begin{aligned}\mathcal{V} = \mathcal{E} - \int_0^l \left[R_x(x' - \cos\theta) + R_y(y' - \sin\theta)\right] \mathrm{d}\mathsf{s} - N_y\, y(l) + \\ - N_x[x(l) - d] - M_l\Big[\theta_l - \theta(l)\Big] - M_0\Big[\theta_0 - \theta(0)\Big],\end{aligned} \tag{2.4}$$

where $\mathcal{E}$ is the elastic energy stored within the rod

$$\mathcal{E} = \frac{B}{2}\int_0^l \theta'(\mathsf{s})^2\, \mathrm{d}\mathsf{s}, \tag{2.5}$$

while the quantities R_x and R_y are the Lagrangian multipliers representing the internal forces' components along the x and y directions, N_x and N_y are those related to the reaction forces at both ends along the x and y directions and, similarly, M_l and M_0 are those referred to the rotational degrees of freedom of the rod's coordinates $\mathsf{s} = l$ and $\mathsf{s} = 0$.

The fundamental variables considered in the total potential energy (2.4) are

$$\boldsymbol{w} = \{\theta,\, \theta', \theta(0),\, \theta(l),\, x(l),\, y(l),\, x',\, y', R_x,\, R_y,\, N_x,\, N_y,\, M_0,\, M_l\} \tag{2.6}$$

and where the fulfilment of the imposed boundary conditions leads to the following vanishing variations of the variables (2.6)

$$\{\delta\theta(0),\, \delta\theta(l),\, \delta x(l),\, \delta y(l)\} = \mathbf{0} \tag{2.7}$$

which are complemented by the following vanishing variations of the displacements x and y at the origin of the reference system

$$\delta x(0) = 0, \qquad \delta y(0) = 0 \tag{2.8}$$

so that the first variation becomes

$$\begin{aligned}\delta\mathcal{V} = \int_0^l \left[R_x'\delta x + R_y'\delta y\right] \mathrm{d}\mathsf{s} - \int_0^l \left[\delta R_x(x' - \cos\theta) + \delta R_y(y' - \sin\theta)\right] \mathrm{d}\mathsf{s} + \\ - \int_0^l \delta\theta\left[B\theta'' + R_x\sin\theta - R_y\cos\theta\right] \mathrm{d}\mathsf{s} - \delta N_x\left[x(l) - d\right] - \delta N_y\, y(l) + \\ - \delta M_l\Big[\theta_l - \theta(l)\Big] - \delta M_0\Big[\theta_0 - \theta(0)\Big],\end{aligned} \tag{2.9}$$

The stationarity of the total potential energy for arbitrary perturbations leads to the following system of governing equations

$$\begin{cases} R_x' = 0 \quad \rightarrow \quad R_x = \text{const}_1 & \text{(2.10a)} \\ R_y' = 0 \quad \rightarrow \quad R_y = \text{const}_2 & \text{(2.10b)} \\ x' - \cos\theta = 0 & \text{(2.10c)} \\ y' - \sin\theta = 0 & \text{(2.10d)} \\ B\theta'' + R_x \sin\theta - R_y \cos\theta = 0 & \text{(2.10e)} \\ x(l) - d = 0 & \text{(2.10f)} \\ y(l) = 0 & \text{(2.10g)} \\ \theta_l = \theta(l) & \text{(2.10h)} \\ \theta_0 = \theta(0) & \text{(2.10i)} \end{cases}$$

finally leading to the following equilibrium equation for the rotation field

$$\theta''(\mathsf{s}) + \frac{R_x}{B} \sin\theta(\mathsf{s}) - \frac{R_y}{B} \cos\theta(\mathsf{s}) = 0 \tag{2.11}$$

which is complemented by the following Dirichlet boundary conditions on the rotation field

$$\theta(0) = \theta_0, \qquad \theta(l) = \theta_l \tag{2.12}$$

and by the integral isoperimetric constraints on $\theta(\mathsf{s})$

$$0 = \int_0^l \sin\theta(\mathsf{s})\, \mathrm{d}\mathsf{s}, \qquad d = \int_0^l \cos\theta(\mathsf{s})\, \mathrm{d}\mathsf{s}, \tag{2.13}$$

Moreover, the following global equilibrium equation has to be satisfied

$$M(0) + R_y\, d - M(l) = 0 \tag{2.14}$$

where $M(0)$ and $M(l)$ are the values of the bending moment at the end coordinates $\mathsf{s} = 0$ and $\mathsf{s} = l$, respectively.

2.1 Exact solution for the governing equation

The following changes of variables are introduced

$$\psi(s) = \theta(s) - \beta, \qquad \Gamma^2 = \frac{|R|\, l^2}{B}, \qquad s = \frac{\mathsf{s}}{l} \tag{2.15}$$

where $\beta \in [-\pi, \pi]$ is the unknown angle assumed by the resultant force $|R| = \sqrt{R_x^2 + R_y^2}$ at both ends taken with respect to the x-axis (see Fig.2.1, right) and where

$$\frac{R_x\, l^2}{B} = \Gamma^2 \cos\beta, \qquad \frac{R_y\, l^2}{B} = \Gamma^2 \sin\beta \tag{2.16}$$

are the dimensionless x and y components of the reaction forces at both ends, respectively.

It is worth to underline that the proposed formulation is fully dimensionless, being referred to a curvilinear coordinate $s = \mathsf{s}/l$ defined within the interval $[0,\, 1]$ and to a dimensionless 'load' Γ^2.

The change of variables (2.15) lead to the differential equation of the Euler's elastica

$$\psi''(s) + \Gamma^2 \sin\psi(s) = 0 \qquad \forall s \in [0, 1] \tag{2.17}$$

where ' denotes now the derivative taken with respect to the dimensionless coordinate s. In the case of a non-vanishing curvature $\psi'(s)$, the equation (2.17) can be integrated as follows

$$\frac{\mathrm{d}}{\mathrm{d}s}\left[\frac{1}{2}\left(\psi'\right)^2 - \Gamma^2 \cos\psi\right] = 0, \quad \rightarrow \quad \frac{1}{2}\left(\psi'\right)^2 - \Gamma^2 \cos\psi = \mathrm{cost} \tag{2.18}$$

finally obtaining

$$\psi'(s) = \pm\Gamma\sqrt{2}\sqrt{\cos\psi(s) + \Upsilon}, \tag{2.19}$$

where Υ is the constant of integration to be evaluated with reference to the boundary conditions and defining the elastica as a part of a *non-inflectional mother curve* ($\Upsilon \in [1, \infty]$) or an *inflectional mother curve* ($\Upsilon \in [-1, 1]$) (see Love [77]).

In the following paragraphs, the exact description of the deformed configurations is presented with reference to the number $m \in \mathbb{N}^0$ of 'inflection points',

corresponding to the curvilinear coordinates within the set $s \in (0,1)$ where the curvature vanishes. It is remarked that points with null curvature located at both ends are not considered in the definition of m. For convenience, the constant of integration Υ is defined distinguishing the fundamental cases of the absence ($m = 0$) and the presence ($m \neq 0$) of inflection points and the deformed configurations are described, respectively, in terms of the equations related to the so-called *non-inflectional* and *inflectional elastica*. Therefore it is worth to remark that, differently from Love [77], the deformed configurations with $m = 0$ associated with an *inflectional mother curve* are here described for simplicity through the expressions used for the *non-inflectional mother curve* (for which the ideal unlimited elastica, $-\infty < s < \infty$, has no inflection points) but restricted to the physical range of the curvilinear coordinate, $s \in [0,1]$.

Presence of m inflection points along the rod ($m \neq 0$). In this case $\psi'(\widehat{s}_j) = 0$ at the curvilinear coordinates $\widehat{s}_j \in (0,1)$ with $j \in [1,m]$ ordering the inflection points with respect to their curvilinear coordinate, $\widehat{s}_j < \widehat{s}_{j+1}$. Eq.(2.19) implies that the integration constant Υ is a function of the angle $\psi(\widehat{s}_1) = \widehat{\psi}_1$ measured at the inflection point along the rod and closest to the origin as

$$\Upsilon = -\cos\widehat{\psi}_1. \tag{2.20}$$

so that $\Upsilon \in [-1,\,1]$. Being $\cos\widehat{\psi}_j = \cos\widehat{\psi}_1$ with $\psi(\widehat{s}_j) = \widehat{\psi}_j$ $(j = 1,...,m)$ because of Eq.(2.19), the rotation angle at the j-th inflection point is given by

$$\theta(\widehat{s}_j) = -(-1)^j\theta(\widehat{s}_1) + \left[1 + (-1)^j\right]\beta. \tag{2.21}$$

Because the curvature changes sign at each inflection point, the solution (2.19) for the curvature can be rewritten as

$$\psi'(s) = \begin{cases} (-1)^p\Gamma\sqrt{2}\sqrt{\cos\psi(s) - \cos\widehat{\psi}_1}, & \forall s \in [0,\,\widehat{s}_1], \\ (-1)^p(-1)^j\Gamma\sqrt{2}\sqrt{\cos\psi(s) - \cos\widehat{\psi}_1}, & \forall s \in [\widehat{s}_j,\,\widehat{s}_{j+1}] \quad \forall\, j \in [1, m-1], \\ (-1)^p(-1)^m\Gamma\sqrt{2}\sqrt{\cos\psi(s) - \cos\widehat{\psi}_1}, & \forall s \in [\widehat{s}_m,\,1], \end{cases} \tag{2.22}$$

where p is a boolean parameter defining the curvature sign at the left end $s = 0$, namely $p = 0$ ($p = 1$) when the curvature is positive (negative) at the left end,

$\theta'(s=0) > 0$ ($\theta'(s=0) < 0$). [1] The multiplicity of solutions given by the imposed sign $(-1)^p$ is illustrated in Fig.2.2.

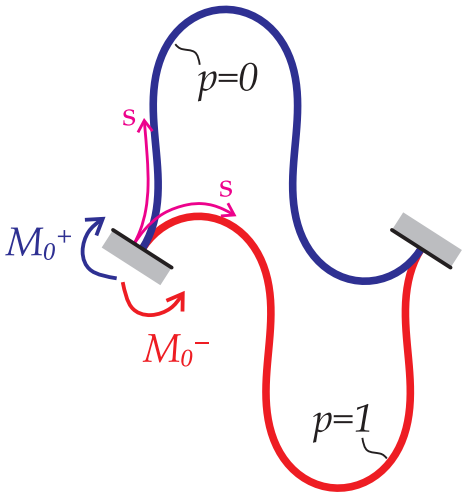

Figure 2.2: Two stable solutions for the Euler's elastica having a different sign $(-1)^p$ of the curvature at $\mathsf{s} = 0$ and satisfying the imposed rotations and displacements at both ends. The blue solution for $p = 0$ corresponds to a positive curvature, and therefore to a positive bending moment $M(0) = M_0^+$, at the initial end $\mathsf{s} = 0$. The red solution for $p = 1$ corresponds to a a configuration having a negative curvature, or equivalently a negative bending moment M_0^-, at the same end. Therefore, p plays the role of an input parameter that has to be imposed in order to focus on a solution having a specific sign of the curvature at the initial end $\mathsf{s} = 0$.

Absence of inflection points along the rod ($m = 0$). In this case $\psi'(s) \neq 0$ for $s \in (0, 1)$ and the integration constant Υ can be defined as a function of an unknown parameter ξ as

$$\Upsilon = \frac{2 - \xi^2}{\xi^2} \tag{2.23}$$

For the classical non-inflectional elastica, the parameter ξ is confined within the interval $[0, 1]$ so that the constant of integration ranges between 1 and

[1] In the case of null curvature at the initial coordinate, $\theta'(0) = 0$, the boolean p is defined by the sign of the curvature at positive infinitesimal values of the coordinate $\theta'(s = 0^+)$.

infinite, $\Upsilon \in [1, \infty)$, namely the range which is non covered by the constant of integration of the inflectional case[2]. However differently from Love [77], in the present work the range of ξ is extended to values higher than 1 in order to describe the behaviour of the curves with zero inflection points along their span but belonging to an inflectional mother curve.

The expression for the curvature (2.19) can be rewritten as

$$\psi'(s) = (-1)^p \, \Gamma \sqrt{2 \left(\cos \psi(s) + \frac{2 - \xi^2}{\xi^2} \right)} \tag{2.24}$$

where in spite of the presence of the sign function $(-1)^p$, the sign of the curvature at $s = 0$ can be proven to be constrained by the sign of the imposed rotations at both ends θ_0 and θ_l, thus implying a uniqueness of the solution in terms of the sign of $\psi'(0)$. Therefore, the value of p can not be considered an input parameter anymore for the case of elasticae having no inflection points. The mathematical proof of this statement is shown in the following sections.

An example of a solution for an elastica having no inflection points is illustrated in Fig.2.3.

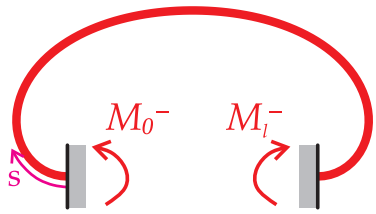

Figure 2.3: The unique stable solution for the non-inflectional Euler's elastica satisfying the imposed rotations $\theta_0 = -\theta_l = \pi$ and displacement $d = 0.4l$ at both ends. In this case, the negative sign of the internal curvature (and therefore of the bending moments at both ends M_0^- and M_l^-) corresponding to $p = 1$ is given by the sign of the imposed rotations at both ends, so that p can not be considered an input parameter for the elasticae having no inflection points anymore.

Moreover, the existence of only one deformed shape of the elastica having no inflection points has been observed for any given combination of the proper boundary conditions. This characteristic, corroborated by a recent demonstration obtained by Batista [12] of the unconditioned stability of the

[2]The limit condition $\Upsilon \to \infty$, or equivalently $\xi = 0$, represents the case of an arc of circumference with constant curvature

non-inflectional elastica subject to Dirichlet boundary conditions, seems to be related to the uniqueness of these type of solutions. However, as far as the author knows, a complete mathematical proof is still missing.

2.2 The elastica with m inflection points

An example of a deformed shape having $m = 7$ inflection points is represented in Fig.2.4, showing the periodicity of the solution. Such behaviour reveals the presence of the aforementioned inflectional mother curve, which in given by an infinite succession of a characteristic structure located between two nearby inflection points (and characterized by the same magnitude of the angle angle $\widehat{\psi}$ at both ends). Moreover, such inflection points are disposed on a line inclined at an angle β with respect to the horizontal, thus representing the inclination of the total reaction force $|R|$.

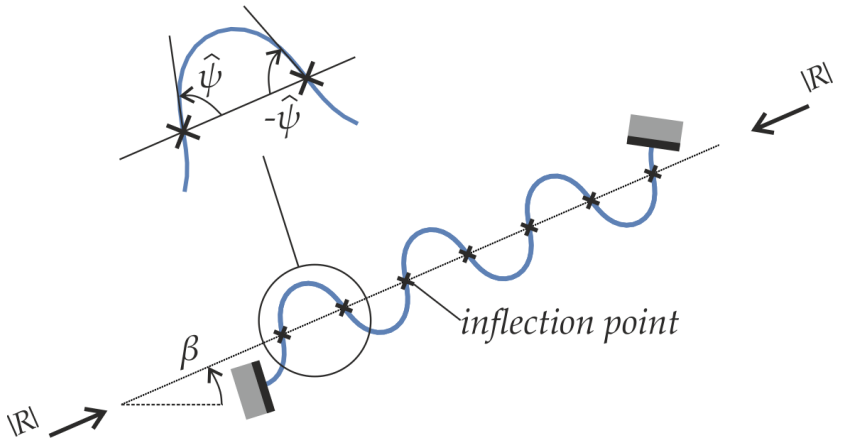

Figure 2.4: Periodic behaviour of a generic elastica with internal inflection points. The line connecting the inflection points is inclined at an angle β, which represents the inclination of the reaction force with respect to the horizontal.

Towards the achievement of a closed-form solution, it is instrumental to introduce the unknown parameter $\eta \in [0, 1]$ and the auxiliary field $\omega(s)$ defined as

$$\eta = \sin\frac{|\widehat{\psi}|}{2}, \qquad \eta \sin\omega(s) = \sin\frac{\psi(s)}{2}. \tag{2.25}$$

where $\widehat{\psi}$ represents the angle ψ at a generic inflection point, so that the following equations hold

$$\cos\psi = 1 - 2\eta^2 \sin^2\omega(s), \qquad \cos\hat{\psi} = 1 - 2\eta^2. \tag{2.26}$$

By considering the equations (2.22) and (2.25) the curvature $\psi'(s)$ can be expressed as

$$\frac{\mathrm{d}\psi}{\mathrm{d}s} = (-1)^p\, \tilde{S}\, 2\Gamma\eta\sqrt{1-\sin^2\omega} = 2\Gamma\eta\cos\omega \tag{2.27}$$

where $\tilde{S}(s)$ is a function expressing the change of sign of the curvature at each inflection point (see Eq. (2.22)) in a more compact form and where in particular

$$\tilde{S}(s)\sqrt{1-\sin^2\omega(s)} = \cos\omega(s)$$

Through the Eq.(2.25) one can write

$$\psi = 2\arcsin(\eta\sin\omega) \quad \longrightarrow \quad \mathrm{d}\psi = \frac{2}{\sqrt{1-\eta^2\sin^2\omega}}\eta\cos\omega\,\mathrm{d}\omega$$

where substitution into the Eq.(2.27) leads to the following condition

$$\frac{\mathrm{d}\omega}{\mathrm{d}s} = (-1)^p\Gamma\sqrt{1-\eta^2\sin^2\omega(s)} \tag{2.28}$$

expressing the derivative of the function ω as a function of the unknown normalized reaction force Γ, the unknown parameter η and the imposed sign of the curvature at the initial end $s = 0$ (through the integer p).

A further integration leads to the following condition

$$\int_0^s \Gamma\,\mathrm{d}s = (-1)^p \int_{\omega(0)}^{\omega(s)} \frac{\mathrm{d}w}{\sqrt{1-\eta^2\sin^2 w}} \tag{2.29}$$

corresponding to

$$\Gamma s = (-1)^p \left(\int_0^{\omega(s)} \frac{\mathrm{d}w}{\sqrt{1-\eta^2\sin^2 w}} - F(\omega(0),\,\eta) \right) \tag{2.30}$$

where

$$F(\sigma,\,\varphi) = \int_0^{\sigma} \frac{\mathrm{d}\phi}{\sqrt{1-\varphi^2\sin^2\phi}} \tag{2.31}$$

is the *Jacobi's incomplete elliptic integral of the first kind*. The 'load' parameter Γ can be therefore obtained from Eq.(2.30)

$$\Gamma = (-1)^p \left[F(\omega(1),\, \eta) - F(\omega(0),\, \eta)\right] \tag{2.32}$$

and represents a function of the values taken by the function ω at the initial $s = 0$ and final end $s = 1$.[3]

Due to the following property

$$F(\sigma, \varphi) = \int_0^{\sigma} \frac{\mathrm{d}\phi}{\sqrt{1 - \varphi^2 \sin^2 \phi}} \longrightarrow \sigma = \mathrm{am}\left[F(\sigma, \varphi),\, \varphi\right] \tag{2.33}$$

one obtains the final formulation of the function ω for the elastica having inflection points ($m \neq 0$) along its span

$$\omega(s) = (-1)^p \,\mathrm{am}\left[\Gamma s + (-1)^p\, F(\omega(0),\, \eta),\, \eta\right] \tag{2.34}$$

where $\mathrm{am}[\sigma, \varphi]$ is the *Jacobi's amplitude function*, representing a monotonic function for every $\eta \in [0,\, 1]$. Through the Eq.(2.32), the Eq.(2.34) can be rewritten as

$$\omega(s) = \mathrm{am}\left[\left[F(\omega(1),\, \eta) - F(\omega(0),\, \eta)\right] s + F(\omega(0),\, \eta),\, \eta\right] \tag{2.35}$$

where, as shown in the next Section, the sign of the initial curvature $(-1)^p$ is contained within the formulation of the term $\omega(1)$.

2.2.1 Values assumed by ω at both ends

By considering Eq.(2.25), the function ω may be obtained through the inversion of a sinus function, but restricting its image within the interval $[-\pi/2,\, \pi/2]$ despite the monotonic trend of the exact solution expressed by the Eq.(2.35). On the other hand, it is instrumental to exploit the Eq.(2.25) in order to explicitly introduce the imposed Dirichlet boundary conditions at both ends $\theta(0) = \theta_0$ and $\theta(1) = \theta_l$ (see (2.12)) through the parameters

$$w_0 = \arcsin\left[\frac{1}{\eta} \sin\left(\frac{\theta_0 - \beta}{2}\right)\right], \qquad w_1 = \arcsin\left[\frac{1}{\eta} \sin\left(\frac{\theta_l - \beta}{2}\right)\right]. \tag{2.36}$$

[3] The positiveness of the parameter Γ leads to the following conditions

$$\begin{aligned} F(\omega(1),\, \eta) > F(\omega(0),\, \eta) \quad &\rightarrow \quad \omega(1) > \omega(0) \quad \text{if} \quad p = 0 \\ F(\omega(1),\, \eta) < F(\omega(0),\, \eta) \quad &\rightarrow \quad \omega(1) < \omega(0) \quad \text{if} \quad p = 1 \end{aligned}$$

Such parameters need therefore to me manipulated in order to restore the correct expressions of $\omega(0)$ and $\omega(1)$ at both ends.

In particular, by considering the Eq.(2.27), the following condition is achieved at any inflection point

$$(-1)^p \cos\omega(\widehat{s}_j) = 0 \tag{2.37}$$

By imposing an initial value $\omega(0) = w_0$ within the interval $[-\pi/2, \pi/2]$[4] and due to the monotonic trend of the function ω, the value assumed by $\omega(\widehat{s}_{j+1})$ at any inflection point $\widehat{s}_{j+1}$ has to be equal to the one at the inflection point $\widehat{s}_j$ but incremented of a factor $(-1)^p\pi$, such that

$$\omega(\widehat{s}_1) = (-1)^p\frac{\pi}{2}, \quad \omega(\widehat{s}_2) = (-1)^p\frac{3\pi}{2}, \qquad \dots \tag{2.38}$$

Therefore, the values of the function $\omega(s)$ attained at the two ends, $\omega(s = 0) = \omega_0$ and $\omega(s = 1) = \omega_1$ as a function of the imposed number of inflection points m and the sign of the initial curvature $(-1)^p$ can be defined as

$$\begin{aligned} \omega_0 &= \arcsin\left[\frac{1}{\eta}\sin\left(\frac{\theta_0 - \beta}{2}\right)\right], \\ \omega_1 &= (-1)^m \arcsin\left[\frac{1}{\eta}\sin\left(\frac{\theta_l - \beta}{2}\right)\right] + (-1)^p\, m\pi, \end{aligned} \tag{2.39}$$

representing the fundamental parameters involved in the problem's resolution, which depend on the unknown parameters β and η.

The main advantage introduced by the relations (2.39) is represented by their generality. In particular, any combination of the imposed boundary conditions $[\theta_0, \theta_l]$, the number of inflection points m and the sign function $(-1)^p$ can be explicitly introduced within the mathematical framework, allowing for the exact evaluation of any deformed shape corresponding to the chosen input data.

However, it is worth to underline that the presented equations are valid for the case $m > 0$ only, while the treatise of the non-inflectional equations having $m = 0$ is deferred to Section 2.3.

[4]It is observed that a 'shifting' in the function ω of a constant factor does not modify the corresponding solution for the elastica.

2.2.2 The exact solution for the elastica with m inflection points

The Eq.(2.35) can be substituted within the condition (2.25) obtaining the exact solution for the angle $\psi(s)$

$$\psi(s) = 2\arcsin\left[\eta\,\mathrm{sn}\left[\left[F(\omega_1,\,\eta) - F(\omega_0,\,\eta)\right]s + F(\omega_0,\,\eta),\,\eta\right]\right] \tag{2.40}$$

where ω_0 and ω_1 are given by the equations (2.39).

For the sake of brevity, the following function is introduced

$$\mathcal{G}_m(s,\,\omega_1,\,\omega_0) = \left[F(\omega_1,\,\eta) - F(\omega_0,\,\eta)\right]s + F(\omega_0,\,\eta) \tag{2.41}$$

Through the Eq.(2.15) and (2.41), the exact expression for the function $\theta(s)$ is given by

$$\theta(s) = 2\arcsin\left[\eta\,\mathrm{sn}\left[\mathcal{G}_m(s,\,\omega_1,\,\omega_0),\,\eta\right]\right] + \beta \tag{2.42}$$

representing the exact formulation of the rotation field for the Euler's elastica having $m > 0$ inflection points as a function of the unknown parameters η and β, where $\mathrm{sn}[\sigma,\,\varphi] = \sin\left(\mathrm{am}[\sigma,\,\varphi]\right)$ is the *Jacobi's sine amplitude function*.

The exact expression for the curvature $\psi' = \theta'$ can be achieved through the derivation of the equation (2.40). Due to the following property of the elliptic functions

$$\begin{aligned}&\frac{\partial}{\partial\sigma}\mathrm{am}[\sigma,\,\varphi] = \sqrt{1-\varphi^2\mathrm{sn}^2[\sigma,\,\varphi]}\\ &\mathrm{dn}[\sigma,\,\varphi] = \sqrt{1-\varphi^2\mathrm{sn}^2[\sigma,\,\varphi]}\end{aligned} \tag{2.43}$$

where $\mathrm{dn}[\sigma,\,\varphi]$ is the *Jacobi's elliptic function*, the following expression for the rod's curvature holds

$$\theta'(s) = 2\eta\left[F(\omega_1,\,\eta) - F(\omega_0,\,\eta)\right]\,\mathrm{cn}\left[\mathcal{G}_m(s,\,\omega_1,\,\omega_0),\,\eta\right] \tag{2.44}$$

where $\mathrm{cn}[\sigma,\,\varphi] = \cos\left(\mathrm{am}[\sigma,\,\varphi]\right)$ is the *Jacobi's cosine amplitude function*.

The inextensibility constraint (2.2) can be exploited through the Eq.(2.42), so that through the well-known properties of trigonometric functions one obtains

$$\begin{bmatrix}x'(s)\\ y'(s)\end{bmatrix} = \begin{bmatrix}\cos\beta & -\sin\beta\\ \sin\beta & \cos\beta\end{bmatrix}\cdot\begin{bmatrix}\mathcal{A}_m(s)\\ \mathcal{B}_m(s)\end{bmatrix} \tag{2.45}$$

where

$$\begin{aligned}\mathcal{A}_m(s) &= 1 - 2\eta^2 \,\mathrm{sn}^2\left[\mathcal{G}_m(s,\,\omega_1,\,\omega_0),\,\eta\right]\\ \mathcal{B}_m(s) &= 2\eta\,\mathrm{sn}\left[\mathcal{G}_m(s,\,\omega_1,\,\omega_0),\,\eta\right]\,\mathrm{dn}\left[\mathcal{G}_m(s,\,\omega_1,\,\omega_0),\,\eta\right]\end{aligned} \tag{2.46}$$

A further integration of the Eqs.(2.45) leads to the exact expression for the deformed shape of the Euler's elastica having m inflection points. In particular, the following properties are needed

$$\begin{aligned}&\frac{\partial}{\partial\sigma}\mathrm{cn}[\sigma,\,\varphi] = -\mathrm{sn}[\sigma,\,\varphi]\,\mathrm{dn}[\sigma,\,\varphi]\\ &\frac{\partial}{\partial\sigma}\mathscr{E}[\sigma,\,\varphi] = \mathrm{dn}^2[\sigma,\,\varphi]\end{aligned}$$

where $\mathscr{E}$ is the *Jacobi's epsilon function*

$$\mathscr{E}\left[\sigma,\,\varphi\right] = E(\mathrm{am}(\sigma,\,\varphi),\,\varphi) \tag{2.48}$$

and E is the *Jacobi's incomplete elliptic integral of the second kind*

$$E\left(\sigma,\,\varphi\right) = \int_0^{\sigma} \sqrt{1-\varphi^2\sin^2\phi}\,\mathrm{d}\phi. \tag{2.49}$$

The final expression for the deformed shape of the rod is obtained

$$\begin{bmatrix} x(s)/l \\ y(s)/l \end{bmatrix} = \begin{bmatrix} \cos\beta & -\sin\beta \\ \sin\beta & \cos\beta \end{bmatrix} \cdot \begin{bmatrix} \mathbb{A}_m(s) \\ \mathbb{B}_m(s) \end{bmatrix} \tag{2.50}$$

where

$$\begin{aligned}\mathbb{A}_m(s) &= \int_0^s \mathcal{A}_m(\varsigma)\mathrm{d}\varsigma = 2\frac{\mathscr{E}\left[\mathcal{G}_m(s,\,\omega_1,\,\omega_0),\,\eta\right] - \mathscr{E}\left[F(\omega_0,\,\eta),\,\eta\right]}{F(\omega_1,\,\eta) - F(\omega_0,\,\eta)} - s\\ \mathbb{B}_m(s) &= \int_0^s \mathcal{B}_m(\varsigma)\mathrm{d}\varsigma = 2\,\eta\,\frac{\mathrm{cn}\left[F(\omega_0,\,\eta),\,\eta\right] - \mathrm{cn}\left[\mathcal{G}_m(s,\,\omega_1,\,\omega_0),\,\eta\right]}{F(\omega_1,\,\eta) - F(\omega_0,\,\eta)}\end{aligned} \tag{2.51}$$

Finally, the exact expression for the dimensionless elastic energy (2.5) is obtained through the equation of the curvature of the rod (2.44). After many calculations, the following expression is obtained

$$\begin{aligned}\frac{\mathcal{E}}{B}l = 2\left[F(\omega_1,\,\eta) - F(\omega_0,\,\eta)\right]^2 \Bigg(&\int_0^1 \mathrm{dn}^2\left[\mathcal{G}_m(s,\,\omega_1,\,\omega_0),\,\eta\right]\mathrm{d}s + \\ &- \int_0^1 (1-\eta^2)\mathrm{d}s\Bigg)\end{aligned} \tag{2.52}$$

leading to the final expression for the elastic energy

$$\frac{\mathcal{E}}{B}l = 2\big[F(\omega_1,\,\eta) - F(\omega_0,\,\eta)\big]^2 \left[\frac{E(\omega_1,\,\eta) - E(\omega_0,\,\eta)}{F(\omega_1,\,\eta) - F(\omega_0,\,\eta)} - (1-\eta^2)\right] \quad (2.53)$$

2.2.3 Evaluation of the unknown parameters η and β

In the previous sections, the exact solution for the rotation field θ has been obtained. The imposed rotations at both ends θ_0 and θ_l (see Eq.(2.12)), together with the imposed values of the sign of the curvature $(-1)^p$ at $s = 0$ and the number of inflection points m are explicitly introduced through the parameters ω_1 and ω_0 in the expressions (2.39).

However, the solution is a function of two unknown parameters, namely given by η, representing the characteristic parameter of the elastica, and the angle β representing the inclination of the reaction force $|R|$ with respect to the x-axis. The values of $[\eta,\,\beta]$ corresponding to the imposed set of boundary conditions are therefore obtained by exploiting the further integral equations expressing the isoperimetric constraints (2.13), which can be in turn expressed through the exact solution for the deformed shape of the elastic rod given by Eq.(2.50).

The functions $\mathbb{A}_m$ and $\mathbb{B}_m$ evaluated at the final end of the rod $s = 1$ are given by

$$\begin{aligned}
\mathbb{A}_m(1) &= 2\frac{E\,(\omega_1,\,\eta) - E\,(\omega_0,\,\eta)}{F(\omega_1,\,\eta) - F(\omega_0,\,\eta)} - 1 \\
\mathbb{B}_m(1) &= 2\,\eta\,\frac{\cos\omega_0 - \cos\omega_1}{F(\omega_1,\,\eta) - F(\omega_0,\,\eta)}
\end{aligned} \quad (2.54)$$

such that the isoperimetric constraints (2.13) assume the following form

$$\begin{bmatrix} d/l \\ 0 \end{bmatrix} = \begin{bmatrix} \cos\beta & -\sin\beta \\ \sin\beta & \cos\beta \end{bmatrix} \cdot \begin{bmatrix} \mathbb{A}_m(1) \\ \mathbb{B}_m(1) \end{bmatrix} \quad (2.55)$$

Finally, the following non-linear system is obtained

$$\begin{cases} d/l\cos\beta = \mathbb{A}_m(1), \\ d/l\sin\beta = -\mathbb{B}_m(1), \end{cases} \quad (2.56)$$

whose roots provide all the couples of the unknown parameters $[\eta,\,\beta]$ corresponding to the combination of the imposed kinematical conditions at both ends. In particular, the non-linearity of the system (2.56) leads to possible non-uniqueness for the equilibrium configuration, providing interesting conditions of

bifurcation or snap instability during a quasi-static variation of the boundary conditions.

Finally, the Eq.(2.14) governing the global equilibrium of the Euler's elastica is satisfied. In fact, the dimensionless equation of Eq.(2.14)

$$\theta'(0) + \frac{R_y\, l^2}{B}\,\frac{d}{l} - \theta'(1) = 0 \tag{2.57}$$

is automatically verified by substituting the exact expressions of the curvature at both ends $\theta'(0)$ and $\theta'(1)$ (Eq.(2.44)), the expression for the reaction force R_y (Eq.(2.16)), the load parameter Γ (Eq.(2.32)) and the imposed displacement $d/l = -\mathbb{B}_m(1)/\sin\beta$ (through Eqs.(2.56)).

As a final remark, the proposed exact solution for the Euler's elastica can be directly exploited to attack various boundary value problems, so that the present formulation can also be considered to treat structural systems as an alternative to previously adopted procedures[124]. In fact, different boundary conditions, corresponding in general to different sets of unknown parameters (which are always contained within the set $\{\eta, \beta, \theta(0), \theta(1)\}$), can be considered by properly re-arranging the non-linear system (2.56).

2.3 The elastica with $m = 0$ inflection points

The governing equations of an Euler's elastica having no inflection points within its span are obtained in this Section, thus representing solutions exhibiting a constant sign of the curvature at any coordinate $s \in (0\,1)$.

Under this circumstance, the imposed boundary conditions are such that the bending moment cannot vanish at any internal point, with the exception of limit configurations exhibiting a null curvature exactly at one or both ends $s = 0$ and $s = 1$. As previously sentenced at the end of Section 2.1, the expressions used for the *non-inflectional mother curve*[77] are here extended to elasticae belonging to *inflectional mother curves* but exhibiting no inflection point within the restricted domain $s \in (0, 1)$.

The Eq.(2.24) expressing the curvature ψ' along the span of the rod is firstly rewritten in the following form

$$\psi'(s) = (-1)^p\,\frac{2\Gamma}{\xi}\sqrt{1 - \xi^2 \sin^2\left(\frac{\psi(s)}{2}\right)} \tag{2.58}$$

Furthermore, an auxiliary rotation field is introduced as

$$\zeta(s) = \frac{\psi(s)}{2} \tag{2.59}$$

whose values at the two ends are defined as $\zeta(0) = \zeta_0$ and $\zeta(1) = \zeta_1$, can be directly explicitly expressed as a function of the imposed ends rotations, thus

$$\zeta_0 = \frac{\theta_0 - \beta}{2}, \qquad \zeta_1 = \frac{\theta_l - \beta}{2}. \tag{2.60}$$

The equation (2.58) can be therefore rewritten as

$$\zeta'(s) = (-1)^p \frac{\Gamma}{\xi} \sqrt{1 - \xi^2 \sin^2 \zeta(s)} \tag{2.61}$$

expressing the counterpart of the Eq.(2.28) for the elastica having no inflection points. A first integration of equation (2.61) leads to

$$\int_0^s \frac{\Gamma}{\xi} \, \mathrm{d}s = (-1)^p \int_{\zeta_0}^{\zeta(s)} \frac{\mathrm{d}\phi}{\sqrt{1 - \xi^2 \sin^2 \phi}} \tag{2.62}$$

or equivalently

$$\frac{\Gamma}{\xi} \, s = (-1)^p \left(\int_0^{\zeta(s)} \frac{\mathrm{d}\phi}{\sqrt{1 - \xi^2 \sin^2 \phi}} - F(\zeta_0, \, \xi) \right) \tag{2.63}$$

The load parameter Γ can be therefore expressed as

$$\Gamma = (-1)^p \xi \left[F(\zeta_1, \, \xi) - F(\zeta_0, \, \xi) \right] \tag{2.64}$$

where due to its positiveness (see Eq.(2.15))

$$\begin{cases} p = 1 & \rightarrow & F(\zeta_0, \, \xi) > F(\zeta_1, \, \xi) & \rightarrow & \zeta_0 > \zeta_1 \\ p = 0 & \rightarrow & F(\zeta_0, \, \xi) < F(\zeta_1, \, \xi) & \rightarrow & \zeta_0 < \zeta_1 \end{cases}$$

so that through the Eqs.(2.60) one can demonstrate that the choice of the imposed rotation boundary conditions θ_0 and θ_l leads necessarily to a certain sign of the curvature at $s = 0$, namely

$$\begin{aligned} p = 1 \quad & \leftrightarrow \quad \theta_0 > \theta_l \\ p = 0 \quad & \leftrightarrow \quad \theta_l > \theta_0 \end{aligned} \tag{2.65}$$

so that the parameter p does not represent a true input parameter for the evaluation of an elastica without inflection points, being it fully determined by the values of the imposed rotations at both ends.

The Eq.(2.63) is finally exploited obtaining the general solution for the elastica with no inflection points

$$\zeta(s) = (-1)^p \operatorname{am}\left[\frac{\Gamma}{\xi}\, s + (-1)^p\, F(\zeta_0,\, \xi),\, \xi\right] \tag{2.66}$$

or equivalently through Eq.(2.64)

$$\zeta(s) = \operatorname{am}\left[\left[F(\zeta_1,\, \xi) - F(\zeta_0,\, \xi)\right] s + F(\zeta_0,\, \xi),\, \xi\right] \tag{2.67}$$

Finally, it is remarked that when the deformed configuration is associated with an inflectional mother curve, $\Upsilon \in [-1, 1]$, but there are no inflection points along the rod, $m = 0$, the exact representation of the normalized load Γ and of the rotation field $\psi(s) = 2\zeta(s)$ for the case $m = 0$ coincides with that for the case $m \neq 0$.[5]

2.3.1 The exact solution for the elastica with no inflection points $m = 0$

The rotation filed ψ can be obtained exploiting the equation (2.59), thus

$$\psi(s) = 2 \operatorname{am}\left[\left[F(\zeta_1,\, \xi) - F(\zeta_0,\, \xi)\right] s + F(\zeta_0,\, \xi),\, \xi\right] \tag{2.70}$$

For the sake of brevity, the following function is introduced

$$\mathcal{G}_0(s,\, \zeta_1,\, \zeta_0) = \left[F(\zeta_1,\, \xi) - F(\zeta_0,\, \xi)\right] s + F(\zeta_0,\, \xi) \tag{2.71}$$

Through the Eq.(2.15) and (2.71), the expression for the unknown rotation field $\theta(s)$ is obtained

$$\theta(s) = 2 \operatorname{am}\left[\mathcal{G}_0(s,\, \zeta_1,\, \zeta_0),\, \xi\right] + \beta \tag{2.72}$$

[5] In addition to the general property for the reciprocal modulus transformation for the Jacobi's sine amplitude function (Byrd [27], his Eq.162.01, pag 38)

$$\operatorname{sn}\left(\sigma\varphi,\, \frac{1}{\varphi}\right) = \varphi\, \operatorname{sn}\left(\sigma, \varphi\right), \tag{2.68}$$

under the circumstance $\Upsilon \in [-1, 1]$ and $m = 0$ the following properties hold:

$$\xi = 1/\eta, \qquad \sin\omega(s) = \xi \sin\zeta(s), \qquad F\left(\omega(s),\, \eta\right) = \xi F\left(\zeta(s),\, \xi\right). \tag{2.69}$$

representing the exact formulation of the rotation field for the Euler's elastica having no inflection points. The expression (2.72) is again a function of two unknown parameters, namely ξ and β, representing the unknown parameter of the elastica and the inclination of the total reaction force at both ends, respectively.

The exact expression for the curvature $\psi' = \theta'$ can be achieved through derivation of the Eq.(2.70), which by means of the following property

$$\frac{\partial}{\partial\sigma}\mathrm{am}[\sigma,\,\varphi] = \mathrm{dn}[\sigma,\,\varphi]$$

leads to the following expression

$$\theta'(s) = 2\left[F(\zeta_1,\,\xi) - F(\zeta_0,\,\xi)\right]\,\mathrm{dn}\left[\mathcal{G}_0(s,\,\zeta_1,\,\zeta_0),\,\xi\right]. \tag{2.73}$$

where the positive sign of the elliptic function $\mathrm{dn}\,[\sigma,\,\varphi] \geq 0$ causes a never sign-changing curvature within the whole domain $s \in (0,\,1)$. It is also remarked that an acceptable solution may also be characterized by a vanishing moment exactly at one or at both ends of the rod, while the 'inflectional' solution is needed in all the other cases. Moreover, the sign of the curvature is entirely specified by the difference of the two integrals $F(\zeta_1,\,\xi) - F(\zeta_0,\,\xi)$, and namely by the difference of the imposed angles at both ends $\theta_l - \theta_0$.

The inextensibility constraint (2.2) is exploited through the Eq.(2.72) leading to

$$\begin{bmatrix} x'(s) \\ y'(s) \end{bmatrix} = \begin{bmatrix} \cos\beta & -\sin\beta \\ \sin\beta & \cos\beta \end{bmatrix} \cdot \begin{bmatrix} \mathcal{A}_0(s) \\ \mathcal{B}_0(s) \end{bmatrix} \tag{2.74}$$

where

$$\begin{aligned} \mathcal{A}_0(s) &= -\frac{2-\xi^2}{\xi^2} + \frac{2}{\xi^2}\mathrm{dn}^2\left[\mathcal{G}_0(s,\,\zeta_1,\,\zeta_0),\,\xi\right] \\ \mathcal{B}_0(s) &= 2\,\mathrm{sn}\left[\mathcal{G}_0(s,\,\zeta_1,\,\zeta_0),\,\xi\right]\,\mathrm{cn}\left[\mathcal{G}_0(s,\,\zeta_1,\,\zeta_0),\,\xi\right] \end{aligned} \tag{2.75}$$

A further integration of the Eqs.(2.74) leads to the exact expression for the deformed shape of the Euler's elastica having no inflection points. The following properties are needed

$$\begin{aligned} &\frac{\partial}{\partial\sigma}\mathrm{dn}[\sigma,\,\varphi] = -\varphi^2\,\mathrm{sn}[\sigma,\,\varphi]\,\mathrm{cn}[\sigma,\,\varphi] \\ &\frac{\partial}{\partial\sigma}\mathscr{E}[\sigma,\,\varphi] = \mathrm{dn}^2[\sigma,\,\varphi] \end{aligned}$$

so that the final expression for the deformed shape of the rod is obtained

$$\begin{bmatrix} x(s)/l \\ y(s)/l \end{bmatrix} = \begin{bmatrix} \cos\beta & -\sin\beta \\ \sin\beta & \cos\beta \end{bmatrix} \cdot \begin{bmatrix} \mathbb{A}_0(s) \\ \mathbb{B}_0(s) \end{bmatrix} \tag{2.77}$$

where

$$\begin{aligned} \mathbb{A}_0(s) &= \int_0^s \mathcal{A}_0(\varsigma)\mathrm{d}\varsigma = \frac{2}{\xi^2}\left(\frac{\mathscr{E}\left[\mathcal{G}_0(s,\,\zeta_1,\,\zeta_0),\,\xi\right] - \mathscr{E}\left[F(\zeta_0,\,\xi),\,\xi\right]}{F(\zeta_1,\,\xi) - F(\zeta_0,\,\xi)} - \frac{2-\xi^2}{2}s\right) \\ \mathbb{B}_0(s) &= \int_0^s \mathcal{B}_0(\varsigma)\mathrm{d}\varsigma = \frac{2}{\xi^2}\,\frac{\mathrm{dn}\left[F(\zeta_0,\,\xi),\,\xi\right] - \mathrm{dn}\left[\mathcal{G}_0(s,\,\zeta_1,\,\zeta_0),\,\xi\right]}{F(\zeta_1,\,\xi) - F(\zeta_0,\,\xi)} \end{aligned} \tag{2.78}$$

Finally, the exact expression for the elastic energy (2.5) is obtained through the equation of the curvature of the rod (2.73). After many calculations, the following expression for the dimensionless energy is obtained

$$\frac{\mathcal{E}}{B}l = 2\left[F(\zeta_1,\,\xi) - F(\zeta_0,\,\xi)\right]^2 \int_0^1 \mathrm{dn}^2\left[\mathcal{G}_0(s,\,\zeta_1,\,\zeta_0),\,\xi\right]\mathrm{d}s \tag{2.79}$$

leading to the final expression for the elastic energy

$$\frac{\mathcal{E}}{B}l = 2\left[F(\zeta_1,\,\xi) - F(\zeta_0,\,\xi)\right]\left[E(\zeta_1,\,\xi) - E(\zeta_0,\,\xi)\right] \tag{2.80}$$

2.3.2 Evaluation of the unknown parameters ξ and β

The solution for the Euler's elastica having no inflection points has been obtained, showing its dependence on the imposed rotations at both ends θ_0 and θ_l (2.12). Differently from the case of presence of inflection points, the sign of the curvature $(-1)^p$ does not represent an input parameter, being it prescribed once the rotational boundary conditions are imposed to the system. Moreover, the parameter m is constrained to be equal to 0.

The solution is now a function of two unknown parameters, namely given by ξ, representing the characteristic parameter of the elastica, and the angle β representing the inclination of the reaction force $|R|$ with respect to the x-axis. Again, the unkonown $[\xi,\,\beta]$ are obtained by exploiting the further integral equations expressing the isoperimetric constraints (2.13), which can be now expressed through the exact solution for the 'non-inflectional' deformed shape given by the Eq.(2.77).

The functions $\mathbb{A}_0$ and $\mathbb{B}_0$ evaluated at the $s = 1$ end of the rod are given by

$$\begin{aligned} \mathbb{A}_0(1) &= \frac{2}{\xi^2}\left(\frac{E(\zeta_1, \xi) - E(\zeta_0, \xi)}{F(\zeta_1, \xi) - F(\zeta_0, \xi)} - \frac{2-\xi^2}{2}\right) \\ \mathbb{B}_0(1) &= \frac{2}{\xi^2}\,\frac{\sqrt{1-\xi^2\sin^2\zeta_0} - \sqrt{1-\xi^2\sin^2\zeta_1}}{F(\zeta_1, \xi) - F(\zeta_0, \xi)} \end{aligned} \tag{2.81}$$

such that the isoperimetric constraints (2.13) assume the following form

$$\begin{bmatrix} d/l \\ 0 \end{bmatrix} = \begin{bmatrix} \cos\beta & -\sin\beta \\ \sin\beta & \cos\beta \end{bmatrix} \cdot \begin{bmatrix} \mathbb{A}_0(1) \\ \mathbb{B}_0(1) \end{bmatrix} \tag{2.82}$$

Finally, the following non-linear system is obtained

$$\begin{cases} d/l\cos\beta = \mathbb{A}_0(1), \\ d/l\sin\beta = -\mathbb{B}_0(1), \end{cases} \tag{2.83}$$

whose roots provide all the couples of the unknown parameters $[\xi, \beta]$ corresponding to any combination of the imposed kinematical conditions at both ends. It is worth to underline that for any given combination of the boundary conditions corresponding to the existence of elasticae having no inflection points, the number of the obtained solutions of this type is found to be always equal to one. This observation strongly suggests the uniqueness of the solution for elasticae having no inflection points and subject to Dirichlet boundary conditions, even though no mathematical proofs have been obtained by the author.

As for the elastica with inflection points, the Eq.(2.14) governing the global equilibrium is satisfied. Such condition can be easily proved by substituting exact expressions of the quantities $\theta'(0)$, $\theta'(1)$, R_y, Γ and d introduced in the present Section.

3

The exact solution for the Reissner beam

In this chapter, the exact formulation of a shear-deformable and extensible beam undergoing large rotations and subject to kinematically controlled boundary conditions at both ends is proposed. More specifically, the beam is modelled through the kinematics proposed by Reissner [97], where the unknown deformed shape, together with the unknown internal quantities and measures of strain, is expressed in a referential description, as a function of the curvilinear coordinate $\mathsf{s} \in [0, l]$, which is defined along the centerline of the unstressed and straight configuration. As for the case of the Euler's elastica, a local reference system $x - y$ is adopted, so that rigid motions can be neglected, and self-contact phenomena are disergarded. Moreover, neither distributed nor concentrated loads are applied within the span of the beam, which is only deformed through the imposition of displacements and rotations of the cross sections at both ends $\mathsf{s} = 0$ and $\mathsf{s} = l$. The general closed-form solution for the Reissner beam is obtained following the works of Batista[9, 11] and Goto et al.[51], where in particular the closed-form solution for the 'non-inflectional' Reissner beam (without points of null curvature within its span) was not considered, so that it is addressed here for the first time.

Following Reissner [97], the fundamental kinematical fields are represented by the rotation angle $\theta(\mathsf{s})$, which measures the rotation of the generic cross

section with respect to the x-axis, the angle $\chi(\mathsf{s})$, representing the rotational gap (null for an Euler's elastica) between the normal to the cross section and the tangent to the centerline, and the strain $e(\mathsf{s})$ of the centerline; in this way, the total length of the centerline in its deformed configuration is given by

$$L = [1 + e(l)]\, l. \tag{3.1}$$

The kinematical fields are sketched in Fig.3.1 together with a (calculated) deformed shape of the Reissner beam, showing how the generic cross sections are not in general orthogonal to the centerline (because the rotation field χ does not vanish).

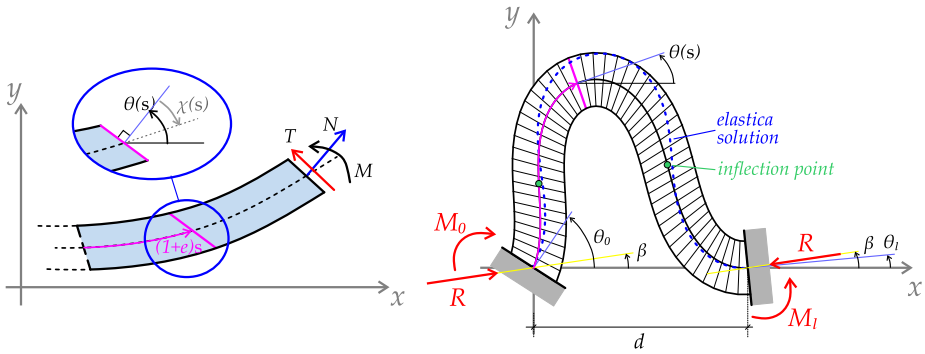

Figure 3.1: (Left) Inclination of the cross section $\theta(\mathsf{s})$ (positive when anticlockwise) with respect to the x-axis. The angle $\chi(\mathsf{s})$ measures the gap between the cross section normal and the tangent to the centerline, so that this angle is null for the Euler's elastica. The strain measure $e(\mathsf{s})$ represents the elongation of the centerline. The internal axial and shear forces (N and T respectively) and the bending moment M are also shown (assumed positive). (Right) Deformed shape of the Reissner beam with imposed displacements and rotations of the cross sections at both ends compared to the solution for the Euler's elastica (dashed-blue).

The following kinematical conditions determine the derivative of coordinates x and y of the deformed centerline

$$\begin{aligned} x'(\mathsf{s}) &= (1+e)\cos(\theta+\chi), \\ y'(\mathsf{s}) &= (1+e)\sin(\theta+\chi), \end{aligned} \tag{3.2}$$

which are taken in accordance with Fig.3.2.

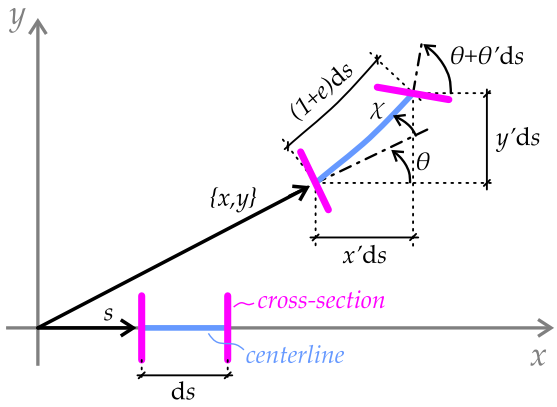

Figure 3.2: Geometrical representation of the kinematics of the Reissner beam. An element of length ds is mapped onto a deformed element of length $(1+e)$ds. The angle χ represents the gap between the normal to the cross-section (purple) and the tangent to the centerline (blue), while θ represents the inclination of the normal to the cross-section with respect to the x axis. The components x' and y' in Eqs.(3.2) are also highlighted.

It is instrumental now to introduce the following strain measures

$$\begin{cases} \varepsilon = (1+e)\cos\chi - 1 \\ \gamma = (1+e)\sin\chi, \end{cases} \tag{3.3}$$

so that $\varepsilon(\mathsf{s})$ and $\gamma(\mathsf{s})$ represent the axial strain and the shear deformation, respectively, which are non-linear functions of the aforementioned unknown fields $e(\mathsf{s})$ and $\chi(\mathsf{s})$. In particular, the following limitation is introduced[11]

$$1+\varepsilon > 0 \tag{3.4}$$

so that the deformed centerline of the rod can not 'contract' into a point ($e > -1$) and χ is restricted to the range $-\pi/2, \pi/2$, thus preventing the normal to the cross section to overcome the inclination orthogonal to the centerline.

The kinematical conditions (3.2) can be expressed in terms of the new strain measures,

$$\begin{aligned} x'(\mathsf{s}) &= (1+\varepsilon)\cos\theta - \gamma\sin\theta, \\ y'(\mathsf{s}) &= (1+\varepsilon)\sin\theta + \gamma\cos\theta, \end{aligned} \tag{3.5}$$

so that the coordinates of the centerline can be obtained as

$$\begin{aligned} x(\mathsf{s}) &= \int_0^{\mathsf{s}} ((1+\varepsilon)\cos\theta - \gamma\sin\theta)\,\mathrm{d}\varsigma, \\ y(\mathsf{s}) &= \int_0^{\mathsf{s}} ((1+\varepsilon)\sin\theta + \gamma\cos\theta)\,\mathrm{d}\varsigma, \end{aligned} \tag{3.6}$$

which reduce to the equations holding for the Euler's elastica when $\varepsilon = \gamma = 0$, which in turn correspond to $e = \chi = 0$.

It is worth to underline that, except for the condition (3.4), no restrictions are imposed on the magnitude of the unknown rotations and displacements of the deformed configurations. Thus, the position fields (3.6) represent the exact formulation for a planar beam undergoing finite shear and axial deformations, under the assumption that the cross sections remain straight.

As for the Euler's elastica, see Chapter 2, both ends are assumed to be constrained through kinematical boundary conditions in terms of positions and rotations, while only the quasi-static case is addressed. Such boundary conditions are represented by

$$x(l) = d, \qquad \theta(0) = \theta_0, \qquad \theta(l) = \theta_l, \tag{3.7}$$

where no upper-bound restrictions are imposed to $d > 0$, because the beam is extensible. Moreover, the boundary conditions θ_0 and θ_l represent now the imposed inclinations of the cross sections at both ends.

A linear elastic constitutive law is introduced for the bending moment $M(\mathsf{s})$ and for the axial and shear internal actions $N(\mathsf{s})$ and $T(\mathsf{s})$

$$\begin{cases} M(\mathsf{s}) = B\,\theta'(\mathsf{s}) \\ N(\mathsf{s}) = EA\,\varepsilon(\mathsf{s}) \\ T(\mathsf{s}) = GA_s\,\gamma(\mathsf{s}) \end{cases} \tag{3.8}$$

where the symbol $'$ stands for the derivative with respect to the curvilinear coordinate s and B, EA and GA_s are the constant bending, axial and shear stiffness, respectively, which are assumed to be independent of the current deformation of the system. Moreover, the axial and shear internal actions $N(\mathsf{s})$ and $T(\mathsf{s})$ are respectively the normal and parallel components of the total internal action with respect to the cross section.

The total potential energy $\mathcal{V}$ for the Reissner beam can be expressed as

$$\begin{aligned}\mathcal{V} =&\mathcal{E} + R_x \left[-d + \int_0^l \left((1+\varepsilon)\cos\theta - \gamma\sin\theta\right) \mathrm{d}\mathsf{s}\right] + \\ &+ R_y \int_0^l \left((1+\varepsilon)\sin\theta + \gamma\cos\theta\right) \mathrm{d}\mathsf{s} - M_l\left[\theta_l - \theta(l)\right] + \\ &- M_0\left[\theta_0 - \theta(0)\right],\end{aligned} \tag{3.9}$$

where in contrast with the formulation introduced for the Euler's elastica (2.4), the holonomic constraints $x(l) = d$ and $y(l) = 0$ are made explicit through the displacement fields (3.6). The elastic energy $\mathcal{E}$ stored within the beam is a quadratic form of the introduced strain measures

$$\mathcal{E} = \frac{1}{2}\int_0^l \left(B\,\theta'^2 + EA\,\varepsilon^2 + GA_s\,\gamma^2\right) \mathrm{d}\mathsf{s}. \tag{3.10}$$

The quantities R_x and R_y are Lagrangian multipliers representing the reaction forces at both ends along the x and y directions and M_l and M_0 are the reaction bending moments at the ends $\mathsf{s} = l$ and $\mathsf{s} = 0$, respectively.

The fundamental variables considered in the total potential energy (3.9) are in this case , $\theta(0)$, $\theta(l)$,

$$\boldsymbol{w} = \{\theta,\, \theta', \theta(0),\, \theta(l),\, \varepsilon,\, \gamma,\, R_x,\, R_y,\, M_0,\, M_l\}, \tag{3.11}$$

where the fulfilment of the imposed boundary conditions imposes the vanishing of the variations

$$\{\delta\theta(0),\, \delta\theta(l)\} = \mathbf{0}. \tag{3.12}$$

The first variation of the total potential energy is

$$\begin{aligned}&\delta\mathcal{V} = \\ &-\int_0^l \delta\theta\left[B\theta'' + R_x\left((1+\varepsilon)\sin\theta + \gamma\cos\theta\right) - R_y\left((1+\varepsilon)\cos\theta - \gamma\sin\theta\right)\right] \mathrm{d}\mathsf{s} + \\ &+\int_0^l \delta\varepsilon\left[EA\,\varepsilon + R_x\cos\theta + R_y\sin\theta\right] \mathrm{d}\mathsf{s} + \int_0^l \delta\gamma\left[GA_s\gamma - R_x\sin\theta + R_y\cos\theta\right] \mathrm{d}\mathsf{s} + \\ &+\delta R_x\left[\int_0^l \left((1+\varepsilon)\cos\theta - \gamma\sin\theta\right) \mathrm{d}\mathsf{s} - d\right] - \delta M_l\Big[\theta_l - \theta(l)\Big] - \delta M_0\Big[\theta_0 - \theta(0)\Big] + \\ &+\delta R_y\int_0^l \left((1+\varepsilon)\sin\theta + \gamma\cos\theta\right) \mathrm{d}\mathsf{s}\end{aligned}$$

(3.13)

so that the stationarity of the total potential energy (3.13) for arbitrary perturbations $\{\delta\theta, \delta\varepsilon, \delta\gamma, \delta M_l, \delta M_0, \delta R_x, \delta R_y\}$ leads to the following system of equations

$$\begin{cases} B\theta'' + R_x\left[(1+\varepsilon)\sin\theta + \gamma\cos\theta\right] - R_y\left[(1+\varepsilon)\cos\theta - \gamma\sin\theta\right] = 0 & \text{(3.14a)} \\ EA\,\varepsilon + R_x\cos\theta + R_y\sin\theta = 0 & \text{(3.14b)} \\ GA_s\gamma - R_x\sin\theta + R_y\cos\theta = 0 & \text{(3.14c)} \\ \theta_l = \theta(l) & \text{(3.14d)} \\ \theta_0 = \theta(0) & \text{(3.14e)} \\ d = \displaystyle\int_0^l \left((1+\varepsilon)\cos\theta - \gamma\sin\theta\right)\mathsf{ds} & \text{(3.14f)} \\ 0 = \displaystyle\int_0^l \left((1+\varepsilon)\sin\theta + \gamma\cos\theta\right)\mathsf{ds} & \text{(3.14g)} \end{cases}$$

Denoting with R the total reaction force at both ends,

$$R_x = |R|\cos\beta, \qquad R_y = |R|\sin\beta, \tag{3.15}$$

where $|R| = \sqrt{R_x^2 + R_y^2}$ (or equivalently, through the axial and shear components, $|R| = \sqrt{N(\mathsf{s})^2 + T(\mathsf{s})^2}$), the following equilibrium equations are obtained for the unknown rotation and strain fields

$$\begin{cases} B\theta'' + (1+\varepsilon)|R|\sin(\theta-\beta) + \gamma|R|\cos(\theta-\beta) = 0 \\ \varepsilon = -\dfrac{|R|}{EA}\cos(\theta-\beta) \\ \gamma = \dfrac{|R|}{GA_s}\sin(\theta-\beta) \end{cases} \tag{3.16}$$

where the axial strain and shear deformation can be expressed as non-linear functions of the rotation field θ. Eqs.(3.16) are complemented by the Dirichlet boundary conditions on the cross sections' rotations at both ends

$$\theta(0) = \theta_0, \qquad \theta(l) = \theta_l \tag{3.17}$$

and by the following integral isoperimetric constraints

$$0 = \int_0^l \left((1+\varepsilon)\sin\theta + \gamma\cos\theta\right) \mathrm{d}\mathsf{s}, \quad d = \int_0^l \left((1+\varepsilon)\cos\theta - \gamma\sin\theta\right) \mathrm{d}\mathsf{s}. \tag{3.18}$$

Moreover, the following global equilibrium equation has to be satisfied

$$M(0) + R_y\, d - M(l) = 0 \tag{3.19}$$

where $M(0)$ and $M(l)$ are the values of the bending moment at both ends, which are parametrized by the coordinates $\mathsf{s} = 0$ and $\mathsf{s} = l$, respectively.

3.1 Exact solution for the governing equation

Following Batista[9, 11] and Goto et al.[51] a dimensionless formulation is introduced through the following changes of variables

$$\begin{gathered} \psi(s) = \theta(s) - \beta, \qquad \Gamma^2 = \frac{|R|\, l^2}{B}, \qquad \frac{1}{\lambda^2} = \frac{B}{l^2}\left(\frac{1}{GA_s} + \frac{1}{EA}\right), \\ \nu = \frac{GA_s - EA}{GA_s + EA}, \qquad s = \frac{\mathsf{s}}{l} \in [0,\, 1] \end{gathered} \tag{3.20}$$

where $\beta \in [-\pi,\, \pi]$ is the unknown angle assumed by the resultant force $|R|$ at both ends, measured with respect to the x-axis (see Fig.3.1, right) and where the dimensionless curvilinear coordinate s ranges from 0 to 1. λ is a positive slenderness parameter, so that the equations governing the dimensionless Euler's elastica can be recovered in the limit for $\lambda \to \infty$. The dimensionless equilibrium equations can be written as

$$\begin{cases} \psi'' + \Gamma^2 \sin\psi \left[1 - \dfrac{\nu\,\Gamma^2}{\lambda^2}\cos\psi\right] = 0, \\ \varepsilon = -\dfrac{1+\nu}{2\lambda^2}\Gamma^2\cos\psi, \\ \gamma = \dfrac{1-\nu}{2\lambda^2}\Gamma^2\sin\psi, \end{cases} \tag{3.21}$$

where the limits of null axial strain $\varepsilon = 0$ (inextensible rod) or null shear deformations $\gamma = 0$ (extensible Euler's elastica) can be recovered by setting the parameter ν equal to -1 and 1, respectively. Moreover, the condition (3.4)

can be substituted into the Eq.$(3.21)_2$ thus obtaining the following limit for the dimensionless load

$$\frac{\Gamma^2}{\lambda^2} < \frac{2}{1+\nu}, \tag{3.22}$$

so that for the shearless beam ($\nu = 1$) the limit $\Gamma^2 < \lambda^2$ holds, while no limitations exist in the case of an inextensible beam ($\nu = -1$).

In the case of a non-vanishing curvature $\psi'(s)$, Eq.(3.21) can be rewritten as follows

$$\frac{\mathrm{d}}{\mathrm{d}s}\left[\frac{1}{2}\left(\psi'\right)^2 - \Gamma^2\left(\cos\psi - \frac{\nu\,\Gamma^2}{2\lambda^2}\cos^2\psi\right)\right] = 0, \tag{3.23}$$

and finally integrated to yield

$$\psi' = \pm\,\Gamma\sqrt{2\left(\cos\psi - \frac{\nu\,\Gamma^2}{2\lambda^2}\cos^2\psi + \Upsilon\right)}, \tag{3.24}$$

where the constant of integration Υ is introduced.

As for the problem of the Euler's elastica, the exact description of the Reissner beam can be obtained through a discrimination between the two cases of presence and absence of inflection points (say, m points), which in this specific case are related to the vanishing points of the field ψ' and not of the curvature of the centerline. Moreover, new expressions for the constant of integration Υ for the dual cases of presence and absence of inflection points are proposed, so that the formulations (2.20) and (2.23) reported for the Euler's elastica can be recovered by imposing $\lambda \to \infty$.

Presence of m points of null curvature ψ' ($m \neq 0$). As proposed by Batista[11], the constant of integration is obtained by imposing a vanishing curvature ψ' at the first point of null curvature $\widehat{s}_1$, thus obtaining

$$\Upsilon = -\cos\widehat{\psi}_1\left(1 - \frac{\nu\,\Gamma^2}{2\lambda^2}\cos\widehat{\psi}_1\right), \tag{3.25}$$

an expression which represents an extension of the definition (2.20) introduced by Love[77] for the inflectional elastica. Moreover, also in this case a multiplicity of solutions is given in terms of the sign of the field ψ' at the coordinate $s = 0$, so that the sign function $(-1)^p$ is introduced together with the sign function

$\tilde{S}(s)$ expressing the change of sign of the curvature at each inflection point. The Eq.(3.24) can be represented in compact notation as

$$\psi'(s) = (-1)^p \tilde{S}\,\Gamma \sqrt{2\left(\cos\psi(s) - \cos\widehat{\psi}_1\right)\left[1 - \frac{\nu\,\Gamma^2}{2\,\lambda^2}\left(\cos\psi(s) + \cos\widehat{\psi}_1\right)\right]}. \tag{3.26}$$

The multiplicity of solutions given by the imposed sign $(-1)^p$ is illustrated in Fig.3.3, where two solutions, symmetric with respect to the x-axis, are presented for the Reissner beam suject to the same boundary conditions (both solutions are also compared with the solution for the Euler's elastica).

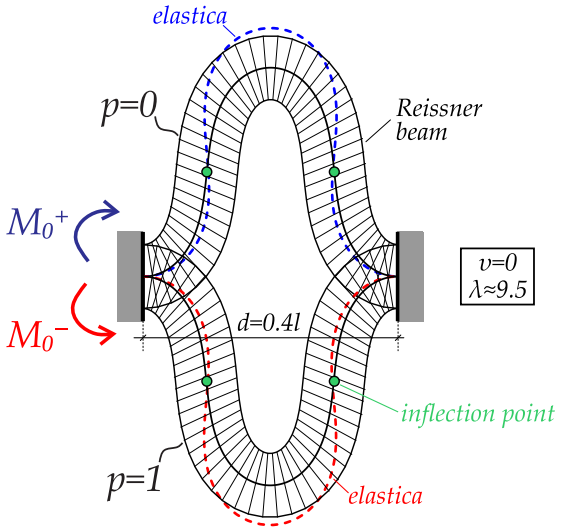

Figure 3.3: Two solutions for the Reissner beam having a different sign $(-1)^p$ of the curvature at $s = 0$ and satisfying the same imposed rotations and displacements at both ends. The particular case $\theta_0 = \theta_l = 0$, $d = 0.4l$, $\nu = 0$ and $\lambda \approx 9.5$ is represented. In order to better appreciate the effect of extensibility of the centerline and of shear deformations (resulting in the fact that the cross sections are not orthogonal to the centerline), a comparison is also reported with the Euler's elastica (highlighted with blue and red dashed lines) subject to the same boundary conditions.

Absence of points of null curvature for ψ' ($m = 0$). In this case $\psi'(s) \neq 0$ for every coordinate $s \in (0, 1)$ and the following form of the integration constant Υ is proposed, function of the unknown parameter $\xi > 0$,

$$\Upsilon = \frac{2 - \xi^2}{\xi^2} \left(1 + \frac{\nu \Gamma^2}{2\lambda^2} \frac{2 - \xi^2}{\xi^2} \right), \tag{3.27}$$

where the upper bound of ξ is set to be greater than 1 in order to catch solutions without inflection points within the span, but belonging to the inflectional problem. In any case, the generalization of the non-inflectional mother curve for the Reissner beam is given for every value of the unknown parameter $\xi \in [0, 1]$.

The expression for the curvature (3.24) can be rewritten as

$$\psi'(s) = (-1)^p \Gamma \sqrt{2 \left(\cos\psi(s) + \frac{2 - \xi^2}{\xi^2} \right) \left[1 - \frac{\nu \Gamma^2}{2 \lambda^2} \left(\cos\psi(s) - \frac{2 - \xi^2}{\xi^2} \right) \right]}, \tag{3.28}$$

where again the sign function $(-1)^p$ is specified by the imposed rotations θ_0 and θ_l at both cross sections' ends, so that p cannot be considered as an input parameter. A solution for the Reissner beam without inflection points is illustrated in Fig.3.4 together with the comparison solution for the Euler's elastica. As in the previous Chapter, only one solution is found for the specific combination of the boundary conditions.

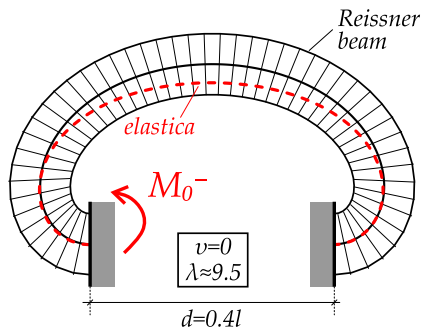

Figure 3.4: Solution for the Reissner beam without inflection points, subject to the imposed rotations $\theta_0 = -\theta_l = \pi$ and displacement $d = 0.4l$ at both ends. As for the problem of the Euler's elastica, the sign $(-1)^p$ is specified by the values of rotations at both ends.

3.2 The Reissner beam with m points of null curvature

As for the case of integration of the Euler's elastica, it is instrumental to introduce the unknown parameter $\eta \in [0,1]$ and the auxiliary field $\omega(s)$ defined as

$$\eta = \sin\frac{|\widehat{\psi}_1|}{2}, \qquad \eta\sin\omega(s) = \sin\frac{\psi(s)}{2}, \tag{3.29}$$

so that the curvature can be rewritten as

$$\frac{\mathrm{d}\psi}{\mathrm{d}s} = (-1)^p\, 2\,\Gamma\,\eta\,\cos\omega\,\sqrt{1-\frac{\nu\,\Gamma^2}{\lambda^2}+\frac{\nu\,\Gamma^2}{\lambda^2}\eta^2(1+\sin^2\omega)}. \tag{3.30}$$

Through Eq.(3.29) one can write

$$\psi = 2\arcsin(\eta\sin\omega) \quad \longrightarrow \quad \mathrm{d}\psi = \frac{2}{\sqrt{1-\eta^2\sin^2\omega}}\eta\cos\omega\,\mathrm{d}\omega$$

which can be substituted into Eq.(3.30) to obtain

$$\frac{\mathrm{d}\omega}{\mathrm{d}s} = (-1)^p\frac{\tilde{\Gamma}}{\sqrt{1+n^2}}\sqrt{\big(1-\eta^2\sin^2\omega(s)\big)\,\big(1+n^2\sin^2\omega(s)\big)}, \tag{3.31}$$

where the following parameters have been introduced

$$n^2 = \frac{\dfrac{\nu\,\Gamma^2\eta^2}{\lambda^2}}{1+\dfrac{\nu\,\Gamma^2}{\lambda^2}\,(\eta^2-1)}, \qquad \tilde{\Gamma} = \Gamma\sqrt{1+\frac{\nu\,\Gamma^2}{\lambda^2}\,(2\eta^2-1)}. \tag{3.32}$$

The integration of Eq.(3.31) requires a first change of variables, namely,

$$u(s) = \sin\omega(s) \qquad \to \qquad u' = \cos\omega\,\omega' = \tilde{S}\sqrt{1-u^2}\,\omega', \tag{3.33}$$

where $\tilde{S}(s)$ is a function expressing the change in the sign of the curvature occurring at each inflection point (see Eq. (3.26)) in a compact form, and where in particular

$$\tilde{S}(s)\sqrt{1-\sin^2\omega(s)} = \cos\omega(s).$$

Moreover, $u(s) \in [-1, 1]$ so that the Eq.(3.31) can be rewritten as

$$\frac{\mathrm{d}u}{\mathrm{d}s} = (-1)^p \frac{\tilde{\Gamma}}{\sqrt{1+n^2}} \tilde{S} \sqrt{1-u^2} \sqrt{1-\eta^2 u^2} \sqrt{1+n^2 u^2} \tag{3.34}$$

A second change of variables is introduced

$$u(s) = \frac{t(s)}{\sqrt{1+n^2(1-t^2(s))}}, \qquad \rightarrow \qquad u' = \frac{t'(1+n^2)}{(1+n^2(1-t^2))^{\frac{3}{2}}}, \tag{3.35}$$

where the new function $t(s)$ is in turn defined within the interval $t(s) \in [-1, 1]$. The expression for u' can be substituted in Eq.(3.34) leading to the following condition

$$\frac{\mathrm{d}t}{\mathrm{d}s} = (-1)^p \tilde{\Gamma} \tilde{S} \sqrt{1-t^2} \sqrt{1-\tilde{\eta}^2 t^2}, \tag{3.36}$$

where

$$\tilde{\eta}^2 = \frac{\eta^2 + n^2}{n^2 + 1}. \tag{3.37}$$

A third (and last) change of variables is introduced,

$$t(s) = \sin \tau(s) \qquad \rightarrow \qquad \tilde{S} \sqrt{1-t^2} = \cos \tau, \tag{3.38}$$

so that the following equation can be obtained for the unknown field $\tau(s)$

$$\frac{\mathrm{d}\tau}{\mathrm{d}s} = (-1)^p \tilde{\Gamma} \sqrt{1 - \tilde{\eta}^2 \sin^2 \tau}, \tag{3.39}$$

which can be integrated between 0 and the generic coordinate s, to yield

$$\int_0^s \tilde{\Gamma} \, \mathrm{d}s = (-1)^p \int_{\tau(0)}^{\tau(s)} \frac{\mathrm{d}\tilde{t}}{\sqrt{1 - \tilde{\eta}^2 \sin^2 \tilde{t}}}. \tag{3.40}$$

The properties of the elliptic integrals allow to obtain the load parameter $\tilde{\Gamma}$ by setting the second integration endpoint equal to $s = 1$ (which singles out to the right end of the Reissner beam)

$$\tilde{\Gamma} = (-1)^p \left[F(\tau(1), \tilde{\eta}) - F(\tau(0), \tilde{\eta}) \right]. \tag{3.41}$$

The load parameter $\tilde{\Gamma}$ is therefore a function of the values assumed by the unknown function τ at the initial $s = 0$ and final $s = 1$ ends.[1] The parameter Γ can be therefore obtained as the positive roots of the following equation

$$\Gamma\sqrt{1+\frac{\nu\,\Gamma^2}{\lambda^2}\,(2\eta^2-1)} = (-1)^p\,[F(\tau(1),\,\tilde{\eta}) - F(\tau(0),\,\tilde{\eta})]\,, \tag{3.42}$$

which has been obtained through the Eqs.$(3.32)_2$ and (3.41). Note that the unknown coefficient Γ is also implicitly present in Eq.(3.42) through the coefficients $\tilde{\eta}$, n, $\tau(1)$ and $\tau(0)$. Note that the limit $\lambda \to \infty$ leads to the condition

$$\Gamma = (-1)^p\,[F(\omega(1),\,\eta) - F(\omega(0),\,\eta)]\,, \tag{3.43}$$

so that the limit of the Euler's elastica is recovered.

The function $\tau(s)$ for the Reissner beam having points of null curvature θ' is therefore equal to

$$\tau(s) = (-1)^p\,\mathrm{am}\left[\tilde{\Gamma}s + (-1)^p\,F(\tau(0),\,\tilde{\eta}),\,\tilde{\eta}\right]. \tag{3.44}$$

By considering $\tau(0) = \tau_0$ and $\tau(1) = \tau_1$, the following function is introduced

$$\mathcal{R}_m(s,\,\tau_1,\,\tau_0) = [F(\tau_1,\,\tilde{\eta}) - F(\tau_0,\,\tilde{\eta})]\,s + F(\tau_0,\,\tilde{\eta}), \tag{3.45}$$

so that by means of Eq.(3.41), Eq.(3.44) can be rewritten in the following compact form

$$\tau(s) = \mathrm{am}\,[\mathcal{R}_m(s,\,\tau_1,\,\tau_0),\,\tilde{\eta}]\,. \tag{3.46}$$

Therefore, the equation governing the field $t(s)$ can be obtained through the change of variables (3.38), to yield

$$t(s) = \mathrm{sn}\,[\mathcal{R}_m(s,\,\tau_1,\,\tau_0),\,\tilde{\eta}]\,. \tag{3.47}$$

The function $u(s)$ can now be obtained by substituting the latter equation into Eq.(3.35), thus obtaining

$$u(s) = \frac{\mathrm{sn}\,[\mathcal{R}_m(s,\,\tau_1,\,\tau_0),\,\tilde{\eta}]}{\sqrt{1+n^2\mathrm{cn}^2\,[\mathcal{R}_m(s,\,\tau_1,\,\tau_0),\,\tilde{\eta}]}}. \tag{3.48}$$

[1] The positiveness of the parameter $\tilde{\Gamma}$ leads to the following conditions

$$F(\tau(1),\,\tilde{\eta}) > F(\tau(0),\,\tilde{\eta}) \quad \to \quad \tau(1) > \tau(0) \quad \text{if} \quad p = 0$$
$$F(\tau(1),\,\tilde{\eta}) < F(\tau(0),\,\tilde{\eta}) \quad \to \quad \tau(1) < \tau(0) \quad \text{if} \quad p = 1$$

Consistently with the formulation of the inflectional Euler's elastica, the dependency on the sign of the initial curvature $(-1)^p$ is implicitly contained in Eq.(3.48) through the parameter τ_1, as shown in the next Section.

The following identity is finally obtained

$$\sin\omega = \frac{\sin\tau}{\sqrt{1+n^2\cos^2\tau}}, \tag{3.49}$$

so that in the limit $\lambda \to \infty$, namely once the Euler's elastica is recovered, one obtains $n^2 \to 0$ and then $\sin\tau = \sin\omega$.

3.2.1 Values assumed by τ at both ends

By considering Eq.(3.30), the following condition is achieved at any point $\widehat{s}_j$ corresponding to a null curvature ψ'

$$\cos\omega(\widehat{s}_j)\sqrt{1+n^2\,\sin^2\omega(\widehat{s}_j)} = 0, \tag{3.50}$$

where due to the strict positiveness of the term under square root, condition (3.50) reduces to the vanishing of $\cos\omega(\widehat{s}_j)$. Through Eq.(3.49), one can obtain the following expression

$$\sin\omega(\widehat{s}_j) = \sin\tau(\widehat{s}_j), \tag{3.51}$$

proving the identity between the sinus of the functions ω and τ at any inflection point (note that the identity above is not in general extended to the whole domain of the aforementioned functions, being the latter case verified only under the assumption $\lambda \to \infty$ or in the particular case $n^2 = \nu = 0$). Due to the fact that the function $\tau(s)$ is monotonic (see Eq.(3.46)) and following the same procedure developed for the Euler's elastica, the values of τ at any inflection point is equal to

$$\tau(\widehat{s}_1) = (-1)^p\frac{\pi}{2}, \quad \tau(\widehat{s}_2) = (-1)^p\frac{3\pi}{2}, \qquad \dots \tag{3.52}$$

where the initial value τ_0 belongs to the interval $[-\pi/2,\, \pi/2]$.

The Dirichlet boundary conditions can be explicitly introduced by rewriting the function τ with respect to θ through Eqs.(3.29_2) and (3.49), so that one can write

$$\sin\tau = \sin\left(\frac{\theta-\beta}{2}\right)\sqrt{\frac{1+n^2}{\eta^2+n^2\sin^2\left(\dfrac{\theta-\beta}{2}\right)}}. \tag{3.53}$$

As for the problem of the Euler's elastica, the values of the function $\tau(s)$ attained at both ends, $\tau(0) = \tau_0$ and $\tau(1) = \tau_1$, can therefore be expressed as functions of the number of inflection points m and of the sign of the initial curvature $(-1)^p$, so that

$$\tau_0 = \arcsin\left[\sin\left(\frac{\theta_0 - \beta}{2}\right)\sqrt{\frac{1+n^2}{\eta^2 + n^2\sin^2\left(\dfrac{\theta_0-\beta}{2}\right)}}\right],$$
$$\tau_1 = (-1)^m \arcsin\left[\sin\left(\frac{\theta_l - \beta}{2}\right)\sqrt{\frac{1+n^2}{\eta^2 + n^2\sin^2\left(\dfrac{\theta_l-\beta}{2}\right)}}\right] + (-1)^p\, m\pi. \tag{3.54}$$

Eqs.(3.54) provide the two fundamental parameters involved in the solution, which both depend on the unknown parameters β, η and Γ (the latter only through coefficient n).

The main advantage introduced with relations (3.54) is represented by their generality. In particular, for every combination of the imposed boundary conditions $[\theta_0, \theta_l]$, the number of inflection points m and the sign function $(-1)^p$ can explicitly be imposed, allowing for the evaluation of every deformed shape which corresponds to prescribed boundary conditions.

However, it is worth to underline that the presented equations are valid for the case $m > 0$ only, while the treatment of the non-inflectional equations, $m = 0$, is deferred to Section 3.3.

3.2.2 The solution for the Reissner beam with m points of null curvature

Eq.(3.49) can be substituted into Eq.$(3.29)_2$ to obtain the solution for the angle $\psi(s)$

$$\psi(s) = 2\arcsin\left[\eta\,\frac{\mathrm{sn}\left[\mathcal{R}_m(s,\,\tau_1,\,\tau_0),\,\tilde{\eta}\right]}{\sqrt{1+n^2\mathrm{cn}^2\left[\mathcal{R}_m(s,\,\tau_1,\,\tau_0),\,\tilde{\eta}\right]}}\right], \tag{3.55}$$

where τ_0 and τ_1 are explicitly expressed by Eqs.(3.54).

Through Eq.(3.20), the exact expression for the function $\theta(s)$ can be obtained as

$$\theta(s) = 2\arcsin\left[\eta\,\frac{\mathrm{sn}\left[\mathcal{R}_m(s,\,\tau_1,\,\tau_0),\,\tilde{\eta}\right]}{\sqrt{1+n^2\mathrm{cn}^2\left[\mathcal{R}_m(s,\,\tau_1,\,\tau_0),\,\tilde{\eta}\right]}}\right]+\beta \tag{3.56}$$

representing the solution for the cross sections' rotations of the Reissner beam in the case when $m>0$ points of null curvature for θ' are present. It is worth to underline that expression (3.56) contains the unknown parameters η, β and Γ.

The exact expression for the curvature $\psi'=\theta'$ can be achieved by a differentiation of the Eq.(3.56), thus obtaining

$$\theta'(s) = 2\eta\left[F(\tau_1,\,\tilde{\eta})-F(\tau_0,\,\tilde{\eta})\right]\,\frac{\sqrt{1+n^2}\,\mathrm{cn}\left[\mathcal{R}_m(s,\,\tau_1,\,\tau_0),\,\tilde{\eta}\right]}{1+n^2\mathrm{cn}^2\left[\mathcal{R}_m(s,\,\tau_1,\,\tau_0),\,\tilde{\eta}\right]}. \tag{3.57}$$

Further calculations lead to the exact expressions for the strain measures ε and γ (Eqs.$(3.21)_2$ and (3.21_3)), which can be expressed as

$$\varepsilon = -\frac{1+\nu}{2\lambda^2}\Gamma^2\left(1-2\,\eta^2\frac{\mathrm{sn}^2\left[\mathcal{R}_m(s,\,\tau_1,\,\tau_0),\,\tilde{\eta}\right]}{1+n^2\mathrm{cn}^2\left[\mathcal{R}_m(s,\,\tau_1,\,\tau_0),\,\tilde{\eta}\right]}\right), \tag{3.58}$$

and

$$\gamma = \frac{1-\nu}{\lambda^2}\Gamma^2\eta\sqrt{1+n^2}\frac{\mathrm{sn}\left[\mathcal{R}_m(s,\,\tau_1,\,\tau_0),\,\tilde{\eta}\right]\,\mathrm{dn}\left[\mathcal{R}_m(s,\,\tau_1,\,\tau_0),\,\tilde{\eta}\right]}{1+n^2\mathrm{cn}^2\left[\mathcal{R}_m(s,\,\tau_1,\,\tau_0),\,\tilde{\eta}\right]}, \tag{3.59}$$

respectively.

The kinematics equations (3.5) can be rewritten in terms of the closed-form solution for the rotation ψ, namely

$$\begin{bmatrix}x'(s)\\ y'(s)\end{bmatrix} = \begin{bmatrix}\cos\beta & -\sin\beta\\ \sin\beta & \cos\beta\end{bmatrix}\cdot\begin{bmatrix}\mathcal{A}_{R,m}(s)\\ \mathcal{B}_{R,m}(s)\end{bmatrix}, \tag{3.60}$$

where

$$\begin{aligned}\mathcal{A}_{R,m}(s) &= \cos\psi-\frac{\Gamma^2}{2\lambda^2}-\frac{\nu\,\Gamma^2}{2\lambda^2}\left(2\cos^2\psi-1\right),\\ \mathcal{B}_{R,m}(s) &= \sin\psi-\frac{\nu\,\Gamma^2}{2\lambda^2}\sin 2\psi = -\frac{\psi''(s)}{\Gamma^2}.\end{aligned} \tag{3.61}$$

The exact expression for the centerline's coordinates $x(s)$ and $y(s)$ can be obtained by integrating the equations above. In particular, the integration of

the second term $\mathcal{B}_{R,m}(s)$ can be immediately obtained through the following condition

$$\mathbb{B}_{R,m}(s) = -\frac{1}{\Gamma^2}\int_0^s \psi''(\varsigma)\mathrm{d}\varsigma = \frac{1}{\Gamma^2}\left(\psi'(0) - \psi'(s)\right),$$

which leads to the following expression

$$\mathbb{B}_{R,m}(s) = \frac{2\eta\sqrt{1+n^2}}{\Gamma^2}\left[F(\tau_1,\,\tilde{\eta}) - F(\tau_0,\,\tilde{\eta})\right]\left(\frac{\cos\tau_0}{1+n^2\cos^2\tau_0} + \right. \\ \left. - \frac{\mathrm{cn}\left[\mathcal{R}_m(s,\,\tau_1,\,\tau_0),\,\tilde{\eta}\right]}{1+n^2\mathrm{cn}^2\left[\mathcal{R}_m(s,\,\tau_1,\,\tau_0),\,\tilde{\eta}\right]}\right). \tag{3.62}$$

On the other hand, the integration of $\mathcal{A}_{R,m}(s)$ turns out to be extremely tedious. More specifically, a first integration of the Eq.$(3.61)_1$ leads to

$$\mathbb{A}_{R,m}(s) = -\frac{\Gamma^2\, s}{2\lambda^2}(1-\nu) + \int_0^s \cos\psi(\varsigma)\mathrm{d}\varsigma - \nu\frac{\Gamma^2}{\lambda^2}\int_0^s \cos^2\psi(\varsigma)\mathrm{d}\varsigma. \tag{3.63}$$

Through the exact solution for the rotation field ψ in Eq.(3.55), the first of the two integrals in Eq.(3.63) can be separated as

$$\begin{aligned}\int_0^s \cos\psi(\varsigma)\mathrm{d}\varsigma &= \frac{2\eta^2+n^2}{n^2}s - \frac{2\eta^2}{n^2}\int_0^s\left[\frac{1}{1-\frac{n^2\mathrm{sn}^2[\mathcal{R}_m(\varsigma,\,\tau_1,\,\tau_0),\tilde{\eta}]}{n^2+1}}\right]\mathrm{d}\varsigma \\ &= \frac{2\eta^2}{n^2}\frac{\Pi\left(\frac{n^2}{n^2+1},\tau_0,\tilde{\eta}\right) - \Pi\left(\frac{n^2}{n^2+1},\mathrm{am}\left[\mathcal{R}_m(s,\,\tau_1,\,\tau_0),\tilde{\eta}\right],\tilde{\eta}\right)}{F(\tau_1,\,\tilde{\eta}) - F(\tau_0,\,\tilde{\eta})} + \\ &\quad + \frac{2\eta^2+n^2}{n^2}s\end{aligned} \tag{3.64}$$

where

$$\Pi\left(\alpha^2,\mathrm{am}\left[\sigma,\varphi\right],\varphi\right) = \int_0^\sigma \frac{\mathrm{d}\phi}{1-\alpha^2\,\mathrm{sn}^2\left[\phi,\varphi\right]} \tag{3.65}$$

is the *incomplete elliptic integral of the third kind*.

The second integral in Eq.(3.63) can be rewritten as the sum of two integrals I_1 and I_2

$$\int_0^s \cos^2\psi(\varsigma)\mathrm{d}\varsigma = I_1 + I_2, \tag{3.66}$$

where

$$I_1 = \frac{\left(n^2+2\eta^2\right)^2}{n^4}s - \int_0^s \left[\frac{4\eta^2}{n^2\left(1-\frac{n^2\mathrm{sn}^2[\mathcal{R}_m(s,\,\tau_1,\,\tau_0),\tilde{\eta}]}{n^2+1}\right)} + \frac{8\eta^4}{n^4\left(1-\frac{n^2\mathrm{sn}^2[\mathcal{R}_m(s,\,\tau_1,\,\tau_0),\tilde{\eta}]}{n^2+1}\right)}\right]\mathrm{d}s, \tag{3.67}$$

and

$$I_2 = \frac{4\eta^4}{n^4}\int_0^s \left[\frac{\mathrm{dn}^2\left[\mathcal{R}_m(s,\,\tau_1,\,\tau_0),\tilde{\eta}\right]}{\left(1-\frac{n^2\mathrm{sn}^2[\mathcal{R}_m(s,\,\tau_1,\,\tau_0),\tilde{\eta}]}{n^2+1}\right)^2} + \frac{\tilde{\eta}^2\mathrm{sn}^2\left[\mathcal{R}_m(s,\,\tau_1,\,\tau_0),\tilde{\eta}\right]}{\left(1-\frac{n^2\mathrm{sn}^2[\mathcal{R}_m(s,\,\tau_1,\,\tau_0),\tilde{\eta}]}{n^2+1}\right)^2}\right]\mathrm{d}s. \tag{3.68}$$

The integral I_1 in Eq.(3.67) can be expressed in terms of elliptic integrals of the third kind as

$$\begin{aligned} I_1 = &\frac{\left(n^2+2\eta^2\right)^2}{n^4}s + \\ &\frac{4\eta^2\left(n^2+2\eta^2\right)}{n^4}\frac{\Pi\left(\frac{n^2}{n^2+1},\tau_0,\tilde{\eta}\right)-\Pi\left(\frac{n^2}{n^2+1},\mathrm{am}\left[\mathcal{R}_m(s,\,\tau_1,\,\tau_0),\tilde{\eta}\right],\tilde{\eta}\right)}{F(\tau_1,\,\tilde{\eta})-F(\tau_0,\,\tilde{\eta})} \end{aligned} \tag{3.69}$$

The solution for the integral I_2 introduced in Eq.(3.68) is not trivial and has been performed using formulas found in Byrd and Friedman[27], not reported here for brevity (see Eqs.362.15 and 362.17 at page 218). Skipping long calculations, finally, the following equation expressing the sum of the two integrals $I_1 + I_2$ can be obtained

$$\begin{aligned} \int_0^s \cos^2\psi(\varsigma)\mathrm{d}\varsigma = &\frac{4\eta^2}{n^2}s - \frac{2\eta^4\left(n^2-1\right)}{n^4}s + s + \\ &\frac{2\eta^2}{n^4}\frac{n^2(1+n^2)\left(n^2\Delta\mathscr{G}(s)-\Delta\mathscr{E}(s)\right)+\Delta\Pi(s)\left(n^2(\eta^2-1)-\eta^2\right)}{\Delta F} \end{aligned} \tag{3.70}$$

where the following quantities have been introduced

$$\begin{aligned}
\Delta\mathscr{E}(s) &= \mathscr{E}\left[\mathcal{R}_m(s,\,\tau_1,\,\tau_0),\,\tilde{\eta}\right] - E(\tau_0,\,\tilde{\eta}) \\
\Delta\mathscr{G}(s) &= \frac{\mathrm{cn}\left[\mathcal{R}_m(s,\,\tau_1,\,\tau_0),\,\tilde{\eta}\right]\,\mathrm{dn}\left[\mathcal{R}_m(s,\,\tau_1,\,\tau_0),\,\tilde{\eta}\right]\,\mathrm{sn}\left[\mathcal{R}_m(s,\,\tau_1,\,\tau_0),\,\tilde{\eta}\right]}{1+n^2\mathrm{cn}^2\left[\mathcal{R}_m(s,\,\tau_1,\,\tau_0),\,\tilde{\eta}\right]} + \\
&\quad - \frac{\cos\tau_0\,\sin\tau_0\sqrt{1-\tilde{\eta}^2\sin\tau_0}}{1+n^2\cos^2\tau_0} \\
\Delta\Pi(s) &= \Pi\left(\frac{n^2}{n^2+1}, \mathrm{am}\left[\mathcal{R}_m(s,\,\tau_1,\,\tau_0),\tilde{\eta}\right],\tilde{\eta}\right) - \Pi\left(\frac{n^2}{n^2+1},\tau_0,\tilde{\eta}\right) \\
\Delta F &= F(\tau_1,\,\tilde{\eta}) - F(\tau_0,\,\tilde{\eta}).
\end{aligned} \tag{3.71}$$

The sum of the two integrals in Eq.(3.63) and performed through Eqs.(3.64), (3.66) and (3.70) leads surprisingly to the simplification of the elliptic integrals of the third kind, so that the final expression for equation (3.63) becomes

$$\mathbb{A}_{R,m}(s) = 2\frac{\Delta F}{\Gamma^2}\left(\Delta\mathscr{E}(s) - n^2\Delta\mathscr{G}(s) - \frac{\Delta F}{2}s\right) - (1-\nu)\frac{\Gamma^2\,s}{2\lambda^2}. \tag{3.72}$$

The final expression for the centerline's position is obtained through Eqs.(3.72) and (3.62) in the form

$$\begin{bmatrix} x(s)/l \\ y(s)/l \end{bmatrix} = \begin{bmatrix} \cos\beta & -\sin\beta \\ \sin\beta & \cos\beta \end{bmatrix} \cdot \begin{bmatrix} \mathbb{A}_{R,m}(s) \\ \mathbb{B}_{R,m}(s) \end{bmatrix}. \tag{3.73}$$

Elastic energy

Finally, the expression for the elastic energy (3.10) is obtained through the the curvature θ', Eq.(3.57), and through the equations for the axial and shear strain, Eqs.(3.58) and (3.59), respectively.

The dimensionless elastic energy can be written as

$$\begin{aligned}
\frac{\mathcal{E}}{B}l &= \frac{1}{2}\int_0^1 \theta'^2\mathrm{d}s + \frac{EA\,l^2}{2B}\int_0^1 \varepsilon^2\mathrm{d}s + \frac{GA_s\,l^2}{2B}\int_0^1 \gamma^2\mathrm{d}s \\
&= \frac{1}{2}\int_0^1 \theta'^2\mathrm{d}s + \frac{1}{4}\frac{\Gamma^4}{\lambda^2}(1-\nu) + \frac{\nu}{2}\frac{\Gamma^4}{\lambda^2}\int_0^1 \cos^2\psi\,\mathrm{d}s,
\end{aligned} \tag{3.74}$$

so that in the limit of $\lambda \to \infty$, the elastic energy of the Euler's elastica can easily be recovered.

The contribution to the elastic energy associated to bending can be written as[2]

$$\frac{\mathcal{E}_\theta}{B} l = 2\eta^2 \frac{\Delta F}{n^2+1} \int_{\mathcal{R}_m(0,\tau_1,\tau_0)}^{\mathcal{R}_m(1,\tau_1,\tau_0)} \left[\frac{\mathrm{cn}^2\,[r]}{\left(1 - \frac{n^2 \mathrm{sn}^2[r]}{n^2+1}\right)^2} \right] \mathrm{d}r, \tag{3.75}$$

an integral which can be evaluated using Byrd and Friedman[27] (see Es. 362.16 at page 218) to obtain the final expression for $\mathcal{E}_\theta$

$$\frac{\mathcal{E}_\theta}{B} l = \Delta F \left[\Delta E - n^2 \Delta \mathscr{G}(1) + \frac{\eta^2}{n^2} \left(\Delta F + \frac{n^2(\eta^2-1) - \eta^2}{\eta^2(1+n^2)} \Delta \Pi(1) \right) \right], \tag{3.76}$$

where

$$\Delta E = \Delta \mathscr{E}(1) = E(\tau_1,\, \tilde{\eta}) - E(\tau_0,\, \tilde{\eta}), \tag{3.77}$$

and the further expressions defined in Eqs.(3.71) have been particularized at the coordinate $s = 1$ as follows

$$\begin{aligned} \Delta \mathscr{G}(1) &= \frac{\cos\tau_1 \, \sin\tau_1 \sqrt{1 - \tilde{\eta}^2 \sin\tau_1}}{1 + n^2 \cos^2\tau_1} - \frac{\cos\tau_0 \, \sin\tau_0 \sqrt{1 - \tilde{\eta}^2 \sin\tau_0}}{1 + n^2 \cos^2\tau_0}, \\ \Delta \Pi(1) &= \Pi\left(\frac{n^2}{n^2+1}, \tau_1, \tilde{\eta} \right) - \Pi\left(\frac{n^2}{n^2+1}, \tau_0, \tilde{\eta} \right). \end{aligned} \tag{3.78}$$

The contribution to the elastic energy associated to the axial and shear strains can be calculated taking advantage of Eq.(3.70) particularized at the coordinate $s = 1$, thus obtaining

$$\begin{aligned} \frac{\mathcal{E}_{\varepsilon,\gamma}}{B} l = \frac{\Gamma^4}{4\lambda^2}(1+\nu) + \frac{\nu\,\Gamma^4}{\lambda^2} \frac{\eta^2}{n^4} \Bigg[& 2n^2 - \eta^2 \left(n^2 - 1\right) + \\ & + \frac{n^2(1+n^2)\left(n^2 \Delta \mathscr{G}(1) - \Delta E\right) + \Delta \Pi(1) \left(n^2(\eta^2-1) - \eta^2\right)}{\Delta F} \Bigg]. \end{aligned} \tag{3.79}$$

[2]The substitution $r = \mathcal{R}_m(s,\, \tau_1,\, \tau_0)$ has been performed, so that

$\mathrm{d}r = \Delta F \mathrm{d}s$

The final expression for the elastic energy is therefore given by

$$\begin{aligned}\frac{\mathcal{E}}{B}l =&\Delta F\left[\Delta E - n^2\Delta\mathscr{G}(1) + \frac{\eta^2}{n^2}\left(\Delta F + \frac{n^2(\eta^2-1)-\eta^2}{\eta^2(1+n^2)}\Delta\Pi(1)\right)\right] + \\ &+ \frac{\Gamma^4}{4\lambda^2}(1+\nu) + \frac{\nu\,\Gamma^4}{\lambda^2}\frac{\eta^2}{n^4}\left[2n^2 - \eta^2\left(n^2-1\right) + \right. \\ &\left. + \frac{n^2(1+n^2)\left(n^2\Delta\mathscr{G}(1) - \Delta E\right) + \Delta\Pi(1)\left(n^2(\eta^2-1)-\eta^2\right)}{\Delta F}\right].\end{aligned} \tag{3.80}$$

3.2.3 Evaluation of the unknown parameters η, β and Γ

Differently from the problem of the Euler's elastica, the closed-form solution for the Reissner beam with inflection points is a function of three unknown parameters η, β and Γ, which can be obtained by exploiting the integral equations of the isoperimetric constraints (3.18) together with the Eq.(3.42). The exact solution for the deformed shape given by Eqs.(3.73) is calculated at the final end $s = 1$ of the Reissner beam as

$$\begin{aligned}\mathbb{A}_{R,m}(1) &= 2\frac{\Delta F}{\Gamma^2}\left(\Delta E - n^2\Delta\mathscr{G}(1) - \frac{\Delta F}{2}\right) - (1-\nu)\frac{\Gamma^2}{2\lambda^2} \\ \mathbb{B}_{R,m}(1) &= \frac{2\eta\sqrt{1+n^2}}{\Gamma^2}\Delta F\left(\frac{\cos\tau_0}{1+n^2\cos^2\tau_0} - \frac{\cos\tau_1}{1+n^2\cos^2\tau_1}\right)\end{aligned} \tag{3.81}$$

so that the dimensionless isoperimetric constraints (3.18) assume the following form

$$\begin{bmatrix} d/l \\ 0 \end{bmatrix} = \begin{bmatrix} \cos\beta & -\sin\beta \\ \sin\beta & \cos\beta \end{bmatrix} \cdot \begin{bmatrix} \mathbb{A}_{R,m}(1) \\ \mathbb{B}_{R,m}(1). \end{bmatrix} \tag{3.82}$$

Finally, the following non-linear system is obtained

$$\begin{cases} d/l\cos\beta = \mathbb{A}_{R,m}(1), \\ d/l\sin\beta = -\mathbb{B}_{R,m}(1), \\ \Gamma\sqrt{1+\dfrac{\nu\,\Gamma^2}{\lambda^2}\left(2\eta^2-1\right)} = (-1)^p\left[F(\tau_1,\,\tilde{\eta}) - F(\tau_0,\,\tilde{\eta})\right], \end{cases} \tag{3.83}$$

whose roots provide all the (non-unique) triplets of unknown parameters $[\eta,\,\beta,\,\Gamma]$ corresponding to every combination of the boundary conditions at both ends of the beam.

3.3 The Reissner beam with $m = 0$ points of null curvature

By considering the following change of variable

$$\zeta(s) = \frac{\psi(s)}{2}, \tag{3.84}$$

Eq.(3.28), expressing the non-vanishing curvature ψ' within the span of the rod, can be rewritten as

$$\zeta'(s) = (-1)^p \frac{\tilde{\Gamma}_0}{\sqrt{1+n_0^2}} \sqrt{\left(1-\xi^2 \sin^2\zeta\right)\left(1+n_0^2 \sin^2\zeta\right)}, \tag{3.85}$$

where the following parameters have been introduced

$$n_0^2 = \frac{\dfrac{\nu\,\Gamma^2}{\lambda^2}}{1+\dfrac{\nu\,\Gamma^2}{\lambda^2\xi^2}\left(1-\xi^2\right)}, \qquad \tilde{\Gamma}_0 = \frac{\Gamma}{\xi}\sqrt{1+\frac{\nu\,\Gamma^2}{\lambda^2\xi^2}}. \tag{3.86}$$

Moreover, the values of $\zeta(s)$ at the two ends are defined as $\zeta(0) = \zeta_0$ and $\zeta(l) = \zeta_l$ and can be expressed as functions of the imposed ends rotations,

$$\zeta_0 = \frac{\theta_0 - \beta}{2}, \qquad \zeta_l = \frac{\theta_l - \beta}{2}. \tag{3.87}$$

Eq.(3.85) is definitely similar to the expression for the curvature (3.57) for the Reissner beam with inflection points. Therefore, the exact solution for the rotation field θ and for the axial and shear strains can be obtained using the same procedure introduced in the previous Section. In particular, the following change of variables is introduced

$$u(s) = \sin\zeta(s), \tag{3.88}$$

so that further changes of variables (3.35) and (3.38) lead to the final expression for the field $u(s)$

$$u(s) = \frac{\mathrm{sn}\left[\mathcal{R}_0(s,\,\tau_1,\,\tau_0),\,\tilde{\xi}\right]}{\sqrt{1+n_0^2\mathrm{cn}^2\left[\mathcal{R}_0(s,\,\tau_1,\,\tau_0),\,\tilde{\xi}\right]}}, \tag{3.89}$$

so that

$$\tilde{\Gamma}_0 = (-1)^p \left[F(\tau_1, \tilde{\xi}) - F(\tau_0, \tilde{\xi}) \right], \tag{3.90}$$

where

$$\mathcal{R}_0(s, \tau_1, \tau_0) = \left[F(\tau_1, \tilde{\xi}) - F(\tau_0, \tilde{\xi}) \right] s + F(\tau_0, \tilde{\xi}), \qquad \tilde{\xi}^2 = \frac{\xi^2 + n_0^2}{n_0^2 + 1}. \tag{3.91}$$

Moreover, the unknown dimensionless load parameter Γ is given by the positive roots of the following equation

$$\frac{\Gamma}{\xi} \sqrt{1 + \frac{\nu \Gamma^2}{\lambda^2 \xi^2}} = (-1)^p \left[F(\tau_1, \tilde{\xi}) - F(\tau_0, \tilde{\xi}) \right], \tag{3.92}$$

which has been obtained through Eqs.$(3.86)_2$ and (3.90).

The expression for ζ can therefore be implicitly expressed through the following two equivalent expressions

$$\sin\zeta = \frac{\mathrm{sn}\left[\mathcal{R}_0(s, \tau_1, \tau_0), \tilde{\xi} \right]}{\sqrt{1 + n_0^2 \mathrm{cn}^2 \left[\mathcal{R}_0(s, \tau_1, \tau_0), \tilde{\xi} \right]}}, \qquad \tan\zeta = \frac{\mathrm{tn}\left[\mathcal{R}_0(s, \tau_1, \tau_0), \tilde{\xi} \right]}{\sqrt{1 + n_0^2}}, \tag{3.93}$$

where $\mathrm{tn}[\sigma, \varphi] = \mathrm{sn}[\sigma, \varphi]/\mathrm{cn}[\sigma, \varphi]$ is the *Jacobi's tangent amplitude function* and the expression holding for the Euler's elastica can be recovered by setting $n_0 \to 0$.

In the non-inflectional case, however, the monotonic function ζ cannot be expressed through inverse trigonometric functions as in Eq.(3.55), because the right-hand sides of the expressions (3.93) may not be restrained to belong to the interval $[-1, 1]$. The exact expression for the rotation field can therefore be obtained through the following integral expression

$$\zeta(s) = \Delta F_0 \sqrt{1 + n_0^2} \int_0^s \left[\frac{\mathrm{dn}\left[\mathcal{R}_0(s, \tau_1, \tau_0), \tilde{\xi} \right]}{1 + n_0^2 \mathrm{cn}^2 \left[\mathcal{R}_0(s, \tau_1, \tau_0), \tilde{\xi} \right]} \right] \mathrm{d}s + \frac{\theta_0 - \beta}{2}, \tag{3.94}$$

where

$$\Delta F_0 = F(\tau_1, \tilde{\xi}) - F(\tau_0, \tilde{\xi}), \tag{3.95}$$

so that one can directly compute the function $\zeta(s)$ through a numerical evaluation of integral (3.94).

3.3.1 Values assumed by τ at both ends

The Dirichlet boundary conditions can explicitly be introduced by rewriting the function ζ through the angle θ. By means of Eqs.(3.84) and $(3.93)_1$, one can write

$$\sin\tau = \sin\left(\frac{\theta-\beta}{2}\right)\sqrt{\frac{1+n_0^2}{1+n_0^2\sin^2\left(\dfrac{\theta-\beta}{2}\right)}}. \tag{3.96}$$

which is similar to the equation holding for the inflectional case.

In contrast to the problem of the Euler's elastica, the values of the monotonic function $\tau(s)$ attained at both ends, $\tau(0)=\tau_0$ and $\tau(1)=\tau_1$, can not be directly expressed through the inverse trigonometric functions in the general case $n_0 \neq 0$. In fact, differently from the inflectional case, the solution strongly depends not only on the difference between the values assumed by τ at both ends, but also on their actual value. Consequently, the introduction of the Dirichlet boundary conditions θ_0 and θ_l cannot be pursued through the inversion of Eq.(3.96) via function 'arcsin'.

For that reason, τ_1 and τ_0 for the Reissner beam having no points with null curvature are treated as true unknown parameters, governed by the following implicit equations

$$\begin{aligned}
\sin\tau_0 &= \sin\left(\frac{\theta_0-\beta}{2}\right)\sqrt{\frac{1+n_0^2}{1+n_0^2\sin^2\left(\dfrac{\theta_0-\beta}{2}\right)}},\\
\sin\tau_1 &= \sin\left(\frac{\theta_l-\beta}{2}\right)\sqrt{\frac{1+n_0^2}{1+n_0^2\sin^2\left(\dfrac{\theta_l-\beta}{2}\right)}}.
\end{aligned} \tag{3.97}$$

Finally, the particular condition $n_0 = 0$ leads to the following simplified expressions

$$\tau_0 = \frac{\theta_0-\beta}{2}, \qquad \tau_1 = \frac{\theta_l-\beta}{2}. \tag{3.98}$$

3.3.2 The exact solution for the Reissner beam with 0 points of null curvature

The rotation ψ can be obtained by exploiting Eq.(3.94), together with the change of variable (3.84), yielding

$$\psi(s) = 2\Delta F_0 \sqrt{1+n_0^2} \int_0^s \left[\frac{\mathrm{dn}\left[\mathcal{R}_0(s,\,\tau_1,\,\tau_0), \tilde{\xi}\right]}{1+n_0^2 \mathrm{cn}^2\left[\mathcal{R}_0(s,\,\tau_1,\,\tau_0), \tilde{\xi}\right]} \right] \mathrm{d}s + \theta_0 - \beta \quad (3.99)$$

so that through Eq.(3.20), the exact expression for the function $\theta(s)$ becomes

$$\theta(s) = 2\Delta F_0 \sqrt{1+n_0^2} \int_0^s \left[\frac{\mathrm{dn}\left[\mathcal{R}_0(s,\,\tau_1,\,\tau_0), \tilde{\xi}\right]}{1+n_0^2 \mathrm{cn}^2\left[\mathcal{R}_0(s,\,\tau_1,\,\tau_0), \tilde{\xi}\right]} \right] \mathrm{d}s + \theta_0, \quad (3.100)$$

a function of the unknown parameters η, β and Γ and of the two unknowns τ_1 and τ_0. Differentiation of Eq.(3.100) leads to the expression for the curvature $\psi' = \theta'$

$$\theta'(s) = 2\Delta F_0 \frac{\sqrt{1+n_0^2}\,\mathrm{dn}\left[\mathcal{R}_0(s,\,\tau_1,\,\tau_0),\,\tilde{\xi}\right]}{1+n_0^2 \mathrm{cn}^2\left[\mathcal{R}_0(s,\,\tau_1,\,\tau_0),\,\tilde{\xi}\right]}. \quad (3.101)$$

Further calculations lead to the expression for the strain measures ε and γ (Eqs.$(3.21)_2$ and $(3.21)_3$, respectively) which can be written as

$$\varepsilon = -\frac{1+\nu}{2\lambda^2}\Gamma^2 \left(1 - 2\frac{\mathrm{sn}^2\left[\mathcal{R}_0(s,\,\tau_1,\,\tau_0),\,\tilde{\xi}\right]}{1+n_0^2 \mathrm{cn}^2\left[\mathcal{R}_0(s,\,\tau_1,\,\tau_0),\,\tilde{\xi}\right]} \right), \quad (3.102)$$

and

$$\gamma = \frac{1-\nu}{\lambda^2}\Gamma^2 \sqrt{1+n_0^2}\, \frac{\mathrm{sn}\left[\mathcal{R}_0(s,\,\tau_1,\,\tau_0),\,\tilde{\xi}\right]\,\mathrm{cn}\left[\mathcal{R}_0(s,\,\tau_1,\,\tau_0),\,\tilde{\xi}\right]}{1+n_0^2 \mathrm{cn}^2\left[\mathcal{R}_0(s,\,\tau_1,\,\tau_0),\,\tilde{\xi}\right]}, \quad (3.103)$$

respectively.

The kinematic equations (3.5) can therefore be rewritten in terms of the solution for the rotation field ψ in the form

$$\begin{bmatrix} x'(s) \\ y'(s) \end{bmatrix} = \begin{bmatrix} \cos\beta & -\sin\beta \\ \sin\beta & \cos\beta \end{bmatrix} \cdot \begin{bmatrix} \mathcal{A}_{R,0}(s) \\ \mathcal{B}_{R,0}(s) \end{bmatrix} \quad (3.104)$$

where again

$$\begin{aligned}\mathcal{A}_{R,0}(s) &= \cos\psi - \frac{\Gamma^2}{2\lambda^2} - \frac{\nu\,\Gamma^2}{2\lambda^2}\left(2\cos^2\psi - 1\right)\\ \mathcal{B}_{R,0}(s) &= \sin\psi - \frac{\nu\,\Gamma^2}{2\lambda^2}\sin 2\psi = -\frac{\psi''(s)}{\Gamma^2}.\end{aligned} \tag{3.105}$$

As for the inflectional case, the expression for the centerline's coordinates $x(s)$ and $y(s)$ can be obtained firstly by integrating the equations above. The integration of the second term $\mathcal{B}_{R,0}(s)$ is immediate

$$\mathbb{B}_{R,0}(s) = \frac{2\sqrt{1+n_0^2}}{\Gamma^2}\Delta F_0\left(\frac{\sqrt{1-\tilde{\xi}^2\sin^2\tau_0}}{1+n_0^2\cos^2\tau_0} - \frac{\mathrm{dn}\left[\mathcal{R}_0(s,\,\tau_1,\,\tau_0),\,\tilde{\xi}\right]}{1+n_0^2\mathrm{cn}^2\left[\mathcal{R}_0(s,\,\tau_1,\,\tau_0),\,\tilde{\xi}\right]}\right), \tag{3.106}$$

while the integration of $\mathcal{A}_{R,0}(s)$ leads to

$$\mathbb{A}_{R,0}(s) = -\frac{\Gamma^2\,s}{2\lambda^2}(1-\nu) + \int_0^s \cos\psi(\varsigma)\mathrm{d}\varsigma - \nu\frac{\Gamma^2}{\lambda^2}\int_0^s \cos^2\psi(\varsigma)\mathrm{d}\varsigma. \tag{3.107}$$

The first integral in Eq.(3.107) can be expressed as

$$\int_0^s \cos\psi(\varsigma)\mathrm{d}\varsigma = s + 2\frac{\Delta F_0 s - \Delta\Pi_0(s)}{\Delta F_0 n_0^2}, \tag{3.108}$$

where

$$\Delta\Pi_0(s) = \Pi\left(\frac{n_0^2}{n_0^2+1}, \mathrm{am}\left[\mathcal{R}_0(s,\,\tau_1,\,\tau_0), \tilde{\xi}\right], \tilde{\xi}\right) - \Pi\left(\frac{n_0^2}{n_0^2+1}, \tau_0, \tilde{\xi}\right). \tag{3.109}$$

Following a procedure similar to that adopted for the inflectional case, the second integral of Eq.(3.107) can be obtained as

$$\begin{aligned}&\int_0^s \cos^2\psi(\varsigma)\mathrm{d}\varsigma = s + 4\frac{\Delta F_0 s - \Delta\Pi_0(s)}{\Delta F_0 n_0^2} +\\ &2\frac{\left[\Delta\Pi_0(s) + (1+n_0^2)\left(n_0^2\Delta\mathscr{G}_0(s) - \Delta\mathscr{E}_0(s)\right)\right]n_0^2 + (n_0^2-1)\xi^2\left(\Delta\Pi_0(s) - \Delta F_0 s\right)}{\Delta F_0\, n_0^4\,\xi^2},\end{aligned} \tag{3.110}$$

where

$$\begin{aligned}\Delta\mathscr{E}_0(s) &= \mathscr{E}\left[\mathcal{R}_0(s,\,\tau_1,\,\tau_0),\,\tilde{\xi}\right] - E(\tau_0,\,\tilde{\xi})\\ \Delta\mathscr{G}_0(s) &= \frac{\mathrm{cn}\left[\mathcal{R}_0(s,\,\tau_1,\,\tau_0),\,\tilde{\xi}\right]\,\mathrm{dn}\left[\mathcal{R}_0(s,\,\tau_1,\,\tau_0),\,\tilde{\xi}\right]\,\mathrm{sn}\left[\mathcal{R}_0(s,\,\tau_1,\,\tau_0),\,\tilde{\xi}\right]}{1+n_0^2\mathrm{cn}^2\left[\mathcal{R}_0(s,\,\tau_1,\,\tau_0),\,\tilde{\xi}\right]}+\\ &\quad-\frac{\cos\tau_0\,\sin\tau_0\sqrt{1-\tilde{\xi}^2\sin\tau_0}}{1+n_0^2\cos^2\tau_0}.\end{aligned} \tag{3.111}$$

The term $\mathbb{A}_{R,0}(s)$ can finally be expressed as

$$\mathbb{A}_{R,0}(s) = \frac{\Gamma^2 s}{2\lambda^2}\frac{2\nu-\xi^2(\nu+1)}{\xi^2}+2\frac{\Delta F_0}{\Gamma^2}\left(\Delta\mathscr{E}_0(s)-n_0^2\Delta\mathscr{G}_0(s)-\Delta F_0\frac{(2-\xi^2)}{2}s\right), \tag{3.112}$$

where, as for the inflectional case, the above expression results to be independent of the elliptic integrals of the third kind.

The final expression for the centerline's position can be obtained through the Eqs.(3.112) and (3.106) in the form

$$\begin{bmatrix}x(s)/l\\ y(s)/l\end{bmatrix} = \begin{bmatrix}\cos\beta & -\sin\beta\\ \sin\beta & \cos\beta\end{bmatrix}\cdot\begin{bmatrix}\mathbb{A}_{R,0}(s)\\ \mathbb{B}_{R,0}(s)\end{bmatrix} \tag{3.113}$$

Elastic energy

The expression for the elastic energy stored in the Reissner beam can be obtained through Eqs.(3.74), (3.101) and (3.110), where the involved integrals are particularized at the coordinate $s = 1$. Following a route similar to that followed for the inflectional case, the contribution to the elastic energy associated to bending can be written as

$$\frac{\mathcal{E}_\theta}{B}l = 2\frac{\Delta F}{n_0^2+1}\int_{\mathcal{R}_0(0,\tau_1,\tau_0)}^{\mathcal{R}_0(1,\tau_1,\tau_0)}\left[\frac{\mathrm{dn}^2\,[r]}{\left(1-\frac{n_0^2\mathrm{sn}^2[r]}{n_0^2+1}\right)^2}\right]\mathrm{d}r, \tag{3.114}$$

so that the above integral can be evaluated ([27], Es. 362.17 at page 218) leading to the final expression for $\mathcal{E}_\theta$

$$\frac{\mathcal{E}_\theta}{B} l = \Delta F_0 \left[\Delta E_0 - n_0^2 \Delta \mathscr{G}_0(1) + \frac{\xi^2}{n_0^2} \left(\Delta F_0 + \frac{n_0^2(1-\xi^2) - \xi^2}{\xi^2(1+n_0^2)} \Delta \Pi_0(1) \right) \right], \tag{3.115}$$

where

$$\begin{aligned} \Delta E_0 &= \Delta \mathscr{E}_0(1) = E(\tau_1, \tilde{\xi}) - E(\tau_0, \tilde{\xi}) \\ \Delta \mathscr{G}_0(1) &= \frac{\cos\tau_1 \, \sin\tau_1 \sqrt{1 - \tilde{\xi}^2 \sin\tau_1}}{1 + n_0^2 \cos^2\tau_1} - \frac{\cos\tau_0 \, \sin\tau_0 \sqrt{1 - \tilde{\xi}^2 \sin\tau_0}}{1 + n_0^2 \cos^2\tau_0} \\ \Delta \Pi_0(1) &= \Pi\left(\frac{n_0^2}{n_0^2+1}, \tau_1, \tilde{\xi} \right) - \Pi\left(\frac{n_0^2}{n_0^2+1}, \tau_0, \tilde{\xi} \right). \end{aligned} \tag{3.116}$$

The contribution to the elastic energy associated to the axial and shear strains can be calculated by taking advantage of Eq.(3.110) particularized at the coordinate $s = 1$, thus obtaining

$$\begin{aligned} \frac{\mathcal{E}_{\varepsilon,\gamma}}{B} l = &\frac{\Gamma^4}{4\lambda^2}(1+\nu) + \frac{\nu \Gamma^4}{\lambda^2 n_0^4} \Bigg[n_0^2 + 1 + \\ &+ \frac{n_0^2(1+n_0^2)\left(n_0^2 \Delta \mathscr{G}_0(1) - \Delta E_0 \right) + \Delta \Pi_0(1) \left(n_0^2(1-\xi^2) - \xi^2 \right)}{\Delta F_0 \, \xi^2} \Bigg]. \end{aligned} \tag{3.117}$$

The final expression for the elastic energy is therefore given by

$$\begin{aligned} \frac{\mathcal{E}}{B} l = &\Delta F_0 \left[\Delta E_0 - n_0^2 \Delta \mathscr{G}_0(1) + \frac{\xi^2}{n_0^2} \left(\Delta F_0 + \frac{n_0^2(1-\xi^2) - \xi^2}{\xi^2(1+n_0^2)} \Delta \Pi_0(1) \right) \right] + \\ &\frac{\Gamma^4}{4\lambda^2}(1+\nu) + \frac{\nu \Gamma^4}{\lambda^2 n_0^4} \Bigg[n_0^2 + 1 + \\ &+ \frac{n_0^2(1+n_0^2)\left(n_0^2 \Delta \mathscr{G}_0(1) - \Delta E_0 \right) + \Delta \Pi_0(1) \left(n_0^2(1-\xi^2) - \xi^2 \right)}{\Delta F_0 \, \xi^2} \Bigg]. \end{aligned} \tag{3.118}$$

3.3.3 Evaluation of the unknown parameters ξ, β, Γ, τ_1 and τ_0

In the non-inflectional case, the closed-form solution is parametrized by three unknown parameters η, β and Γ, which can be obtained by exploiting the integral equations expressing the isoperimetric constraints (3.18) together with Eq.(3.92). In the general case $n_0 \neq 0$, the two further parameters τ_0 and τ_1 are now unknown, which represent the solution for the implicit Eqs.(3.97).

The exact solution for the deformed shape of the beam, given by Eqs.(3.113), is particularized at the right end $s = 1$ of the rod, through functions $\mathbb{A}_{R,0}$ and $\mathbb{B}_{R,0}$, thus obtaining

$$\begin{aligned}
\mathbb{A}_{R,0}(1) &= \frac{\Gamma^2}{2\lambda^2}\frac{2\nu - \xi^2(\nu+1)}{\xi^2} + 2\frac{\Delta F_0}{\Gamma^2}\left(\Delta E_0 - n_0^2 \Delta \mathscr{G}_0(1) - \Delta F_0 \frac{\left(2-\xi^2\right)}{2}\right) \\
\mathbb{B}_{R,0}(1) &= \frac{2\sqrt{1+n_0^2}}{\Gamma^2}\Delta F_0 \left(\frac{\sqrt{1-\tilde{\xi}^2\sin^2\tau_0}}{1+n_0^2\cos^2\tau_0} - \frac{\sqrt{1-\tilde{\xi}^2\sin^2\tau_1}}{1+n_0^2\cos^2\tau_1}\right),
\end{aligned} \tag{3.119}$$

so that the dimensionless expression for the isoperimetric constraints (3.18) is given by

$$\begin{bmatrix} d/l \\ 0 \end{bmatrix} = \begin{bmatrix} \cos\beta & -\sin\beta \\ \sin\beta & \cos\beta \end{bmatrix} \cdot \begin{bmatrix} \mathbb{A}_{R,0}(1) \\ \mathbb{B}_{R,0}(1) \end{bmatrix} \tag{3.120}$$

Finally, the following non-linear system is obtained

$$\begin{cases}
d/l\cos\beta = \mathbb{A}_{R,0}(1), \\
d/l\sin\beta = -\mathbb{B}_{R,0}(1), \\
\dfrac{\Gamma}{\xi}\sqrt{1+\dfrac{\nu\,\Gamma^2}{\lambda^2\xi^2}} = (-1)^p\left[F(\tau_1,\,\tilde{\xi}) - F(\tau_0,\,\tilde{\xi})\right], \\
\sin\tau_0 = \sin\left(\dfrac{\theta_0-\beta}{2}\right)\sqrt{\dfrac{1+n_0^2}{1+n_0^2\sin^2\left(\dfrac{\theta_0-\beta}{2}\right)}}, \\
\sin\tau_1 = \sin\left(\dfrac{\theta_l-\beta}{2}\right)\sqrt{\dfrac{1+n_0^2}{1+n_0^2\sin^2\left(\dfrac{\theta_l-\beta}{2}\right)}}.
\end{cases} \tag{3.121}$$

whose roots provide all the (non-unique) sets of the unknown parameters [ξ, β, Γ, τ_0, τ_1], corresponding to every combination of boundary conditions at both ends. Note that in the particular case $n_0 = 0$ the number of unknowns reduces from 5 to 3, as the parameters τ_0 and τ_1 can be expressed as functions of the unknown parameter β through Eqs.(3.98).

Part II

Snapping of the Euler's elastica with controlled ends

4

Stability of the elastica with controlled ends

Extending the procedures presented by other authors [10],[18], [76], the stability of the equilibrium configurations for the Euler's elastica (as shown in Chapter 2) is judged with reference to small and compatible perturbations in the rotation field $\theta(\mathsf{s})$. In particular, the stability is connected to the sign of the second variation of the total potential energy (2.4), which referring to weak perturbations can be written as

$$\begin{aligned}\delta^2\mathcal{V} = \int_0^l \Big[& B\delta\theta'^2 - 2\big[\delta R_x(\delta x' + \sin\theta\delta\theta) + \delta R_y(\delta y' - \cos\theta\delta\theta)\big] \\ & - \delta\theta^2\big[R_x\cos\theta + R_y\sin\theta\big]\Big]\,\mathrm{ds} - 2\left(\delta N_x\,\delta x(l) + \delta N_y\,\delta y(l)\right) + \\ & + 2\left(\delta M_l\,\delta\theta(l) + \delta M_0\,\delta\theta(0)\right),\end{aligned} \tag{4.1}$$

Integration by parts together with the conditions on vanishing variations at both ends (see Eqs.(2.7) and (2.8)) leads to the following identity

$$\begin{aligned}\delta^2\mathcal{V} = - \int_0^l \delta\theta \Big[& B\delta\theta'' + \delta\theta\big[R_x\cos\theta + R_y\sin\theta\big] + \\ & + 2\big[\delta R_x\sin\theta - \delta R_y\cos\theta\big]\Big]\,\mathrm{ds} + 2\int_0^l \Big[\delta R_x'\delta x + \delta R_y'\delta y\Big]\,\mathrm{ds}.\end{aligned}$$

(4.2)

It is worth to underline that, according to Eqs.$(2.10)_1$ and $(2.10)_2$, the internal forces R_x and R_y, and consequently their variations δR_x and δR_y, are independent on the curvilinear coordinate s. Moreover, the constant parameters $C_3 = -2\,\delta R_x/B$ and $C_4 = 2\,\delta R_y/B$ are introduced, so that, operating the substitutions (2.16), the second variation can be finally written by as

$$\delta^2\mathcal{V} = -B\int_0^l \delta\theta\,\left[\delta\theta'' + \delta\theta\frac{\Gamma^2}{l^2}\cos(\theta-\beta) - C_3\sin\theta - C_4\cos\theta\right]\mathsf{ds}. \tag{4.3}$$

A generic equilibrium configuration can be therefore judged stable when $\delta^2\mathcal{V}$ is positive definite ($\delta^2\mathcal{V} > 0$ for every compatible perturbation $\delta\theta(\mathsf{s})$), while unstable when $\delta^2\mathcal{V}$ is indefinite or negative definite. Differently, in the case that $\delta^2\mathcal{V}$ is semi-positive definite, the configuration is critical and higher order variations have to be considered (as described at the end of this Chapter).

Moreover, the null perturbations (2.7) at both ends provide the boundary conditions on the perturbation field $\delta\theta(0) = \delta\theta(l) = 0$, together with the following isoperimetric constraints

$$\int_0^l \delta\theta\sin\theta\,\mathsf{ds} = 0, \qquad \int_0^l \delta\theta\cos\theta\,\mathsf{ds} = 0. \tag{4.4}$$

which are in turn derived from vanishing of the variations $\delta x(l)$ and $\delta y(l)$ through Eqs.$(2.3)_1$ and (2.13).

The change of variables $s = \mathsf{s}/l$ is introduced, so that the dimensionless equation of the second variation (4.3) is given by

$$\frac{\delta^2\mathcal{V}}{B}l = -\int_0^1 \delta\theta(s)\,\left[\delta\theta''(s) + \delta\theta(s)\Gamma^2\cos(\theta(s)-\beta) - \tilde{C}_3\sin\theta(s) - \tilde{C}_4\cos\theta(s)\right]\mathrm{d}s \tag{4.5}$$

where the symbol ' denotes now the derivative with respect to the dimensionless curvilinear coordinate s. The dimensionless parameters $\tilde{C}_3 = -2\,\delta R_x l^2/B$ and $\tilde{C}_4 = 2\,\delta R_y l^2/B$ have also been introduced. The perturbation field $\delta\theta(s)$ is therefore subject to the following homogeneous boundary conditions

$$\delta\theta(0) = 0, \qquad \delta\theta(1) = 0 \tag{4.6}$$

and to the following dimensionless version of the isoperimetric constraints (4.4)

$$\int_0^1 \delta\theta \sin\theta \, \mathrm{d}s = 0, \qquad \int_0^1 \delta\theta \cos\theta \, \mathrm{d}s = 0. \tag{4.7}$$

At this stage, the stability of a generic configuration of the system with total potential energy (2.4) can be studied through the conjugate points method (see for instance Bolza[25]), where the perturbation field $\delta\theta$ is subject to the homogeneous boundary conditions $\delta\theta(0) = \delta\theta(1) = 0$ and to the isoperimetric constraints (4.7).

Hovewer, the equivalent procedure proposed by Levyakov and Kuznetsov [75] and Bigoni et al.[19] is adopted, because of its immediate applicability to problems subject to boundary conditions different from those of the Dirichlet type. More specifically, the eigenfunction $\phi_n(s)$ is introduced, which is subject to the boundary conditions

$$\phi_n(0) = 0, \quad \phi_n(1) = 0, \quad \int_0^1 \phi_n(s) \sin\theta(s) \, \mathrm{d}s = 0, \quad \int_0^1 \phi_n(s) \cos\theta(s) \, \mathrm{d}s = 0, \tag{4.8}$$

so that the positive definiteness of the second variation, Eq.(4.5), can be analyzed investigating the non-trivial solutions for the following Sturm-Liouville problem

$$\phi_n''(s) + \zeta_n \, w(s) \, \phi_n(s) = \tilde{C}_{3,n} \sin\theta(s) + \tilde{C}_{4,n} \cos\theta(s), \tag{4.9}$$

where $n \in \mathbb{N}$ and w is the *weight function*, defined as

$$w(s) = \Gamma^2 \cos\big(\theta(s) - \beta\big). \tag{4.10}$$

The inclination β, the normalized load Γ and the rotation field $\theta(s)$ are known at this stage from the definition of equilibrium configuration, while ζ_n is the eigenvalue related to the eigenfunction $\phi_n(s)$. In particular, according to Broman[26], there exist for the problem (4.9) a countably infinite set of eigenvalues ζ_n which are all non-negative and which can be disposed into an increasing sequence (so that $\zeta_n < \zeta_{n+1}$). Moreover, $\zeta_n \to \infty$ as $n \to \infty$ and the following ortogonality condition with the weight function (4.10) holds [19] for any $n \neq m$

$$\int_0^1 w \, \phi_n \phi_m \, \mathrm{d}s = 0 \tag{4.11}$$

while for $n = m$

$$\zeta_n \int_0^1 w\,\phi_n^2\,\mathrm{d}s = \int_0^1 {\phi_n'}^2\,\mathrm{d}s \tag{4.12}$$

and therefore any compatible perturbation $\delta\theta$ can be expressed as the Fourier series expansion of the eigenfunctions $\phi_n(s)$

$$\delta\theta(s) = \sum_{n=1}^{\infty} c_n \phi_n(s), \tag{4.13}$$

where c_n are the Fourier coefficients. The proof of the Eq.(4.11) can be easily obtained by considering an eigenfunction $\phi_m(s)$ (with $m \neq n$) being a solution for the following equation

$$\phi_m''(s) + \zeta_m\, w(s)\, \phi_m(s) = \tilde{C}_{3,m} \sin\theta(s) + \tilde{C}_{4,m} \cos\theta(s), \tag{4.14}$$

and satisfying the same boundary conditions (4.8) holding for ϕ_n . The Eqs.(4.9) and (4.14) can be multiplied by $\phi_m(s)$ and $\phi_n(s)$ respectively and then integrated between $s = 0$ and $s = 1$. The isoperimetric constraints $(4.8)_3$ and $(4.8)_4$ provide the right-hand sides of both equations to vanish, so that one obtains

$$\int_0^1 \phi_n''\phi_m\,\mathrm{d}s + \zeta_n \int_0^1 w\,\phi_n\phi_m\,\mathrm{d}s = 0, \quad \int_0^1 \phi_m''\phi_n\,\mathrm{d}s + \zeta_m \int_0^1 w\,\phi_m\phi_n\,\mathrm{d}s = 0.$$

Taking the difference of the latter equations and integrating by parts, the fulfilment of the boundary conditions $(4.8)_1$ and $(4.8)_2$ leads to the condition (4.11) for every $\zeta_n \neq \zeta_m$. On the other hand, the proof of the Eq.(4.12) can be obtained through a similar procedure, but multiplying the Eq.(4.9) by ϕ_n. The desired conclusion can be proven again through the fulfilment of the isoperimetric constraints $(4.8)_3$ and $(4.8)_4$ and then integrating by parts.

By considering the properties (4.11) and (4.12) together with the aforementioned Fourier series expansion (4.13), the second variation of the total potential energy (4.3) can be rewritten as

$$\frac{\delta^2\mathcal{V}}{B} l = \sum_{n=1}^{\infty} \left(1 - \frac{1}{\zeta_n}\right) c_n^2 \int_0^1 \phi_n'(s)^2\,\mathrm{d}s, \tag{4.15}$$

so that the equilibrium configuration is stable whenever $\zeta_n \notin [0,1]$ for every n, unstable when $\zeta_n \in (0,1)$ for at least one value of n, and to be investigated through higher-order variations otherwise. It follows that the condition of smallest eigenvalue greater than one implies that the configuration is stable.

The proof of Eq.(4.15) can be obtained by firstly eliminating the terms $\tilde{C}_3 \sin\theta(s)$ and $\tilde{C}_4 \cos\theta(s)$ from the equation of the dimensionless second variation (4.5) through the constraints (4.4) and then substituting the expression (4.13). The following equation is obtained

$$\frac{\delta^2 \mathcal{V}}{B} l = -\int_0^1 \left[\sum_{m=1}^{\infty} c_m \phi_m\right] \left[\sum_{n=1}^{\infty} c_n \left(\phi_n'' + w\,\phi_n\right)\right] \mathrm{d}s,$$

where substituting the function ϕ_n'' through Eq.(4.9) and exploiting again the isoperimetric constraints (4.4), the previous equation reduces to

$$\frac{\delta^2 \mathcal{V}}{B} l = \int_0^1 \left[\sum_{m=1}^{\infty} c_m \phi_m\right] \left[\sum_{n=1}^{\infty} c_n \left(1 - \frac{1}{\zeta_n}\right) \zeta_n\, w\, \phi_n\right] \mathrm{d}s.$$

As a result of the orthogonality condition (4.11), the second variation reduces to the following sum of integrals

$$\frac{\delta^2 \mathcal{V}}{B} l = \sum_{n=1}^{\infty} c_n^2 \left(1 - \frac{1}{\zeta_n}\right) \zeta_n \int_0^1 w\, \phi_n^2 \,\mathrm{d}s,$$

so that employing the condition (4.12) leads to the final formulation of the Eq.(4.15).

4.1 Numerical evaluation of the stability property

Following Levyakov and Kuznetsov [75], the eigenfunction $\phi_n(s)$ can be represented as the linear combination of the functions $\varphi_n^{(j)}(s)$ $(j = 1, ..., 4)$

$$\phi_n(s) = \sum_{j=1}^{4} \tilde{C}_{j,n} \varphi_n^{(j)}(s), \tag{4.16}$$

where the four functions are defined respectively as the solutions for the following four second order differential problems

$$\begin{cases} \varphi_n^{(1)''}(s) + \zeta_n\, w(s)\, \varphi_n^{(1)}(s) = 0, \\ \varphi_n^{(1)}(0) = 1, \\ \varphi_n^{(1)'}(0) = 0, \end{cases} \qquad \begin{cases} \varphi_n^{(2)''}(s) + \zeta_n\, w(s)\, \varphi_n^{(2)}(s) = 0, \\ \varphi_n^{(2)}(0) = 0, \\ \varphi_n^{(2)'}(0) = 1, \end{cases}$$

$$\begin{cases} \varphi_n^{(3)''}(s) + \zeta_n\, w(s)\, \varphi_n^{(3)}(s) = \sin\theta(s), \\ \varphi_n^{(3)}(0) = 0, \\ \varphi_n^{(3)'}(0) = 0, \end{cases} \qquad \begin{cases} \varphi_n^{(4)''} + \zeta_n\, w(s)\, \varphi_n^{(4)}(s) = \cos\theta(s), \\ \varphi_n^{(4)}(0) = 0, \\ \varphi_n^{(4)'}(0) = 0. \end{cases} \tag{4.17}$$

By considering the boundary condition $(4.8)_1$, and the boundary conditions defined for each function $\varphi_n^{(j)}(s)$ $(j = 1, ..., 4)$ in the differential problems (4.17), it follows that $\tilde{C}_{1,n} = 0$ so that the evaluation of the function $\varphi_n^{(1)}(s)$ can be disregarded. Imposing the remaining boundary conditions $(4.8)_2$, $(4.8)_3$, and $(4.8)_4$, the homogeneous linear problem $\mathbf{A}(\zeta_n)\mathbf{C} = \mathbf{0}$ is obtained for the vector $\mathbf{C} = \left\{\tilde{C}_{2,n}, \tilde{C}_{3,n}, \tilde{C}_{4,n}\right\}$, where

$$\mathbf{A}(\zeta_n) = \begin{bmatrix} \varphi_n^{(2)}(1) & \varphi_n^{(3)}(1) & \varphi_n^{(4)}(1) \\ \int_0^1 \varphi_n^{(2)}(s)\cos\theta(s)\,\mathrm{d}s & \int_0^1 \varphi_n^{(3)}(s)\cos\theta(s)\,\mathrm{d}s & \int_0^1 \varphi_n^{(4)}(s)\cos\theta(s)\,\mathrm{d}s \\ \int_0^1 \varphi_n^{(2)}(s)\sin\theta(s)\,\mathrm{d}s & \int_0^1 \varphi_n^{(3)}(s)\sin\theta(s)\,\mathrm{d}s & \int_0^1 \varphi_n^{(4)}(s)\sin\theta(s)\,\mathrm{d}s \end{bmatrix}, \tag{4.18}$$

so that the eigenvalues ζ_n can be finally evaluated from the condition of vanishing determinant, $\det\mathbf{A}(\zeta_n) = 0$. From the operational point of view, with reference to every equilibrium rotation field $\theta(s)$, the differential system (4.17) can be numerically solved as a function of $\zeta_n \in [0, 1]$ and the configuration judged stable when $\det\mathbf{A}(\zeta_n) \neq 0$ for $\zeta_n \in [0, 1]$, while unstable if this condition is not fulfilled.

It is noted that if $\det\mathbf{A}(\zeta_n)$ vanishes for $\zeta_1 = 1$, the related equilibrium configuration is unstable if the third variation is non-null for the related eigenfunction $\phi_n(s)$, while if this latter variation vanishes the analysis should consider higher-order variations. In particular, if the next even variation is positive (negative) for $\delta\theta(s) = \phi_n(s)$, the configuration is stable (unstable). Otherwise, if

the next even variation is null for $\delta\theta(s) = \phi_n(s)$, the next odd variation should be considered and if not null the configuration is unstable.

Moreover, the limit condition $\zeta_n = 1$ causes the perturbation $\delta\theta = \phi_n$, which is a solution for the differential equation (4.9), to be also a solution for the differential equation within the integral of the second variation (4.5), which is known in literature as *Jacobi's accessory equation*[25], and satisfying the imposed boundary conditions at both ends. Consequently, the second variation is null, so that the corresponding equilibrium configuration having $\zeta_1 = 1$ is at the stability limit. All the snapping configurations obtained in the present work correspond to the aforementioned condition, which is always complemented by a non-null third variation of the total potential energy $\delta^3\mathcal{V}$ (unstable 'saddle' points). In contrast, supercritical or subcritical pitchfork bifurcations have null second and third variations, which are complemented by a positive fourth variation $\delta^4\mathcal{V}$ (stable stationary points).

Finally, the k-th variation of the total potential energy can be written for $k \geq 3$ as

$$\frac{\delta^k \mathcal{V}\, l}{B} = \begin{cases} (-1)^{\frac{k+1}{2}} \Gamma^2 \displaystyle\int_0^1 [\delta\theta(s)]^k \, \sin\big(\theta(s) - \beta\big) \, \mathrm{d}s, & k \text{ odd}, \\ (-1)^{\frac{k}{2}} \Gamma^2 \int_0^1 [\delta\theta(s)]^k \, \cos\big(\theta(s) - \beta\big) \, \mathrm{d}s, & k \text{ even}. \end{cases} \tag{4.19}$$

5

Snapping of rods with controlled ends

5.1 Introduction

Snap instability is a well-known phenomenon in mechanics for which a structural system suffers a sudden and dramatic change in the deformed configuration triggered by a small variation in the loading conditions. This behaviour is explained as the consequence of the stability loss for the deformed configuration, so that the structure dynamically moves towards a non-adjacent configuration through a partial release of its elastic energy. Classical examples of snap mechanisms can be found in shell structures, also in everyday life, as for instance when squeezing an empty can of soda. Other examples may be found in nature, as in the case of click-beetles (elateridae) [44], insects able to turn on their side when initially lying on their back by means of a jump realized by a snap mechanism.

Following the new paradigm of exploiting (instead of avoiding) instabilities in the structural design for advanced applications [56, 96], in the last years many researchers have investigated the snap mechanisms towards the realization of bistable or multistable devices [4, 28, 29, 32, 36, 37, 98, 105], metamaterials [48, 83, 95], locomotion [82, 112, 115, 116], and energy harvesting [54, 61]. Because the typical approach adopted in these investigations is to focus on specific evolutive mechanical problems and specific structural properties, the

evaluation of the whole set of critical snap conditions is missed from a general perspective.

The present chapter provides a general criterion to be exploited in the non-linear design of structures to obtain (or to avoid) snap mechanisms. With reference to the model of an inextensible (weightless) linearly elastic strip, modelled as a planar Euler's elastica, the number of stable equilibrium configurations is disclosed by varying the parameters defining the kinematics of the rod ends, which are reduced to a normalized distance between the two ends and the two rotations of the ends. The stability of the equilibrium configurations, expressed in closed form through elliptic integrals as shown in Chapter 2, is assessed by analyzing the sign of the second variation of the total potential energy through the procedure show in Chapter4. This analysis allows one to define the correspondence between the ends' kinematics and the presence of multiple stable configurations, so that the set of boundary conditions for which one of these configurations loses its stability follows.

The obtained results are used to define *universal snap surfaces*, collecting the whole sets of critical boundary conditions for which the system snaps. The energy release at snapping is also estimated and investigated by means of a dimensionless analysis for varying the snap conditions. The theoretical predictions are experimentally validated through comparisons with data available for specific symmetric boundary conditions and observations on a physical model proposed for investigating non-symmetric cases. Finally, finite element simulations performed with ABAQUS show the reliability of the presented universal surface in the case of evolutions with moderate velocity and its limits in the case of very fast ends evolutions. The presented results have been published in an international journal (see Cazzolli and Dal Corso[33]).

5.2 Number of stable solutions, bifurcations and universal snap conditions

For any triad of parameters $\{d, \theta_0, \theta_l\}$ representing the imposed boundary conditions (2.3) at both ends of the rod, the non-linear systems (2.56) and (2.83) can be solved to numerically evaluate the existing pairs of parameters (β and ξ for $m = 0$, or β and η for $m \neq 0$, respectively) associated with the possible stable equilibrium configurations. Reference is made solely to configurations with $m \in [0, 2]$ because those with $m > 2$ are numerically found to be always unstable (although a general analytical proof seems awkward, [77]). The number of stable

solutions has been observed to vary from 1 to 3 within the kinematical parameter space defined by $\{d, \theta_0, \theta_l\}$.[1] Furthermore, being the developed model referred to the case of rods with loads applied only at the two ends, configurations of self-intersecting elastica are found through the presented numerical evaluation for a set of boundary conditions, while the respective self-contact configurations between different parts of the rod are excluded (see Section 5.2.4 for further details).

A typical map in the plane $[\theta_0, \theta_l]$ representing the number of stable solutions is shown in Fig. 5.1 (left) for a distance $d = 0.6l$, where the existence of one, two, and three stable configurations for a specific triad $\{d, \theta_0, \theta_l\}$ is identified by the regions I, II, and III, respectively. The figure shows that the regions within this plane are characterized by a periodicity vector $[2\pi, 2\pi]$ related to the shifting in the solution for $2j\pi$ $(j \in \mathbb{Z})$ when the imposed rotations are modified by $2j\pi$ at both ends,

$$\begin{cases} \theta^*(0) = \theta(0) + 2j\pi, \\ \theta^*(l) = \theta(l) + 2j\pi, \end{cases} \quad \Leftrightarrow \quad \theta^*(s) = \theta(s) + 2j\pi, \qquad \forall j \in \mathbb{Z}, \tag{5.1}$$

With reference to such periodicity property, it is instrumental to introduce the angles θ_A and θ_S, respectively defined as the antisymmetric and symmetric parts of the imposed rotations,

$$\theta_A = \frac{\theta_0 + \theta_l}{2}, \qquad \theta_S = \frac{\theta_l - \theta_0}{2}, \tag{5.2}$$

which are reported in Fig. 5.1 (left) through grey axes inclined at an angle $\pi/4$ with respect to the axes $\theta_0 - \theta_l$. By considering the shifting of the rotation field expressed by Eq.(5.1) it follows that

$$\theta_A^* = \theta_A + 2j\pi, \qquad \theta_S^* = \theta_S, \qquad \forall j \in \mathbb{Z}, \tag{5.3}$$

highlighting the mentioned periodicity property of the equilibrium configurations which is given only in the θ_A variable within the $\theta_A - \theta_S$ reference system.[2]

[1] It is remarked that the end rotations θ_0 and θ_l have no restriction on their value, being unlimited their difference $\theta_l - \theta_0 = \int_0^l \theta'(s)\mathrm{d}s$. If the angles θ_0 and θ_l were referred to the end inclinations (instead of being referred to the end rotations, as in the present analysis), their respective sets would be limited due to angular periodicity, for example to $\theta_0 \in (-\pi, \pi)$ and $\theta_l \in (-\pi, \pi)$, and more than 3 stable configurations could be found as solution to the same end inclinations problem [3].

[2] The periodicity for the solution in the rotation field for the elastica is similar to that observed in the kinematic description of the physical pendulum, which is insensitive to an increase of an angle $2j\pi$ $(j \in \mathbb{Z})$.

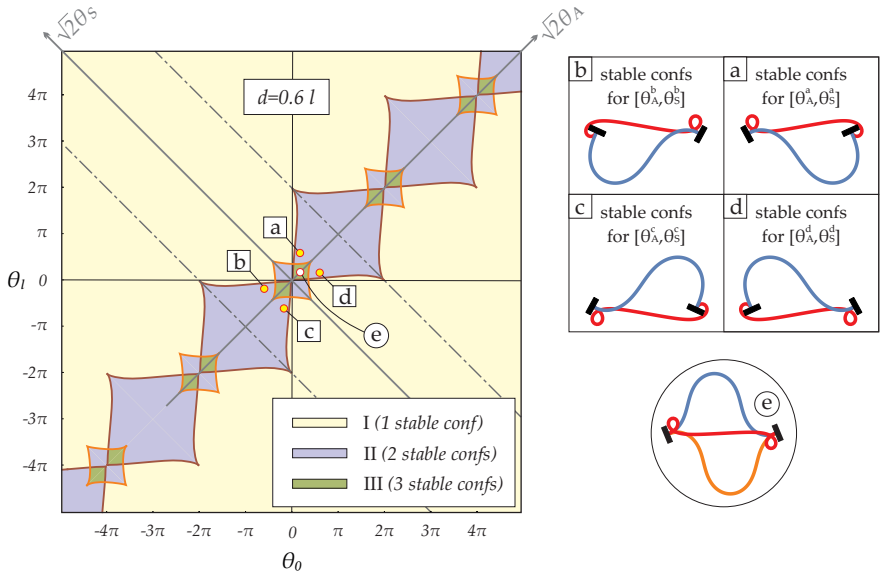

Figure 5.1: (Left) Number of stable equilibrium configurations for a distance $d = 0.6l$ for varying θ_0 and θ_l (or equivalently, θ_A and θ_S). Regions with different colors and marked with I, II, and III identify triads $\{d, \theta_0, \theta_l\}$ for which one, two, and three stable configurations exist, respectively. (Right, upper part) Pairs of stable equilibrium configurations possible for the boundary conditions a, b, c, and d highlighting the mirroring properties when the modulus of the antisymmetric and the symmetric parts of the rotations is kept constant. (Right, bottom part) The three stable equilibrium configurations possible for the boundary conditions e.

Another interesting property is now pointed out. A change in sign for each of the two parameters θ_A and θ_S is related to a specific 'mirror' in the boundary conditions for the parameters θ_0 and θ_l, namely

$$\text{Conf. a:} \left\{ \begin{array}{l} \theta_A^{\mathrm{a}} = \overline{\theta}_A \\ \theta_S^{\mathrm{a}} = \overline{\theta}_S \end{array} \right\} \Leftrightarrow \left\{ \begin{array}{l} \theta_0^{\mathrm{a}} = \overline{\theta}_0 \\ \theta_l^{\mathrm{a}} = \overline{\theta}_l \end{array} \right\}, \qquad \text{Conf. b:} \left\{ \begin{array}{l} \theta_A^{\mathrm{b}} = -\overline{\theta}_A \\ \theta_S^{\mathrm{b}} = \overline{\theta}_S \end{array} \right\} \Leftrightarrow \left\{ \begin{array}{l} \theta_0^{\mathrm{b}} = -\overline{\theta}_l \\ \theta_l^{\mathrm{b}} = -\overline{\theta}_0 \end{array} \right\},$$

$$\text{Conf. c:} \left\{ \begin{array}{l} \theta_A^{\mathrm{c}} = -\overline{\theta}_A \\ \theta_S^{\mathrm{c}} = -\overline{\theta}_S \end{array} \right\} \Leftrightarrow \left\{ \begin{array}{l} \theta_0^{\mathrm{c}} = -\overline{\theta}_0 \\ \theta_l^{\mathrm{c}} = -\overline{\theta}_l \end{array} \right\}, \qquad \text{Conf. d:} \left\{ \begin{array}{l} \theta_A^{\mathrm{d}} = \overline{\theta}_A \\ \theta_S^{\mathrm{d}} = -\overline{\theta}_S \end{array} \right\} \Leftrightarrow \left\{ \begin{array}{l} \theta_0^{\mathrm{d}} = \overline{\theta}_l \\ \theta_l^{\mathrm{d}} = \overline{\theta}_0 \end{array} \right\}. \tag{5.4}$$

It follows that the respective deformed configurations of the cases b, c and d

can be obtained through the mirroring of the reference deformed configurations of the case a, Fig. 5.1 (right, upper part). The mirroring properties can be summarized as:

- a change in sign for the parameter θ_A defines a configuration obtained as the mirroring with respect to the line orthogonal to that joining the two ends and passing at its center;
- a change in sign for the parameter θ_S defines a configuration obtained as two mirrorings, one with respect to the line joining the two ends and the other with respect to the orthogonal line at its mid point;
- a change in sign for both the parameters θ_A and θ_S defines a configuration obtained as the mirroring with respect to the line joining the two ends.

These mirroring properties allow a simplified representation of the number of stable solutions within the plane $|\theta_A| - |\theta_S|$, so that only the first quadrant is drawn and restricted to the condition $|\theta_A| \leq \pi$ because of the periodicity vector. In this way, the map of solutions number reported in Fig. 5.1 (left) for a distance $d = 0.6l$ is represented in Fig. 5.2 (right), where the inflection points number m related to each stable solution is specified as listed in the subscript within parentheses. As a further example, the representation of the number of stable solutions is also reported for a distance $d = 0.3l$ in Fig. 5.2 (left). Lines crossing and lines bounding the regions I, II, and III are reported in Fig. 5.2, in particular:

- the grey thin lines crossing the regions define the transition for which the number m of inflection points along the rod changes, while the number of stable solutions is kept constant. These lines can be defined imposing null curvature at one of the two ends (so that the rod has one hinged end while the other is a rotating clamp);
- the thick lines bounding the regions define the transition for which the number of stable solutions changes, so that they represent the critical condition of snap for one of the stable solutions. The lines are reported as thick orange and thick brown in order to identify the two possible different snap-back conditions (described in the following).

Because of the simple reference (clamped-hinged) structure to which are related, the grey lines can be found from straightforward computations. Indeed, for a given distance d, the relation $\theta_S = \theta_S(\theta_A)$ tracing the grey line can be computed

from the nonlinear system (**??**) by imposing the condition of null moment at one of the two rod's ends, for example considering $\omega_0 = (-1)^p \pi/2$ if the hinge is located at the coordinate $s = 0$. Differently, drawing the orange and brown thick lines is a more complex task because they are related to the issue of stability loss for one of the possible equilibrium configurations. Such analysis requires a further representation for the solution domains which is now introduced.

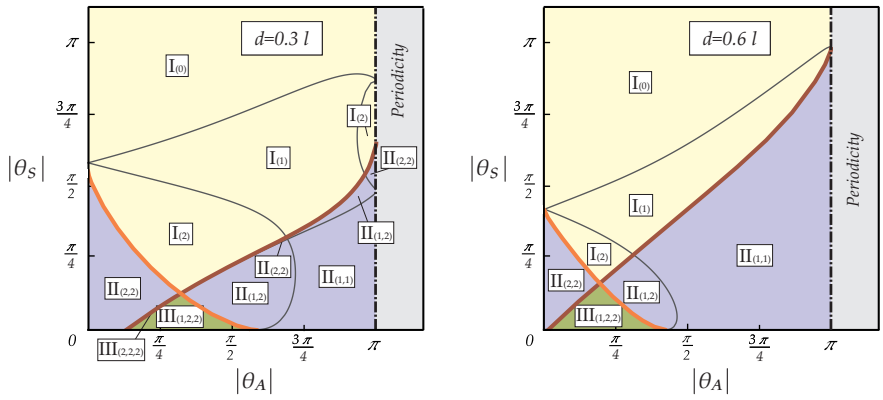

Figure 5.2: Number of stable equilibrium configurations in the plane $|\theta_A| - |\theta_S|$, with the specification of the inflection points number m related to each stable solution listed in the subscript within parentheses, for the distances $d = 0.3l$ (left) and $d = 0.6l$ (right).

5.2.1 Equilibrium paths for a fixed distance d

In the attempt to simplify the visualization of the solution domains for a fixed distance d, reference is made to the quasi-static evolutions of the rotations θ_A and θ_S starting from a stable configuration for null angles at both clamps, $\theta_0 = \theta_l = 0$ so that $\theta_A = \theta_S = 0$ (namely, a shortening of the distance between the two clamps is imposed starting from the straight configuration). Only two stable solutions can be obtained for these 'initial' boundary conditions, both characterized by the same number of inflection points ($m = 2$) but differing in the value of p, and representative of the two possible buckled configurations for a rod clamped at both ends and subject to a shortening $l - d$. By considering this, the solution maps of Fig. 5.1 and of Fig. 5.2 (right) for a fixed distance $d = 0.6l$ can be split in two separate representations, each of these restricted to a specific value of p (identifying the positiveness, $p = 0$, or negativeness, $p = 1$,

of the curvature at the coordinate $s = 0$) as shown in Fig. 5.3 and therefore related to one of the two initial configurations possible for $\theta_A = \theta_S = 0$. In this way, the generic evolution for the boundary conditions can be represented with a continuous curve in the plane $\theta_A - \theta_S$ starting from its origin. Despite the non-linearity of the problem, each point along this curve is related to a (when existing) unique deformed configuration whenever snap conditions or bifurcation points are not encountered along the considered evolution. Consequently, such a representation provides a fundamental tool in the definition of the solution domains and of the snap-back conditions for every possible evolution of the imposed rotations at a fixed distance d, showing the critical and bifurcation conditions depending on the value of p.

The moment-rotation response curve associated with each evolution of the boundary conditions reveals the presence of snap-back instabilities (related to the annihilation of the second variation, $\delta^2\mathcal{V} = 0$) when a point with vertical tangent in the response curve is reached and no smooth stable[3] evolutions of the deformed configuration can be obtained for a further monotonic variation in the rotation. The set of boundary conditions $\{d, \theta_A, \theta_S\}$ corresponding to the vertical tangency in the moment-rotation response are identified by means of a standard bisection algorithm applied to the analyzed equilibrium path.

The above described analysis provides the domains and lines as reported in Fig. 5.3, where also specific equilibrium configurations are displayed for some critical pairs of boundary conditions. The solution domains are reported with different colors, identifying different properties as follows:

- *blue/green/red regions* – the unique stable equilibrium configuration corresponding to the considered p has zero, one, and two inflection points along the rod for the blue, green, and red regions, respectively;

- *white regions* – no stable equilibrium configuration is possible for that specific value of p. However, for the mirroring property, the stable equilibrium configuration exists for the other value of p;

- *grey regions* – the equilibrium configuration related to a pair $\overline{\theta}_A, \overline{\theta}_S$ belonging to this region can be represented by that related to the pair within the colored or white regions (namely, outside the grey regions) considering the shifting of the solution as highlighted by Eq.(5.3). The corresponding

[3]In general, the equilibrium path smoothly continues after the snap point with an opposite change of the rotation value. However, this path is not considered here due to its unstable nature.

dual values can be evaluated from $\overline{\theta}_A$ and $\overline{\theta}_S$ as

$$\theta_A = \overline{\theta}_A - 2\pi \left\lfloor \frac{1}{2} + \frac{\overline{\theta}_A}{2\pi} \right\rfloor, \qquad \theta_S = \overline{\theta}_S, \tag{5.5}$$

where the symbol $\lfloor \cdot \rfloor$ represents the floor function, which evaluates the greatest integer that is less than or equal to the relevant argument. Note that, from Eq.(5.5) follows that $\theta_A \in [-\pi, \pi]$ for every $\overline{\theta}_A$.

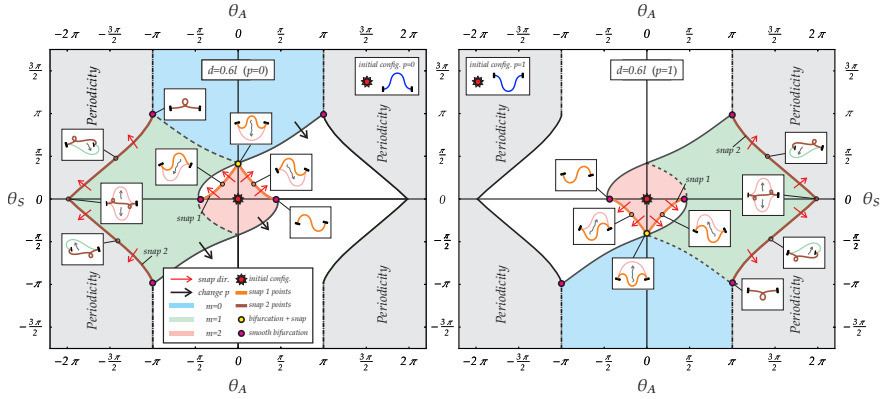

Figure 5.3: Domains of unique stable solutions within the plane $\theta_A - \theta_S$ for $p = 0$ (left) and $p = 1$ (right) for evolutions with a fixed distance $d = 0.6l$ and starting from the boundary conditions $\theta_A = \theta_S = 0$. Regions with the same color identify stable equilibrium configurations having the same number m of inflection points along the rod (note the mirroring property of the domains for varying p). See the main text for the definition of the domain and line colors.

Similarly, the lines separating the different domains are drawn with various styles, representing the type of transition in the equilibrium configuration occurring when the evolution of the boundary conditions passes from one region to another.

With reference to any continuous evolution in the set of applied rotations $\{\theta_A(\tau), \theta_S(\tau)\}$ from an initial ($\tau = \tau_i$) to a final instant ($\tau = \tau_f$), where τ is a time-like parameter, the following cases are possible:

- if a *dashed grey line* is crossed, the equilibrium configuration smoothly varies changing the number m of the inflection points, while the value of p is kept constant;

- if a *continuous grey line* is crossed, the equilibrium configuration smoothly varies changing both the number m of the inflection points and the value of p, in particular $p(\tau_f) = 1 - p(\tau_i)$. Therefore, the final configuration is related to a solution map dual to that of the initial value of $p(\tau_i)$. As it can be noted in Fig. 5.3, the continuous grey lines are present only at the borders between one of the colored regions with a white region;

- if a *dashdotted grey line* is crossed, the equilibrium configuration smoothly varies keeping fixed both the number m of the inflection points and the value of p. As it can be noted in Fig. 5.3, these lines appears only at $\theta_S = \pm\pi$ and are connected to the shifting property of the solution, Eq.(5.3), so that, by considering Eq.(5.5), the final equilibrium configuration has to be referred to the values $\{\theta_A(\tau_f) - 2\pi\lfloor 1/2 + \theta_A(\tau_f)/(2\pi)\rfloor\ ,\ \theta_S(\tau_f)\}$;

- if a *thick orange line* is crossed, a critical configuration of snap-back type 1 instability is encountered so that a small variation in the boundary conditions realizes a large variation in the equilibrium configuration. Therefore, the final equilibrium configuration is achieved by means of a dynamic motion from the initial one. The initial and final configurations are described by a different value of p, namely, $p(\tau_f) = 1 - p(\tau_i)$. From the present analysis it is also observed that before and after the snap-back type 1 mechanism there are always two inflection points, $m(\tau_f) = m(\tau_i) = 2$;

- if a *thick brown line* is crossed, the critical condition of snap-back type 2 instability is encountered. However, differently from crossing the thick orange line, in this case the boundary conditions of the final configuration $\{\theta_A(\tau_f)/(2\pi), \theta_S(\tau_f)\}$ lie within the grey region, so that the interpretation of the considered solution map requires a further effort. Indeed, from the solution shifting principle, the final configuration should be referred to the values $\{\theta_A(\tau_f) - 2\pi\lfloor 1/2 + \theta_A(\tau_f)/(2\pi)\rfloor, \theta_S(\tau_f)\}$. If these values correspond to a white region for the solution map with $p(\tau_i)$, the final configuration is the one associated with the same values but related to the dual map for which $p(\tau_f) = 1 - p(\tau_i)$;

- if no line is crossed, the initial and final configurations have the same values for p and m, and therefore are represented within the same solution map corresponding to $p(\tau_i) = p(\tau_f)$.

It is worth to remark that crossing a colored thick line does not always provide a snap-back instability. Indeed, this phenomenon is strictly related to the equilibrium configuration taken by the structural system before crossing this

condition. More specifically, referring to the $\theta_A - \theta_S$ plane and a fixed distance d, the snap mechanism is realized whenever the scalar product between the incremental vector connecting the initial to the final boundary conditions and the normal (defined as the derivative of the tangent) to the snap-back curve is non-negative.

Moreover, the snap-back curves display the typical structure of cusps (a typical shape analysed within the theory of catastrophes [6, 13, 109, 119]), revealing how the magnitude of the so-called control parameter at a critical point decreases with respect to the perfect case (maximum critical rotation at the cusp) due to the presence of increasing imperfections. In particular, the role of such control parameter is played by the symmetric part of the rotation θ_S for snap-back curves of type 1 and by the antisymmetric part θ_A for snap-back curves of type 2, while the role of the imperfection is respectively played by θ_A and θ_S.

It is finally noted that all the regions and lines reported in Fig. 5.3 satisfy the mirroring properties shown in Eqs.(5.4) and highlighted in Fig. 5.1 (right). Therefore, when p is switched from 0 to 1, the domains of the case $p = 1$ (Fig. 5.3, right) can be obtained from those of the case $p = 0$ (Fig. 5.3, left) through a mirroring with respect to the axis θ_S for the configurations with $m = 1$ and through a double mirroring (with respect to both axes, θ_A and θ_S) for those with $m = 0$ and $m = 2$.

Similarly to Fig. 5.3, the domains are reported in Figs. 5.4 and 5.5 for different values of the end's distance, respectively for $d = \{0.05, 0.1, 0.2, 0.3\}\, l$ and $d = \{0.4, 0.5, 0.7, 0.8\}\, l$. The maps are reported only for $p = 0$, since those are related to the case $p = 1$ through mirroring.

A last comment is made about the two limit cases of maximum and minimum distance between the ends, respectively $d \simeq l$ and $d = 0$:

- In the former case ($d \simeq l$), although the analysis should be improved by considering stretching energy, the present model (based on the inextensibility assumption) shows that the curve of snap-back type 1 reduces to the point with coordinates $\theta_A = \theta_S = 0$ while the curve of snap-back type 2 reduces to the four line segments defined by $|\theta_S| = 2\pi - |\theta_A|$ with $|\theta_A| \in [\pi, 2\pi]$;

- Differently, in the case when the two ends have the same position ($d = 0$), the mechanical system shows the independence of the parameter θ_A, because in the case of null distance the angle θ_A merely expresses a rigid rotation of the entire structure and the elastic energy stored within the

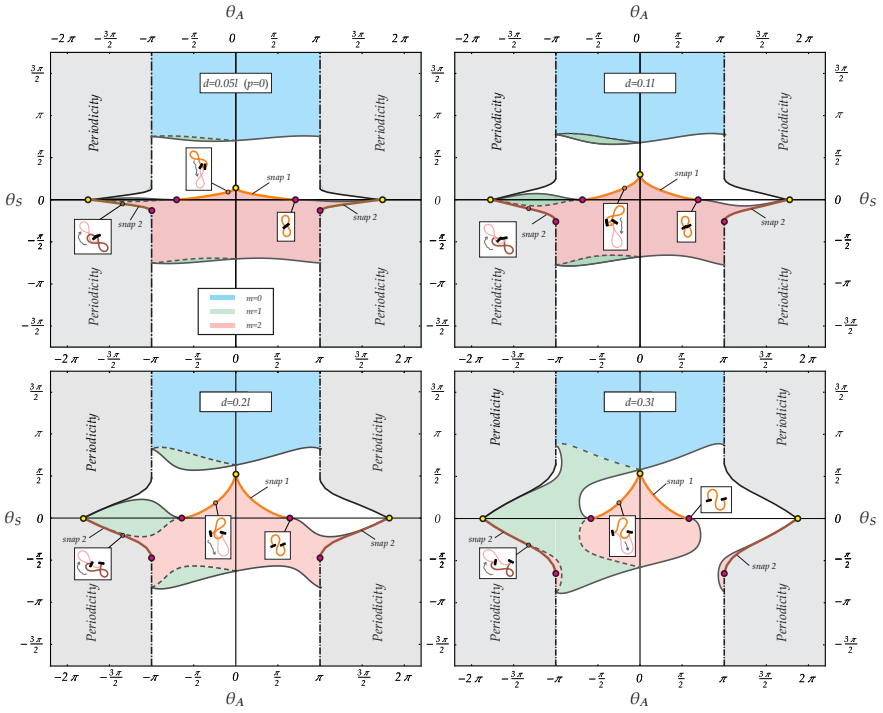

Figure 5.4: Domains of unique stable solutions within the plane $\theta_A - \theta_S$ for evolutions starting from the boundary conditions $\theta_A = \theta_S = 0$ and related to $p = 0$ (the domains related to $p = 1$ can be obtained through the respective mirroring properties highlighted in the text and visible in Fig. 5.3). The domains are reported for different values of fixed distance between the two ends, $d = \{0.05, 0.1, 0.2, 0.3\}\, l$. See the main text for the definition of the domain and line colors.

structure is only a function of the angle θ_S. In this case, the curve of snap-back type 1 becomes the segment lines given by $\theta_S = 0$ and $|\theta_A| \lesssim 0.726\pi$ while the curve of snap-back type 2 becomes the segment lines given by $\theta_S = 0$ and $|\theta_A| \in [1, 1.726]\pi$. It is also worth to mention that in the very special case of $\theta_S = 0$, an infinite set of stable and equivalent (namely, corresponding to the same elastic energy) solutions exists for the rod with fixed end rotations, provided by a '8-shaped' configuration [74, 102].

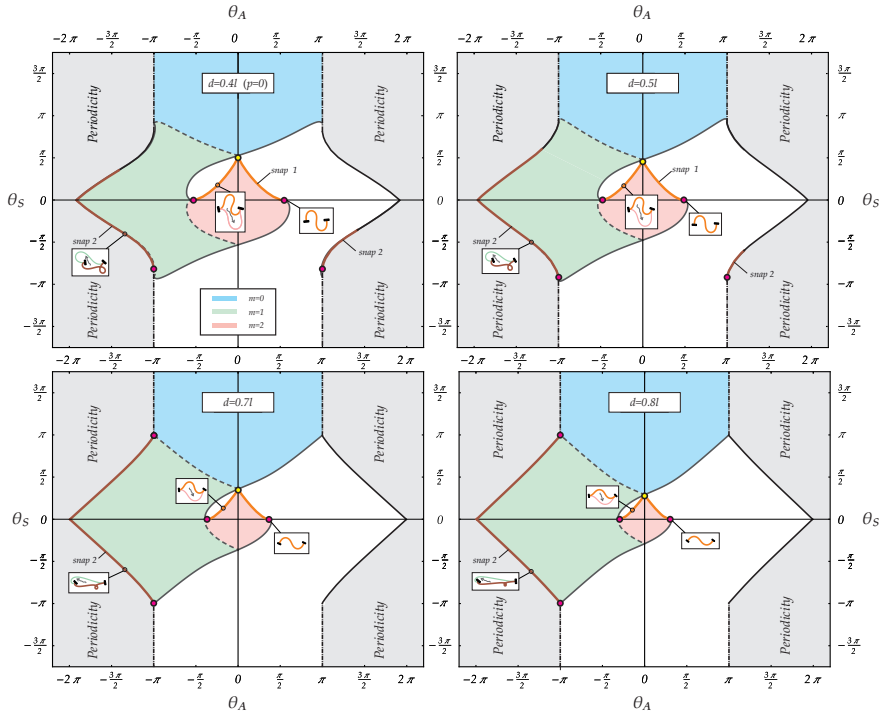

Figure 5.5: As for Fig. 5.4, but for higher values of fixed distance between the two ends, $d = \{0.4, 0.5, 0.7, 0.8\}\, l$. See the caption of Fig. 5.3 and the main text for the definition of the domain colors and the other lines. Being $d > 0.369l$, the yellow points (associated with bifurcations) are absent at the cusps of the snap-back curves type 2 (see Sect. 5.2.3).

5.2.2 Equilibrium paths for a variable distance d

The families of snap curves reported for fixed values of d in Figs. 5.3, 5.4 and 5.5 suggest the existence of snap surfaces within the space $d/l - \theta_A - \theta_S$. These snap surfaces can be disclosed by interpolating the snap curves within specific planes. The snap curves evaluated for twenty planes, taken for computational convenience at constant θ_A and θ_S for snap types 1 and 2, respectively, have been exploited to generate the snap-back surfaces by means of the function `Interpolation` in Mathematica®. Due to mirroring properties, the snap surfaces are entirely described through their representations within one octant

of the space $d/l - \theta_A - \theta_S$, displayed in Fig. 5.6 for snap-back type 1 (left) and type 2 (right) surfaces. Such snap surfaces represent a fundamental tool in the investigation about snap mechanisms and the definition of the correspondent critical boundary conditions during a quasi-static evolution of rods with controlled ends. Before exploiting the concept of universal snap surfaces in some applicative examples presented in Sect. 5.3, it is worth to discuss the possibility of bifurcations during a loading process, the amount of elastic energy release, and the conditions of self-intersecting elastica.

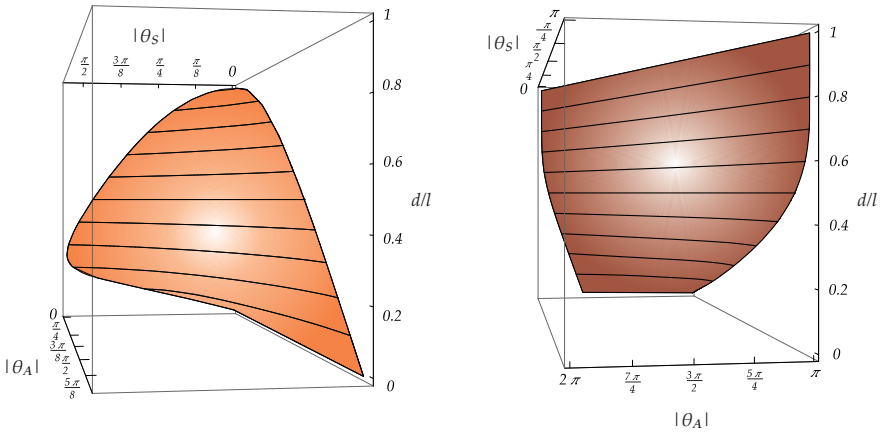

Figure 5.6: Surfaces defining the critical boundary conditions in the $\{|\theta_A|, |\theta_S|, d/l\}$ space for which snap-back type 1 (left) and type 2 (right) occurs. The surfaces are built from the related snap-back curves, respectively orange and brown, obtained for different values of d and reported in Figs. 5.3, 5.4, and 5.5.

5.2.3 Bifurcations at snap

The boundary conditions corresponding to (almost all) the intersections of the orange and brown snap-back curves with the lines $\theta_A = \{-\pi, 0, \pi\}$ and with the line $\theta_S = 0$ (corresponding to the cusps and end points of the snap curves) are marked with colored spots in Figs. 5.3, 5.4, and 5.5. For the boundary conditions corresponding to these points, the semi-positive definiteness of the second variation $\delta^2\mathcal{V}$ is complemented by the annihilation of the third variation $\delta^3\mathcal{V}$ for the related eigenfunction (while $\delta^3\mathcal{V}$ is different from zero for the other points along the snap curve) and a positive value is found for the corresponding

fourth variation $\delta^4\mathcal{V}$. These special points (some of them also observed in [79]) are marked as red and yellow spots, respectively corresponding to pitchfork (with no snapping) and unstable-symmetric bifurcation points (with snapping), and defined as follows.

Red spots. These points are located at the intersections of the orange thick curve with the condition $\theta_S = 0$ and of the brown thick curve with the condition $\theta_A = \pm\pi$. Snap never occurs when the snap curve is crossed through these points; however when the snap curve is crossed from outside to inside, a bifurcation may be encountered. More specifically, a pitchfork bifurcation is found when crossing the orange (brown) curve from outside to inside at the red point with a null increment in the angle θ_S (θ_A), namely a purely antisymmetric (symmetric) variation in the boundary conditions at the critical point. These bifurcative behaviours are displayed in Fig. 5.7 and Fig. 5.8, where specific loading processes are considered for a fixed distance $d = 0.4l$ and crossing the *red spots* located at the edges of the snap-back type 1 and type 2 curves.

The antisymmetric case, $\theta_S = 0$, at increasing θ_A is considered in Fig. 5.7, where in the first line the loading path is reported on the left and the moment M_0 at the left clamp as a function of the angle parameter θ_A on the right. The evolution of the deformed shape is displayed in the second, third, and fourth lines and is reported for the six specific stages of the boundary conditions, highlighted both in the solution maps and moment-angle response through the alphabetic letters a, b, c, d, e, f, g, h, and i. During the evolution, the bifurcation occurs when the stage c is attained, namely, when the snap curve is crossed from outside to inside, and corresponds to the condition of null moment at both clamps. Just after the stage c is passed, the structure may equally evolve through two different loading paths, namely, the structure may equally reach configuration $d1$ or $d2$. Once that one of these two branches is undertaken, the evolution continues on that specific branch. However, at increasing the rotation parameter, both branches finally join together when the stage g is reached and, after this stage (from g to i), the structure follows the only possible evolution. It is also important to highlight that the configurations c and g are stable solutions having $m = 1$ internal inflection point and null curvature at both ends (similar configurations are also present for all the bifurcation conditions, red spots, on snap-back curve type 1 for every distance d, and for some bifurcation conditions, yellow spots, on snap-back curve type 2 as discussed below).

A similar behaviour is also displayed in Fig. 5.8 with reference to $\theta_A = -\pi$ and decreasing θ_S. Differently from Fig. 5.7, here the bifurcation occurs for a

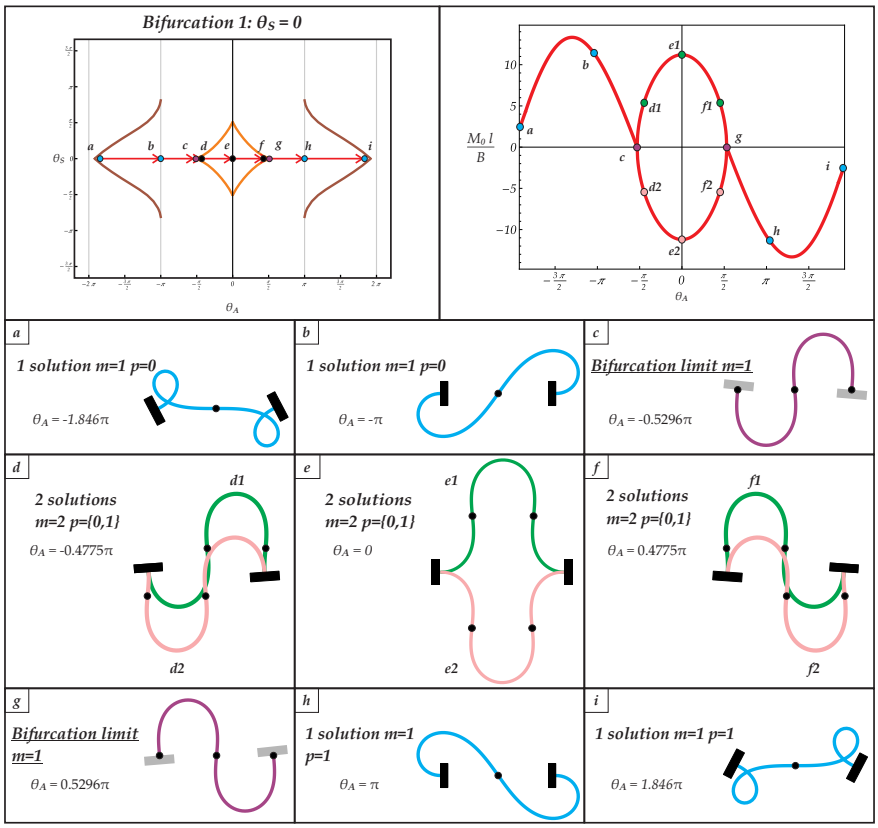

Figure 5.7: Evolution of the left clamp moment M_0 for increasing θ_A (upper line, right column), showing the existence of pitchfork bifurcation points at c and g along the antisymmetric loading path $\theta_S = 0$ at fixed distance $d = 0.4l$ (upper line, left column). The evolutions of the stable equilibrium configurations along the considered path are shown in the second, third and fourth line.

symmetric configuration and is associated with a non-null moment value at both clamps. The pitchfork bifurcation at the point c reveals a symmetry-breaking behaviour. In fact, the initial symmetric configuration becomes unstable after the bifurcation point is reached, and the system may only follow two other stable paths described by the mirrored configurations. A similar behaviour has also been detected in the case of a ring pinched by two radial loads [75], while the

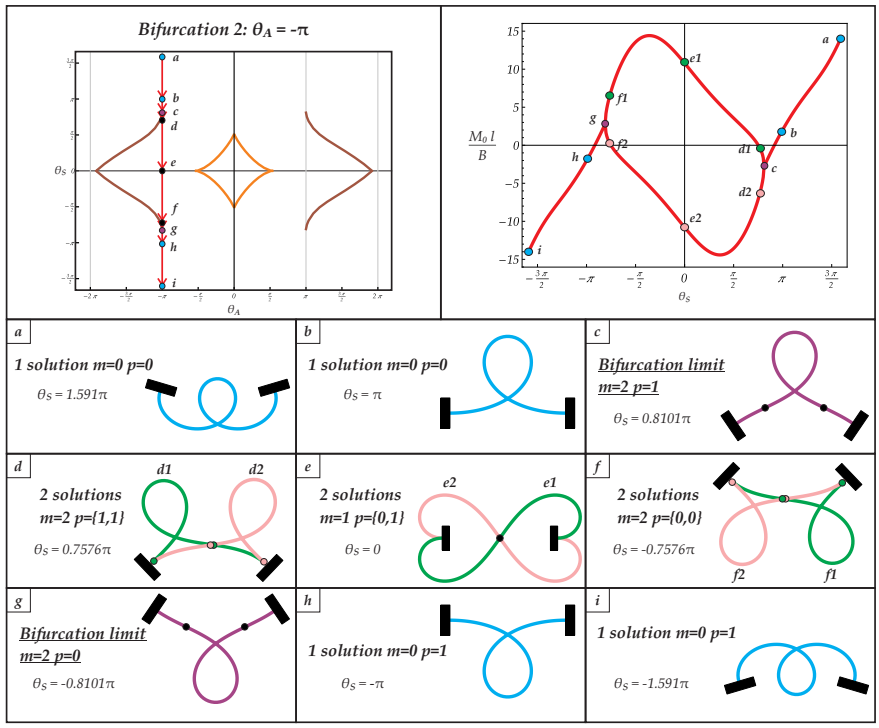

Figure 5.8: As for Fig. 5.7, but for varying θ_S with $\theta_A = -\pi$ and $d = 0.4l$. As the configuration c is reached, a pitchfork bifurcation occurs at the limit configuration (purple, $m = 2$) followed by symmetry-breaking in both branches, as shown by the two stable configurations (green and pink) at stages d, e, and f.

existence of a central unstable and symmetric solution has also been reported by [19] and [75], where the symmetric configuration for the double-clamped rod with null rotations at its ends is proven to snap towards the S-shaped configurations $e1$ or $e2$.

Yellow spots. These points are located at the intersections of the orange thick curve with the condition $\theta_A = 0$ and, only for $d \leq 0.369\,l$, of the brown

thick curve with the condition $\theta_S = 0$.[4] Snap occurs when the snap curve is crossed through these points from inside to outside and a bifurcation may be even encountered. More specifically, an unstable-symmetric bifurcation is found at the snap when crossing the orange (brown) curve from inside to outside at the yellow point with a null increment in the angle θ_A (θ_S), namely a purely symmetric (antisymmetric) variation in the boundary conditions at the critical point. The moment rotation response at increasing value of θ_S crossing the snap type 1 curve is displayed in Fig. 5.9 for a fixed distance $d = 0.4l$ and at very small fixed values of $\theta_A = \{0, 10^{-4}, 10^{-3}, 10^{-2}\}$. An example of unstable-symmetric behaviour can be envisaged in the purely symmetric case, $\theta_A = 0$, where the symmetric response (for which the moments at the two clamps have the same value, $M_0 = M_l$) intersects the two other unstable paths. Differently, if a small constant value is assumed for the antisymmetric part of rotation θ_A, the moment rotation response reaches a critical condition of snap-back, for which the tangent of the response curve is vertical.

5.2.4 Self-intersecting elastica

The snap surfaces reported in Fig. 5.6 have been obtained assuming that the rod is only loaded at its ends. It follows that the obtained critical conditions hold whenever the development of self-contact points along the rod is excluded.[5] This circumstance is trivially realized when the deformed configuration is not self-intersecting, but also when the self-intersection is made possible by the out-of plane geometry. The latter case is realized with rods shaped along the out-of-plane direction in such a way that during the planar intersection two external halves of the rod contain a central rod, namely a Y-shaped rod with specific out-of-plane variations [18, 75].

In order to detect when self-intersection does occur before snapping and, equivalently, when it does not, it is of practical interest to define the boundary conditions for which a contact point is first realized. This information can be consequently used to determine which portions of snap surfaces are attained

[4] It is remarked that the yellow points given by the intersection of the brown snap-back curve with the axis $\theta_S = 0$ exist only for $d \leq 0.369\,l$ and correspond to stable configurations with $m = 1$ inflection point and null curvature at both ends. This behaviour is not observed for $d > 0.369\,l$, where the third variation $\delta^3\mathcal{V}$ is not null and snap mechanism occurs without any bifurcation as soon as the snap curve is crossed at any other point. It follows that no yellow point appears in Fig. 5.5 for snap-back curves of type 2, being the considered distances $d > 0.369\,l$.

[5] Analysis of elasticae with self-contact points requires the resolution for two or more elasticae subject only to end loadings [90].

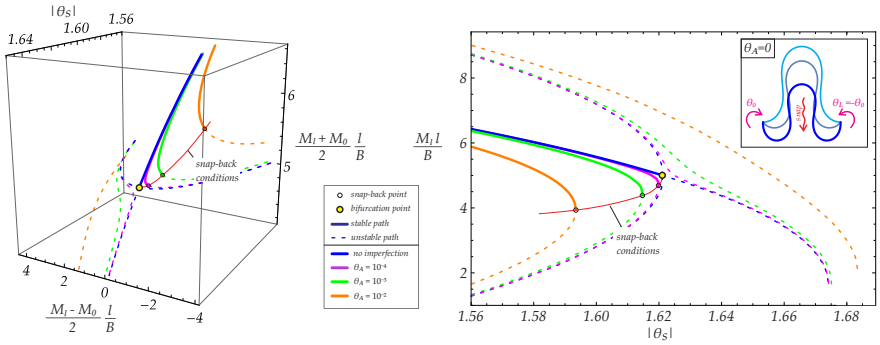

Figure 5.9: Moment-rotation responses at increasing modulus of θ_S (crossing the snap type 1 curve) for a fixed distance $d = 0.4l$ and $\theta_A = \{0, 10^{-4}, 10^{-3}, 10^{-2}\}$. The presence of an unstable-symmetric bifurcation point (yellow spot) is reported for symmetric loading condition, $\theta_A = 0$. (Left) Responses in terms of normalized symmetric and antisymmetric parts of the moment at the clamps, $(M_0+M_l)/2$ and $(M_0-M_l)/2$. (Right) Responses in terms of the normalized moment at the right clamp, M_l, and (inset) three deformed configurations before snapping and corresponding to $\theta_S = \{0, 0.9, 1.621\}$ and to $\theta_A = 0$.

only after an evolution involving the self-intersection. The boundary conditions of first self-contact can be found imposing that for one and only one pair of curvilinear coordinates $s^{(1)}$ and $s^{(2)}$ have the same position,

$$x\left(s^{(1)}\right) = x\left(s^{(2)}\right), \qquad y\left(s^{(1)}\right) = y\left(s^{(2)}\right), \qquad \left\{s^{(1)}, s^{(2)}\right\} \in [0, l]. \quad (5.6)$$

Evaluating the conditions of first self-contact, it is observed that:

- the conditions of snap-back type 1 (orange surface, Fig. 5.6 left) are always reached without developing a self-intersecting elastica if $d \gtrsim l/4$. For $d \lesssim l/4$, the snap-back most likely occurs after developing a self-intersecting configuration, however the exact limit distance for which the self-intersection is realized depends on the values of θ_A and θ_S, Fig. 5.10;
- the conditions of snap-back type 2 (brown surface, Fig. 5.6 right) are always reached after developing a self-intersecting elastica.

It is finally observed that self-contact may occur during snapping although the rod has no self-contact at the critical snap condition. Indeed, the dynamic transition from the pre and post snap configurations may evolve requiring self-intersecting shapes, which could be not geometrically feasible even for Y-shaped rods.

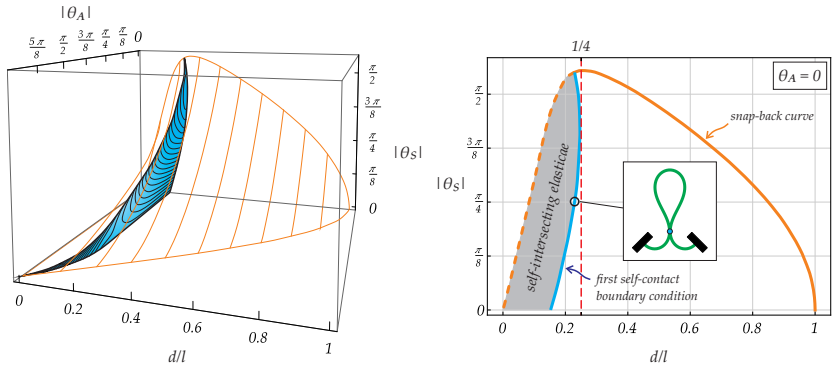

Figure 5.10: (Left) Surface portion for the boundary conditions of first self-contact within the space $d/l - |\theta_A| - |\theta_S|$, which are contained within the snap-back type 1 surface (represented only through its contour levels). (Right) The most restrictive condition of self-contact, corresponding to the case $\theta_A = 0$, is reported as a blue curve within the plane $d/l - |\theta_S|$ showing that self-intersecting elasticae may realize before attaining snap-back type 1 (orange curve) only when $d \lesssim l/4$. An example of self-intersecting elastica is also reported for $|\theta_S| = \pi/4$.

5.2.5 Energy release at snapping

The design of snapping devices can be optimized through the maximization of the energy release during mechanisms. In a first approximation, the energy release $\Delta\mathcal{E}$ can be estimated as the difference in the energy amounts $\mathcal{E}$, Eq.(2.5), between the stages before and after the snap-back and evaluated under the quasi-static assumption through Eq.(2.53).

Restricting attention only to snap-back type 1, the elastic energy difference $\Delta\mathcal{E}$ is reported in Fig. 5.11. Two nondimensionalizations are considered, division by B/l (Fig. 5.11, upper part) and division by the elastic energy before snapping $\mathcal{E}_0$ (Fig. 5.11, lower part). On the left part of Fig. 5.11, the elastic energy difference $\Delta\mathcal{E}$ is shown for different distances $d/l = \{\ 0.05, 0.1, 0.2, 0.3, 0.4, 0.5, 0.6, 0.7, 0.8, 0.9\ \}$ for varying the angle for which the snap-back type 1 occurs. The angle measure is expressed as the modulus of θ_A^{sb1}, the antisymmetric critical angle at the snap-back, normalized through division by $\theta_A^{sb1,bif}$, the antisymmetric angle at bifurcation for snap-back (the red spots on the θ_A axis in Fig. 5.3, 5.4 and 5.5 and for which no snap occurs, $\theta_A^{sb1,bif}(d) = \max_{\theta_S}\left\{\theta_A^{sb1}(\theta_S, d)\right\} = \theta_A^{sb1}(\theta_S = 0, d)$). For all the reported cases it can be concluded that the maximum elastic energy release for a fixed distance d is always attained under symmetric conditions, $\theta_A^{sb1} = 0$. For such symmetric

condition, the elastic energy difference $\Delta\mathcal{E}$ is shown on the right part of Fig. 5.11 as a function of the distance d between the rods' ends. The plot on the upper right part shows that the energy release $\Delta\mathcal{E}$ has a maximum value of about $76.67B/l$ at $d \approx 0.189l$ and has null values for both the limit-cases $d = l$ and $d = 0$. The plot on the lower right part shows that the relative energy release $\Delta\mathcal{E}/\mathcal{E}_0$ monotonically increases with the increase of the distance d and attains its maximum ratio of about 0.889 in the limit condition of $d = l$. With reference to this last case, it is also worth to highlight that the relative energy release is approximately constant for $d > l/4$, more specifically it varies from $\Delta\mathcal{E}/\mathcal{E}_0(d = l/4) = 0.884$ to $\Delta\mathcal{E}/\mathcal{E}_0(d \to l) = 0.889$.

5.3 Validation of the analytical predictions

The universal critical surface for snap type 1 is validated through comparison with experimental observations and results from numerical simulations. The available experimental data [15],[91], restricted to symmetric boundary conditions ($\theta_A = 0$), are complemented by testing a physical model developed to cover non-symmetric paths ($\theta_A \neq 0$). Finally, the influence of dynamical effects on the system response is assessed through numerical simulation of evolutive problems performed in ABAQUS. Reliability of the quasi-static predictions obtained through the universal surface is shown in the case of evolutions with moderate velocity.

5.3.1 Experimental results

A physical model (Fig. 5.12, left) is developed in order to experimentally investigate the snap conditions of the structural system under non-symmetric paths. Two forks in steel are exploited to control in practice the clamps, constraining the position and the rotation at both ends of an elastic rod. The rod is obtained from cutting a transparency film by Folex and has cross section 12 mm width times 0.1 mm height and length $l = 200$ mm. Restricting the kinematics of the two forks, specific non-symmetric paths are covered with the developed device. More specifically, the fork constraining the left end has a fixed position while the fork constraining the right end imposes null inclination, $\theta_l = 0$, and may move along the x-axis. From these boundary conditions it follows that the evolution expressed in terms of the three main kinematic quantities is given by

$$d = d(\tau), \qquad \theta_0 = \theta_0(\tau), \qquad \theta_l = 0, \tag{5.7}$$

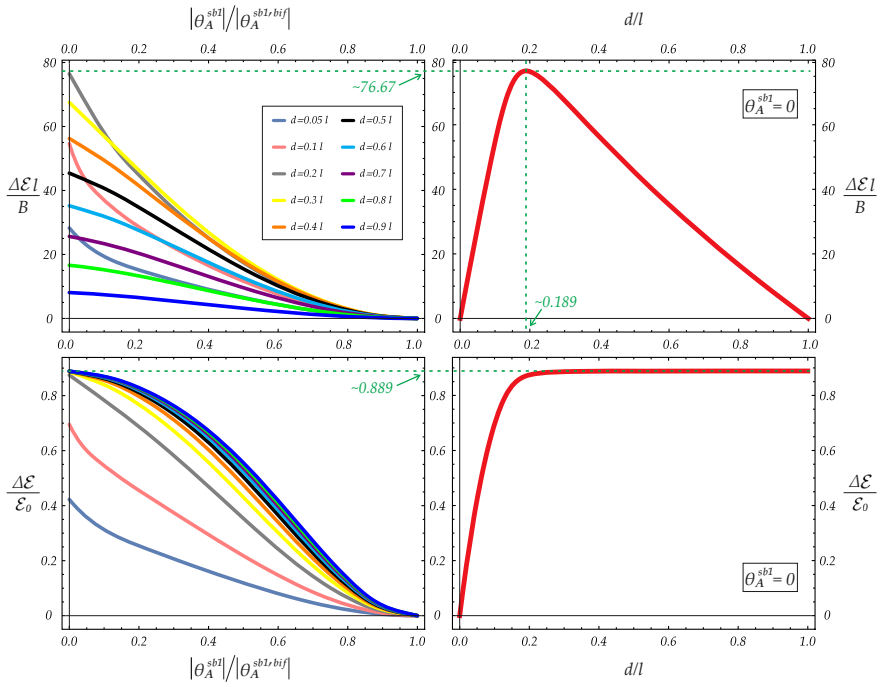

Figure 5.11: Energy release $\Delta\mathcal{E}$ estimated as the difference in the energy amounts $\mathcal{E}$, Eq.(2.5), between the stages before and after the snap-back of type 1, normalized by B/l (upper part) and by the elastic energy before snapping $\mathcal{E}_0$ (lower part). The energy release $\Delta\mathcal{E}$ is shown in the left column for different distances d/l for varying the modulus of the angle for which the snap-back type 1 occurs, θ_A^{sb1}, normalized through division by $\theta_A^{sb1,bif} = \max_{\theta_S}\{\theta_A^{sb1}(\theta_S, d)\}$. With reference to symmetric condition, $\theta_A = 0$, the energy release is shown in the right column as a function of the normalized distance d/l.

so that the non-symmetric paths characterized by $\theta_A(\tau) = -\theta_S(\tau) = \theta_0(\tau)/2$ can be investigated. Varying only one kinematical parameter, the two following types of experiments are performed:

Exp. A – keeping a fixed distance $d(\tau) = \overline{d}$ between the two forks, the rotation at the left end $\theta_0(\tau)$ changes in time;

Exp. B – keeping a fixed rotation at the left end $\theta_0(\tau) = \overline{\theta}_0$, the distance $d(\tau)$ between the two forks changes in time.

During each experiment, the rotation $\theta_0(\tau)$ or the distance $d(\tau)$ is slowly varied by hand. The variation in the kinematical parameter is stopped as soon as the rod snaps and the respective critical value is measured for the rotation $\theta_{0,cr}(\overline{d})$ in Exp. A or for the distance $d_{cr}(\overline{\theta_0})$ in Exp. B with the goniometer or the ruler mounted on the device, respectively. The critical conditions experimentally collected from Exp. A and Exp. B are respectively reported as dots and crosses within the plane $\theta_0 - d/l$ in Fig. 5.12 (right) together with the theoretical critical curve, namely the intersection of the universal snap surface type 1 (Fig. 5.6, left) with the plane $\theta_A = -\theta_S$. These experimental measures are also reported

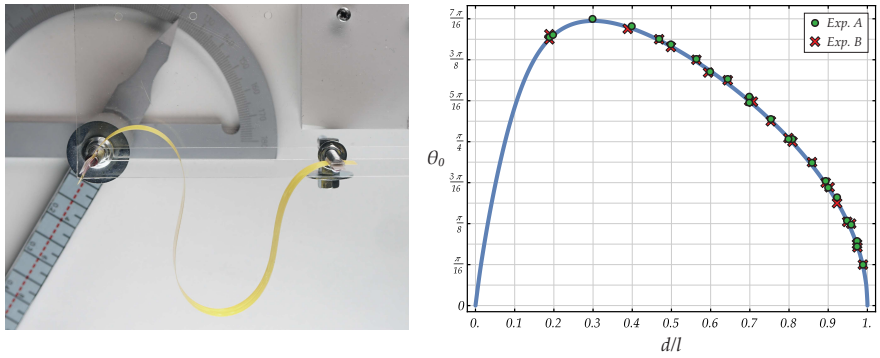

Figure 5.12: (Left) The developed physical model used to experimentally detect the critical snap configurations of the considered system, realized as a rod (obtained from cutting a transparency film) constrained at its ends by two forks. (Right) Critical snap conditions $\theta_0 - d/l$ from Exp. A (dots) and Exp. B (crosses) confirming the theoretical predictions (curve) from the present model.

together with those measured in the case of purely symmetric rotation $\theta_A = 0$ by Beharic et al. [15] (for $\overline{d}/l \backsimeq \{0.833, 0.862, 0.893, 0.926, 0.962, 0.980, 0.990\}$) and by Plaut and Virgin [91] (for $\overline{d}/l \backsimeq \{0.413, 0.637, 0.827, 0.955\}$) in Fig. 5.13, where the universal snap surface type 1 and its intersection with planes at constant values of d/l, $|\theta_A|$, and $|\theta_S|$ are represented, fully confirming the reliability of the predictions from the present model.

5.3.2 Numerical simulations and dynamic effects

In order to evaluate the possible influence of inertia on the snapping conditions of the system, the presented quasi-static predictions are finally com-

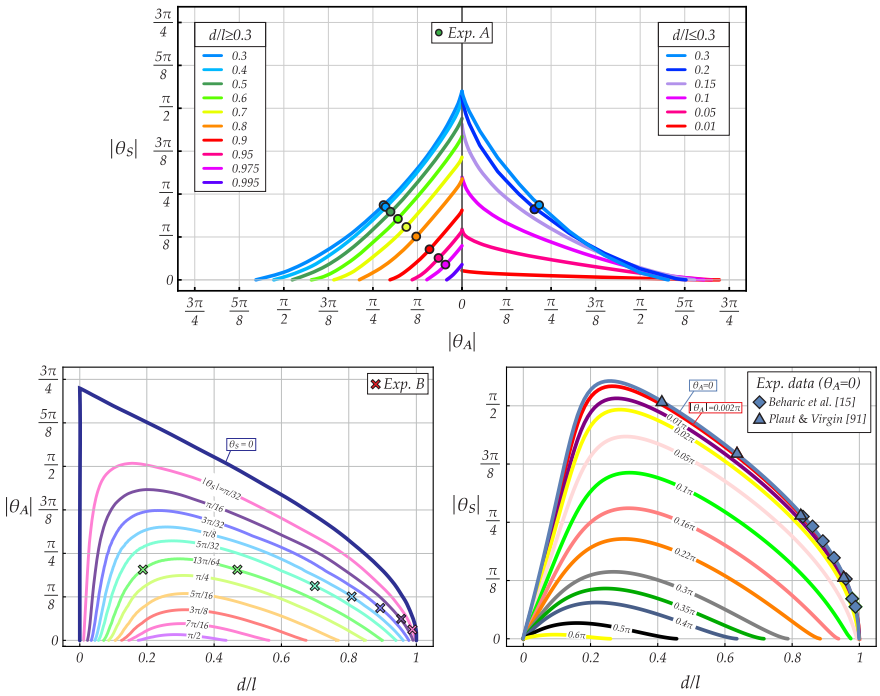

Figure 5.13: Intersections of the universal snap surface type 1 with planes at constant values of d/l (upper part), $|\theta_A|$ (lower part, left), and $|\theta_S|$ (lower part, right). Critical conditions assessed from Exp. A and Exp. B (performed on the developed physical model, Fig. 5.12, left) confirm the theoretical predictions reported for fixed d and for fixed $|\theta_A|$, respectively. Experimental results performed for the purely symmetric case ($\theta_A = 0$) by other authors [15], [91] are also reported (lower part, right), further confirming the excellent agreement between the experiments and the theoretical predictions from the present model.

pared with the response obtained from the numerical simulations performed in ABAQUS (v.6.13) for two different evolutive problems.

Sim. I – Clamps rotating cyclically and with opposite velocity. By considering a fixed distance $\overline{d}$, the kinematics for the rod's ends is described by

$$d = \overline{d}, \qquad \theta_0(\tau) = -\vartheta(\tau) + \overline{\theta}_A, \qquad \theta_l(\tau) = \vartheta(\tau) + \overline{\theta}_A, \qquad (5.8)$$

or equivalently, through Eq.(5.2), in terms of symmetric and antisym-

metric parts of the angles as

$$\theta_S(\tau) = \vartheta(\tau), \qquad \theta_A = \overline{\theta}_A, \tag{5.9}$$

from which it is evident that the function $\vartheta(\tau)$ represents the evolution of the symmetric part of the two angles in the time-like parameter τ while $\overline{\theta}_A$ represents a constant anti-symmetric angle during the evolution. Referring to the physical time $t = T\tau$, where $T = \sqrt{\rho l^4/B}$ is the characteristic time for the system having a linear mass density ρ, results from Sim. I are reported for a fixed antisymmetric rotation $\overline{\theta}_A = 0.16\pi$ and two fixed distances $\overline{d}/l = 0.4$ (Fig. 5.14, upper part, left) and $\overline{d}/l = 0.8$ (Fig. 5.14, lower part, left). In both cases, the cyclic evolution in the boundary conditions is realized through the succession of the increase and decrease in the symmetric rotation within the range $\theta_S \in [-\pi/2, \pi/2]$ keeping a constant modulus in the velocity,

$$\left|\dot{\vartheta}(\tau = t/T)\right| = \frac{\Omega}{T}, \tag{5.10}$$

where a superimposed dot corresponds to the derivative in the physical time t and Ω is the dimensionless (angular) velocity. The cyclic path prescribed in Sim. I theoretically encounters two snap conditions given by the same modulus of θ_S.

Sim. II – Monotonic variation in the clamps distance. Constant rotations $\overline{\theta}_0$ and $\overline{\theta}_l$ are assumed for the two ends, so that the kinematical evolution of the rod's ends is given by

$$d = d(\tau), \qquad \theta_0 = \overline{\theta}_0, \qquad \theta_l = \overline{\theta}_l, \tag{5.11}$$

where the function $d(\tau)$ defines a monotonic increase or decrease in the distance between the two clamps. Results from Sim. II are reported for fixed rotations $\overline{\theta}_0$ and $\overline{\theta}_l$ such that $\overline{\theta}_S = \pi/8$ (Fig. 5.14, upper part, right) and $\overline{\theta}_S = \pi/4$ (Fig. 5.14, lower part, right), and in both cases $\overline{\theta}_A = 0.16\pi$. In both cases, the monotonic variation in the distance d is considered from the value $d(\tau = 0)/l = 0.336$ with a constant velocity,

$$\left|\dot{d}(\tau = t/T)\right| = \frac{\Delta\, l}{T}, \tag{5.12}$$

where Δ is the dimensionless velocity. During both the monotonic shortening and the monotonic lengthening in the clamps distance prescribed in Sim. II, a snap mechanism is theoretically predicted for each evolution.

A linear viscous Rayleigh damping acting on the mechanical system, modeled as 100 planar beam elements with linear elastic constitutive behaviour, is considered in all the simulations through the mass-proportional and the stiffness-proportional damping coefficients respectively as $A_d = 8.25 \times 10^{-3}/T$ and $B_d = 6.06 \times 10^{-3}T$. The inherent extensibility of the rod modeled in ABAQUS has been considered through the axial stiffness $EA = 10^6 \times B/l^2$. All the presented analyses are performed using the nonlinear geometry option and started from the undeformed straight configuration with null rotations, $d = l$ and $\theta_0 = \theta_l = 0$. All the simulations share the first two static steps, while are different in the last dynamic step as follows:

Step 1 – Static: An end's distance $d(0)$ is imposed and a transversal load is applied in order to achieve the buckled configuration;

Step 2 – Static: the transversal load is removed and the clamp rotations are imposed in order to set the initial values of $\overline{\theta}_A$ and $\theta_S(0)$;

Step 3 – Dynamic implicit: inertial effects are analyzed during the evolution in the boundary conditions at velocity with constant modulus from $t = 0$ to $t = t_f$ as

Sim. I – initial and final configurations have $\theta_S(0) = \vartheta(0) = \vartheta(t_f) = 0$. Introducing the reference time $T_r = \pi T/(2\Omega)$, the duration of the evolution is given by $t_f = 4T_r$. The rotation velocity is assumed $\dot{\vartheta} = \Omega/T$ for $t \in [0, T_r]$ and $t \in [3T_r, 4T_r]$, while is assumed $\dot{\vartheta} = -\Omega/T$ as for $t \in [T_r, 3T_r]$, so that the velocity changes sign whenever the modulus of rotation reaches $|\theta_S| = \pi/2$;

Sim. II – the initial and final configurations have the ends distance given by $d(0)$ and $d(t_f)$. The transition between these two conditions occurs with constant velocity and has a duration $t_f = T_r$, where $T_r = 0.637T/\Delta$. The constant velocity is taken positive or negative in order to investigate the snap mechanism during lengthening or shortening.

The results of the simulations of the two evolutive problems are reported in Fig. 5.14 and compared with the respective quasi-static behaviour predictions using the inextensible elastica (and highlighting the snap angles and snap distances, defined by the snap curve $\theta_A = 0.16\pi$ in Fig.5.13 right, lower part). In particular, results for the Sim. I are reported in Fig. 5.14 (left) in terms of the moment (at the right end) at cyclically varying (symmetric) rotation θ_S, while those for the second evolutive problem are reported in Fig. 5.14 (right) in terms of the horizontal reaction (at the right end) for monotonic increase and decrease in the clamps distance. The respective numerical results are reported for three values of dimensionless velocities, $\Omega = \{0.01,\ 0.1,\ 1\}$ and $\Delta = \{0.001,\ 0.01,\ 0.1\}$, showing that the quasi-static model accurately describes the mechanical behaviour of the structural system until approaching the snap-back conditions, identified as the intersection of the loading path with presented snap-back surface type 1. Due to the presence of dissipative effects, the post-snap quasi-static path is reached after a transient time from the snap for which the dynamical effects are decayed. More specifically, non-negligible dynamic effects lead to a delay in the occurrence of snap with respect to the quasi-static prediction for high velocities. Oppositely, the dynamic response becomes almost completely superimposed (except for a small transient) to the quasi-static curve in the case of a velocity $\Omega = 0.01$ and $\Delta = 0.001$, values defining the velocity orders below which the present model, although obtained within the quasi-static framework, fully represents a reliable model.

5.4 Conclusions

Within a quasi-static framework, the number of stable equilibrium configurations has been disclosed for an elastic rod for varying the parameters controlling the kinematics of its ends. This analysis has led to the definition of universal snap surfaces, collecting the critical values of ends distance and rotations for which the rod shows a snap mechanism. Available experimental data and experimental results from testing a developed physical model fully validate the presented theoretical universal snap surface. Finally, finite element simulations show the influence of inertia on the snapping mechanisms and, in the case when the controlled ends move moderately, confirm the theoretical predictions based on the present quasi-static model. These results are complemented by the dimensionless analysis of elastic energy release at snapping, towards the optimal design of impulsive motion. In addition to the relevant contribution to the stability of structures, the present results may find application in a wide range of

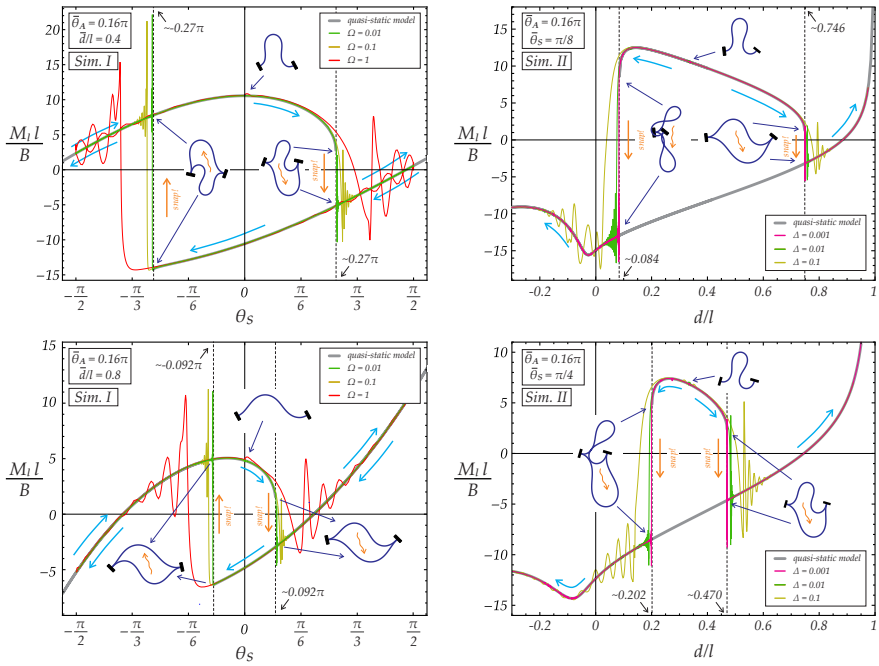

Figure 5.14: Theoretical predictions from the quasi-static model versus results from numerical simulations performed through finite element code (ABAQUS) for different values of the dimensionless velocities Ω and Δ. (Left column) $M_l - \theta_S$ response from Sim. I for a cyclically varying symmetric rotation θ_S at fixed antisymmetric rotation $\overline{\theta}_A = 0.16\pi$ and fixed clamps distance $\overline{d}/l = 0.4$ (upper part) and $\overline{d}/l = 0.8$ (lower part). (Right column) $M_l - d/l$ response from Sim. II for a monotonic increase and decrease in the distance d from $d(\tau = 0)/l = 0.336$, with fixed antisymmetric rotation $\overline{\theta}_A = 0.16\pi$ and fixed symmetric rotations $\overline{\theta}_S = \pi/8$ (upper part) and $\overline{\theta}_S = \pi/4$ (lower part).

technological fields, ranging from energy harvesting to jumping robots.

6

Elastica catastrophe machine: theory, design and experiments

6.1 Introduction

Catastrophe theory is a well-established mathematical framework initiated by R. Thom [108] for analyzing complex systems exhibiting instability phenomena. From its birth, concepts of this theory have been exploited over the years in several fields to provide the interpretation of sudden large changes in the configuration as the result of a small variation in the boundary conditions. Owing to its multidisciplinary application, catastrophe theory has found relevance in the mechanics of fluids, solids, and structures [38, 53, 73, 86, 94, 110, 120], but also in optics, physical chemistry, economics, biology and sociology [6, 49, 93, 109].

About fifty years ago, E.C. Zeeman invented and realized a simple but intriguing mechanical device [118] to illustrate for the first time concepts of catastrophe theory. The pioneering (planar) two-spring system, also known as 'Zeeman's catastrophe machine', can be easily home-built by fixing two elastic rubber bands and a cardboard disk on a desktop through three drawing pins (Fig. 6.1, left). More specifically, the two elastic bands are tied together through a knot pinned on the cardboard disk. The other end of the first elastic band is pinned on the table while that of the second elastic band is held by hand,

controlling its position within the plane. Lastly, in turn, the disk is pinned to the desktop. The resulting system has *two control parameters* (the hand position coordinates X_c and Y_c) and *one state variable* (the rotation angle ϑ of the cardboard disk). The number of equilibrium configurations for the system varies by changing the two control parameters (hand coordinates). In particular, the physical plane is split into two complementary regions separated by a symmetric concave diamond-shaped curve (with four cusps): the monostable region outside the closed curve and the bistable region inside. These two regions are respectively associated to hand position providing either a unique or two different stable equilibrium configurations (expressed by the state variable ϑ). The separating closed curve is called the *catastrophe locus* because when crossed by the hand position from inside to outside[1] provides the snapping of the system, as visual representation of the catastrophic behaviour.

Several modified versions of the Zeeman's catastrophe machine have been proposed with the purpose to display various concepts of catastrophe theory. Different two-spring [55] and three-spring [117] systems have been shown to possibly display more (than one) separated closed curves representing the *catastrophe locus* by choosing specific design parameters. A different behaviour, the butterfly catastrophe, has been displayed when the elastic band pinned to the desktop is replaced by two identical elastic bands, with their ends symmetrically pinned to the desktop [114]. The analysis of catastrophe locus has been also extended to discrete systems with elastic hinges [30, 31]. Moreover, Zeeman's machine has also been used to show chaotic motion [84] and its principle has been exploited to motivate the electro-mechanical instabilities of a membrane under polar symmetric conditions [78]. However, the elastic response in all of these systems has been considered to depend only on a finite number of degrees of freedom.

In this chapter, the design of a catastrophe machine is extended for the first time to an elastic continuous element, namely the planar elastica, within the finite rotation regime.[2] The increase of the number of degrees of freedom

[1] Snapping occurs only for the configuration inside the bistable region which loses stability when crossing the catastrophe locus. For the classical machine this is strictly related to the sign of the rotation angle ϑ and, similarly, for the presented elastica machine to that of the curvature at the rod's ends.

[2] The framework of catastrophe theory is found in the literature to be only exploited for continuous systems in investigating their equilibrium configurations as small perturbations of the undeformed one, as in the buckling problem for a pin ended rod under a lateral load [120, 121] or for a stiffened plate [58]. Differently, the catastrophe framework is here exploited for the whole set of equilibrium configurations, without any restriction on the amplitude of the related rotation field, being the analytical solutions for the Euler's elastica equation.

(from finite to infinite) together with the increase in the number of kinematic boundary conditions (from two to three) requires a more complex formulation in comparison with that considered for treating the classical discrete systems.

More specifically, by considering as fixed the position of one end of the elastica, the three kinematic boundary conditions X_l, Y_l (the two coordinates) and Θ_l (the rotation angle) at the other end are imposed through two control parameters. This relationship introduces a multiplicity issue for the configuration associated with the same coordinates X_l, Y_l of the final end (because of the sensitivity of the angular periodicity for the rotation angle) to be overcome for a proper representation of the catastrophe locus in the physical plane.

Furthermore, the analysis of catastrophe loci for elastica based machines requires to consider a further space, the primary kinematical space, in addition to the two spaces usually considered in the analysis of classical machines, the control parameter and the physical planes (no longer coincident here). It is shown that the catastrophe locus is provided by the projection in the physical plane of the intersection of the elastica machine set (defined by design parameters chosen for a specific machine) and the snap-back surfaces (universal for elasticae with controlled ends, see Chapter 5) within the primary kinematical space.

Among the infinite set of *elastica catastrophe machines* (ECMs), two families are proposed and thoroughly investigated through the developed theoretical formulation, fully confirmed by experiments performed on a physical model (Fig. 6.1, right).

An example of snapping motion displayed by the realized physical model of the *elastica catastrophe machine* (Fig. 6.1, right) is illustrated in Fig. 6.2. Two sequences of deformed configurations are shown for two different evolutions of the rod's final end position (controlled by hand). Both evolutions start from the bistable (green) domain (first column) and end to the monostable (white) domain (third column). Snapping occurs at crossing the catastrophe locus from inside to outside (second column highlighted in purple), as the elastic rod dynamically reaches the reverted stable configuration.

A parametric analysis performed by varying design parameters shows that the introduced families define catastrophe loci in a large variety of shapes, very different from those realized with classical catastrophe machines. In contrast to the classical machines, it is shown that such sets may display unexpected geometrical properties. On one hand, the number of bifurcation points along the catastrophe locus can be different than four. On the other hand, the convexity measure [125] of catastrophe locus is found to change significantly, while that

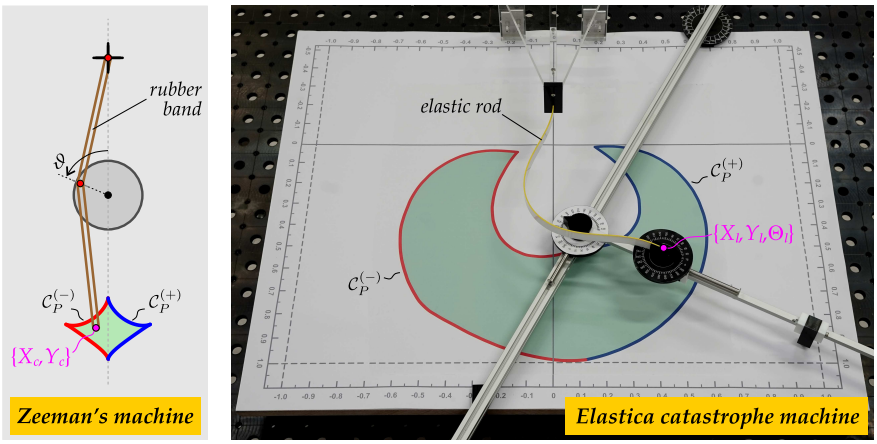

Figure 6.1: A sketch of the classical (discrete) catastrophe machine (left, cf. Fig. 5.1 in [93]) and a photo of the prototype realized for the proposed *elastica catastrophe machine* (right). The respective catastrophe locus $\mathcal{C}_P$ is reported for both machines as the union of $\mathcal{C}_P^{(+)}$ (blue line) and $\mathcal{C}_P^{(-)}$ (red line). Two stable equilibrium configurations exist for the elastic systems when the hand position, controlling the rubber's end coordinates X_c, Y_c (left) or the elastica's end coordinates X_l, Y_l, is within the bistable (green background) region enclosed by catastrophe locus. Differently, the stable equilibrium configuration is unique when the hand position is located within the monostable region (non-green background) defined as outside of the closed curve defining the catastrophe locus. Crossing the catastrophe locus from inside may provide snapping of the system.

of classical machines (Fig. 6.1, left) is usually around 0.65.[3] In particular, the convexity measure is found to possibly approach 1 with obtuse corners at the bifurcation points. This property facilitates reaching high-energy release snapping conditions, while these are difficult to attain in classical machines because associated with acute corner points.

The combination of the variable number of bifurcation points and the approximately unit value for the convex measure paves the way to realize very efficient snapping devices. Therefore, in addition to the interesting mechanical and mathematical features with reference to catastrophe theory in combination with snapping mechanisms [4, 19, 28, 36, 37, 46, 104, 103, 105], the proposed

[3]Convex catastrophe loci can be found for force controlled discrete systems [117]. Nevertheless, convex catastrophe loci are not observed for classical catastrophe machines under displacement control.

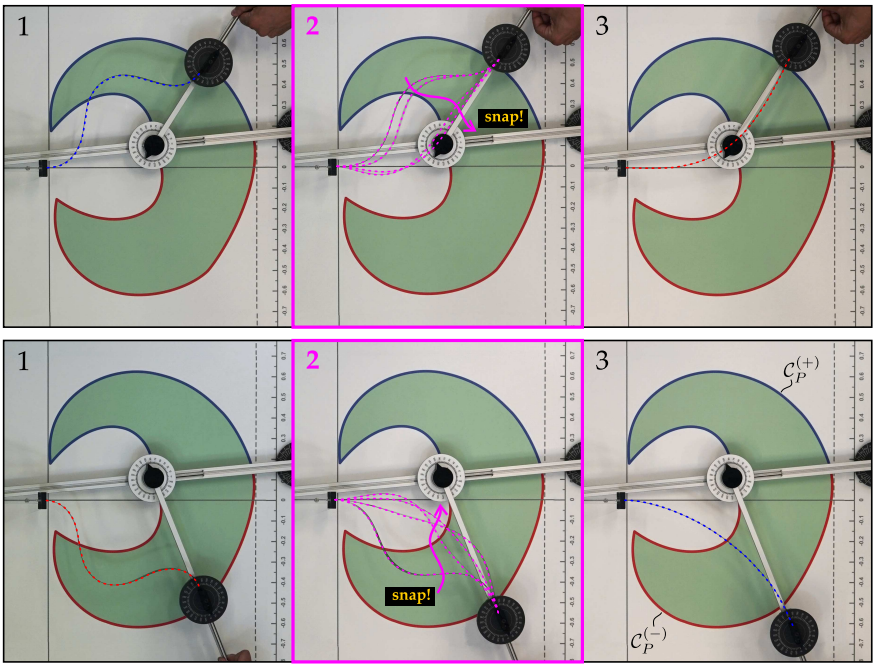

Figure 6.2: Evolution of the deformed configuration for two different sequences in the rod's end position controlled by hand. Snapping occurs at crossing the catastrophe locus through the blue line $\mathcal{C}_P^{(+)}$ (upper part)/red line $\mathcal{C}_P^{(-)}$ (lower part) for the elastica having positive/negative curvature at its ends. Four snapshots taken during snapping are superimposed in the second column (deformed configurations highlighted with purple dashed lines). Experiments are performed using ECM-I (with $\kappa_R = 0.5$, $\lambda_R = 0.1$, $\upsilon = 0$) with a carbon fiber rod by increasing the first control parameter p_1 (radial distance from the rotation point) at fixed value of p_2 (the angle Θ_l at the moving end). Deformed configurations with positive/negative curvature at its ends are highlighted with blue/red dashed line.

model may find application in the design of cycle mechanisms for actuation and dissipation devices towards energy harvesting, locomotion and wave mitigation [16, 40, 47, 54, 65, 95, 116]. The presented results have been published in an international journal, see Cazzolli et al. [34].

6.2 Equilibrium configurations for the elastica and the universal snap surface

The equilibrium configurations and the concept of universal snap surface are recalled for the inextensible Euler's elastica of length l and lying within the $X-Y$ plane, which models the elastic element of the *elastica catastrophe machine*. In particular, the 'global' reference system $X-Y$ is introduced, which is simply related to the 'local' components $x(\mathsf{s})$ and $y(\mathsf{s})$ of the deformed shape introduced in Chapter 2 (see Eqs.(2.2)) through a rotation matrix

$$\begin{bmatrix} X(\mathsf{s})-X(0) \\ Y(\mathsf{s})-Y(0) \end{bmatrix} = \begin{bmatrix} \cos\varpi & -\sin\varpi \\ \sin\varpi & \cos\varpi \end{bmatrix} \begin{bmatrix} x(\mathsf{s}) \\ y(\mathsf{s}) \end{bmatrix}, \tag{6.1}$$

where $\mathsf{s} \in [0,l]$ denotes arc length along the rod and ϖ is the anti-clockwise angle between the X-axis and the line connecting the two clamps of the rod. Moreover, the rotation field of the elastic rod can be represented through the angle $\Theta(\mathsf{s})$ taken with respect to the X-axis, which is connected to the rotation field $\theta(\mathsf{s})$ introduced in Chapter 2 by the simple following rule

$$\Theta(\mathsf{s}) = \theta(\mathsf{s}) + \varpi. \tag{6.2}$$

By considering the flexible element (the rod) kinematically constrained at its two ends, the following six boundary conditions are imposed

$$\begin{aligned} &X(\mathsf{s}=0)=X_0, \qquad Y(\mathsf{s}=0)=Y_0, \qquad \Theta(\mathsf{s}=0)=\Theta_0, \\ &X(\mathsf{s}=l)=X_l, \qquad Y(\mathsf{s}=l)=Y_l, \qquad \Theta(\mathsf{s}=l)=\Theta_l, \end{aligned} \tag{6.3}$$

so that the inclination of the 'global' reference system $X-Y$ with respect to the 'local' one $x-y$ can be expressed through the following equation

$$\varpi = \arctan\left[\frac{Y_l-Y_0}{X_l-X_0}\right]. \tag{6.4}$$

For the sake of clarity, the 'global' $X-Y$ and 'local' $x-y$ reference systems, the related rotation fields Θ and θ and the boundary conditions (2.3) and (6.3) are represented in Fig.6.3.

The inextensibility of the elastic rod constrains the distance d (see Eq.(2.3)) between its two ends to satisfy the following kinematic compatibility condition

$$d(X_0,Y_0,X_l,Y_l) = \sqrt{(X_l-X_0)^2+(Y_l-Y_0)^2} \leq l. \tag{6.5}$$

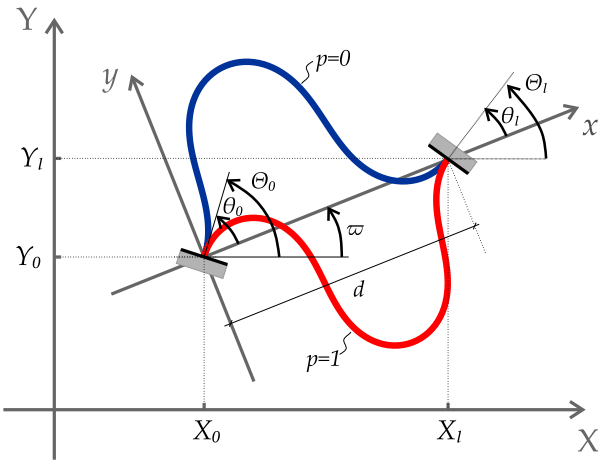

Figure 6.3: Deformed shapes of the inflectional elastica differing in the sign of the curvature at the initial end $\mathsf{s} = 0$ (negative $p = 1$ in red, positive $p = 0$ in blue) and represented within the 'global' $X - Y$ and 'local' $x - y$ reference systems, being the latter rotated by ϖ with respect to the X-axis. The boundary conditions (2.3) and (6.3) are also highlighted.

The inextensibility assumption also introduces the dependence of the coordinate fields $X(s)$ and $Y(s)$ on the rotation field $\Theta(s)$ through the following differential relations

$$X'(\mathsf{s}) = \cos\Theta(\mathsf{s}), \qquad Y'(\mathsf{s}) = \sin\Theta(\mathsf{s}), \tag{6.6}$$

where the symbol $'$ denotes the derivative with respect to the curvilinear coordinate s.

Given the six boundary conditions (6.3), the deformed configuration of the elastic rod at equilibrium can be alternatively described by

$$\begin{cases} X(\mathsf{s}) = X_0 + \dfrac{X_l - X_0}{d} x(\mathsf{s}) - \dfrac{Y_l - Y_0}{d} y(\mathsf{s}), \\ Y(\mathsf{s}) = Y_0 + \dfrac{X_l - X_0}{d} y(\mathsf{s}) + \dfrac{Y_l - Y_0}{d} x(\mathsf{s}), \\ \Theta(\mathsf{s}) = \arctan\left[\dfrac{Y_l - Y_0}{X_l - X_0}\right] + \theta(\mathsf{s}), \end{cases} \tag{6.7}$$

where the 'local' coordinates $x(\mathsf{s}) = x(s)l$, $y(\mathsf{s}) = y(s)l$ and $\theta(\mathsf{s}) = \theta(s\,l)$ (where

$s = \mathsf{s}/l \in [0,1]$) are specified through the exact solution for the Euler's elastica, namely through Eqs.(2.50) and (2.42) in the case when the number m of inflection points is greater than zero, through Eqs.(2.77) and (2.72) for $m = 0$, respectively.

The equilibrium configuration (in general non-unique) can be characterized once the two unknown parameters (ξ and β for $m = 0$, η and β for $m \neq 0$) are evaluated for a given set of kinematical boundary conditions, Eq.(6.3). The pair(s) of these parameters can be obtained by solving the following non-linear system,

$$\begin{cases} x(s) = \dfrac{d}{l}, \\ y(s) = 0, \end{cases} \tag{6.8}$$

which is particularized as in Eq.(2.56) in the case $m \neq 0$ and in Eq.(2.83) in the case $m = 0$.

Towards the stability analysis of a specific equilibrium configuration related to the six boundary conditions X_0, X_l, Y_0, Y_l, Θ_0, Θ_l, it is instrumental to refer to the following three primary kinematical quantities: the distance d, Eq.(6.5), and the angles θ_A and θ_S, as introduced in Eqs.(5.2), respectively defined as the antisymmetric and symmetric parts of the imposed end rotations. These latter angles can be expressed through the 'global' coordinates as

$$\theta_A = \frac{\Theta_l + \Theta_0}{2} - \arctan\left[\frac{Y_l - Y_0}{X_l - X_0}\right], \qquad \theta_S = \frac{\Theta_l - \Theta_0}{2}. \tag{6.9}$$

In particular, the triads $\{d, \theta_A, \theta_S\}$ can be related to a unique or two different stable configurations through a function $S_K(d,\, \theta_A,\, \theta_S)$ as in Chapter 5 (see Cazzolli and Dal Corso [33])

$$\begin{aligned} &S_K(d,\, \theta_A,\, \theta_S) > 0 \qquad \Leftrightarrow \qquad \text{monostable domain: one stable configuration,} \\ &S_K(d,\, \theta_A,\, \theta_S) < 0 \qquad \Leftrightarrow \qquad \text{bistable domain: two stable configurations.} \end{aligned} \tag{6.10}$$

Universal snap surface. The transition between the aforementioned bistable and monostable domains (6.10) occurs for the set of critical conditions of snap-back for one of the two stable configurations, differing by the sign of curvature at the two ends. Such a condition can be represented through the concept of

universal snap surface (restricted here to type 1 only, see Chapter 5 and Cazzolli and Dal Corso [33]), which can be expressed in the following implicit form

$$S_K(d,\,\theta_A,\,\theta_S)=0 \qquad \Leftrightarrow \qquad \text{one stable and one critical configuration at snap,} \tag{6.11}$$

The equation (6.11) defines a closed surface within the space of the primary kinematical quantities $\{d, \theta_A, \theta_S\}$, with two planes of symmetry defined by $\theta_A = 0$ and $\theta_S = 0$ (Fig. 6.4, left).[4] The intersection of the surface S_K with its two symmetry planes provides two closed curves representing the whole set of pitchfork bifurcation points. More specifically, the pitchfork bifurcation points are distinguished as *supercritical* or *subcritical*, the former corresponding to the intersection curve with $\theta_S = 0$ and the latter with $\theta_A = 0$. Therefore, the generic planar section of S_K at fixed values of d has shape and physical meaning definitely similar to those of the catastrophe locus of the classical Zeeman machine (see Fig. 6.1 left) having two canonical and two dual cusps, see [33] and [93]. A critical configuration with a certain sign of curvature at the two ends is characterized by symmetric angle θ_S with the same sign. Due to the symmetry properties described above, the implicit function $S_K(d,\,\theta_A,\,\theta_S)$ can be described through two single value functions $\theta_S^{sb\,(+)}$ and $\theta_S^{sb\,(-)}$ of the two primary kinematical quantities d and θ_A,

$$\theta_S^{sb\,(+)}=\theta_S^{sb\,(+)}(d,\theta_A), \qquad \theta_S^{sb\,(-)}=\theta_S^{sb\,(-)}(d,\theta_A), \tag{6.12}$$

where the sign enclosed by the superscript parentheses is related to the sign of curvature at the two ends before snapping, related to the sign of the rod's curvature at the coordinate $s = 0$ (through the sign $(-1)^p$ in Eq.$(2.39)_2$). This sign is also coincident with that of the symmetric angle of the snapping configuration. Furthermore, symmetry properties lead to the following conditions

$$\theta_S^{sb\,(+)}(d,\theta_A)=\theta_S^{sb\,(+)}(d,-\theta_A)=-\theta_S^{sb\,(-)}(d,\theta_A)=-\theta_S^{sb\,(-)}(d,-\theta_A). \tag{6.13}$$

[4] It is noted that a type 1 snapping configuration is always related to an elastica with two inflection points, $m = 2$, which snaps towards another elastica with two inflection points. Therefore, each configuration at snapping displays the same curvature the sign at both ends, changing sign from just before to just after the snap mechanism.

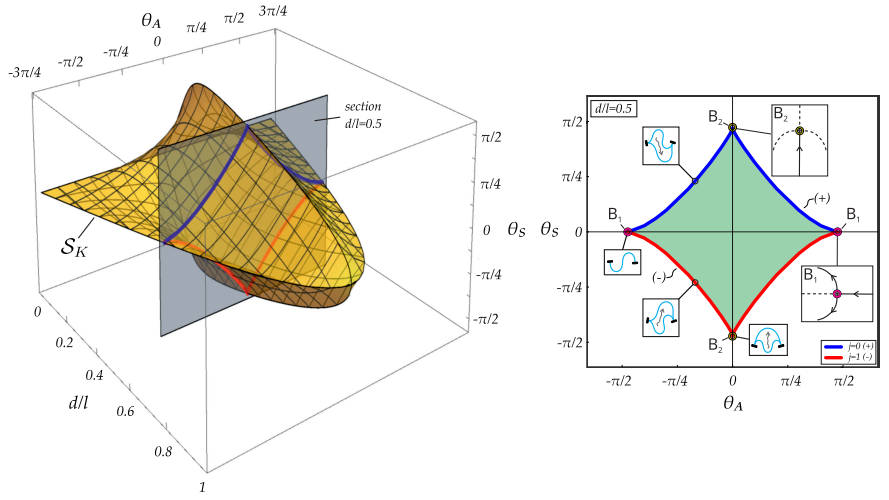

Figure 6.4: (Left) Universal snap surface S_k (type 1) within the space of the primary kinematical quantities $\{d, \theta_A, \theta_S\}$ and its section with the plane $d = 0.5l$. (Right) Snap surface section for $d = 0.5l$ as thick closed curve within the plane $\theta_A - \theta_S$ composed by blue $(+)$ and red $(-)$ parts. The blue (red) part refers to snapping configurations with positive $j = 0$ (negative $j = 1$) curvature at both ends. The bistable (monostable) domain is reported as the green (white) region inside (outside) the closed curve. The deformed shapes of the elastica before and after snapping are reported as insets for some critical condition along the closed curve are reported. The two cusps B_1 (B_2) are supercritical (subcritical) pitchfork bifurcations, and are associated with a non-snapping (a snapping) configuration.

6.3 Theoretical framework for *elastica catastrophe machines*

The aim of this section is to develop the theoretical framework for the realization of the *elastica catastrophe machine*. For the sake of simplicity, the initial coordinate of the elastic rod, $s = 0$, is considered fixed and taken as the origin of the reference system $X - Y$ and with tangent parallel to the X-axis, so that

$$X_0 = Y_0 = \Theta_0 = 0. \tag{6.14}$$

It follows that the three primary kinematical quantities, Eq.(6.9) can be expressed as functions (overtilde symbol) of the position at the final coordinate

$(s = l)$ only,

$$d = \widetilde{d}(X_l, Y_l), \qquad \theta_A = \widetilde{\theta}_A(X_l, Y_l, \Theta_l), \qquad \theta_S = \widetilde{\theta}_S(\Theta_l), \tag{6.15}$$

which simplify as[5]

$$\widetilde{d}(X_l, Y_l) = \sqrt{X_l^2 + Y_l^2}, \quad \widetilde{\theta}_A(X_l, Y_l, \Theta_l) = \frac{\Theta_l}{2} - \arctan\left[\frac{Y_l}{X_l}\right], \quad \widetilde{\theta}_S(\Theta_l) = \frac{\Theta_l}{2}, \tag{6.16}$$

Relations (6.16) can be inverted to provide the position at the final coordinate $(s = l)$ as a function (hat symbol) of the primary kinematical quantities

$$\widehat{X}_l(d, \theta_A, \theta_S) = d\cos(\theta_S - \theta_A), \quad \widehat{Y}_l(d, \theta_A, \theta_S) = d\sin(\theta_S - \theta_A), \quad \widehat{\Theta}_l(\theta_S) = 2\theta_S. \tag{6.17}$$

The definition of a (catastrophe) machine leads to the introduction of control and design parameters, respectively collected in the two vectors $\mathbf{p} = \{p_1, ..., p_M\}$ and $\mathbf{q} = \{q_1, ..., q_N\}$ (with $M, N \in \mathbb{N}$). In particular, $\mathbf{p}$ is the fundamental vector collecting the degrees of freeedom of the considered machine. Thus, the position of the rod at the final curvilinear coordinate $(s = l)$ can be also described as functions (overbar symbol) of such parameters as

$$X_l = \overline{X}_l(\mathbf{p}, \mathbf{q}), \qquad Y_l = \overline{Y}_l(\mathbf{p}, \mathbf{q}), \qquad \Theta_l = \overline{\Theta}_l(\mathbf{p}, \mathbf{q}), \tag{6.18}$$

and similarly, by considering Eqs.(6.16) and (6.18), the three primary kinematical quantities d, θ_A and θ_S as

$$d = \overline{d}(\mathbf{p}, \mathbf{q}), \qquad \theta_A = \overline{\theta}_A(\mathbf{p}, \mathbf{q}), \qquad \theta_S = \overline{\theta}_S(\mathbf{p}, \mathbf{q}). \tag{6.19}$$

Although both the control and design parameters affect the elastica configuration, a distinction is made being the former varied at fixed values of the latter.

In the following, towards the geometrical representation of the *catastrophe locus* (namely, the critical conditions providing snapping for the elastica) within the physical plane $X - Y$, the number of control parameters is taken as $M = 2$, so that $\mathbf{p} = \{p_1, p_2\}$.

[5]Details about overcoming periodicity issues inherent to the trigonometric function arctan are reported in Section A.1.1 of the Appendix A.

Finally, it is assumed that the relations (6.18) and (6.19) can be inverted, thus obtaining

$$p_j = \widetilde{p}_j(X_l, Y_l, \Theta_l, \mathbf{q}) \qquad j = 1, 2, \tag{6.20}$$

and

$$p_j = \widehat{p}_j(d, \theta_A, \theta_S, \mathbf{q}) \qquad j = 1, 2, \tag{6.21}$$

respectively. A generic configuration of the elastica can be therefore represented by the three equivalent parametrisations of the boundary conditions, namely i) by the two control parameters $\{p_1, p_2\}$, ii) by the three coordinates of the rod's final end $\{X_l, Y_l, \Theta_l\}$ or iii) by the three primary kinematical quantities $\{d, \theta_A, \theta_S\}$. This discrepancy in the number of the required parameters suggests that one of the coordinates of the triads $\{X_l, Y_l, \Theta_l\}$ or $\{d, \theta_A, \theta_S\}$ might be expressed as a function of the remaining two. Section A.1.1 of the Appendix A is devoted to the development of such statement.

6.3.1 Three spaces for representing the catastrophe locus

In light of the above, the complete understanding of the principles underlying the present catastrophe machine requires to consider the projection of the controlled end's configuration within the three different spaces,

C: the control parameter plane $p_1 - p_2$;

K: the primary kinematical quantities space $d - \theta_A - \theta_S$;

P: the physical space $X_l - Y_l - \Theta_l$, where the rotational coordinate Θ_l (possibly even more than one) is condensed to the physical plane $X_l - Y_l$.

The need of these three different representations and the (unavoidable) projection of the rotational coordinate Θ_l to the physical plane $X_l - Y_l$ are the new constituents of the *elastica catastrophe machine* with respect to the classical one [118, 119], where the control plane coincides with the physical one and the kinematical space is not needed. Furthermore, differently from the classical catastrophe machine, the values of the control parameters p_1 and p_2, kinematical quantities d, θ_A, and θ_S, and the end's coordinates X_l, Y_l, and Θ_l are here restricted by the inextensibility constraint, Eq.(6.5), so that their variation is limited to the 'inextensibility set' $\mathcal{I}$, which is defined in the three different spaces

as

$$\begin{aligned}
&\mathcal{I}_C := \{\mathbf{p} \in \mathbb{R}^2 \big| \, 0 \leq \overline{d}(\mathbf{p}, \mathbf{q}) \leq l\}, \\
&\mathcal{I}_K := \{\{d,\, \theta_A,\, \theta_S\} \in \mathbb{R}^3 \big| \, 0 \leq d \leq l\}, \\
&\mathcal{I}_P := \{\{X_l,\, Y_l\} \in \mathbb{R}^2 \big| \, 0 \leq \widetilde{d}(X_l,\, Y_l) \leq l\}.
\end{aligned} \tag{6.22}$$

In order to minimize the presence of self-intersecting configurations[6] for the elastica, the symmetric θ_S and antisymmetric θ_A angles are considered to be restricted by

$$\{|\theta_A|\,, |\theta_S|\} < \pi, \tag{6.23}$$

so that the variables within the three spaces are also limited to the 'machine set' $\mathcal{M}$,

$$\begin{aligned}
&\mathcal{M}_C := \left\{\mathbf{p} \in \mathbb{R}^2 \big| \; \left\{\left|\overline{\theta}_A(\mathbf{p}, \mathbf{q})\right|, \left|\overline{\theta}_S(\mathbf{p}, \mathbf{q})\right|\right\} < \pi\right\}, \\
&\mathcal{M}_K := \left\{\{d,\, \theta_A,\, \theta_S\} \in \mathbb{R}^3 \big| \, \{d = \overline{d}(\mathbf{p}, \mathbf{q}),\, \theta_A = \overline{\theta}_A(\mathbf{p}, \mathbf{q}),\, \theta_S = \overline{\theta}_S(\mathbf{p}, \mathbf{q})\}, \mathbf{p} \in \mathcal{M}_C\right\}, \\
&\mathcal{M}_P := \left\{\{X_l,\, Y_l\} \in \mathbb{R}^2 \big| \, \{X_l = \overline{X}_l(\mathbf{p}, \mathbf{q}),\, Y_l = \overline{Y}_l(\mathbf{p}, \mathbf{q})\}, \mathbf{p} \in \mathcal{M}_C\right\}.
\end{aligned} \tag{6.24}$$

The intersection of the inextensibility $\mathcal{I}$ and machine $\mathcal{M}$ sets provides the 'elastica machine set' $\mathcal{E}$, defining the configurations that can be attained by the designed *elastica catastrophe machine*,

$$\mathcal{E}_J := \mathcal{M}_J \cap \mathcal{I}_J, \qquad J = C, K, P. \tag{6.25}$$

The two single-valued functions $\theta_S^{sb\,(+)}(d, \theta_A)$ and $\theta_S^{sb\,(-)}(d, \theta_A)$, Eq.(6.12), introduced in the previous section as the collection of critical snap-back (type 1 [33]) conditions for positive and negative sign of ends' curvature configurations, define respectively the 'snap-back subsets' $\mathcal{S}_K^{(+)}$ and $\mathcal{S}_K^{(-)}$ within the $d - \theta_A - \theta_S$ space

$$\begin{aligned}
&\mathcal{S}_K^{(+)} := \left\{\{d,\, \theta_A,\, \theta_S\} \in \mathcal{I}_K \big| \, \theta_S = \theta_S^{sb\,(+)}(d, \theta_A)\right\}, \\
&\mathcal{S}_K^{(-)} := \left\{\{d,\, \theta_A,\, \theta_S\} \in \mathcal{I}_K \big| \, \theta_S = \theta_S^{sb\,(-)}(d, \theta_A)\right\}.
\end{aligned} \tag{6.26}$$

[6]The considered limitation for the values of the angles θ_A and θ_S also provides that the machine set does not display type 2 snapping mechanisms [33].

The union of the two 'snap-back subsets' $\mathcal{S}_K^{(+)}$ and $\mathcal{S}_K^{(-)}$ provides the 'snap-back set' $\mathcal{S}_K$

$$\mathcal{S}_K = \mathcal{S}_K^{(+)} \cup \mathcal{S}_K^{(-)}, \tag{6.27}$$

splitting the $d - \theta_A - \theta_S$ space into two regions, the 'bistable set' $\mathcal{B}_K$ collecting kinematical quantities for which two stable solutions exist

$$\mathcal{B}_K := \left\{ \{d,\, \theta_A,\, \theta_S\} \in \mathcal{I}_K \middle|\, S_K\left(d, \theta_A, \theta_S\right) < 0 \right\}, \tag{6.28}$$

and the 'monostable set' $\mathcal{U}_K$ collecting kinematical quantities for which only one stable solution exists

$$\mathcal{U}_K := \left\{ \{d,\, \theta_A,\, \theta_S\} \in \mathcal{I}_K \middle|\, S_K\left(d, \theta_A, \theta_S\right) > 0 \right\}. \tag{6.29}$$

The snap-back set $\mathcal{S}_K$ is independent from the design parameters and has only a representation within the primary kinematical space. Its intersection with the 'elastica machine set' $\mathcal{E}_K$ provides the critical kinematical quantities $d^{\mathcal{C}}$, $\theta_A^{\mathcal{C}}$, and $\theta_S^{\mathcal{C}}$ associated with the designed elastica machine and collected in the 'catastrophe set'[7] $\mathcal{C}_K$

$$\begin{aligned} \mathcal{C}_K :=& \mathcal{S}_K \cap \mathcal{E}_K = \Big\{ \{d^{\mathcal{C}},\, \theta_A^{\mathcal{C}},\, \theta_S^{\mathcal{C}}\} \in \mathcal{I}_K \Big| \\ & S_K\left(d^{\mathcal{C}} = \overline{d}(\mathbf{p}, \mathbf{q}),\, \theta_A^{\mathcal{C}} = \overline{\theta}_A(\mathbf{p}, \mathbf{q}),\, \theta_S^{\mathcal{C}} = \overline{\theta}_S(\mathbf{p}, \mathbf{q})\right) = 0 \Big\}. \end{aligned} \tag{6.30}$$

By considering Eqs.(6.18) and (A.6), the 'catastrophe set' (or, equivalently, the *catastrophe locus*) $\mathcal{C}_K$ can be also projected within the control and physical[8] planes

$$\begin{aligned} \mathcal{C}_C &:= \{\mathbf{p}^{\mathcal{C}} \in \mathcal{I}_C \big| \mathbf{p}^{\mathcal{C}} = \widehat{\mathbf{p}}\left(\theta_A^{\mathcal{C}},\, \theta_S^{\mathcal{C}}\right)\}, \\ \mathcal{C}_P &:= \{\{X_l^{\mathcal{C}},\, Y_l^{\mathcal{C}}\} \in \mathcal{I}_P \big|\, X_l = \overline{X}_l(\mathbf{p}^{\mathcal{C}}, \mathbf{q}),\, Y_l = \overline{Y}_l(\mathbf{p}^{\mathcal{C}}, \mathbf{q})\}. \end{aligned} \tag{6.32}$$

[7] It is worth mentioning that the present nomenclature differs from that used by some authors [31, 55] defining the projection $\mathcal{C}_C$ of the catastrophe set in the control (force) plane as bifurcation set and the snap-back set $\mathcal{S}_K$ as catastrophe set.

[8] It is noted that the 'catastrophe set' $\mathcal{C}_P$ is a curve within the physical plane $X_l - Y_l$, obtained as the projection of the 'catastrophe set' $\mathcal{C}_P^{3D}$ collecting the critical rotation angle $\Theta_l^{\mathcal{C}}$ as third physical coordinate

$$\mathcal{C}_P^{3D} := \{\{X_l^{\mathcal{C}},\, Y_l^{\mathcal{C}},\, \Theta_l^{\mathcal{C}}\} \in \mathcal{I}_P \big|\, X_l = \overline{X}_l(\mathbf{p}^{\mathcal{C}}, \mathbf{q}),\, Y_l = \overline{Y}_l(\mathbf{p}^{\mathcal{C}}, \mathbf{q}),\, \Theta_l = \overline{\Theta}_l(\mathbf{p}^{\mathcal{C}}, \mathbf{q})\}. \tag{6.31}$$

Similarly to the 'snap-back set' $\mathcal{S}_K$, the 'catastrophe sets' $\mathcal{C}_J$ are given by the union of the two 'catastrophe subsets' $\mathcal{C}_J^{(+)}$ and $\mathcal{C}_J^{(-)}$ $(J = C, K, P)$, being the sign referred to that of the symmetric angle/ends curvature for which the equilibrium configuration snaps. Due to the non-linearities involved, the catastrophe sets can be evaluated only numerically. The algorithm used for the numerical evaluation of the catastrophe set is presented in Section A.1.3 of the Appendix A.

6.3.2 'Effectiveness' of the *elastica catastrophe machine*

Following the principles of the classical catastrophe machine, the 'effective' *elastica catastrophe machine* should repetitively display snapping mechanisms along specific equilibrium paths. This property corresponds to the *hysteretic* behaviour typical of nonlinear elastic structures characterized by cusp catastrophes when subject to cyclic variations in their control parameters [93]. Therefore, the design of an 'effective' *elastica catastrophe machine* is guided by tuning the design parameters $\mathbf{q}$ towards the morphogenesis of an 'effective' catastrophe set $\mathcal{C}_P$ displaying hysteresis. In particular, this set defines a closed curve in the physical plane which is composed of both the 'catastrophe subsets' $\mathcal{C}_P^{(+)}$ and $\mathcal{C}_P^{(-)}$ joined together, allowing snapping for both signs of symmetric angle/ends curvature.

The hysteretic (non-hysteretic) behaviour associated to the 'effectiveness' ('non-effectiveness') of the catastrophe locus is sketched in the upper (lower) part of in Fig. 6.5 for a cyclic variation in the control parameters.

The points B_1 (magenta in Fig. 6.5, left) common to both $\mathcal{C}_P^{(+)}$ and $\mathcal{C}_P^{(-)}$ subsets are present only for effective sets and always correspond to supercritical pitchfork bifurcations as the limit case displaying a non-snapping elastica [33]. Contrarily, the sharp corner points B_2 (yellow in Fig. 6.5, left) within the subsets $\mathcal{C}_P^{(-)}$ or $\mathcal{C}_P^{(+)}$ are associated with subcritical pitchfork bifurcations displaying high-energy release for the snapping elastica.

Because of its generality, the present theoretical framework can be exploited to design a specific *elastica catastrophe machine* by particularizing the kinematic relations $X_l(\mathbf{p}, \mathbf{q}), Y_l(\mathbf{p}, \mathbf{q})$, and $\Theta_l(\mathbf{p}, \mathbf{q})$. Within the infinite set of possible *elastica catastrophe machines*, as evidence of feasibility, two specific families are proposed and investigated in the next section, showing that catastrophe locus can be attained with peculiar properties by tuning the design parameters vector $\mathbf{q}$. More specifically, the catastrophe locus $\mathcal{C}_P$ of the *elastica catastrophe machine* might exhibit a number of bifurcation points not necessarily equal

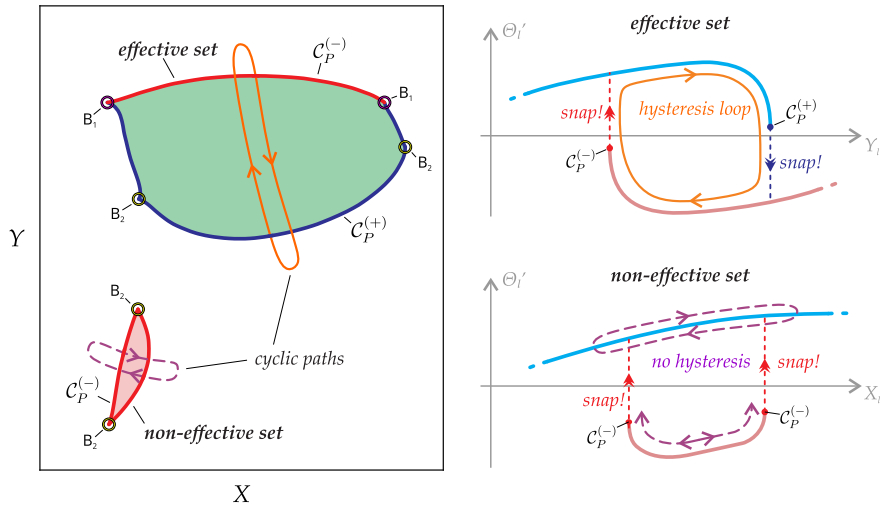

Figure 6.5: (Left) Sketch of effective and non-effective catastrophe sets within the physical plane, the former composed of the two subsets $\mathcal{C}_P^{(+)}$ (blue curve) and $\mathcal{C}_P^{(-)}$ (red curve) while the latter of a unique closed subset $\mathcal{C}_P^{(-)}$ (red closed curve). Cyclic paths crossing the two sets are drawn as orange and purple closed loops, respectively. Green areas represent the set of coordinates $\{X_l, Y_l\}$ of the rod's end corresponding to bistability of the equilibrium. Sharp corner points B_1 (magenta) and B_2 (yellow) denote supercritical and subcritical bifurcations for the elastica with controlled ends, respectively. (Right) Sketch of the structural response in terms of the end's curvature Θ_l' versus the evolution of the end's coordinate X_l (Y_l) along the orange/continuous (purple/dashed) cyclic path and providing hysteretic (non-hysteretic) behaviour.

to four. Indeed, such multiplicity can vary here because coincident with the number, variable through the design parameters, of intersections of the elastica machine set $\mathcal{E}_K$ (which is in general not a plane) with the snap-back set $\mathcal{S}_K$ with $\theta_S = 0$ (points B_1) or $\theta_A = 0$ (points B_2). Even more unusual, the catastrophe locus $\mathcal{C}_P$ may substantially vary its non-convexity, differently from the classical machines. This property is fundamental for crossing bifurcation points at high-energy release. Indeed, convexity facilitates reaching bifurcation points, otherwise confined within acute angles in the classical machines. Because an analytical proof is awkward, with the purpose to evaluate the convex property

of the catastrophe locus $\mathcal{C}_P$, the convexity measure $\mathsf{C}(\mathcal{C}_P)$ is introduced [125]

$$\mathsf{C}(\mathcal{C}_P) = \frac{\text{Area}(\mathcal{C}_P)}{\text{Area}(\mathbf{CH}(\mathcal{C}_P))}. \tag{6.33}$$

In eqn. (6.33) $\mathbf{CH}(\mathcal{C}_P)$ is the *convex hull* of $\mathcal{C}_P$, namely the smallest convex set including the shape of the catastrophe locus. The convexity measure C ranges between 0 and 1, being equal to 1 if and only if the planar shape is convex.

6.4 Two families of *elastica catastrophe machines*

With the purpose to explicitly evaluate catastrophe loci generated by *elastica catastrophe machines*, the two families ECM-I (Fig. 6.6, left) and ECM-II (Fig. 6.6, right) are considered and investigated by means of the general theoretical framework presented in the previous section. The elastica's end $s = l$ is considered attached to an external rigid bar, which configuration is defined by the two control parameters p_1 and p_2. In both ECM-I and ECM-II the control parameter p_2 is taken coincident with the rigid bar rotation, so that, introducing the design angle parameter υ between the rigid bar and the elastica end tangent, the rotation Θ_l imposed at the final curvilinear coordinate is given by

$$\Theta_l(\mathbf{p}, \mathbf{q}) = p_2 + \upsilon. \tag{6.34}$$

For each one of the two proposed families, the dependence on the control parameters is specified for the physical coordinates $X_l(\mathbf{p}, \mathbf{q})$ and $Y_l(\mathbf{p}, \mathbf{q})$. Therefore, the respective inextensibility and machine sets, introduced in the previous Section with a general perspective, can be explicitly identified. Finally, the shape change of the corresponding catastrophe set and the achievement of 'effective' catastrophe sets are disclosed with varying the design parameters vector $\mathbf{q}$.

6.4.1 The *elastica catastrophe machine* ECM-I

In the first family of catastrophe machine (Fig. 6.6, left), the external rigid bar is constrained by a sliding sleeve, centered at the fixed point $R = (\kappa_R l; \lambda_R l)$ and whose inclination with respect to the X-axis corresponds to the control parameter p_2. By sliding the rigid bar, the distance $p_1 l$ between the elastica

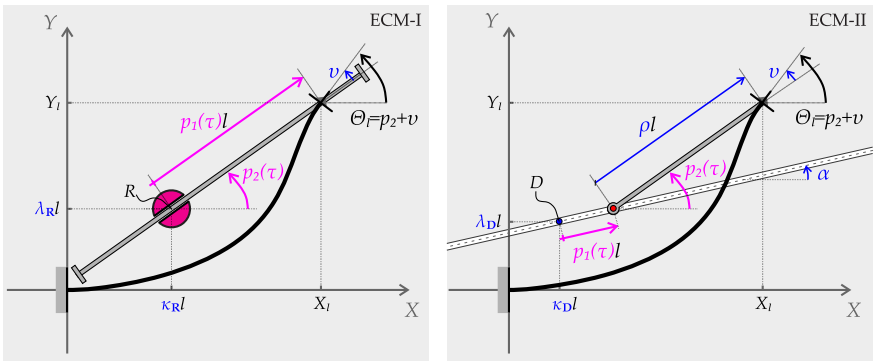

Figure 6.6: The two proposed families of *elastica catastrophe machine*: ECM-I (left) and ECM-II (right). An inextensible elastic rod of length l has an end with a fixed position and rotation. The kinematics of the elastic rod, considered within the plane $X-Y$, is ruled by the configuration of an external rigid bar defined through two control parameters p_1 and p_2. The design parameter vectors $\mathbf{q}^I = \{\kappa_R, \lambda_R, \upsilon\}$ and $\mathbf{q}^{II} = \{\kappa_D, \lambda_D, \alpha, \rho, \upsilon\}$ define respectively a family of *elastica catastrophe machines* ECM-I and ECM-II.

end $s = l$ and the sliding sleeve rotation center is ruled by the control parameter p_1, so that the coordinates of the elastica's end are

$$\frac{\overline{X}_l(\mathbf{p}, \mathbf{q}^I)}{l} = \kappa_R + p_1 \cos p_2, \qquad \frac{\overline{Y}_l(\mathbf{p}, \mathbf{q}^I)}{l} = \lambda_R + p_1 \sin p_2, \tag{6.35}$$

with p_1 restricted to positive values ($p_1 > 0$)[9] and the control parameters vector has length $N = 3$ and is given by

$$\mathbf{q}^I = \{\kappa_R, \lambda_R, \upsilon\}. \tag{6.36}$$

The different relations connecting the configuration representation through control parameters, primary kinematical quantities and physical coordinates can be derived from the explicit kinematical rules (6.34) and (6.35). These are reported in the Appendix A (Section A.2.1).

The 'elastica machine set' $\mathcal{E}_C$ is defined in the control parameters plane $p_1 - p_2$ as the intersection of the inextensibility set $\mathcal{I}_C$, provided by the inextensibility

[9]It is noted that the catastrophe sets related to negative values (disregarded here) of p_1 can be obtained from those restricted to positive values, being the configuration corresponding to a control vector $\mathbf{p} = \{p_1^\flat, p_2^\flat\}$ and a design vector $\mathbf{q}^I = \{\kappa_R^\flat, \lambda_R^\flat, \upsilon^\flat\}$ the same of that corresponding to $\mathbf{p} = \{-p_1^\flat, p_2^\flat + \pi\}$ and $\mathbf{q}^I = \{\kappa_R^\flat, \lambda_R^\flat, \upsilon^\flat - \pi\}$.

condition (6.5) as

$$\mathcal{I}_C = \left\{ \mathbf{p} : \; p_1^2 + 2p_1 \left(\kappa_R \cos p_2 + \lambda_R \sin p_2 \right) + {\kappa_R}^2 + {\lambda_R}^2 \leq 1 \right\}, \tag{6.37}$$

with the set machine domain $\mathcal{M}_C$, Eq.(6.23), expressed as

$$\mathcal{M}_C = \left\{ \mathbf{p} : \; \left| \frac{p_2 + \upsilon}{2} \right| < \pi, \left| \frac{p_2 + \upsilon}{2} - \arctan\left(\frac{\lambda_R + p_1 \sin p_2}{\kappa_R + p_1 \cos p_2} \right) \right| < \pi \right\}. \tag{6.38}$$

The different sets in the primary kinematical space and in the physical plane can be obtained from the respective projections of $\mathcal{I}_C$ (6.37) and $\mathcal{M}_C$ (6.38) by means of equations (A.14)-(A.22).

The $\mathcal{I}$, $\mathcal{M}$, $\mathcal{E}$, and $\mathcal{C}$ sets are reported in Fig. 6.7 for the control parameters $\kappa_R = 0.5$, $\upsilon = 0$ and $\lambda_R = \{0.3, 0.35, 0.4\}$. Therefore, the considered ECMs-I differ only in the position of the rigid bar rotation center R, slightly moving up from the first to the third line. In the Figure, three different spaces are depicted: the control plane (left column), the primary kinematical space (central column, also containing the snap-back surface $\mathcal{S}_K$), and the physical plane (right column). The catastrophe set $\mathcal{C}_K$ is evaluated within the primary kinematical space as the curve defined by the intersection of two surfaces, representing the snap set $\mathcal{S}_K$ and the elastica set $\mathcal{E}_K$. The obtained catastrophe curve has projections $\mathcal{C}_C$ and $\mathcal{C}_P$ within the control and physical planes as planar curves. The positive and negative sign of ends' curvature related to the configuration at snapping is highlighted along the catastrophe curves $\mathcal{C}$ with blue ($\mathcal{C}^{(+)}$) and red ($\mathcal{C}^{(-)}$) colour, respectively. How the catastrophe set changes with increasing the design parameter λ_R may be appreciated from the figure. In particular, the sets of coordinates corresponding to two stable equilibrium configurations are given by the union of one ($\lambda_R = 0.3$), two ($\lambda_R = 0.35$), and three ($\lambda_R = 0.4$) simply connected domains in the physical plane. However, for each of the three cases, only one of these simply connected domains (drawn as a thick line) provides hysteresis when crossed during a cyclic path. When existing ($\lambda_R = \{0.35, 0.4\}$), the other simply connected domains have boundary (drawn with thin line) for which snapping occurs only for a positive *or* for a negative sign of the ends' curvature, so that *no more than one* snap (and therefore *no hysteresis*) can be related to these during a cyclic path. The existence and properties of these simply connected domains are strictly dependent on the selected design vector. With this regard, by considering[10] only non-negative values of λ_R and $\upsilon \in [0, 2\pi)$ and restricting the attention to the physical plane representation,

[10]Symmetry and periodicity properties of expressions (6.34) and (6.35) in the design parameters λ_R and υ define symmetry properties for the catastrophe sets. More specifically, a

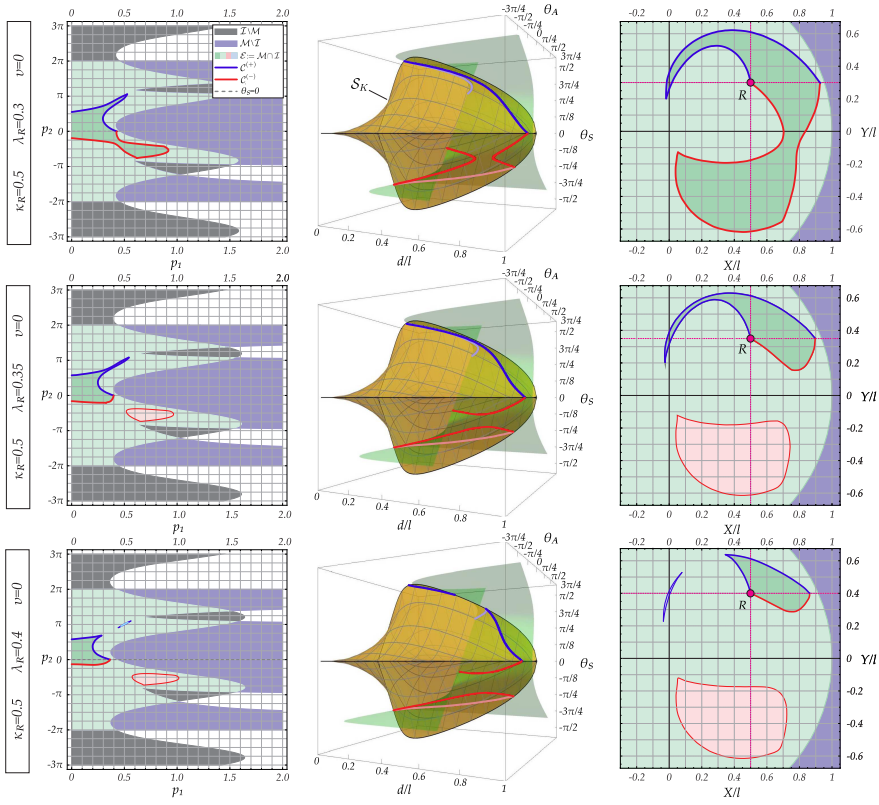

Figure 6.7: Inextensibility $\mathcal{I}$, machine $\mathcal{M}$, elastica $\mathcal{E}$, and catastrophe $\mathcal{C}$ sets within the three different spaces (from the left to right: control plane, primary kinematical space, physical plane) for three ECMs-I with $\kappa_R = 0.5$, $\upsilon = 0$ and $\lambda_R = \{0.3, 0.35, 0.4\}$ increasing from the first to the third line. The yellow surface appearing in the primary kinematical space $\{d/l, \theta_A, \theta_S\}$ is the snap-back set $\mathcal{S}_K$. The portions $\mathcal{C}^{(+)}/\mathcal{C}^{(-)}$ of the 'catastrophe sets' are reported as blue/red lines. The effective 'catastrophe sets' are reported as thick lines and are those defined by the union of $\mathcal{C}^{(+)}$ with $\mathcal{C}^{(-)}$ (where the superscript is related to the sign of the ends' curvature of the snapping configuration). The shifting of the rotation centre R parallel to the Y-axis provides a change of the catastrophe locus, with the realization of possible non-effective sets (closed thin lines drawn with only one colour).

change in the sign of both the design parameters λ_R and υ provides a mirroring of the catastrophe set (with respect to the X axis within the physical plane and with respect to the p_2

the influence of the design parameters is shown through the following effective and non-effective catastrophe sets:

- for $\kappa_R = 0.5$, $\upsilon = \{0, 1\}\pi$, and $\lambda_R = \{0.1, 0.2, 0.3, 0.35, 0.4, 0.5, 0.6, 0.7\}$ in Fig. 6.8, showing that the *elastica catastrophe machine* is non-effective for both the considered values of υ when $\lambda_R = 0.7$, while effective in the remaining cases;
- for $\kappa_R = \{0.25, 0.5, 0.75, 1\}$, $\upsilon = \{0, 1/4, 1/2, 3/4, 1, 5/4, 3/2, 7/4\}\pi$, and $\lambda_R = 0$ in Fig. 6.9, showing that the *elastica catastrophe machine* is non-effective for $\kappa_R = 1$ when $\upsilon = \{0, 1/4, 1/2, 3/2, 7/4\}\pi$, while effective in the remaining cases.

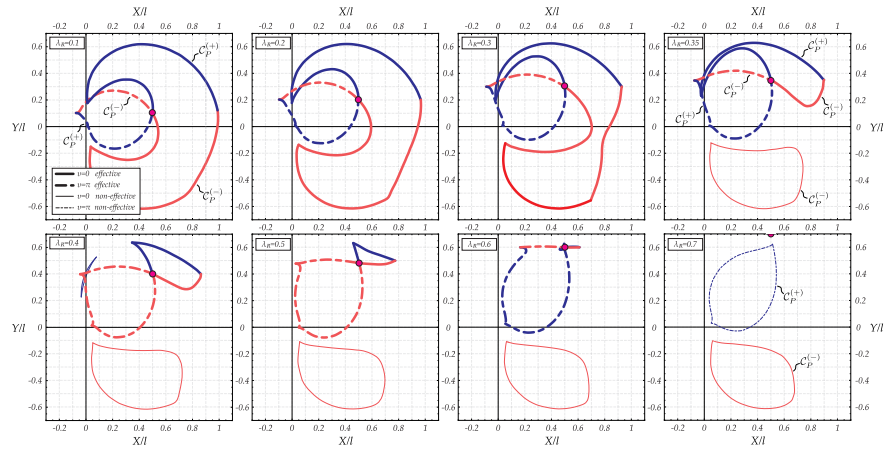

Figure 6.8: Catastrophe loci in the physical plane $X - Y$ for ECM-I with $\kappa_R = 0.5$, $\lambda_R = \{0.1, 0.2, 0.3, 0.35, 0.4, 0.5, 0.6, 0.7\}$, and $\upsilon = \{0, 1\}\pi$. The red spots identify the position rotation center R of the rigid bar. Effectiveness and non-effectiveness of the catastrophe loci is distinguished through thick and thin coloured lines, respectively.

Dramatic changes in the projection of the catastrophe set within the physical plane can be observed from these figures, as the result of changing the design parameter vectors $\mathbf{q}$. In particular, a loss of symmetry in the catastrophe locus

within the control plane) and a change in sign for the related curvature displaying snapping. An increase of $2k\pi$ ($k \in \mathbb{Z}$) in υ provides a shifting of $-2k\pi$ of the catastrophe set with respect to the p_2 axis within the control plane and no change within the physical plane.

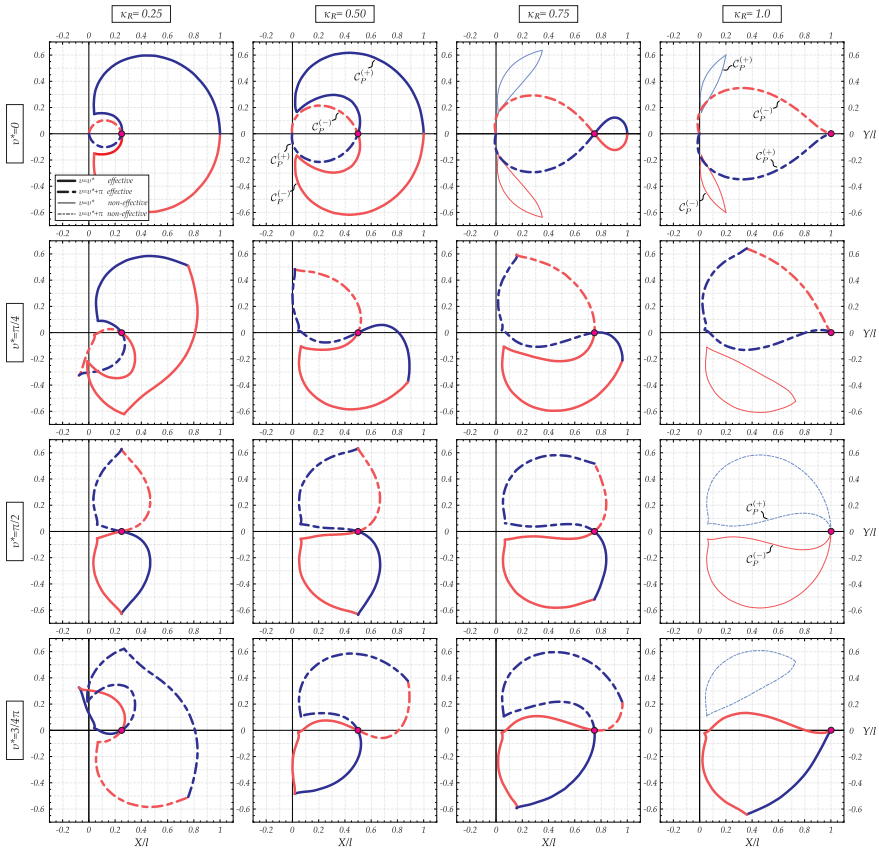

Figure 6.9: As for Fig. 6.8, but for $\lambda_R = 0$, $\kappa_R = \{0.25, 0.5, 0.75, 1\}$ and $\upsilon = \{0, 1/4, 1/2, 3/4, 1, 5/4, 3/2, 7/4\}\pi$. The parameter υ^* is introduced to represent the two cases $\upsilon = \upsilon^*$ and $\upsilon = \upsilon^* + \pi$ in the same plot. The position rotation center R of the rigid bar is identified as red spots.

occurs when $\upsilon \neq \{0, \pi\}$ or $\lambda_R \neq 0$. Furthermore, the catastrophe loci that may be generated by ECM-I encompass a large variety of shapes, very different from those related to the classical catastrophe machines. In particular, the following new features of the catastrophe sets are found:

- *Variable number of bifurcation points.* The effective catastrophe loci, re-

ported for different values of $\mathbf{q}$ in Figs. 6.8 and 6.9, display a variable number of bifurcation points depending on the number of intersections of $\mathcal{E}_K$ with $\mathcal{S}_K$ for $\theta_S = 0$ and $\theta_A = 0$. In Fig. 6.8, the reported effective sets have two (e.g. second row, first column, $\upsilon = 0$) or four bifurcation points (e.g. first row, second column, $\upsilon = 0$). In Fig. 6.9, the number of bifurcation points can be equal to one (e.g. first row, first column, $\upsilon = \pi$), two (e.g. second row, second column, $\upsilon = \pi/4$), three (first row, first column, $\upsilon = 0$) or four (second row, first column, $\upsilon = \pi/4$);

- *Convex measure of the catastrophe locus $\mathcal{C}_P$.* In Fig. 6.9, the catastrophe sets for $\{\upsilon = \pi,\ \kappa_R = 0.25\}$ (first row, first column) and for $\{\upsilon = 0,\ \kappa_R = 0.75\}$ (first row, third column) have convex measure approaching the unit value, $\mathsf{C} \simeq 1$. The catastrophe set for $\{\upsilon = \pi,\ \kappa_R = 0.5\}$ (first row, second column) has $\mathsf{C} = 0.9997$ while that for $\{\upsilon = \pi,\ \kappa_R = 0.75\}$ (first row, third column) has $\mathsf{C} = 0.998$. Finally, the catastrophe sets for $\upsilon = 0$ and $\lambda_R = \{0.3, 0.35, 0.4\}$ shown in Figs. 6.7 and 6.8 have $\mathsf{C} = \{0.5707,\ 0.4475,\ 0.9402\}$.

The recommendations about how to select the initial values of the control parameters $\mathbf{p}(\tau_0)$ to belong to the inextensibility set $\mathcal{I}_C$ are included in Sect. A.2.1 of the Appendix A. Some considerations drawn for ECM-I under the two special conditions for the position center R are respectively reported in Sects. A.2.1 and A.2.1) of the Appendix A.
Similarly to the classical Zeeman machine, all the sharp corner points, when not coincident with the rotation centre R, correspond to pitchfork bifurcations.

6.4.2 The *elastica catastrophe machine* ECM-II

In the catastrophe machine ECM-II (Fig. 6.6, right) the rigid bar of fixed length ρl can rotate and has one end constrained to slide along a straight line, inclined at an angle α with respect to the X-axis. The center of rotation of the rigid bar is at a controlled distance $p_1 l$ from a fixed point D, of coordinates $\{X_D, Y_D\} = \{\kappa_D, \lambda_D\}l$, located on the straight line. By controlling the inclination p_2 and the distance $p_1 l$ of the movable rotation center of coordinates $\{\kappa_D + p_1 \cos\alpha, \lambda_D + p_1 \sin\alpha\}l$ from the reference point D, the elastica end $s = l$ has coordinates

$$\frac{\overline{X}_l(\mathbf{p}, \mathbf{q}^{II})}{l} = \kappa_D + p_1 \cos\alpha + \rho \cos p_2, \quad \frac{\overline{Y}_l(\mathbf{p}, \mathbf{q}^{II})}{l} = \lambda_D + p_1 \sin\alpha + \rho \sin p_2, \tag{6.39}$$

while the design parameters vector (of length $N = 5$) for ECM-II is

$$\mathbf{q}^{II} = \{\kappa_D, \lambda_D, \alpha, \rho, \upsilon\}. \tag{6.40}$$

The equations relating the control parameters, the primary kinematical quantities and the physical coordinates are obtained through the equations (6.34) and (6.39) and reported in the Appendix A (Section A.2.2).

The control parameters vector $\mathbf{p}$ for ECM-II is restricted to the set $\mathcal{E}_C$, given by the intersection of the inextensibility set $\mathcal{I}_C$,

$$\begin{aligned}\mathcal{I}_C = \Big\{ \mathbf{p} : p_1^2 + \rho^2 + 2\big[p_1\rho\cos(\alpha - p_2) + \kappa_D\,(p_1\cos\alpha + \rho\cos p_2) + \\ + \lambda_D\,(p_1\sin\alpha + \rho\sin p_2)\big] + {\kappa_D}^2 + {\lambda_D}^2 \leq 1 \Big\},\end{aligned} \tag{6.41}$$

with the machine domain $\mathcal{M}_C$

$$\mathcal{M}_C = \left\{ \mathbf{p} : \left| \frac{p_2 + \upsilon}{2} \right| < \pi, \left| \frac{p_2 + \upsilon}{2} - \arctan\left(\frac{\lambda_D + p_1\sin\alpha + \rho\sin p_2}{\kappa_D + p_1\cos\alpha + \rho\cos p_2} \right) \right| < \pi \right\}. \tag{6.42}$$

In order to have a non-null elastica machine set $\mathcal{E}$, the first four design parameters are constrained to satisfy the following inequality

$$|\kappa_D \sin\alpha - \lambda_D \cos\alpha| - \rho < 1. \tag{6.43}$$

From Eq.(6.39), it may also be noted that two different control parameters vectors $\mathbf{p}^\flat$ and $\mathbf{p}^\sharp$ provide the same end's coordinates $\{X_l(\mathbf{p}^\flat, \mathbf{q})) = X_l(\mathbf{p}^\sharp, \mathbf{q})$, $Y_l(\mathbf{p}^\flat, \mathbf{q})) = Y_l(\mathbf{p}^\sharp, \mathbf{q})\}$ when

$$p_1^\sharp = p_1^\flat + 2\rho\cos(p_2^\flat - \alpha), \qquad p_2^\sharp = \pi + 2\alpha - p_2^\flat. \tag{6.44}$$

Therefore, in addition to the natural multiplicity due to the angular periodicity in the physical angle Θ_l, the same position X_l, Y_l in the physical plane is associated to two physical angles $\Theta_l(\mathbf{p}^\sharp, \mathbf{q}) \neq \Theta_l(\mathbf{p}^\flat, \mathbf{q})$ not differing by $2k\pi$ ($k \in \mathbb{Z}$), namely

$$\Theta_l(\mathbf{p}^\sharp, \mathbf{q}) = \pi + 2(\alpha + \upsilon) - \Theta_l(\mathbf{p}^\flat, \mathbf{q}). \tag{6.45}$$

Due to this additional multiplicity, it is instrumental to analyze the behaviour of ECM-II through the analysis of two machine subtypes, ECM-IIa and ECM-IIb, having the control parameter p_2 (ruling the rigid bar rotation) restricted to

specific sets $p_2^{(a)}$ and $p_2^{(b)}$,

$$\begin{aligned} &\text{ECM-IIa}: \quad p_2^{(a)} \in \bigcup_{k\in\mathbb{Z}} \left[-\frac{\pi}{2}+\alpha+2k\pi, \frac{\pi}{2}+\alpha+2k\pi\right], \\ &\text{ECM-IIb}: \quad p_2^{(b)} \in \bigcup_{k\in\mathbb{Z}} \left[\frac{\pi}{2}+\alpha+2k\pi, \frac{3\pi}{2}+\alpha+2k\pi\right]. \end{aligned} \tag{6.46}$$

The inextensibility $\mathcal{I}$, the machine $\mathcal{M}$, the elastica $\mathcal{E}$ and catastrophe $\mathcal{C}$ sets for ECM-II are shown in Fig. 6.10 within the control plane (left column), primary kinematical space (central column), and the physical plane (right column) for $\kappa_D = \lambda_D = \alpha = \upsilon = 0$ and $\rho = \{0.5, 0.6, 0.65\}$, with increasing values from the upper to the lower line. The portions $\mathcal{C}_P^{(+)}/\mathcal{C}_P^{(-)}$ of catastrophe loci are reported as blue/red lines, continuous for ECM-IIa and dashed for ECM-IIb. In the figure, the blue/red line defines configurations for which elastica with positive/negative ends curvature snaps. The thick line identifies an effective catastrophe locus while a thin line a non-effective one, so that, in Fig. 6.10, the catastrophe sets of EMC-IIa are all effective while those of ECM-IIb are not. It is evident that for $\rho = \{0.5, 0.6\}$ the catastrophe sets of ECM-IIa and ECM-IIb have in common their end points (also at the boundary of $\mathcal{I}/\mathcal{M}$ in the physical plane) while for $\rho = 0.65$ the two machine subtypes do not share any point with each other.

The catastrophe sets of ECM-IIa and ECM-IIb for $\kappa_D = \lambda_D = \alpha = \upsilon = 0$ and $\rho = 0.5$ shown in Fig. 6.10 (upper part, right) are also reported separately for the two machine subtypes in Fig. 6.11 (upper part). This latter representation contains also some elasticae, highlighting the two possible equilibrium configurations for a state within the bistable region and the only possible configuration after crossing the catastrophe locus. The catastrophe sets are also reported in the lower part of Fig. 6.11 for a machine with the same design parameters of that considered in the upper part of Fig. 6.11 except for the value of υ, taken as $\upsilon = \pi$ (instead of $\upsilon = 0$).

It can be appreciated that for the same design parameters no more than one of the two machine subtypes is effective, namely ECM-IIa with $\upsilon = 0$ and ECM-IIb with $\upsilon = \pi$. The remaining two machine subtypes are non-effective, but each of them displays a different behaviour. ECM-IIb with $\upsilon = 0$ has a non-effective catastrophe set so that only one snap may occur during a continuous evolution while ECM-IIa with $\upsilon = \pi$ has no catastrophe locus so that no snap is possible with this machine subtype. Performing a parametric analysis of ECM-II (by varying the design parameters) it can be concluded that a principle of exclusion about the effectiveness for the two subtypes of machine exists, namely,

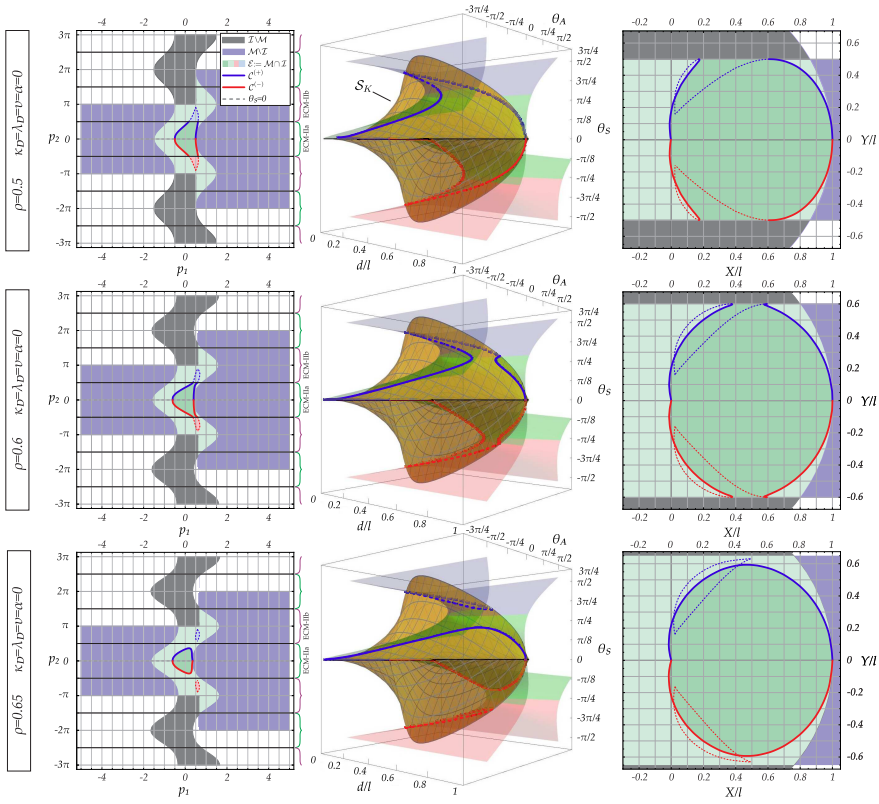

Figure 6.10: As for Fig. 6.7, but for three ECMs-II with $\kappa_D = \lambda_D = \upsilon = \alpha = 0$ and $\rho = \{0.5, 0.6, 0.65\}$ increasing from the first to the third line. The portions $\mathcal{C}^{(+)}/\mathcal{C}^{(-)}$ of the 'catastrophe sets' are reported as blue/red lines, continuous for ECM-IIa and dashed for ECM-IIb. For the reported cases, the effective 'catastrophe sets' are related only to ECM-IIa. The increase in the rigid bar parameter length ρ provides a change of the catastrophe locus, as the detachment from the elastica machine set boundary in the case $\rho = 0.65$.

if ECM-IIa (or ECM-IIb) is an effective machine then ECM-IIb (or ECM-IIa) is not. This principle finds also evidence in the Figs. 6.12-6.15, referred to different design parameters vectors (restricted to $\upsilon \in [0, 2\pi)$ due to periodicity) as follows:

- for $\kappa_D = \lambda_D = \alpha = 0$, $\rho = \{0.1, 0.2, 0.3, 0.5, 0.6, 0.7, 0.8, 1\}$ and $\upsilon = 0$ in

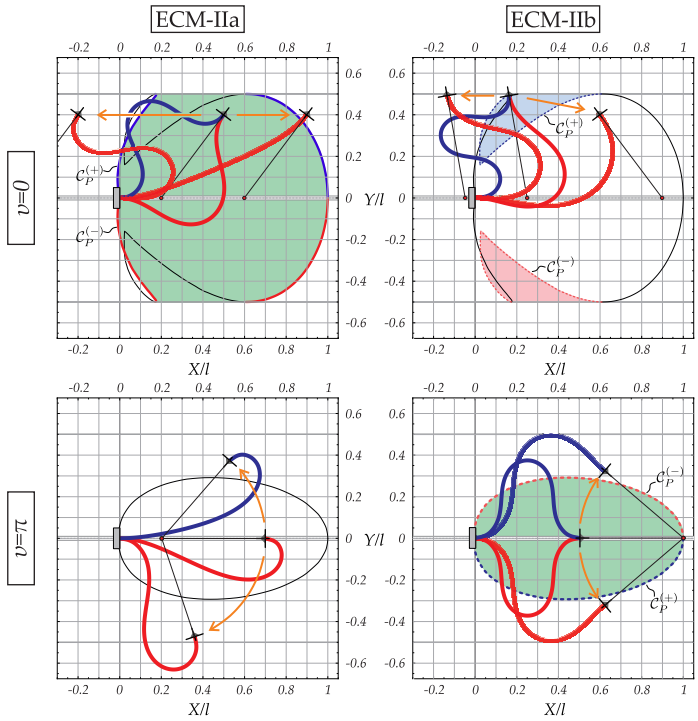

Figure 6.11: Catastrophe sets of ECM-IIa and ECM-IIb with $\kappa_D = \lambda_D = \alpha = 0$, $\rho = 0.5$, and $\upsilon = 0$ (upper part) or $\upsilon = \pi$ (lower part). While ECM-IIa is effective for $\upsilon = 0$, ECM-IIb is effective for $\upsilon = \pi$. Deformed configurations are also displayed for some specific end's position, highlighting equilibrium multiplicity (when existing).

Fig. 6.12 and for the same values of λ_D, κ_D, α, and ρ but $\upsilon = \pi$ in Fig. 6.13, showing that only ECM-IIa is effective in the former figure while only ECM-IIb is effective in the latter. In particular, ECM-IIa does not display any catastrophe set in all the cases in Fig. 6.13 (similarly to Fig. 6.11, bottom left) except when $\rho = 1$;

- for $\kappa_D = \lambda_D = 0$, $\rho = 0.5$, $\upsilon = \{0, \pi\}$ and $\alpha = \{0, 1/8, 1/4, 1/2\}\pi$ in Fig. 6.14, showing that only ECM-IIa is effective for $\upsilon = 0$ and $\alpha = \{0, 1/8, 1/4\}\pi$, only ECM-IIb is effective for $\upsilon = \pi$ and $\alpha = \{0, 1/8\}\pi$, while no machine subtype is effective in the remaining cases;

- for $\kappa_D = \alpha = 0$, $\rho = 0.5$, $\lambda_D = \{0, 0.2, 0.4, 0.6\}$ and $\upsilon = \{0, 1/4, 1/2, 3/4\}\pi$ in Fig. 6.15, showing that only ECM-IIa is effective for $\upsilon = \{0, 1/4\}\pi$ for all the reported values of λ_D and only ECM-IIb is effective for $\upsilon = 3/4\pi$ for all the reported values of λ_D, while no machine subtype is effective in the remaining cases.

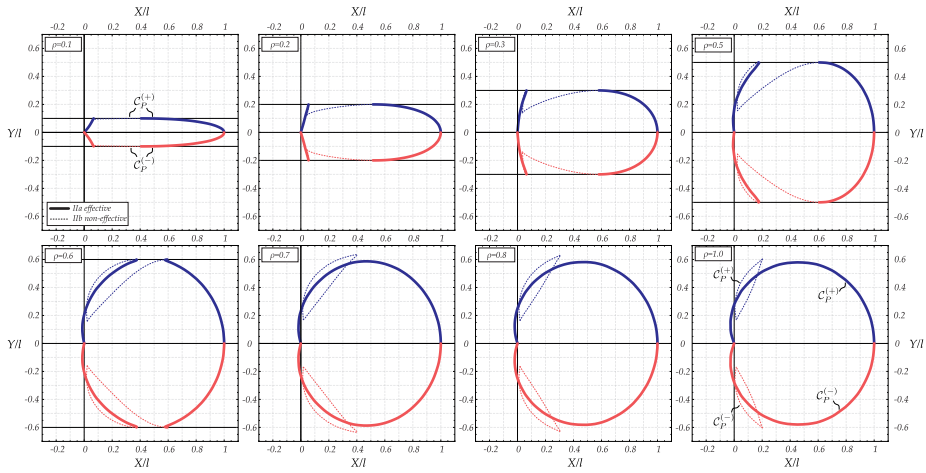

Figure 6.12: Catastrophe loci in the physical plane $X - Y$ for ECM-II with $\kappa_D = \lambda_D = \alpha = \upsilon = 0$ and $\lambda_D = \{0.1, 0.2, 0.3, 0.5, 0.6, 0.7, 0.8, 1\}$. Sets related to ECM-IIa are represented by continuous lines while those releated to EMC-IIb by dashed lines. Effectiveness and non-effectiveness of the catastrophe loci is distinguished through thick and thin coloured lines, respectively.

In analogy with the observations for ECM-I machine, the following new features of the catastrophe sets for ECM-II are displayed:

- *Variable number of bifurcation points.* The catastrophe sets in Figs. 6.12, 6.13, 6.14 and 6.15 exhibit a number of bifurcation points ranging from two to five. For instance, the ECM-IIa machines in Fig. 6.12 and the ECM-IIb machines in Fig. 6.13 have a catastrophe set with two bifurcation points on the symmetry axis. Moreover, In Fig. 6.15, the catastrophe set for the ECM-IIa machine for $\upsilon = \pi/4$ and $\lambda_D = 0.2$ (second row and second column) has five bifurcation points.

- *Convex measure of the catastrophe locus* $\mathcal{C}_P$. The catastrophe sets reported

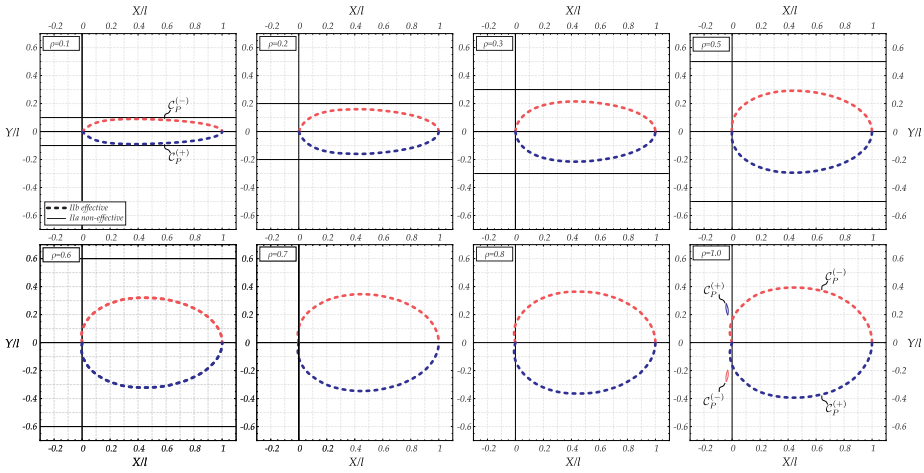

Figure 6.13: As for Fig. 6.12, but for $\upsilon = \pi$.

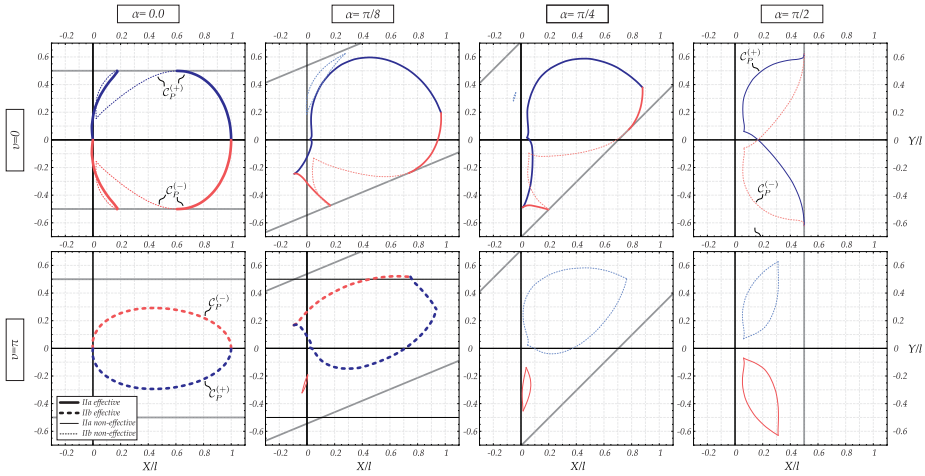

Figure 6.14: As for Fig. 6.12, but for $\kappa_D = \lambda_D = 0$, $\rho = 0.5$. A constant value of υ is considered for each line (first line $\upsilon = 0$, second line $\upsilon = \pi$) and of α for each column ($\alpha = \{0, 1/8, 1/4, 1/2\}\pi$, increasing from left to right).

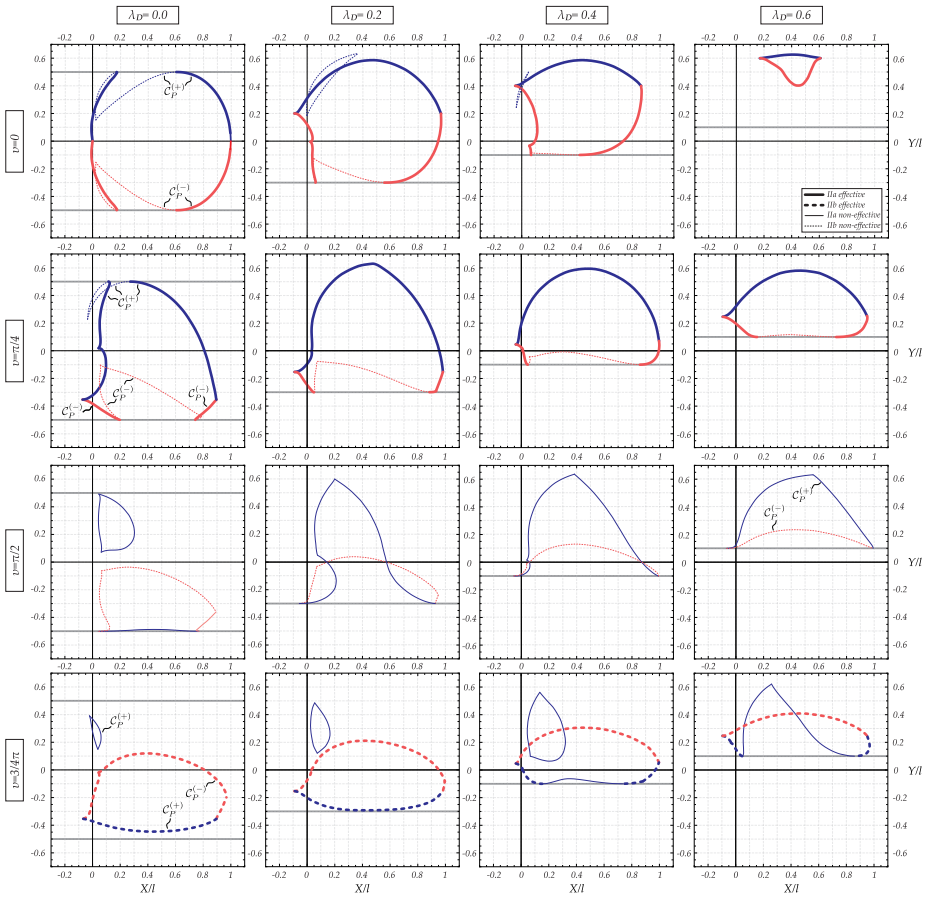

Figure 6.15: As for Fig. 6.12, but for $\kappa_D = \alpha = 0$, $\rho = 0.5$. A constant value of υ is considered for each line ($\upsilon = \{0, 1/4, 1/2, 3/4\}\pi$, increasing from above to bottom) and of λ_D for each column ($\lambda_D = \{0, 0.2, 0.4, 0.6\}$, increasing from left to right).

in the first row of Fig. 6.13 have $\mathsf{C} \simeq 1$ for $\rho = \{0.1, 0.2, 0.3\}$ (first three columns) and $\mathsf{C} = 0.9998$ for $\rho = 0.5$ (fourth column).

The three-dimensional representation in Fig. 6.16 shows the curvature at the final curvilinear coordinate as a function of the two control parameters for ECM-IIb with $\kappa_D = \lambda_D = \alpha = 0$, $\upsilon = \pi$, and $\rho = 0.8$ (corresponding to

the setting considered in the third column, second line, of Fig. 6.13). The same three-dimensional plot is reported on the left and the right under two opposite perspectives. Multiplicity and uniqueness of equilibrium configuration are highlighted for control parameters pairs respectively inside and outside the closed curve defining the catastrophe locus (projection on the $p_1 - p_2$ plane). The jump in the equilibrium configuration, displayed at the catastrophe locus with arrows, implies a change in the curvature sign (for the same value of control parameters).

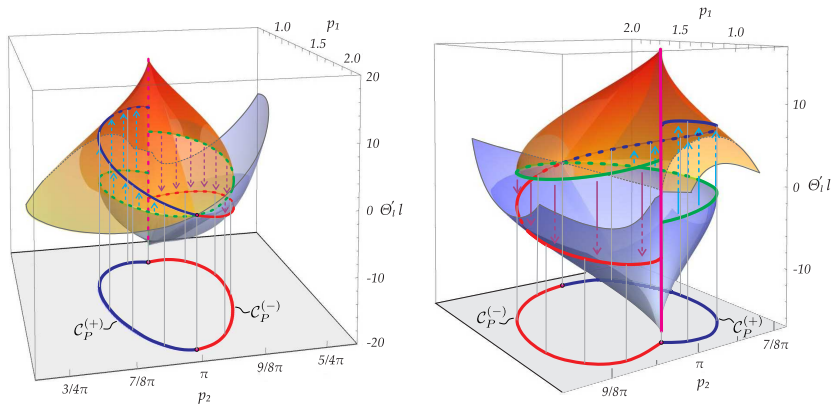

Figure 6.16: Curvature at the final curvilinear coordinate, $\Theta_l' = \Theta'(s = l)$, (made dimensionless by multiplication with the length l) as a function of the control parameters p_1 and p_2 for ECM-IIb with $\kappa_D = \lambda_D = \alpha = 0$, $\upsilon = \pi$, and $\rho = 0.8$ (corresponding to the setting considered in the third column, second line, of Fig. 6.13). Two opposite views of the three-dimensional plot are reported on the left and the right. Green line highlights critical configurations for which snap occurs toward a configuration laying along the blue and red curve having the same control parameters pair but opposite curvature sign. The projection of $\mathcal{C}^{(+)}$ (blue line) and $\mathcal{C}^{(-)}$ (red line) on the $p_1 - p_2$ plane is also reported as the representation of the catastrophe locus within the control plane.

Finally, the analysis of ECM-II is complemented by a discussion about the special case of the rigid bar with infinitely large length reported in Sect. A.2.2 of the Appendix A and the suggestion for the initial values of the control parameters $\mathbf{p}(\tau_0)$ in Sect. A.2.2 of the Appendix A.

6.5 The physical realization of the *elastica catastrophe machine*

A prototype of the *elastica catastrophe machine* was designed and realized at the Instabilities Lab of the University of Trento, Fig. 6.17. This setup, thought to be as versatile as possible, allowed the experimental investigation of both the two proposed families, ECM-I and ECM-II (a and b). The two clamps, one fixed and the other moving, constraining the ends of the elastic rod are assembled on an HDF (High-density fibreboard) desk. This panel acts as a support for mounting the screen printing of the catastrophe locus, which changes by varying the selected design parameters. More specifically, the clamp constraint at the rod coordinate $s = 0$ is fixed and mounted on a PMMA structure. The constraint at the other end of the rod ($s = l$) is provided by a clamp which may slide along a rotating aluminium hollow bar (10×10 mm cross-section) with its end pinned to and possibly sliding along an aluminium rail (aluminium extrusions bar, 20×20 mm cross-section), fixed on the desk through two clips. Three goniometers are mounted to measure during the experiments (i.) the angle between the desk and the rail (design angle α in ECM-II), (ii.) the angle between the rail and the rotating bar (to be used for imposing the control angle p_2), and (iii.) the angle between the rotating bar and the moving clamp inclination (design angle υ).

Each one of the two proposed families can be tested by properly constraining one of the degrees of freedom of the prototype to a fixed value. In particular, ECM-I is attained by fixing the rotating bar end to a specific point R (design parameters κ_R, λ_R) along the fixed rail, while ECM-II by fixing the moving clamp along the rotating bar at a distance ρl from its end and by defining the inclination α and the passing point D (design parameters κ_D, λ_D) for the fixed rail.

Rods of (net) length $l = 40$ cm with different cross-sections and made up of different materials have been tested. In the following, results are shown for two types of rods: a polikristal rod (by Polimark, Young modulus $E = 2750\,\mathrm{MPa}$, density $\rho = 1250\,\mathrm{kg\,m^{-3}}$) with a cross section 20x0.8 mm, and a carbon fiber rod (by CreVeR srl, Young modulus $E = 80\,148\,\mathrm{MPa}$, density $\rho = 1620\,\mathrm{kg\,m^{-3}}$) with a cross section 20x0.45 mm.

The ECM prototype was tested as EMC-I, ECM-IIa, and ECM-IIb for different continuous evolutions of the moving clamp position repetitively crossing the catastrophe locus and providing a sequence of snapping mechanisms. Photos taken at specific stages during the experiments are displayed in Fig. 6.18. In

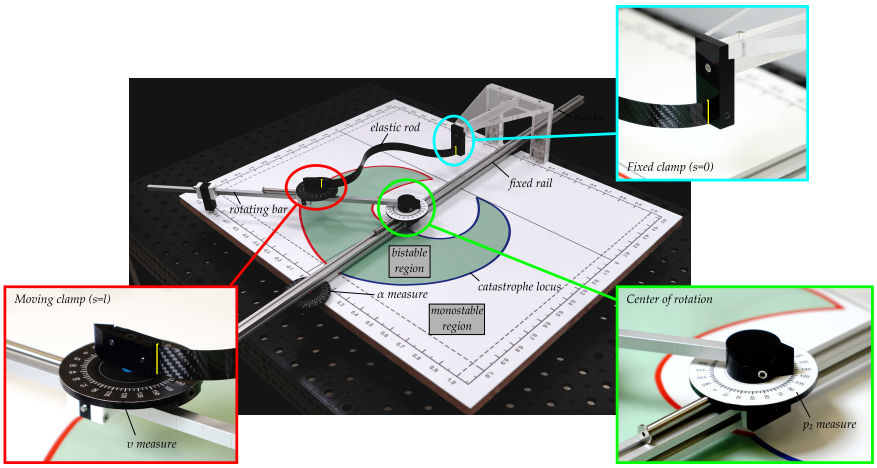

Figure 6.17: Prototype of the *elastica catastrophe machine*. A (carbon fiber) rod constrained at its two ends by a fixed clamp (inset upper right, cyan) and another clamp (inset lower left, red) which may move along a stiff bar, which, in turn, may rotate about its end pinned and possibly moving along a fixed rail (inset lower right, green). The rail is fixed to the plastic desk through two clips. The angles υ and α can be respectively measured from the black goniometers fixed on the movable clamp and the plane, while the angle p_2 can be measured from the white goniometer fixed at the rotation centre of the stiff bar.

the figure, all the stable equilibrium configurations are reported at three stages for ECM-I (with $\kappa_R = 0.5$, $\lambda_R = 0.1$, $\upsilon = 0$). The three stages are related to the position of the moving clamp, located (a) within the bistable region, (b) on the catastrophe locus, and (c) within the monostable region (from left to right in Fig. 6.18). The two equilibrium configurations related to each of the two first stages (left and central column) differ in the curvature sign at the clamps and are displayed as the superposition of two photos. The only 'surviving' configuration is displayed at stage c (right column), which can be reached through a smooth transition from the adjacent deformed configuration or through snapping from the non-adjacent deformed configuration (characterized by an opposite sign of the curvature at both clamps). The experimental results are reported for a clamp position's evolution ruled by different variations of the control parameters: (i) variation in both the control parameters p_1 and p_2 (Fig. 6.18, upper part) and (ii) variation in the control parameter p_1 at fixed value of p_2 (Fig. 6.18, lower part).

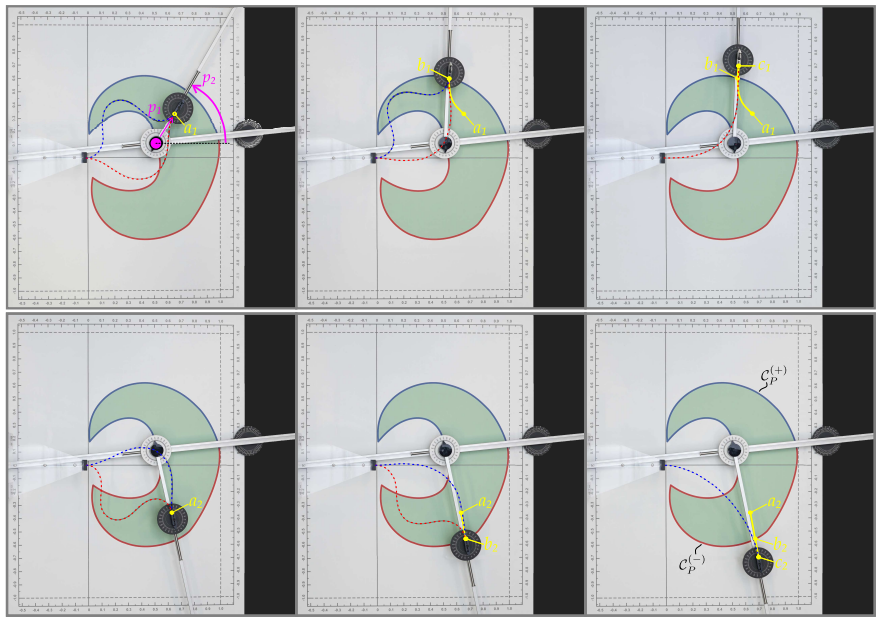

Figure 6.18: Evolution of the equilibrium configurations for a carbon fiber rod in the ECM-I (with $\kappa_R = 0.5$, $\lambda_R = 0.1$, $\upsilon = 0$) with varying the position of the moving clamp: within the bistable (green background) region (stage a, left column), on the catastrophe locus (stage b, central column), and within the monostable region (stage c, right column). The control parameters $\{p_1, p_2\}$ are represented in the upper left figure, while deformed configurations with positive/negative curvature at the fixed clamp are highlighted by blue/red dashed curve. At each stage, the clamp position at the previous stage and its path until then is highlighted. While two deformed configurations are possible for stages a and b, only one stable configuration exists at stage c.

The transition of the deformed configuration during a continuous evolution is highlighted in Figs. 6.2 (for ECM-I with $\kappa_R = 0.5$, $\lambda_R = 0.1$, $\upsilon = 0$). Four snapshots captured during the fast motion at snapping (taken with a high-speed camera *Sony PXW-FS5*, 120 fps) are superimposed in the second column of the figure (the deformed configurations are highlighted with purple dashed lines), where each two consecutive snapshots are referred to a time interval of approximately 0.15 sec. These sequences display the rod motion towards the change of curvature sign at both clamps. Further experiments performed on different ECM are reported in the section A.3 of the Appendix A.

During the experiments, photos were taken with a Sony $\alpha 9$ and videos with a high-speed camera (model *Sony PXW-FS5 4K*, 120 fps). A couple of videos showing example of use of the prototype as ECM-I and ECM-IIb are available as supplementary material.[11]

Finally, the quantitative assessment of the theoretically predicted catastrophe loci is reported in Fig. 6.19 superimposing the experimental critical points for polikristal (star markers) and carbon fiber (crosses markers) rods. The following settings are shown: (i) ECMs-I (with $\kappa_R = 0.5$, $\lambda_R = 0.1$, $\upsilon = 0$, Fig. 6.19a, and with $\kappa_R = 0.5$, $\lambda_R = 0.3$, $\upsilon = 0$, Fig. 6.19b), (ii) ECM-IIb (case $\kappa_D = \lambda_D = \alpha = 0$, $\rho = 1$, $\upsilon = \pi$, Fig. 6.19c) and (iii) ECM-IIa (case $\kappa_D = \lambda_D = \upsilon = 0$, $\rho = 0.5$, $\alpha = \pi/4$, Fig. 6.19d). The comparisons reported in the figure fully display the experimental validation of the theoretical catastrophe loci. During the tests, very small portions of the catastrophe locus were not investigated because of some unavoidable physical limitations (for instance rod's self-intersection). The accuracy in the experimental measure of the critical conditions is observed to be higher when using carbon fiber rods. The inferior accuracy in testing with polikristal rods is expected to be related to the intrinsic viscosity and weight-stiffness ratio of the material.

6.6 Conclusions

For the first time, the design and the experimental validation of a catastrophe machine has been addressed for a system made up of a continuous and elastic flexible element, extending the classical formulation for discrete systems. A theoretical framework referring to primary kinematical quantities and exploiting the concept of the universal snap surface has been introduced. Among the infinite set of *elastica catastrophe machines*, two families have been proposed and the related catastrophe locus investigated to explicitly show the features of the present model. A parametric analysis has disclosed substantial differences in the shape of the catastrophe locus in comparison with those deriving from classical catastrophe machines. In particular, the proposed machines can fulfil peculiar geometrical properties as convexity and a variable number of bifurcation points for the catastrophe loci. These meaningful characteristics may enhance the efficiency of snapping devices exploting high-energy release points otherwise unreachable. The research has been completed by the validation of the theoretical results through the physical realization of a prototype enabling experiments

[11] Movies of experiments can be found in the additional material available at `http://www.ing.unitn.it/~dalcorsf/elastica_catastrophe_machine.html`

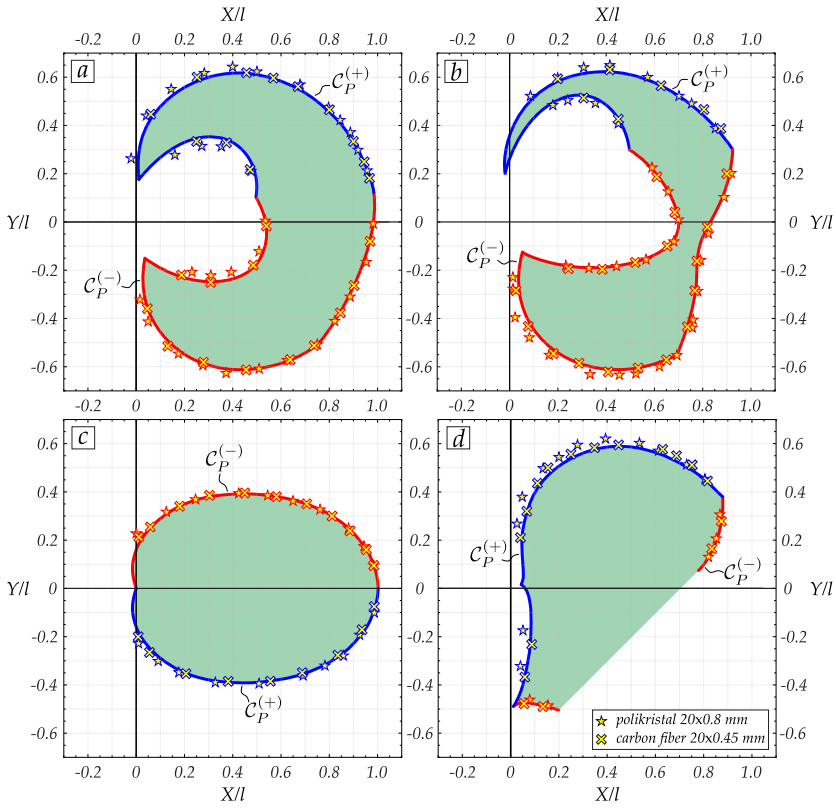

Figure 6.19: Experimental validation of the theoretically predicted catastrophe locus for ECMs-I (*a*: $\{\kappa_R = 0.5,\ \lambda_R = 0.1,\ \upsilon = 0\}$; *b*: $\{\kappa_R = 0.5,\ \lambda_R = 0.3,\ \upsilon = 0\}$), for ECM-IIb (*c*: $\{\kappa_D = \lambda_D = \alpha = 0,\ \rho = 1,\ \upsilon = \pi\}$, for ECM-IIa (*d*: $\{\kappa_D = \lambda_D = \upsilon = 0,\ \alpha = \pi/4,\ \rho = 0.5\}$). Measures from testing polikristal rod of thickness 0.8 mm (stars) and with a carbon fiber rod of thickness 0.45 mm (crosses) show an excellent agreement with the theoretical predictions.

with each of the two presented families of *elastica catastrophe machines*.

Part III

Non-holonomic constraints inducing flutter instability in structures under conservative loadings

7

Fluttering of elastic rods subject to non-holonomic constraints. Discrete model

7.1 Introduction

Flutter and divergence (in a word, 'dynamic') instabilities of elastic structures are connected to a number of counterintuitive and surprising features: (i.) they may occur in the absence of quasi-static bifurcations, and may or may not degenerate into a limit cycle, determining a so-called 'Hopf bifurcation' in the former case; (ii.) they are facilitated by a sufficiently small viscosity. Moreover, (iii.) a vanishing viscosity leads to a discontinuity in the critical load value, an oddity called 'Ziegler paradox', so that (iv.) this value may depend on the direction of limit when more than one dissipative source is present. All these features and the presence itself of flutter and divergence instabilities in structures are believed to be strictly related to the action of non-conservative loads,[1] which are considered of difficult realization.[2] Indeed, quoting Anderson

[1] Bolotin [24] writes 'The Euler method is [only] applicable if the external forces have a potential (i.e. if they are conservative forces), and in general is not applicable if they do not.'

[2] The attempt by Willems [113] of producing a tangential follower load was indicated as misleading by Huang et al. [57]. Elishakoff [43] reports that 'Bolotin felt –if my memory serves me well!– that it should be impossible to produce BeckâĂŹs column experiment via

and Done [2], a 'conservative system can not become dynamically unstable since, by definition, it has no energy source from which to supply the extra kinetic energy involved in the instability'.

It is shown in the present chapter that the last sentence is wrong, as a supply of 'extra kinetic energy' can be provided by means of a mass falling within a gravitational field, or through a release of the elastic energy initially stored in a spring and therefore:

> *We introduce two ways to induce dynamical instablities (such as flutter and divergence), Hopf bifurcation, destabilizing effect of dissipation, Ziegler paradox and directionality of it in visco-elastic mechanical structures under purely conservative loading conditions. The key to this behaviour is the use of non-holonomic constraints.*

Recently, flutter and divergence instabilities have been shown to occur in structures loaded through non-conservative forces produced with frictional devices by Bigoni and Noselli [17], realizing the tangentially follower load postulated by Ziegler [122], and by Bigoni and Misseroni [23], obtaining the fixed-line load introduced by Reut [99]. The same type of instabilities is disclosed here in structural systems subject to conservative loadings, when non-holonomic constraints are applied to the structure. More specifically, similarly to [59, 69, 85], the non-holonomic constraint is realized through two rigid (massless) cylinders

a conservative system of forces.' Anderson and Done [2] write 'Sometimes, the creation of a force like [a follower force] in the laboratory presents awkward practical problems, and the simulation of this force wherever possible by a conservative force would be very convenient. However, because of the differing nature of the fundamental properties of the conservative and non-conservative systems, the simulation could only work in a situation where the two systems behave in similar ways; that is when the conservative system is not operating in a regime of oscillatory instability. (The conservative system can not become dynamically instable since, by definition, it has no energy source from which to supply the extra kinetic energy involved in the instability).' Koiter [66] states that '[...] it appears impossible to achieve any non-conservative loading conditions in the laboratory by purely mechanical means', because 'non-conservative external loads always require an external energy source, much as a fluid flow or an interaction with electro-dynamic phenomenon'. Koiter was strongly convinced that follower forces were a sort of 'physical non-sense' (Koiter, [67], [68]), so that Singer et al. [107] write 'An example in the field of elastic stability of what Drucker referred to as *playing useless games* was presented by Koiter, in his 1985 Prandtl lecture, where he discussed the physical significance of instability due to non-conservative, purely configuration-dependent, external loads.' Several years after these negative views, Bigoni and Noselli [17] and Bigoni and Misseroni [23] respectively showed how to realize a tangentially follower force (Ziegler, 1952 [122]) and a fixed-line force (Reut, 1939 [99]) with devices involving Coulomb friction. Friction is a dissipative and follower force, in the present article we show how this force can be eliminated thus realizing a purely conservative system of load.

in *slipless contact*, one of which can freely rotate about its axis, while the other cannot. The non-existence of a potential [71, 85] characterizes both a frictional device and a non-holonomic constraint, but the latter is conservative and introduces a kinematic condition, prescribed in terms of velocity, corresponding to a (reaction) force acting on the structure and having a modulus varying in time during motion [100]. In particular, the velocity $\dot{\mathbf{r}}_C$ of the instantaneous contact point C between the two cylinders is constrained to have a null component along the axis of the freely rotating cylinder (Fig. 7.1)

$$\dot{\mathbf{r}}_C \cdot \mathbf{e} = 0, \tag{7.1}$$

where a superimposed dot represents the derivative in the time variable t and $\mathbf{e}(t)$ is the unit vector aligned parallel to the rotating cylinder's axis.

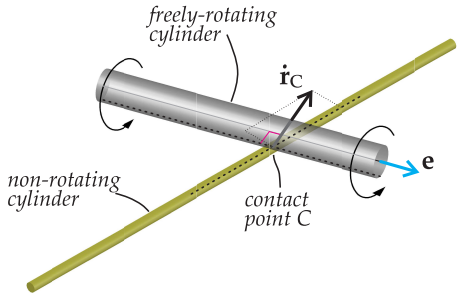

Figure 7.1: A non-holonomic constraint forbidding relative velocity $\dot{\mathbf{r}}_C$ of the instantaneous contact point C along direction $\mathbf{e}(t)$, Eq.(7.1). This constraint is obtained through slipless contact between two rigid (massless and circular) cylinders, one of which is free of rotating about its axis, while the other is not.

When properly connected to the end of a structure, for instance a viscoelastic double pendulum, the two cylinders imposing condition (7.1) may be exploited to realize either a 'skate', or a 'violin bow' constraint, the former transmitting to the structure a tangential follower reaction similar to the Ziegler's load and the latter a reaction acting on a fixed line similar to the Reut's load, but now varying in their modulus during motion. In Fig.7.2, the two proposed structures with non-holonomic constraints (which will be subject to conservative loads) are shown on the left, while the non-conservative counterparts are shown on the right. In particular, the 'skate' constraint can be realized (i.) with a freely-rotating, but non-sliding wheel, or (ii.) with a perfect skate, or (iii.) by connecting the freely-rotating cylinder to the end of the structure, with the

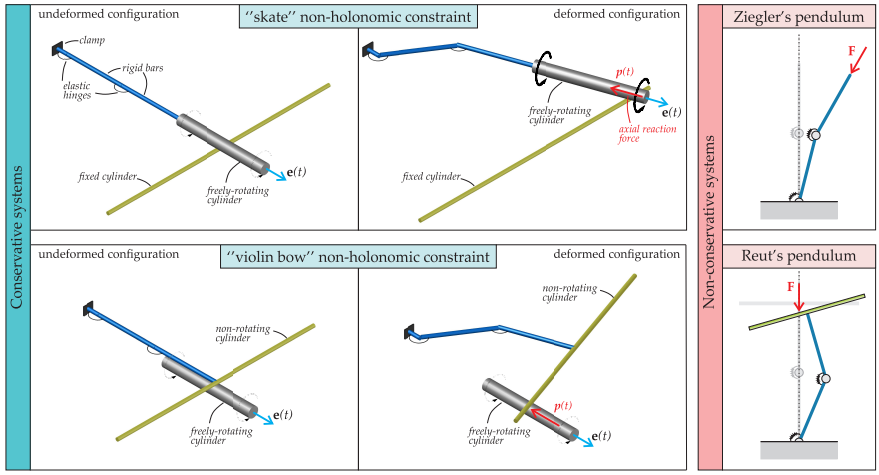

Figure 7.2: (Left) The two rigid circular cylinders (of which only one is free of rotating about its axis) in slipless contact, Fig.7.1, and connected to a double pendulum realize two types of non-holonomic constraints, called in the following 'skate' and 'violin bow' constraints, the former (the latter) transmitting to the structure a reaction tangential to the following structure (a reaction on a fixed line) similar to the force postulated by Ziegler (Reut). Right: the original version of the Ziegler's and Reut's structures, loaded through non-conservative forces.

other cylinder initially orthogonal to it and fixed in space. On the other hand, the 'violin bow' constraint can be obtained by connecting the fixed cylinder to the end of the structure, with the freely-rotating cylinder initially orthogonal to it and fixed in space, Fig.7.2.

In the present article, a generalization of the structures shown in Fig.7.2 to a system made up of N rigid bars and inclined non-holonomic constraints is proposed. Such structures are loaded in a conservative way, namely, either with a dead force F, or with a deformed linear spring (see Figs.7.4 and 7.5 and details presented in the next Section).

The non-holonomic constraint acting on these structures permits the existence of infinite equilibrium configurations [85] and of Hopf bifurcations connected to stable limit cycles in the presence of dissipation, as partially anticipated by the motion of the non-holonomic Chaplygin's sleigh on an inclined plane [85] and by the problem of shimmy instability [45, 123].

With reference to a column made up of N rigid segments and subject to a

perfectly aligned non-holonomic constraint (realized for $\beta_0 = 0$ in Figs.7.4 and 7.5), the trivial configuration becomes the unique quasi-static solution. It is shown that:

> *A visco-elastic column subject to the 'skate' or the 'violin bow' constraint and the same structure subject to non-conservative load, respectively of the Ziegler or Reut type, evidences exactly the same critical loads for flutter (Hopf bifurcation) and divergence, and the same Ziegler paradox, with the same directionality dependence occurring when multiple sources of dissipation are considered.*

More specifically, the directionality dependence in the limit of null viscosity has been analyzed by Bolotin [24] and Kirillov [62] for non-conservative systems subject to follower forces, showing that the ideal critical load for the undamped system may be recovered only for special ratios between different viscosities.

In addition, a *'viscosity-independent Ziegler paradox'* is found, in which the flutter load becomes independent of the viscosity, but cannot become higher than that evaluated for the corresponding system assumed without viscosity 'from the beginning'. In particular, such a surprising behaviour is shown to be related to the presence of two specific damping parameters acting on the proposed structures subject to non-holonomic constraints.

The stability of Hopf bifurcation, and therefore the achievement of limit cycles in the neighbourhood of the critical point, is influenced by the considered mechanical system, so that a perfect match between the mechanical behaviour of the proposed non-holonomic systems and of their non-conservative counterparts is lost, particularly when non-linearities dominate.

A typical dynamic evolution of a double visco-elastic column connected to a non-holonomic 'skate' constraint at its final end (represented as a non-sliding wheel) is shown in Fig.7.3. The structure is loaded on the left end through a dead force of constant magnitude (a conservative load), selected within the flutter region. The occurrence of flutter is shown, through evaluation of the first Lyapunov coefficient [70, 80], to correspond to a supercritical Hopf bifurcation, so that the complex motion taking place after bifurcation [sketched in parts (a)-(f) of Fig.7.3] reaches a periodic orbit in the neighbourhood of the bifurcation point (lower part of Fig.7.3). It may be interesting to note that the structure shown in Fig. 7.3 is subject to a constant force, so that it would suffer a varying acceleration in the absence of viscosity. However, *the presence of viscosity (only the rotational viscosity at the hinges is enough) is sufficient to allow the mechanical system to reach, after a transient phase, a steady motion with a constant mean velocity,* as detailed in Section 7.5.

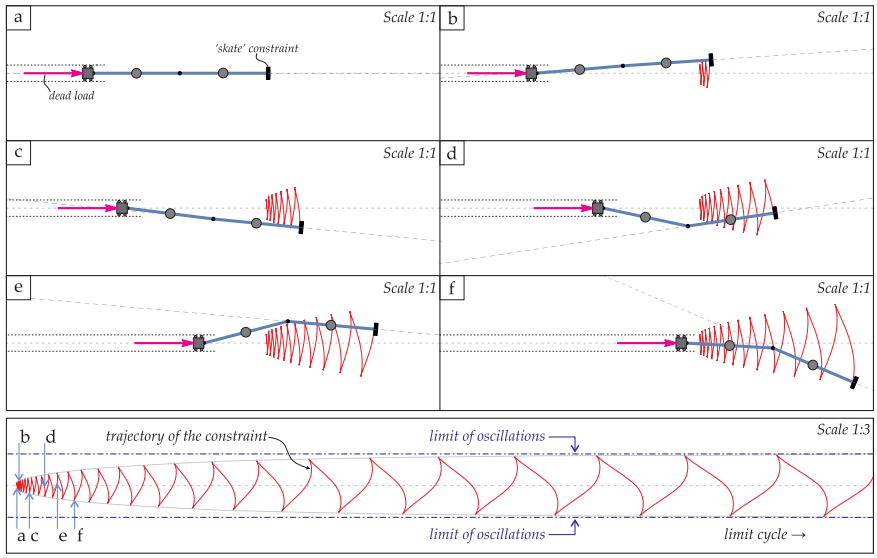

Figure 7.3: Dynamics of a visco-elastic double pendulum subject to a 'skate' non-holonomic constraint (realized with a non-sliding wheel) at one end and to a dead load at the other. When the applied dead force lies within the flutter region, a complex motion is generated (parts a-f), leading the structure to reach a limit cycle. Such behaviour is visible in the trajectory of the structure's end shown in the lower part, exhibiting sharp corners induced by the non-holonomic constraint. Note that instability permits motion to a structure that would be at rest in the trivial configuration as the friction parallel to the wheel axis is assumed to be infinite (non-slip condition).

The presented results provide a new key to theoretically interpret and experimentally realize dynamic instabilities until now believed to be possible only as connected to non-conservative loads. Several applications in energy harvesting and soft robotics can be envisaged, but two in particular merit a special attention, namely, frictional contact and locomotion. In particular, our results show how a micromechanism might act at a sliding surface between two solids to reduce friction through instability. Moreover, it will be shown that imposing *rotations* (instead than applying forces) to the structures that will be analyzed, a motion is induced, which means that our results have implications in the problem of *limbless locomotion*. The presented results have been submitted to an international journal [35].

7.2 Elastic columns with non-holonomic constraints

7.2.1 The column and its loadings

The motion in the X–Y plane is analyzed for an elastic column of total length L, discretized as a chain of N rigid bars of length l_i ($i = 1, ..., N$, so that $L = \sum_{i=1}^{N} l_i$), connected to each other with visco-elastic hinges of elastic stiffness k_i and viscous parameter c_i, Fig.7.4. It is also worth to underline that no self-contact phenomena are taken into account in the present analysis.

The first hinge is connected to a rigid block which may only slide along the X-direction and is loaded in one of the following *conservative* ways :

- **A - elastic device**: the rigid block is loaded by imposing a compressive displacement Δ at the left end of a linear spring of stiffness K, whose right end is attached to the rigid block (Fig.7.5);
- **B - dead load**: the rigid block is subject to a force F (for instance produced by gravity) of fixed direction parallel to the X-axis (Fig.7.5).

Denoting with $\Theta_i(t)$ the anti-clockwise inclination of the i-th bar with respect to X-axis and with $X_0(t)$ the position of the sliding block along the X-axis (Fig.7.5), the configuration of the column at generic instant of time t is fully described through the generalized coordinates vector $\mathbf{q}(t)$ with the following $N + 1$ components

$$\mathbf{q}(t) = [\Theta_1(t), \quad ..., \quad \Theta_i(t), \quad ..., \quad \Theta_N(t), \quad X_0(t)]. \tag{7.2}$$

The undeformed trivial configuration of the system ($\mathbf{q}(t) = \underline{0}$) is given by all the rigid bars aligned with the X-axis ($\Theta_i = 0$, $i = 1, ..., N$) and $X_0 = 0$ (thus neglecting horizontal rigid motions).

The mass of the column is discretized in N masses m_i, one for each rigid bar and located at a distance $d_i \leq l_i$ from the i-th hinge, so that the position in time for each mass m_i is given by the coordinates $X_i(t)$ and $Y_i(t)$, namely,

$$X_i = X_0 + d_i \cos\Theta_i + \sum_{j=1}^{i-1} l_j \cos\Theta_j, \qquad Y_i(t) = d_i \sin\Theta_i + \sum_{j=1}^{i-1} l_j \sin\Theta_j. \tag{7.3}$$

Moreover, the sliding block is considered to have mass M_X. Generic deformed configurations are reported in Fig.7.5 for the two considered structures subject to conservative loads and to the non-holonomic 'skate' and 'violin bow' constraints (detailed in the next section).

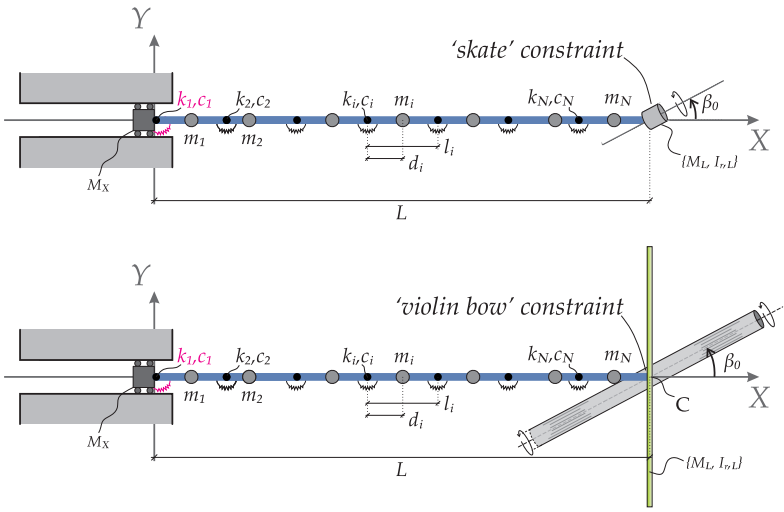

Figure 7.4: Two undeformed structures differing only in the non-holonomic constraint applied at the right end. Each structure is discretized as a chain made up of N rigid bars of mass m_i and connected to each other through rotational visco-elastic springs (with viscosity parameter c_i and stiffness k_i, $i = 1, ..., N$). The first rigid bar on the left ($i = 1$) is connected to a rigid block sliding along the $X-$axis. The two non-holonomic constraints are inclined at an angle β_0 with respect to the last bar. These constraints are a 'skate' (upper part) or a 'violin bow' (lower part) and constrain the velocity to have a null component in the direction orthogonal to the skate (realized for instance with a non-sliding wheel) or parallel to a non-sliding freely rotating cylinder (which is in turn in contact with the 'violin bow'). In the case $\beta_0 = 0$, the two structures reduce to the non-holonomic counterpart of the non-conservative Ziegler and Reut columns, respectively. Note that the last rigid element of the column reported in the lower part is 'T–shaped', so that the freely-rotating cylinder can continue to transmit a force to the structure during motion.

7.2.2 The non-holonomic constraints

Two types of non-holonomic constraints (both sketched in Figs.7.4 and 7.5) are assumed to be acting at the end of the elastic column, singled out by the coordinates

$$X_L = X_0 + \sum_{i=1}^{N} l_i \cos\Theta_i, \qquad Y_L = \sum_{i=1}^{N} l_i \sin\Theta_i. \tag{7.4}$$

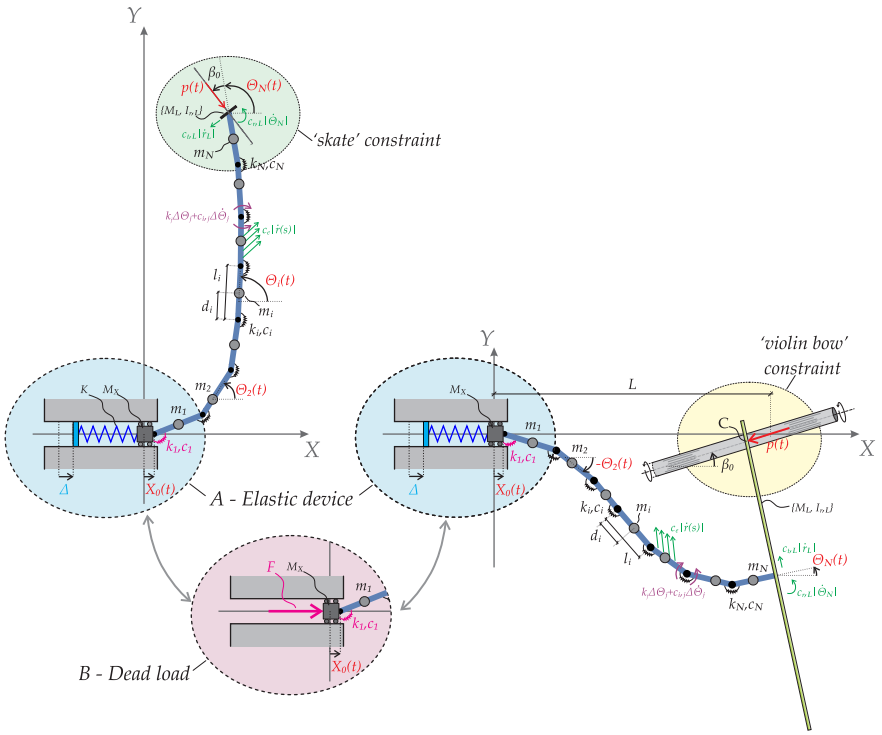

Figure 7.5: Deformed configuration for the elastic column subject to the non-holonomic 'skate' (left) and 'violin bow' (right) constraints. The *conservative* load is applied via (A) a prescribed compressive displacement Δ at the left end of a linear elastic spring of stiffness K attached to the rigid block or through (B) a dead load F. The particular condition $\beta_0 = 0$ leads to uniqueness of the trivial quasi-static solution.

Each one of these two constraints generates an unknown reaction $p(t)$ (positive when compressive), through the imposition of the linear kinematic restriction on the velocity, Eq.(7.1), which can be expressed in terms of generalized velocities $\dot{q}_k$ $(k = 1, ..., N+1)$ as

$$\sum_{k=1}^{N+1} a_k(\mathbf{q},\, \beta_0)\dot{q}_k = 0, \tag{7.5}$$

where $a_k(\mathbf{q}, \beta_0)$ is the vector of coefficients expressing the specific type of non-holonomic constraint ('skate' or 'violin bow'). Taking into account the reaction force p, the problem is characterized by $N+2$ unknowns. Each of the non-holonomic constraints is characterized by a mass M_L and a rotational moment of inertia $I_{r,L}$, both applied at the end of the final bar ($i = N$).

As sketched in Figs.7.4 and 7.5, the two non-holonomic constraints can be obtained from condition (7.1) as follows.

- A **'skate' type constraint** applied with inclination β_0, representing the angle between the 'skate' and the last bar of the column; the skate can freely rotate about its vertical axis and is constrained to slide parallely to its cutting edge, so that the only non-null component of the velocity is parallel to it:

$$\begin{bmatrix}\dot{X}_L & \dot{Y}_L\end{bmatrix} \cdot \begin{bmatrix}\cos(\Theta_N + \beta_0)\\ \sin(\Theta_N + \beta_0)\end{bmatrix} = \\ \dot{X}_0 \cos(\Theta_N + \beta_0) + \sum_{i=1}^{N} l_i \dot{\Theta}_i \sin(\Theta_N + \beta_0 - \Theta_i) = 0. \tag{7.6}$$

  The vector of the non-holonomic coefficients $\mathbf{a}(\mathbf{q},\ \beta_0)$ shown in the Eq.(7.5) for this type of constraint is therefore given by

$$\mathbf{a}(\mathbf{q},\ \beta_0) = \Big[l_1 \sin(\Theta_N + \beta_0 - \Theta_1), \ldots, l_{N-1} \sin(\Theta_N + \beta_0 - \Theta_{N-1}), \\ l_N \sin(\beta_0),\ \cos(\Theta_N + \beta_0) \Big]. \tag{7.7}$$

  Finally, the reaction force $p(t)$ is always orthogonal to the sliding direction of the 'skate'.

- A **'violin bow' type constraint** applied with inclination β_0, representing the angle between the freely-rotating cylinder and the $X-$axis; the 'T-shaped' rigid element (attached to the N-th rigid bar of the column) can freely rotate about the contact point with the cylinder and can translate orthogonally to the cylinder's axis, such that the velocity component parallel to it must vanish. The coordinates X_C and Y_C of the contact point C (see Fig.7.5) between the 'T-shaped' rigid element and the freely rotating cylinder is singled out by the coordinates

$$X_C = X_L + \zeta \tan\Theta_N, \qquad Y_C = Y_L - \zeta, \quad \text{where} \quad \zeta = \frac{Y_L + (L - X_L)\tan\beta_0}{1 + \tan\beta_0\ \tan\Theta_N},$$

(7.8)

so that its velocity can be obtained through the Poisson's theorem as

$$\begin{bmatrix}\dot{X}_C\\ \dot{Y}_C\end{bmatrix} = \begin{bmatrix}\dot{X}_L\\ \dot{Y}_L\end{bmatrix} + \dot{\Theta}_N \mathbf{e}_3 \times \begin{bmatrix}X_C - X_L\\ Y_C - Y_L\end{bmatrix} = \begin{bmatrix}\dot{X}_L + \dot{\Theta}_N \zeta\\ \dot{Y}_L + \dot{\Theta}_N \zeta \tan\Theta_N,\end{bmatrix}, \quad (7.9)$$

where $\mathbf{e}_3$ is the unit vector orthogonal to the $X - Y$ plane. The non-holonomic constraint is therefore expressed by the vanishing of the component of the velocity along the cylinder's axis at the point C, namely

$$\left(\dot{X}_L + \dot{\Theta}_N\, \zeta\right) \cos\beta_0 + \left(\dot{Y}_L + \dot{\Theta}_N\, \zeta \tan\Theta_N\right) \sin\beta_0 = 0 \quad (7.10)$$

which, recalling Eq.(7.4), can be rewritten as

$$\dot{X}_0 \cos\beta_0 + \dot{\Theta}_N \sin\beta_0 L + \sum_{i=1}^{N-1} l_i \sin(\beta_0 - \Theta_i)(\dot{\Theta}_i - \dot{\Theta}_N) = 0. \quad (7.11)$$

Therefore, the vector $\mathbf{a}(\mathbf{q},\, \beta_0)$, representing the non-holonomic constraint as introduced in the Eq.(7.5), is given by

$$\mathbf{a}(\mathbf{q},\, \beta_0) = \Bigg[l_1 \sin(\beta_0 - \Theta_1),\ \ldots,\ l_{N-1} \sin(\beta_0 - \Theta_{N-1}),\\ l_N \left(\sin\beta_0 L - \sum_{i=1}^{N-1} l_i \sin(\beta_0 - \Theta_i) \right),\ \cos\beta_0 \Bigg]. \quad (7.12)$$

Finally, the reaction force $p(t)$ is always directed along the axis of the freely-rotating cylinder.

7.2.3 Energies and dissipation

The total potential energy $\mathcal{V}(\mathbf{q}) = \mathcal{E}(\mathbf{q}) - \mathcal{W}(\mathbf{q})$, equal to the difference between the elastic energy $\mathcal{E}$ and the work $\mathcal{W}$ done by the external loads, is given for the considered structural systems by

$$\mathcal{V}(\mathbf{q}) = \Xi(\mathbf{q}) + \frac{1}{2} k_1 \Theta_1^2 + \frac{1}{2} \sum_{i=2}^{N} k_i \left(\Theta_i - \Theta_{i-1}\right)^2, \quad (7.13)$$

where (note that Δ is independent of time)

$$\Xi(\mathbf{q}) = \begin{cases} \frac{1}{2}K\left[X_0 - \Delta\right]^2 & \text{for elastic device A,} \\ -F\,X_0 & \text{for dead loading B.} \end{cases} \tag{7.14}$$

The expression for the kinetic energy $\mathcal{T}$ is the same for both systems A and B and given by

$$\mathcal{T}(\mathbf{q},\dot{\mathbf{q}}) = \frac{1}{2}M_X \dot{X_0}^{\,2} + \frac{1}{2}M_L\left(\dot{X}_L^2 + \dot{Y}_L^2\right) + \frac{1}{2}\sum_{i=1}^{N} m_i\left(\dot{X}_i^2 + \dot{Y}_i^2\right) + \frac{1}{2}I_{r,L}\dot{\Theta}_N^2. \tag{7.15}$$

Dissipative effects are taken into account from different viscous sources through the following Rayleigh dissipation function

$$\begin{aligned} \mathcal{F}_d(\dot{\mathbf{q}}) =& \frac{1}{2}c_e\sum_{i=1}^{N}\int_0^{l_i}(\dot{X}_i(s_i)^2 + \dot{Y}_i(s_i)^2)\mathrm{d}s + \frac{1}{2}\,c_{t,L}(\dot{X}_L^2 + \dot{Y}_L^2) + \frac{1}{2}\,c_{r,L}\dot{\Theta}_N^2 + \\ &+ \frac{1}{2}\,c_i\,\dot{\Theta}_1^2 + \frac{1}{2}c_i\sum_{i=2}^{N}(\dot{\Theta}_i - \dot{\Theta}_{i-1})^2, \end{aligned} \tag{7.16}$$

where $X_i(s_i)$ and $Y_i(s_i)$ are coordinates of the generic point located at the curvilinear coordinate s_i along the i-th bar, which can be written as

$$X_i(s_i) = X_0 + s_i\cos\Theta_i + \sum_{j=1}^{i-1} l_j\cos\Theta_j, \qquad Y_i(s_i) = s_i\sin\Theta_i + \sum_{j=1}^{i-1} l_j\sin\Theta_j. \tag{7.17}$$

Each (non-negative) linear damping coefficient c_e, c_i, $c_{t,L}$, and $c_{r,L}$ introduced in Eq.(7.16) is related to a specific viscous source:

- *external translational damping* c_e, providing a distributed viscous force along each bar, which may model the air drag during motion;
- *internal rotational damping* c_i, modelling a viscous dissipation induced by torsion at the hinges (and identical for all the hinges);

- *translational damping of the non-holonomic constraint* $c_{t,L}$, modelling the effects of the air drag generated by the device realizing the constraint;

- *rotational damping of the non-holonomic constraint* $c_{r,L}$, modelling the damping generated by pivoting movements at the contact of the device realizing the constraints, for instance the rotational resistance of a wheel on a plane.

The presence of these four viscous sources allows to analyze their different influences on the stability of the structure, an influence which is often stronger than one might expect [111]. In the quasi-static case, the velocity is null and so the dissipation function $\mathcal{F}_d$ vanishes.

It is remarked that both the loading systems A and B are conservative, so that the supply of energy is provided for System A by the elastic energy initially stored in the spring through the compressive displacement Δ and for system B by the potential energy of the dead load F. In the stability evaluations concerning the loading system A, perturbations on the distance Δ will not be considered. Finally, functionals (7.13), (7.15) and (7.16) are independent of the choice of the non-holonomic constraint [which acts on the system via Eq.(7.5)] and of its inclination β_0.

7.2.4 Equations of motion

The equations of motion for the visco-elastic column subject to non-holonomic constraints can be derived from the d'Alembert-Lagrange equation [85] expressed for virtual displacements δq_k as

$$\sum_{k=1}^{N+1} \left(\frac{d}{dt} \frac{\partial \mathcal{T}(\mathbf{q}, \dot{\mathbf{q}})}{\partial \dot{q}_k} - \frac{\partial \mathcal{T}(\mathbf{q}, \dot{\mathbf{q}})}{\partial q_k} - Q_k(\mathbf{q}, \dot{\mathbf{q}}) + p(t)\, a_k(\mathbf{q}, \beta_0) \right) \delta q_k = 0, \quad (7.18)$$

where the generalized forces Q_k are given by

$$Q_k(\mathbf{q}, \dot{\mathbf{q}}) = -\frac{\partial \mathcal{V}(\mathbf{q})}{\partial q_k} - \frac{\partial \mathcal{F}_d(\dot{\mathbf{q}})}{\partial \dot{q}_k}, \qquad k = 1, ..., N+1, \quad (7.19)$$

and account for the dissipative forces obtained from the dissipation function $\mathcal{F}_d$, Eq.(7.16), and for the presence of the external energy supply, contained in the total potential energy $\mathcal{V}$ in terms of parameter Δ for the elastic device A, or force F for the dead load B, Eq.(7.14).

In the d'Alembert-Lagrange equation (7.18), the unknown reaction force $p(t)$ transmitted to the column by the non-holonomic constraint plays the role of a Lagrangian multiplier enforcing condition (7.5).

Invoking arbitrariness of the virtual displacements δq_k, the d'Alembert-Lagrange equation (7.18) yields

$$\frac{d}{dt}\frac{\partial \mathcal{T}(\mathbf{q},\dot{\mathbf{q}})}{\partial \dot{q}_k} - \frac{\partial \mathcal{T}(\mathbf{q},\dot{\mathbf{q}})}{\partial q_k} - Q_k(\mathbf{q},\dot{\mathbf{q}}) + p(t)\, a_k(\mathbf{q},\beta_0) = 0, \qquad \forall\ k = 1,2,...,N+1, \tag{7.20}$$

which, together with the non-holonomic constraint, Eq.(7.5), provides a system of $N+2$ equations in $N+2$ unknowns, namely, the $N+1$ generalized coordinates $q_k(t)$ and the non-holonomic constraint reaction $p(t)$.

The equations of motion (7.20) are obtained through the Lagrange formalism, where in particular the existence of non-holonomic conditions on the variations of the generalized coordinates is introduced by means of the Lagrange multiplier method. Following Greenwood [52] and Neimark and Fufaev [85], an alternative formulation based on the so-called *quasi-coordinates* can also be exploited, thus leading to a new version of the system (7.20) known in literature as *Boltzmann-Hamel equations*. In particular, this latter formulation allows to eliminate the reaction forces from the analysis, as the non-holonomic constraints can be introduced by means of some mathematical tricks.

In Appendix B, the governing equations for a non-holonomic system in quasi-coordinates are shown for the general case and then particularised in the case of the non-holonomic discrete chain considered in the present Chapter. Moreover, a numerical simulation is performed in order to compare the solutions obtained through the Lagrange equations (7.20) and the aforementioned Boltzmann-Hamel equations, showing an excellent agreement between their results.

7.2.5 Quasi-static response of the column with non-holonomic constraints

Under quasi-static conditions ($\dot{\mathbf{q}}(t) = \underline{0}$) the kinetic energy and the dissipation are null ($\mathcal{T} = \mathcal{F}_d = 0$, so that $Q_k = \partial \mathcal{V}/\partial q_k$) and the equations of motion (7.20) simplify to the $N+1$ equilibrium equations

$$\frac{\partial \mathcal{V}(\mathbf{q}^{\mathrm{QS}})}{\partial q_k^{\mathrm{QS}}} + p^{\mathrm{QS}}\, a_k(\mathbf{q}^{\mathrm{QS}},\beta_0) = 0, \qquad \forall\ k = 1,2,...,N+1, \tag{7.21}$$

to be solved for the unknown reaction force p^{QS} at prescribed values of the spring displacement Δ or dead load F. In particular, the total potential energy (7.13) is a polynomial of degree 2 in the generalized coordinates, so that Eq.(7.21) can be rewritten as

$$\begin{cases} \mathbb{K}_{ik}^{(N)} q_k^{\text{QS}} + p^{\text{QS}}\, a_k(\mathbf{q}^{\text{QS}},\, \beta_0) = 0 & \forall\ i,k = 1,2,...,N \\ \dfrac{\partial\, \Xi(\mathbf{q}^{\text{QS}})}{\partial X_0} + p^{\text{QS}}\, a_{N+1}(\mathbf{q}^{\text{QS}},\, \beta_0) = 0 \end{cases} \tag{7.22}$$

where the dependence of the vector a_k on the considered quasi-static solution q_k^{QS} and on the inclination angle β_0 is highlighted and

$$\frac{\partial\, \Xi(\mathbf{q})}{\partial X_0} = \begin{cases} K\,[X_0(t) - \Delta] & \text{elastic device A,} \\ -F & \text{dead load B,} \end{cases} \tag{7.23}$$

while the $N \times N$ stiffness matrix $\mathbb{K}^{(N)}$

$$\mathbb{K}^{(N)} = \begin{bmatrix} k_1 + k_2 & -k_2 & & & & & \\ -k_2 & k_2 + k_3 & -k_3 & & & & \\ & -k_3 & k_3 + k_4 & \ddots & & & \\ & & \ddots & \ddots & -k_{N-1} & & \\ & & & -k_{N-1} & k_{N-1} + k_N & -k_N & \\ & & & & -k_N & k_N \end{bmatrix}, \tag{7.24}$$

is tridiagonal, symmetric and positive-definite. Moreover, it is also independent of the type of non-holonomic constraint applied at the end of the structure and of the loading condition. It can be proven (this delicate proof is deferred to Appendix C.1) that the determinant of matrix (7.24) is given by the product of the N rotational stiffness parameters k_j, so that

$$\det \mathbb{K}^{(N)} = \prod_{j=1}^{N} k_j. \tag{7.25}$$

Note that the loading condition in the specific case of a straight column with $\beta_0 = 0$ is given by the $(N+1)$–th equation of system (7.22) where $a_{N+1}(\mathbf{0},\, 0) = 1$, yielding

$$p^{\text{QS}} = \begin{cases} K\,[\Delta - X_0] & \text{elastic device A,} \\ F & \text{dead load B.} \end{cases} \tag{7.26}$$

Under the quasi-static assumption the velocities are null and the non-holonomic constraint (7.1) is automatically satisfied but the equilibrium equations (7.21), which still depend on the non-holonomic constraint through the coefficients a_k, contain $N + 2$ unknowns. As a consequence, the value of one of the generalized coordinates q_k^{QS} or the reaction force p^{QS} can be selected within a one-dimensional *manifold of equilibrium states* [85] and the remaining unknowns solved using Eqs.(7.21). In other words, the columns admit an infinite set of quasi-static solutions.

As examples of multiple solutions, non-trivial equilibrium configurations are shown in Fig.7.6 for two columns made up of 7 rigid bars and loaded through the horizontal spring (loading condition A). The two columns differ in the dimensionless parameter $KL\Delta/k$, being equal to 0.1 (above) or 1.5 (below), and in the inclination of the 'skate', $\beta_0 = \pi/4$ (above) or $\pi/2$ (below). The two columns are loaded by a force $K(X_0^{\text{QS}} - \Delta)$, which is prescribed through the application of both Δ and $X_0^{\text{QS}} = 0$.

The straight configuration (with null bar rotations, $\Theta_k^{\text{QS}} = 0$) can be a solution for the equilibrium equations (7.21) for both non-holonomic 'skate' and 'violin' bow constraints, at every inclination β_0, in the following cases:

- When $\beta_0 \neq 0$, the straight configuration is a solution whenever the reaction force at the non-holonomic constraint is null ($p^{\text{QS}} = 0$), corresponding to an unstressed column and which occurs when $X_0^{\text{QS}} = \Delta$ for the elastic device A or when $F = 0$ for every value of X_0^{QS} in the case of the dead loading B.

  This statement can be proven by considering that the first N equations of the system (7.22) at $\mathbf{q}^{\text{QS}} = 0$ are characterized by a non-null vector $a_k(\mathbf{0}, \beta_0) \neq 0$, so that the trivial configuration corresponds to a null value of the reaction force $p^{\text{QS}} = 0$, and consequently to null external load $\partial\,\Xi/\partial X_0 = 0$ (namely $X_0^{\text{QS}} = \Delta$ for the device A or $F = 0$ for the device B), as shown by the $(N + 1)$-th equation of the system (7.22);

- When $\beta_0 = 0$, the straight configuration is the unique equilibrium solution admitted by the system (7.21). The proof of this statement can be demonstrated with equilibrium consideration; a formal proof is difficult and deferred to Appendix C.2.

  In contrast with the case $\beta_0 \neq 0$, now the reaction force provided by the non-holonomic constraint p^{QS} may be different from zero, so that the elastic chain in its straight configuration may be *axially-stressed* as the

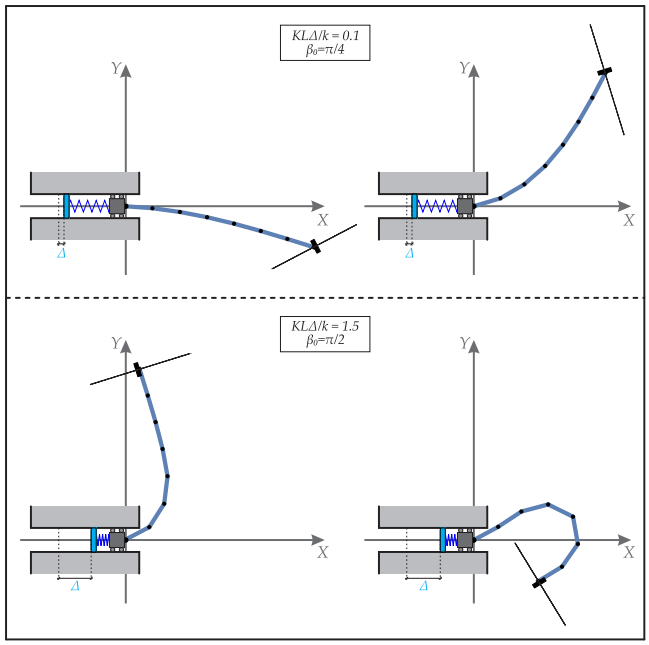

Figure 7.6: Examples of non-unique (and non-trivial) equilibrium configurations for a column made up of 7 rigid bars and subject to the non-holonomic 'skate' constraint. Equilibrium has been solved by fixing both $X_0^{\rm QS} = 0$ and Δ, in particular, two pairs of non-unique solutions are reported for $KL\Delta/k = 0.1$ and $\beta_0 = \pi/4$ (upper part), and $KL\Delta/k = 1.5$ and $\beta_0 = \pi/2$ (lower part).

result of the imposition of F or Δ (when $X_0^{\rm QS} \neq \Delta$).[3]

In the next Section, the stability is analyzed for a generic configuration of the elastic column subject to both loading conditions A and B and both the non-holonomic constraints. The condition $\beta_0 = 0$ finally restricts the analysis to the trivial configuration $\mathbf{q}^{\rm QS} = \underline{0}$ only, where rigid body motions are neglected by setting $X_0^{\rm QS} = 0$.

[3]The fact that the straight configuration for $\beta_0 = 0$ can be arbitrarily stressed is obvious. Formally, since $a_k(\mathbf{0}, 0) = 0$ but $a_{N+1}(\mathbf{0}, 0) \neq 0$ for both the non-holonomic constraints, the first N equations of system (7.22) particularized for $\mathbf{q}^{\rm QS} = 0$ are always satisfied for any value of the reaction force $p^{\rm QS}$, which is given by $\partial\,\Xi/\partial X_0$ and a_{N+1} through the $(N+1)$-th equation in (7.22).

7.3 Linearized dynamics and stability of the column with non-holonomic systems

A first-order expansion of Eqs.(7.20) about a generic quasi-static solution for both the generalized coordinates $\mathbf{q}^{\text{QS}}$ and the Lagrangian multiplier p^{QS}, therefore satisfying Eqs.(7.21), can be performed by assuming

$$\mathbf{q}(t) = \mathbf{q}^{\text{QS}} + \epsilon\hat{\mathbf{q}}(t), \quad p(t) = p^{\text{QS}} + \epsilon\hat{p}(t), \tag{7.27}$$

where ϵ is an arbitrarily small real parameter and $\{\hat{\mathbf{q}}(t),\, \hat{p}(t)\}$ is the set denoting the perturbation fields. From the quasi-static nature of the configuration $\mathbf{q}^{\text{QS}}$, it follows that

$$\dot{\mathbf{q}}(t) = \epsilon\dot{\hat{\mathbf{q}}}(t), \quad \ddot{\mathbf{q}}(t) = \epsilon\ddot{\hat{\mathbf{q}}}(t). \tag{7.28}$$

A Taylor series expansion of the Eqs.(7.20) about $\epsilon = 0$ yields the following linearized equations of motion for the perturbed fields, which, removing the superscript '$\widehat{\ }$', are expressed by

$$\begin{cases} \mathbf{M}\ddot{\mathbf{q}} + \mathbf{C}\dot{\mathbf{q}} + (\mathbf{K} + p^{\text{QS}}\,\mathbf{G})\,\mathbf{q} + p\,\mathbf{w} = 0, \\ \mathbf{w}\cdot\dot{\mathbf{q}} = 0, \end{cases} \tag{7.29}$$

as functions of the time-dependent 'load' perturbation p. $\mathbf{M}$, $\mathbf{C}$, and $\mathbf{K}$ are, respectively, the mass, damping and elastic stiffness (symmetric and positive definite) matrices of dimension $N+1$, while the geometric stiffness matrix $\mathbf{G}$ is non-symmetric as influenced by the presence of the non-holonomic constraint reaction p^{QS}. The vector $\mathbf{w}$ is related to the linearized version of the non-holonomic constraint (7.6) or (7.11) for the 'skate' and 'violin bow', respectively. A comparison with Eqs.(7.22) and (7.24) shows that the stiffness matrices $\mathbf{K}$ and $\mathbb{K}^{(N)}$ are related through the second derivative of the function Ξ with respect to the generalized coordinate X_0 [see Eq.(7.13)] as

$$\mathbf{K} = \left[\begin{array}{c|c} \mathbb{K}^{(N)} & \mathbf{0} \\ \hline \mathbf{0} & \dfrac{\partial^2\,\Xi(\mathbf{q})}{\partial X_0^2} \end{array}\right] \quad \text{where} \quad \frac{\partial^2\,\Xi(\mathbf{q})}{\partial X_0^2} = \begin{cases} K & \text{for elastic device A,} \\ 0 & \text{for dead load B.} \end{cases} \tag{7.30}$$

The geometric stiffness matrix $\mathbf{G}$ is the gradient of vector $\mathbf{a}(\mathbf{q},\, \beta_0)$ calculated with respect to the generalized coordinates vector $\mathbf{q}$ and evaluated at the generic

quasi-static solution $\mathbf{q}^{\mathrm{QS}}$

$$\mathbf{G} = \left. \frac{\partial\, \mathbf{a}(\mathbf{q},\, \beta_0)}{\partial\, \mathbf{q}} \right|_{\mathbf{q}=\mathbf{q}^{\mathrm{QS}}}, \tag{7.31}$$

and is strictly related to the choice of the non-holonomic constraint through coefficients a_k given by Eqs.(7.7) and (7.12) for the 'skate' or 'violin bow' constraint, respectively. Following the same notations adopted for $\mathbf{K}$, the matrix $\mathbf{G}$ can be represented as

$$\mathbf{G} = \left[\begin{array}{c|c} \mathbb{G}^{(N)} & \mathbf{0} \\ \hline \mathbf{g} & 0 \end{array} \right], \tag{7.32}$$

where

$$\mathbf{g} = \begin{cases} [0,\, 0,\, ...,\, 0,\, -\sin\left(\Theta_N^{\mathrm{QS}} + \beta_0\right)] & \text{for the skate constraint,} \\ \mathbf{0} & \text{for the violin bow constraint.} \end{cases} \tag{7.33}$$

In the previous equations, $\mathbb{G}^{(N)}$ is a $N \times N$ matrix and $\mathbf{g}$ is a N-component vector. The expressions for the $N \times N$ *non-symmetric and singular* geometric stiffness matrices for the 'skate' and 'violin bow' constraints, respectively denoted by $\mathbb{G}_S^{(N)}$ and $\mathbb{G}_V^{(N)}$, are

$$\mathbb{G}_S^{(N)} = \begin{bmatrix} -\gamma_{S,1} & & & & \gamma_{S,1} \\ & -\gamma_{S,2} & & & \gamma_{S,2} \\ & & \ddots & & \vdots \\ & & & -\gamma_{S,N-1} & \gamma_{S,N-1} \\ & & & & 0 \end{bmatrix}, \quad \mathbb{G}_V^{(N)} = \begin{bmatrix} -\gamma_{V,1} & & & & \\ & -\gamma_{V,2} & & & \\ & & \ddots & & \\ & & & -\gamma_{V,N-1} & \\ \gamma_{V,1} & \gamma_{V,2} & \cdots & \gamma_{V,N-1} & 0 \end{bmatrix} \tag{7.34}$$

where the only non-vanishing components lie on the diagonal and on the N-th column (N-th row) for the 'skate' ('violin bow') constraint. The coefficients $\gamma_{S,i}$ and $\gamma_{V,i}$ are given by

$$\gamma_{S,i} = l_i \cos\left(\Theta_N^{\mathrm{QS}} + \beta_0 - \Theta_i^{\mathrm{QS}}\right), \qquad \gamma_{V,i} = l_i \cos\left(\beta_0 - \Theta_i^{\mathrm{QS}}\right), \qquad \forall i = 1, ..., N-1,$$

while $\gamma_{S,N} = \gamma_{V,N} = 0$.

A property that will be useful later, holding for every (null or non-null) value of β_0, is the following (the proof is deferred to Appendix C.3)

$$\det\left(\mathbb{K}^{(N)} + p^{\mathrm{QS}} \mathbb{G}^{(N)}\right) = \det\left(\mathbb{K}^{(N)}\right) = \prod_{j=1}^{N} k_j. \tag{7.35}$$

The symmetric and positive-definite mass and damping matrices defined in Eq.(7.29) can be rewritten as

$$\mathbf{M} = \left[\begin{array}{c|c} \mathbb{M}^{(N)} & \mathbf{m} \\ \hline \mathbf{m}^{\intercal} & \hat{m} \end{array}\right], \qquad \mathbf{C} = \left[\begin{array}{c|c} \mathbb{C}^{(N)} & \mathbf{c} \\ \hline \mathbf{c}^{\intercal} & \hat{c} \end{array}\right] \tag{7.36}$$

where $\mathbb{M}^{(N)}$ and $\mathbb{C}^{(N)}$ are $N \times N$ matrices, $\mathbf{m}$ and $\mathbf{c}$ are $N-$component column vectors, both dependent on vector $\mathbf{q}^{\text{QS}}$, and $\hat{m}$ and $\hat{c}$ are positive real numbers depending on the mass and damping coefficients acting along the X_0 generalized coordinate. Moreover, the superscript ' $^{\intercal}$ ' denotes the transpose operator. It is obvious that $\mathbf{M}$ and $\mathbf{C}$ are independent of the choice of both the non-holonomic constraint (skate or violin bow) and the loading condition (elastic device A or dead load B).

Finally, the $N-$component column vector $\mathbf{w}$ expressing the non-holonomic constraint, linearized about a generic quasi-static solution $\mathbf{q}^{\text{QS}}$, is given by

$$\mathbf{w} = \begin{cases} [l_1 \sin\left(\Theta_N^{\text{QS}} + \beta_0 - \Theta_1^{\text{QS}}\right), l_2 \sin\left(\Theta_N^{\text{QS}} + \beta_0 - \Theta_2^{\text{QS}}\right), ..., l_N \sin\left(\beta_0\right), \cos\left(\Theta_N^{\text{QS}} + \beta_0\right)]^{\intercal} & \text{skate,} \\ [l_1 \sin\left(\beta_0 - \Theta_1^{\text{QS}}\right), ..., l_{N-1} \sin\left(\beta_0 - \Theta_{N-1}^{\text{QS}}\right), L \sin\beta_0 - \sum_{i=1}^{N-1} l_i \sin\left(\beta_0 - \Theta_i^{\text{QS}}\right), \cos\beta_0]^{\intercal} & \text{violin bow.} \end{cases} \tag{7.37}$$

For convenience, the vector $\mathbf{w}$ is rewritten in the following form

$$\mathbf{w} = [\mathbf{w}^{(N)}, w_{N+1}]^{\intercal} \tag{7.38}$$

where $\mathbf{w}^{(N)}$ is the vector collecting the first N components of $\mathbf{w}$.

Assuming time-harmonic perturbations $q_k = A_k e^{\omega t}$ and $p = A_p e^{\omega t}$, the differential system (7.29) reduces to

$$\left[\begin{array}{c|c} \mathbf{M}\omega^2 + \mathbf{C}\omega + \mathbf{K} + p^{\text{QS}}\,\mathbf{G} & \mathbf{w} \\ \hline \omega \mathbf{w}^{\intercal} & 0 \end{array}\right] \mathbf{A} = 0, \tag{7.39}$$

where vector $\mathbf{A}$ collects the unknown $N+2$ amplitudes

$$\mathbf{A} = [A_1,\ A_2,\ ....,\ A_N,\ A_{N+1},\ A_p]^{\intercal}, \tag{7.40}$$

and the singularity of the matrix defined by Eq.(7.39) provides the value of ω for which non-null perturbations $\mathbf{A} \neq 0$ exist.

Because all the coefficients in the last row of the matrix in Eq.(7.39) are linear in ω, the trivial eigenvalue $\omega = 0$ is always a solution for the problem.

According to Neimark and Fufaev [85], this peculiarity is usual in non-holonomic systems, so that the trivial eigenvalue is omitted in order to perform the stability analysis of the configurations belonging to the manifold of equilibrium states. The stability is lost when the determinant of the relevant matrix in Eq.(7.39) vanishes,

$$\det \left[\begin{array}{c|c} \mathbf{M}\omega^2 + \mathbf{C}\omega + \mathbf{K} + p^{\mathrm{QS}}\,\mathbf{G} & \mathbf{w} \\ \hline \mathbf{w}^{\mathsf{T}} & 0 \end{array} \right] = 0, \tag{7.41}$$

a condition depending on the non-holonomic reaction p^{QS}, related through the $(N+1)$–th equation of the system (7.22) to the displacement Δ (loading condition A) or the dead load F (loading condition B).

Due to the fact that the last row and column of the matrix appearing in Eq.(7.41) are independent of the eigenvalue ω, the vanishing of its determinant provides a polynomial equation in ω of order $m = 2N$, with real coefficients ρ_j $(j = 0, ..., m)$ in the form

$$\rho_0\,\omega^m + \rho_1\,\omega^{m-1} + \ ... \ + \rho_{m-1}\,\omega + \rho_m = 0, \tag{7.42}$$

where in the specific case of null damping forces ($\mathbf{C} = \mathbf{0}$) all the terms ρ_j with odd index j are equal to zero.

Two equivalent techniques can be exploited to assess the stability of configurations belonging to the manifold of equilibrium states. The first technique is based on the direct evaluation of the eigenvalues ω, so that a configuration is stable if the real part of every eigenvalue ω is non-positive. The other technique is the Routh-Hurwitz criterion, which, for $\rho_0 > 0$ in Eq.(7.42), relates stability to the positiveness of every determinant D_i of the square matrix $\mathbf{H}_i$ $(i = 1, ..., m)$ defined as the upper-left corner square matrix of rank i of the Hurwitz matrix $\mathbf{H}_m$, defined as

$$\mathbf{H}_m = \begin{bmatrix} \rho_1 & \rho_0 & 0 & \cdots & & & & & 0 \\ \rho_3 & \rho_2 & \rho_1 & \rho_0 & 0 & \cdots & & & 0 \\ \rho_5 & \rho_4 & \rho_3 & \rho_2 & \rho_1 & \rho_0 & 0 & \cdots & 0 \\ \cdots & & & & & & & & \cdots \\ \cdots & & & & & & & & \cdots \\ \cdots & & & & & & & & \cdots \\ \rho_{2m-1} & \rho_{2m-2} & \cdots & & & & & & \rho_m \end{bmatrix}. \tag{7.43}$$

It is worth noting that the direct inspection of the eigenvalues is of difficult use, as analytical expressions for eigenvalues are hardly obtained for systems with many degrees of freedom N.

The determinant condition (7.41) is strongly influenced by both the choice of the non-holonomic constraint, through the geometric stiffness matrix $\mathbf{G}$ and vector $\mathbf{w}$, and the choice of the loading conditions, through the term Ξ appearing in the stiffness matrix (7.30). Therefore, critical loads for $\beta_0 \neq 0$ depend on the quasi-static configuration under consideration, on the type of non-holonomic constraint, and on the loading conditions.

7.3.1 Buckling

Buckling is a quasi-static bifurcation of the equilibrium path driven by a slow increase in either Δ or F, providing a slow variation in the non-holonomic reaction p^{QS}. Therefore, buckling can be determined by setting the inertial terms to zero, $\omega = 0$, in Eq.(7.42), thus imposing the condition $\rho_m = 0$. Once p_{cr}^{QS} is evaluated, Δ_{cr} or F_{cr} follow from the last equation of the system (7.22).

The buckling conditions $\rho_m = 0$ for a generic quasi-static configuration is expanded in the Appendix C.4 for both the non-holonomic constraints and both the loading conditions at the initial end. An interesting result is found, namely, that *buckling loads are excluded for all possible trivial or non-trivial solutions for the 'violin bow' constraint with prescribed force* F, case (B), a result which is not obvious for $\beta_0 \neq 0$.

For $\beta_0 = 0$ and for all considered non-holonomic constraints and loading conditions, the trivial configuration ($\mathbf{q}^{\text{QS}} = \mathbf{0}$) is the unique quasi-static solution (see Appendix C.2). Such statement leads to the obvious conclusion that buckling loads are absent, which is confirmed by the fact that the components of the vector $\mathbf{w}$ always reduce to

$$\mathbf{w}^{(N)} = \mathbf{0}, \qquad w_{N+1} = 1, \tag{7.44}$$

so that the buckling condition $\rho_m = 0$ becomes

$$\det\left(\mathbb{K}^{(N)} + p^{\text{QS}}\mathbb{G}^{(N)}\right) = 0, \tag{7.45}$$

which is never satisfied as condition (7.35) holds true.

Buckling will not be further considered in the following and the stability analysis will be restricted to the straight configuration of the column with $\beta_0 = 0$.

7.3.2 Flutter and divergence instabilities for the straight column with $\beta_0 = 0$

For every specific chain composed by N rigid bars, it is proven now that all the critical loads (for flutter and divergence instability) are the same for both considered non-holonomic constraints (of the 'skate' or 'violin bow' type) in the case $\beta_0 = 0$. This statement can be proven by considering the Eq.(7.34), where in the case $\beta_0 = 0$ the coefficients γ_i for both 'skate' and 'violin bow' constraints become the same $\gamma_{S,i} = \gamma_{V,i} = l_i$, so that

$$\mathbf{G}_S = \mathbf{G}_V^{\mathsf{T}} \qquad \text{and} \qquad \mathbb{G}_S^{(N)} = \mathbb{G}_V^{(N)\mathsf{T}}, \tag{7.46}$$

and therefore the geometric stiffness matrix for the 'skate' constraint is equal to the transpose of the geometric stiffness matrix for the 'violin bow' constraint. Due to the Eqs.(7.44), the determinant condition (7.41) reduces to

$$\det\left[\mathbb{M}^{(N)}\omega^2 + \mathbb{C}^{(N)}\omega + \mathbb{K}^{(N)} + p^{\text{QS}}\mathbb{G}^{(N)}\right] = 0, \tag{7.47}$$

where the symmetric matrices $\mathbb{M}^{(N)}$, $\mathbb{C}^{(N)}$ and $\mathbb{K}^{(N)}$ do not depend on the type of non-holonomic constraint. The property of the determinant $\det\mathbf{B} = \det\mathbf{B}^{\mathsf{T}}$ closes the proof. In fact, the critical loads for both 'skate' and 'violin bow' constraints in the case $\beta_0 = 0$ are the same because the related characteristic polynomial is provided by the same determinant condition (7.47).

In the following, the analysis will be restricted to a double pendulum $N = 2$.

7.4 The double pendulum subject to the skate and violin bow constraints

The geometric and inertial properties are considered for simplicity coincident for the two bars, so that $\{l_i, m_i, d_i\} = \{l, m, d\}$ $(i = 1, 2)$ and $L = 2l$, with a total mass $M = 2m$. By introducing the characteristic time $T = L\sqrt{M/k}$ of the structure and the stiffness $k = k_2$ for the rotational springs, the following dimensionless quantities can be introduced

$$\chi = \frac{X_0}{L}, \quad \tilde{\Delta} = \frac{\Delta}{L}, \quad \tilde{d} = \frac{d}{l}, \quad \tilde{l} = \frac{l}{L} = \frac{1}{2}, \quad \tau = \frac{t}{T}, \quad \tilde{p} = \frac{pL}{k}, \quad \tilde{F} = \frac{FL}{k},$$
$$\tilde{M}_X = \frac{M_X}{M}, \quad \tilde{M}_L = \frac{M_L}{M}, \quad \tilde{m} = \frac{m}{M} = \frac{1}{2}, \quad \tilde{I}_{r,L} = \frac{I_{r,L}}{L^2 M}, \quad \tilde{K} = \frac{KL^2}{k},$$
$$\tilde{k}_1 = \frac{k_1}{k}, \quad \tilde{c}_e = \frac{c_e L^2}{\sqrt{kM}}, \quad \tilde{c}_{t,L} = \frac{c_{t,L} L}{\sqrt{kM}}, \quad \tilde{c}_{r,L} = \frac{c_{r,L}}{L\sqrt{kM}}, \quad \tilde{c}_i = \frac{c_i}{L\sqrt{kM}},$$

(7.48)

Henceforth, the superimposed dot ‘ ˙ ’ denotes the derivative with respect to the dimensionless time τ. For both cases of the ‘skate’ and ‘violin bow’ non-holonomic constraints, the non-linear equations of motion (7.20) are given by

$$\begin{aligned}
&\frac{\tilde{c}_e}{8}\left(\frac{4}{3}\,\dot{\Theta}_1+\frac{1}{2}\,\dot{\Theta}_2\cos(\Theta_1-\Theta_2)-3\sin\Theta_1\dot{\chi}\right)+\tilde{c}_i\left(2\dot{\Theta}_1-\dot{\Theta}_2\right)+\\
&+\frac{\tilde{M}_L}{4}\left(\ddot{\Theta}_1+\ddot{\Theta}_2\cos(\Theta_1-\Theta_2)+\dot{\Theta}_2^2\sin(\Theta_1-\Theta_2)-2\sin\Theta_1\ddot{\chi}\right)+\\
&+\frac{\tilde{c}_{t,L}}{4}\left(\dot{\Theta}_1+\dot{\Theta}_2\cos(\Theta_1-\Theta_2)-2\sin\Theta_1\dot{\chi}\right)+\tilde{p}\,\tilde{a}_1+(1+\tilde{k}_1)\Theta_1+\\
&-\Theta_2+\frac{1}{8}\Big[4\tilde{d}^2\ddot{\Theta}_1+\tilde{d}\,\ddot{\Theta}_2\cos(\Theta_1-\Theta_2)+\tilde{d}\,\dot{\Theta}_2^2\sin(\Theta_1-\Theta_2)+\\
&\qquad-2\ddot{\chi}\left(\tilde{d}\sin\Theta_1+\sin\Theta_2\right)+\ddot{\Theta}_1-2\,\dot{\Theta}_2\cos\Theta_2\dot{\chi}\Big]=0
\end{aligned}\tag{7.49a}$$

$$\begin{aligned}
&\frac{\tilde{c}_e}{8}\left(\frac{1}{2}\,\dot{\Theta}_1\cos(\Theta_1-\Theta_2)+\frac{1}{3}\,\dot{\Theta}_2-\sin\Theta_2\dot{\chi}\right)+\tilde{I}_{r,L}\ddot{\Theta}_2+\tilde{c}_{r,L}\,\dot{\Theta}_2+\\
&+\tilde{c}_i\left(\dot{\Theta}_2-\dot{\Theta}_1\right)+\frac{\tilde{c}_{t,L}}{4}\left(\dot{\Theta}_1\cos(\Theta_1-\Theta_2)+\dot{\Theta}_2-\frac{1}{2}\sin\Theta_2\dot{\chi}\right)+\\
&+\frac{1}{8}\Big(\tilde{d}^2\ddot{\Theta}_2+\tilde{d}\,\ddot{\Theta}_1\cos(\Theta_1-\Theta_2)-\tilde{d}\,\dot{\Theta}_1^2\sin(\Theta_1-\Theta_2)-2\tilde{d}\sin\Theta_2\ddot{\chi}+\\
&\qquad+2\,\dot{\Theta}_1\cos\Theta_2\dot{\chi}\Big)+\tilde{p}\,\tilde{a}_2+\Theta_2-\Theta_1+\\
&+\frac{\tilde{M}_L}{4}\left(\ddot{\Theta}_1\cos(\Theta_1-\Theta_2)-\dot{\Theta}_1^2\sin(\Theta_1-\Theta_2)+\ddot{\Theta}_2-2\sin\Theta_2\ddot{\chi}\right)=0
\end{aligned}\tag{7.49b}$$

$$\begin{aligned}
&\frac{\tilde{c}_e}{8}\left(8\dot{\chi}-3\,\dot{\Theta}_1\sin\Theta_1-\dot{\Theta}_2\sin\Theta_2\right)+\frac{\tilde{c}_{t,L}}{2}\left(2\dot{\chi}-\dot{\Theta}_1\sin\Theta_1-\dot{\Theta}_2\sin\Theta_2\right)+\\
&+\frac{1}{4}\Big(4\ddot{\chi}-\tilde{d}\,\ddot{\Theta}_1\sin\Theta_1-\tilde{d}\,\dot{\Theta}_1^2\cos\Theta_1-\tilde{d}\,\ddot{\Theta}_2\sin\Theta_2-\tilde{d}\,\dot{\Theta}_2^2\cos\Theta_2+\\
&\qquad-\ddot{\Theta}_1\sin\Theta_2-\dot{\Theta}_1\dot{\Theta}_2\cos\Theta_2\Big)+\tilde{M}_X\ddot{\chi}+\tilde{p}\,\tilde{a}_3+\frac{\partial\tilde{\Xi}}{\partial\chi}+\\
&+\frac{\tilde{M}_L}{2}\left(2\ddot{\chi}-\ddot{\Theta}_1\sin\Theta_1-\dot{\Theta}_1^2\cos\Theta_1-\ddot{\Theta}_2\sin\Theta_2-\dot{\Theta}_2^2\cos\Theta_2\right)=0
\end{aligned}\tag{7.49c}$$

$$\tilde{a}_1\,\dot{\Theta}_1+\tilde{a}_2\,\dot{\Theta}_2+\tilde{a}_3\dot{\chi}=0\tag{7.49d}$$

where $\{\chi,\, \Theta_1,\, \Theta_2\}$ are functions of the dimensionless time τ and

$$\tilde{\Xi} = \begin{cases} \dfrac{1}{2}\tilde{K}\left[\chi(\tau) - \tilde{\Delta}\right]^2 & \text{for elastic device A,} \\ -\tilde{F}\,\chi(\tau) & \text{for dead loading B.} \end{cases} \tag{7.50}$$

The dimensionless non-holonomic constraint (7.49d) is expressed through coefficients $\tilde{a}_i$ representing the dimensionless coefficients of Eqs.(7.7) and (7.12). In particular, the coefficients $\tilde{a}_i$ are expressed

- for the 'skate' non-holonomic constraint by

$$\tilde{a}_1 = \frac{1}{2}\,\sin(\beta_0 - \Theta_1 + \Theta_2), \quad \tilde{a}_2 = \frac{1}{2}\,\sin(\beta_0), \quad \tilde{a}_3 = \cos(\beta_0 + \Theta_2), \tag{7.51}$$

- for the 'violin bow' non-holonomic constraint by

$$\tilde{a}_1 = \frac{1}{2}\,\sin(\beta_0 - \Theta_1), \quad \tilde{a}_2 = \sin(\beta_0) - \frac{1}{2}\,\sin(\beta_0 - \Theta_1), \quad \tilde{a}_3 = \cos(\beta_0). \tag{7.52}$$

Henceforth, the analysis is restricted to the case when $\beta_0 = 0$, corresponding to the non-holonomic counterpart of the Ziegler and Reut double pendulums. The mass $\mathbf{M}$, damping $\mathbf{C}$ and elastic stiffness $\mathbf{K}$ matrices in Eqs.(7.29) can easily be evaluated for the trivial equilibrium solution $\mathbf{q}^{\mathrm{QS}} = \mathbf{0}$ and $\beta_0 = 0$. Their dimensionless counterparts can be written as

$$\tilde{\mathbf{M}}^{(2)} = \begin{bmatrix} \frac{1}{8}\left(\tilde{d}^2 + 1 + 2\tilde{M}_L\right) & \frac{1}{8}(\tilde{d} + 2\tilde{M}_L) & 0 \\ \frac{1}{8}(\tilde{d} + 2\tilde{M}_L) & \tilde{I}_{r,L} + \frac{1}{8}(\tilde{d}^2 + 2\tilde{M}_L) & 0 \\ 0 & 0 & \tilde{M}_X + 1 + \tilde{M}_L \end{bmatrix}, \tag{7.53}$$

$$\tilde{\mathbf{C}}^{(2)} = \begin{bmatrix} 2\,\tilde{c}_i + \frac{1}{4}\tilde{c}_{t,L} + \frac{1}{6}\,\tilde{c}_e & \frac{1}{4}\tilde{c}_{t,L} + \frac{1}{16}\tilde{c}_e - \tilde{c}_i & 0 \\ \frac{1}{4}\tilde{c}_{t,L} + \frac{1}{16}\tilde{c}_e - \tilde{c}_i & \tilde{c}_{r,L} + \tilde{c}_i + \frac{1}{4}\tilde{c}_{t,L} + \frac{1}{24}\tilde{c}_e & 0 \\ 0 & 0 & \tilde{c}_{t,L} + \tilde{c}_e \end{bmatrix}, \tag{7.54}$$

$$\tilde{\mathbf{K}}^{(2)} = \begin{bmatrix} 1 + \tilde{k}_1 & -1 & 0 \\ -1 & 1 & 0 \\ 0 & 0 & \dfrac{\partial^2 \tilde{\Xi}}{\partial\, \chi^2} \end{bmatrix}. \tag{7.55}$$

The difference between the 'skate' and the 'violin bow' non-holonomic constraints lies in their respective geometric stiffness matrices $\mathbf{G}_S$ and $\mathbf{G}_V$, which for $\beta_0 = 0$ are one the transpose of the other, Eq.(7.46). The dimensionless expression for these matrices is

$$\tilde{\mathbf{G}}_S^{(2)} = \tilde{\mathbf{G}}_V^{(2)\intercal} = \frac{1}{2}\begin{bmatrix} -1 & 1 & 0 \\ 0 & 0 & 0 \\ 0 & 0 & 0 \end{bmatrix}. \tag{7.56}$$

The characteristic polynomial defining the stability properties for both the 'skate' and 'violin bow' non-holonomic constraints, Eq.(7.47), for a system of two rods ($N = 2$) with $\beta_0 = 0$ becomes

$$\det\left[\tilde{\mathbb{M}}^{(2)}\Omega^2 + \tilde{\mathbb{C}}^{(2)}\Omega + \tilde{\mathbb{K}}^{(2)} + \tilde{p}^{\mathrm{QS}}\tilde{\mathbb{G}}^{(2)}\right] = 0, \tag{7.57}$$

where $\Omega = \omega T$ is the dimensionless eigenvalue and $\tilde{\mathbb{M}}^{(2)}$, $\tilde{\mathbb{C}}^{(2)}$, $\tilde{\mathbb{K}}^{(2)}$ and $\tilde{\mathbb{G}}^{(2)}$ are the 2×2 upper-left corner partitions of matrices (7.53), (7.54), (7.55) and (7.56), respectively.

As a consequence of the determinant property $\det \mathbf{B} = \det \mathbf{B}^{\intercal}$ (holding for every matrix $\mathbf{B}$), the same loads leading to the vanishing of the determinant (7.57), which include the critical loads, are obtained for both non-holonomic constraints of the 'skate' and 'violin bow' type.

Note that the dimensionless mass $\tilde{M}_X$ of the sliding block does not appear in the mass matrix $\tilde{\mathbb{M}}^{(2)}$, Eq.(7.53), so that it does not influence the value of the critical loads.

Eq.(7.57) leads to a 4^{th}-order polynomial equation in the eigenvalues Ω,

$$\rho_0\,\Omega^4 + \rho_1\Omega^3 + \rho_2\Omega^2 + \rho_3\Omega + \rho_4 = 0, \tag{7.58}$$

where coefficients ρ_i ($i = 0, ..., 4$) can be evaluated through the Cayley-Hamilton theorem as (details are deferred to Appendix C.5, while the explicit expression for ρ_i is included in the Appendix C.8)

$$\begin{aligned} \rho_0 &= \det \tilde{\mathbb{M}}^{(2)}, \qquad \rho_1 = \mathrm{tr}\tilde{\mathbb{M}}^{(2)}\,\mathrm{tr}\tilde{\mathbb{C}}^{(2)} - \mathrm{tr}\left[\tilde{\mathbb{M}}^{(2)}\tilde{\mathbb{C}}^{(2)}\right], \\ \rho_2 &= \mathrm{tr}\tilde{\mathbb{M}}^{(2)}\,\mathrm{tr}\tilde{\mathbb{K}}^{(2)}_{\mathrm{Tot}} - \mathrm{tr}\left[\tilde{\mathbb{M}}^{(2)}\tilde{\mathbb{K}}^{(2)}_{\mathrm{Tot}}\right] + \det \tilde{\mathbb{C}}^{(2)}, \\ \rho_3 &= \mathrm{tr}\tilde{\mathbb{C}}^{(2)}\,\mathrm{tr}\tilde{\mathbb{K}}^{(2)}_{\mathrm{Tot}} - \mathrm{tr}\left[\tilde{\mathbb{C}}^{(2)}\tilde{\mathbb{K}}^{(2)}_{\mathrm{Tot}}\right], \qquad \rho_4 = \det \tilde{\mathbb{K}}^{(2)}_{\mathrm{Tot}} = \det \tilde{\mathbb{K}}^{(2)}, \end{aligned} \tag{7.59}$$

where 'tr' defines the trace operator and the following definition has been used

$$\tilde{\mathbb{K}}^{(2)}_{\text{Tot}} = \tilde{\mathbb{K}}^{(2)} + \tilde{p}^{\text{QS}}\tilde{\mathbb{G}}^{(2)}. \tag{7.60}$$

The coefficients ρ_0 and ρ_4 are assumed to be always greater than zero, a condition expressing a non-vanishing determinant for the matrices $\tilde{\mathbb{M}}^{(2)}$ and $\tilde{\mathbb{K}}^{(2)}$, respectively. Such assumption is automatically satisfied when $\tilde{k}_1 > 0$ and at least one of the positive input parameters $\tilde{d}$, $\tilde{M}_L$ and $\tilde{I}_{r,L}$ is different from zero. Moreover, the coefficient ρ_1 is always greater than zero when at least one viscosity parameter takes non null value.

The eigenvalues Ω of the characteristic equation(7.58) can be therefore analyzed as functions of the reaction $\tilde{p}^{\text{QS}}$ of the non-holonomic constraint.

It is important to remark that the polynomial (7.58), obtained for the viscoelastic double pendulum subject to the non-holonomic constraint, coincides with the corresponding equation holding when a non-conservative load (of the Ziegler or Reut type) is applied, so that all the instability thresholds –flutter and divergence– are shared between the non-conservative systems and their conservative counterparts subject to non-holonomic constraint. Therefore,

the presence of non-holonomic constraints may induce flutter and divergence instabilities in mechanical systems subject to conservative loads, a circumstance usually considered impossible.

Flutter instability. According to Ziegler [123], the Hurwitz matrix $\mathbf{H}_4$ for $N = 2$, Eq.(7.43) with $m = 4$, is equal to

$$\mathbf{H}_4 = \begin{bmatrix} \rho_1 & \rho_0 & 0 & 0 \\ \rho_3 & \rho_2 & \rho_1 & \rho_0 \\ 0 & \rho_4 & \rho_3 & \rho_2 \\ 0 & 0 & 0 & \rho_4 \end{bmatrix}. \tag{7.61}$$

Because ρ_1 and ρ_4 are strictly positive, D_1 is also always positive while $D_4 = \rho_4 D_3$ is not fundamental, so that the stability condition is given by the two following inequalities

$$\begin{cases} D_2 = \rho_1\,\rho_2 - \rho_0\,\rho_3 > 0, \\ D_3 = (\rho_1\,\rho_2 - \rho_0\,\rho_3)\;\rho_3 - \rho_1^2\,\rho_4 > 0. \end{cases} \tag{7.62}$$

The imposition of the two inequalities (7.62) is equivalent to impose only that related to the determinant D_3 subject to the condition of positive values for the

coefficients ρ_2 and ρ_3. Therefore, the critical flutter load $\tilde{p}^{\text{QS}}_{\text{flu}}$ is given by the condition

$$(\rho_1\,\rho_2 - \rho_0\,\rho_3)\;\rho_3 - \rho_1^2\,\rho_4 = 0, \qquad \rho_2 > 0, \qquad \rho_3 > 0. \tag{7.63}$$

Divergence instability. By considering the real part of the eigenvalues Ω, the bifurcation for divergence can be obtained as the roots of a fifth-order polynomial in the non-dimensional reaction $\tilde{p}^{\text{QS}}$ (see Appendix C.6 for details) given by

$$\begin{aligned}\left[27\left(\rho_1^2\,\rho_4 + \rho_0\,\rho_3^2\right) - 9\,\rho_2(8\,\rho_0\,\rho_4 + \rho_1\,\rho_3) + 2\,\rho_2^3\right]^2 + \\ - 4\left(\rho_2^2 - 3\,\rho_1\,\rho_3 + 12\,\rho_0\,\rho_4\right)^3 = 0.\end{aligned} \tag{7.64}$$

The real roots $\tilde{p}^{\text{QS}}$ of Eq.(7.64) can be exploited to investigate the divergence load corresponding to vanishing imaginary parts of the eigenvalues. The divergence load $\tilde{p}^{\text{QS}}_{\text{div}}$ can be therefore analytically computed as a root of Eq.(7.64) corresponding to at least a couple of positive eigenvalues Ω. Moreover, the Eq.(7.64) is a quintic in the non-holonomic constraint reaction for the general case and a quartic in the special case $\tilde{c}_e = \tilde{c}_{t,L} = \tilde{c}_{r,L} = 0$ and $\tilde{c}_i \neq 0$.

7.4.1 Critical load for flutter and divergence in the ideal case of null dissipation

In the ideal case of null dissipation, when all the damping forces are absent ($\tilde{\mathbb{C}}^{(2)} = \mathbf{0}$) 'from the beginning', the eigenvalues Ω can be evaluated as

$$\Omega = \pm\sqrt{\frac{\pm\sqrt{\left(\text{tr}\tilde{\mathbb{M}}^{(2)}\,\text{tr}\tilde{\mathbb{K}}^{(2)}_{\text{Tot}} - \text{tr}\left[\tilde{\mathbb{M}}^{(2)}\tilde{\mathbb{K}}^{(2)}_{\text{Tot}}\right]\right)^2 - 4\,\det\tilde{\mathbb{M}}^{(2)}\,\det\tilde{\mathbb{K}}^{(2)}} - \left(\text{tr}\tilde{\mathbb{M}}^{(2)}\,\text{tr}\tilde{\mathbb{K}}^{(2)}_{\text{Tot}} - \text{tr}\left[\tilde{\mathbb{M}}^{(2)}\tilde{\mathbb{K}}^{(2)}_{\text{Tot}}\right]\right)}{2\,\det\tilde{\mathbb{M}}^{(2)}}}, \tag{7.65}$$

so that the critical load $\tilde{p}^{\text{QS}}$ for flutter and divergence instabilities can be computed through the Eq.(7.64) in the case $\rho_1 = \rho_3 = 0$ (for which the Eq.(7.63) is automatically satisfied)

$$\left(\text{tr}\tilde{\mathbb{M}}^{(2)}\,\text{tr}\tilde{\mathbb{K}}^{(2)}_{\text{Tot}} - \text{tr}\left[\tilde{\mathbb{M}}^{(2)}\tilde{\mathbb{K}}^{(2)}_{\text{Tot}}\right]\right)^2 - 4\,\det\tilde{\mathbb{M}}^{(2)}\,\det\tilde{\mathbb{K}}^{(2)} = 0, \tag{7.66}$$

The instability loads corresponding to flutter $\tilde{p}^{\rm QS}_{\rm flu}$ and divergence $\tilde{p}^{\rm QS}_{\rm div}$ can be written introducing the following notation

$$\tilde{p}^{\rm QS}_{\rm flu} = \mathcal{P}_0(\boldsymbol{\xi}), \qquad \tilde{p}^{\rm QS}_{\rm div} = \mathcal{D}_0(\boldsymbol{\xi}), \tag{7.67}$$

where the subscript '0' denotes the absence of damping coefficients within the mathematical model from the beginning and $\boldsymbol{\xi} = [\tilde{d},\, \tilde{M}_L,\, \tilde{I}_{r,L},\, \tilde{k}_1]$ is the vector collecting all the input parameters describing the magnitude and distribution of mass and stiffness of the system. Using the above notation, it follows that

$$\begin{aligned}\left\{ \begin{array}{c} \mathcal{P}_0(\boldsymbol{\xi}) \\ \mathcal{D}_0(\boldsymbol{\xi}) \end{array} \right\} = & 2\frac{\tilde{d}^2(\tilde{k}_1+2)+2\tilde{d}+8\tilde{I}_{r,L}(\tilde{k}_1+1)+2(\tilde{k}_1+4)\tilde{M}_L+1}{\tilde{d}^2+\tilde{d}+8\tilde{I}_{r,L}+4\tilde{M}_L} \\ & \mp 4\frac{\sqrt{\tilde{k}_1\left(\tilde{d}^4+8\tilde{d}^2\tilde{I}_{r,L}+2\tilde{M}_L(2(\tilde{d}-1)\tilde{d}+8\tilde{I}_{r,L}+1)+8\tilde{I}_{r,L}\right)}}{\tilde{d}^2+\tilde{d}+8\tilde{I}_{r,L}+4\tilde{M}_L}.\end{aligned} \tag{7.68}$$

The eigenvalues Ω for the ideal undamped double pendulum are investigated in Fig. 7.7. Assuming $\tilde{d} = 1/2$, $\tilde{M}_L = 15$, $\tilde{I}_{r,L} = 15$, $\tilde{k}_1 = 50$, or equivalently $\hat{\boldsymbol{\xi}} = [1/2,\, 15,\, 15,\, 50]$, two different representations for the real and imaginary parts of Ω are shown as functions of the dimensionless load $\tilde{p}^{\rm QS}$. The figure shows the presence of two critical loads corresponding to flutter (complex conjugate eigenvalues) and divergence (real eigenvalues) instabilities, which can be calculated from Eq.(7.68) as

$$\begin{aligned}\mathcal{P}_0(\hat{\boldsymbol{\xi}}) &= \frac{20}{723}\left(3102-\sqrt{120482}\right) \approx 76.2073, \\ \mathcal{D}_0(\hat{\boldsymbol{\xi}}) &= \frac{20}{723}\left(3102+\sqrt{120482}\right) \approx 95.4109.\end{aligned} \tag{7.69}$$

7.4.2 The damped case and the Ziegler destabilization paradox for structures subject to non-holonomic constraints

The introduction of viscous dissipative forces in the model of structures subject to non-conservative forces leads to the well-known 'Ziegler destabilization paradox' [62],[63],[64],[122]. The paradox consists in a substantial (and unexpected) decrease in the critical load for flutter instability when a small damping

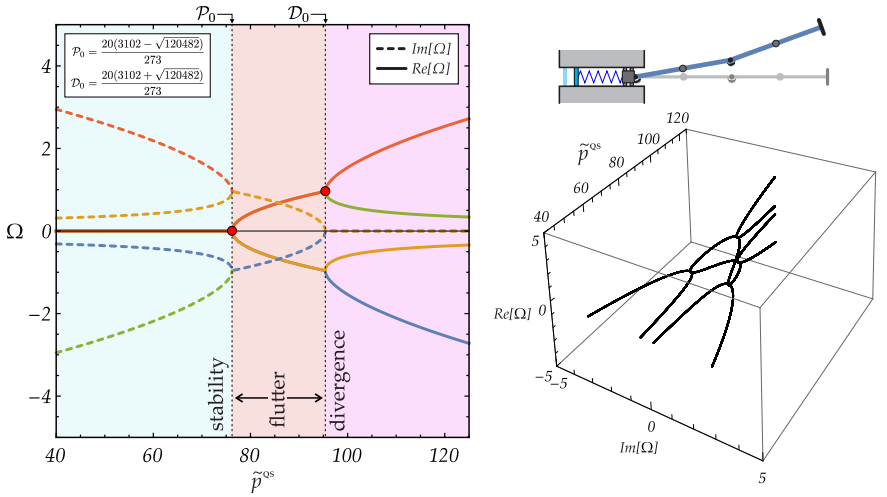

Figure 7.7: Flutter and divergence loads for a (conservative) elastic double pendulum, subject to a non-holonomic constraint and loaded through compression of a linear spring. Real and imaginary parts of the eigenvalues Ω are reported as functions of the load $\tilde{p}^{\rm QS}$. The ideal undamped case is considered, assuming $\tilde{d} = 1/2$, $\tilde{M}_L = 15$, $\tilde{I}_{r,L} = 15$, $\tilde{k}_1 = 50$.

is introduced. Furthermore, such critical load remains lower than the ideal one $\mathcal{P}_0$ (evaluated by considering null viscosity 'from the beginning', Eq.(7.68)) even in the limit of vanishing viscosity.

In order to assess the existence of such a paradox in the presence of non-holonomic constraints, the critical loads for the double pendulum are obtained keeping into account all the four damping sources introduced in the governing equations of motion. The evaluation of the critical loads causing flutter instabilities can be obtained analytically by means of the Routh-Hurwitz criterion (case $m = 4$) through the evaluation of the minor determinants of (7.61), and in particular via Eq.(7.63).

In order to evaluate the critical load of flutter and divergence by considering the effect of the four damping coefficients at the same time, the following notation is introduced

$$\tilde{p}^{\rm QS}_{\rm flu} = \mathcal{P}_d(\mathbf{c}, \boldsymbol{\xi}), \qquad \tilde{p}^{\rm QS}_{\rm div} = \mathcal{D}_d(\mathbf{c}, \boldsymbol{\xi}), \tag{7.70}$$

where the subscript 'd' highlights the presence of dissipation, while $\mathbf{c} = \{\tilde{c}_{t,L}, \tilde{c}_{r,L}, \tilde{c}_i, \tilde{c}_e\}$ is the dissipation vector collecting the four viscosity parameters of

the system. The dissipation vector can be represented as $\mathbf{c} = r\boldsymbol{\varphi}$, where $r \geq 0$ measures the dissipation magnitude while $\boldsymbol{\varphi}$ collects the direction cosines within the four-dimensional space defined by $\mathbf{c}$

$$\boldsymbol{\varphi} = \begin{bmatrix} \cos\phi_1 \\ \sin\phi_1 \cos\phi_2 \\ \sin\phi_1 \sin\phi_2 \cos\phi_3 \\ \sin\phi_1 \sin\phi_2 \sin\phi_3 \end{bmatrix}. \tag{7.71}$$

The three angles ϕ_1, ϕ_2 and ϕ_3 are restricted to range between 0 and $\pi/2$ for limiting the dissipation parameters to non-negative values, so that the critical load for flutter $(7.70)_1$ can be alternatively expressed as

$$\mathcal{P}_d = \mathcal{P}_d(r,\, \phi_1,\, \phi_2,\, \phi_3,\, \boldsymbol{\xi}). \tag{7.72}$$

Eq.(7.71) allows to take limits for the vanishing of any number of damping coefficients, ranging from 1 to 4. The limits for vanishing viscosities obtained keeping some of them fixed and the others tending to zero provide the same flutter loads that can be obtained by neglecting from the beginning the damping sources made to vanish, so that that there is no paradox. Therefore, the Ziegler paradox only occurs in the case when *all the damping sources are made to vanish*.

The limit value $\mathcal{P}_d^*$ for the flutter load $\mathcal{P}_d$, calculated when all 4 viscosities vanish, can be calculated by taking the limit for $r \to 0$, namely,

$$\mathcal{P}_d^*(\phi_1,\, \phi_2,\, \phi_3,\, \boldsymbol{\xi}) = \lim_{r\to 0} \mathcal{P}_d(r,\, \phi_1,\, \phi_2,\, \phi_3,\, \boldsymbol{\xi}). \tag{7.73}$$

The symbolic expression for $\mathcal{P}_d^*$ for a generic direction $\boldsymbol{\varphi}$ and input parameters $\boldsymbol{\xi}$ is cumbersome so that a direct proof of specific behaviours becomes awkward. Nevertheless, based on a very large number of parametric analyses for the vector $\boldsymbol{\varphi}$, the following features were always found to be verified:

- The limit flutter load $\mathcal{P}_d^*$ strongly depends on the direction $\boldsymbol{\varphi}$ and is never higher than the ideal flutter load $\mathcal{P}_0$ found for the undamped system, Eq.(7.68), namely,

  $$\mathcal{P}_d^*(\phi_1,\, \phi_2,\, \phi_3,\, \boldsymbol{\xi}) \leq \mathcal{P}_0(\boldsymbol{\xi}), \tag{7.74}$$

  where, when damping coefficients are non-negative, the equality sign can be attained only for specific directions $\boldsymbol{\varphi}$.

The minimum value for the critical flutter load is always the smallest of the four ones evaluated taking the limit of only one vanishing viscosity (while the remaining three are assumed null),

$$\min_{\phi_1,\,\phi_2,\,\phi_3}\{\mathcal{P}_d^*(\phi_1,\,\phi_2,\,\phi_3,\,\boldsymbol{\xi}))\} \equiv \min\{\mathcal{P}_d^*(0,0,0,\boldsymbol{\xi}),\,\mathcal{P}_d^*(\pi/2,0,0,\boldsymbol{\xi}),\,\mathcal{P}_d^*(\pi/2,\pi/2,0,\boldsymbol{\xi}),\,\mathcal{P}_d^*(\pi/2,\pi/2,\pi/2,\boldsymbol{\xi})\}. \tag{7.75}$$

Differently, the maximum value can either be the maximum over the 4 mentioned values or $\mathcal{P}_0$, the latter obtained along special directions $\boldsymbol{\varphi}$.

- The limit of the divergence load is independent of the direction $\boldsymbol{\varphi}$ and equal to the ideal divergence load $\mathcal{D}_0$ obtained for the system with no damping 'from the beginning',

$$\mathcal{D}_0(\boldsymbol{\xi}) = \lim_{r\to 0}\mathcal{D}_d(r,\,\phi_1,\,\phi_2,\,\phi_3,\,\boldsymbol{\xi}), \tag{7.76}$$

so that, in other words, no paradox is present for divergence instability load.

In the following paragraphs, the analytical expressions for the critical flutter load are reported for the four specific cases where only one and two damping sources are present. Such equations are introduced to illustrate the different effects of dissipative sources on instability and to show that a viscosity-independent Ziegler paradox may exist.

Influence of one damping source

The influence of each dissipation source on the flutter loads is now analyzed in detail, while the remaining three sources are considered null.

Internal damping $\tilde{c}_i$ ($\tilde{c}_e = \tilde{c}_{t,L} = \tilde{c}_{r,L} = 0$). The flutter load can be evaluated through the Routh-Hurwitz criterion, Eq.(7.63), providing the expression for the critical load $\mathcal{P}_d(\tilde{c}_i,\,\boldsymbol{\xi})$ as a function of the internal damping coefficient and the input parameters $\boldsymbol{\xi} = [\tilde{d},\,\tilde{M}_L,\,\tilde{I}_{r,L},\,\tilde{k}_1]$. The exact solution is reported in Appendix C.9, together with the specific case of vanishing damping, $\tilde{c}_i \to 0$. The limit value shows (the proof was obtained using the command `Reduce` of Mathematica®)the occurrence of the Ziegler paradox for every values of $\boldsymbol{\xi}$, so

that the critical load for flutter is never higher than that related to the ideal case of null damping 'from the beginning'.

Assuming $\hat{\boldsymbol{\xi}} = [1/2, 15, 15, 50]$ as seen in Fig.7.7, the value of the critical load of flutter is given by

$$\mathcal{P}_d(\tilde{c}_i, \hat{\boldsymbol{\xi}}) = \frac{64}{723}\tilde{c}_i^2 + \frac{4410529058}{57927483},$$

showing the existence of the Ziegler paradox as $\mathcal{P}_d(\tilde{c}_i \to 0, \hat{\boldsymbol{\xi}}) \approx 76.1388$. The divergence load can be analytically evaluated through Eq.(7.64), which is now a quartic in the load, leading to (7.76) for vanishing viscosity $c_i \to 0$, thus excluding Ziegler paradox for divergence.

The real and imaginary parts of the eigenvalues, solutions for the fourth-order polynomial Eq.(7.58), are reported in Fig.7.8 as functions of the dimensionless reaction load $\tilde{p}^{\text{QS}}$ in the particular case $\tilde{c}_i = 1.5$. Note that the critical loads for flutter and divergence instabilities are $\mathcal{P}_d \approx 76.338$ and $\mathcal{D}_d \approx 108.916$ respectively.

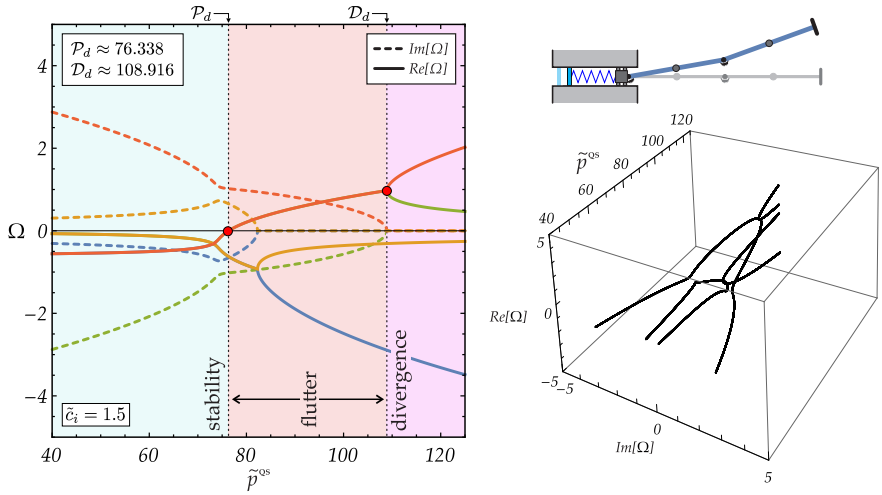

Figure 7.8: Flutter and divergence loads for a visco-elastic double pendulum, subject to a non-holonomic constraint and loaded through compression of a linear spring. Real and imaginary parts of the eigenvalues Ω are reported as functions of the load $\tilde{p}^{\text{QS}}$. The structure is the same reported in Fig.7.7, except that now viscosity is present, $\tilde{c}_i = 1.5$ and $\tilde{c}_e = \tilde{c}_{t,L} = \tilde{c}_{r,L} = 0$.

External damping $\tilde{c}_e$ ($\tilde{c}_i = \tilde{c}_{t,L} = \tilde{c}_{r,L} = 0$). The flutter load can be evaluated through the Routh-Hurwitz criterion, Eq.(7.63), providing the expression for the critical load $\mathcal{P}_d(\tilde{c}_e, \boldsymbol{\xi})$ as a function of the external damping coefficient $\tilde{c}_e$ and the parameters $\boldsymbol{\xi} = [\tilde{d},\, \tilde{M}_L,\, \tilde{I}_{r,L},\, \tilde{k}_1]$. The expression for the critical load $\mathcal{P}_d(\tilde{c}_e, \boldsymbol{\xi})$ as a function of the external damping and the specific load for $\tilde{c}_e \to 0$ is reported in the Appendix C.9. Such limit load $\mathcal{P}_d^*$ is never higher than the ideal load $\mathcal{P}_0$ for any combination of the coefficients $\boldsymbol{\xi}$.

Assuming the values $\hat{\boldsymbol{\xi}} = [1/2,\, 15,\, 15,\, 50]$ used to generate Fig.7.7, the critical load for flutter can be calculated to be

$$\mathcal{P}_d(\tilde{c}_e,\, \hat{\boldsymbol{\xi}}) = \frac{11566752096 + 25235\tilde{c}_e^2 - 721\sqrt{245\,(5\tilde{c}_e^2 + 1465344)\,\tilde{c}_e^2 + 40956144431616}}{169589580},$$

showing the existence of the Ziegler paradox $\mathcal{P}_d(\tilde{c}_e \to 0,\, \hat{\boldsymbol{\xi}}) \approx 40.9964$ (while the divergence load again does not show any Ziegler paradox).

It is also worth mentioning the limiting behaviour of the flutter load for infinite value of viscosity $\tilde{c}_e \to \infty$, which (differently from the limit values obtained with infinite values of internal viscosity $\tilde{c}_i$) remains finite,

$$\lim_{\tilde{c}_e \to \infty} \mathcal{P}_d(\tilde{c}_e,\, \boldsymbol{\xi}) = \frac{4(\tilde{k}_1 + 8)}{5}, \tag{7.77}$$

so that the external damping cannot eliminate flutter instability. Eq.(7.77) reveals that for $\tilde{k}_1 = 50$ the dimensionless critical load at infinite external viscosity is approximately 46.4, smaller than the ideal case, so that the critical load calculated for $\boldsymbol{\xi} = \hat{\boldsymbol{\xi}}$ and $\tilde{c}_e \geq 0$ is always inferior to the ideal case for every value of viscosity. The proof of the aforementioned property is obtained through the command `Reduce` of Mathematica®.

Non-holonomic constraint with translational damping $\tilde{c}_{t,L}$ ($\tilde{c}_i = \tilde{c}_e = \tilde{c}_{r,L} = 0$). The presence of the translational damping $\tilde{c}_{t,L}$ at the non-holonomic constraint leads to the following statement:

the value of the flutter load is independent of the translational damping coefficient and is never higher than that calculated for the ideal undamped case.

This form of dissipation paradox has never been previously encountered and is denoted here as 'viscosity-independent Ziegler paradox'.

In particular, according to the Routh-Hurwitz criterion (7.63), the flutter load is equal to

$$\mathcal{P}_d(\tilde{c}_{t,L},\,\boldsymbol{\xi}) = \mathcal{P}_d^*(0,0,0,\boldsymbol{\xi}) = \begin{cases} \dfrac{2\tilde{k}_1((\tilde{d}-1)\tilde{d}+8\tilde{I}_{r,L})}{8\tilde{I}_{r,L}-1}+4, & \text{if} \quad (\tilde{d}-1)\tilde{d}\tilde{k}_1+8\tilde{I}_{r,L}(\tilde{k}_1+2)<2, \\ \dfrac{16\tilde{I}_{r,L}-2}{(\tilde{d}-1)\tilde{d}+8\tilde{I}_{r,L}}+\tilde{k}_1, & \text{otherwise}, \end{cases} \tag{7.78}$$

(expressions obtained using Mathematica®) leading (through the command `Reduce`) to the conclusion that the critical load is independent of $\tilde{c}_{t,L}$ and never higher than the critical load $\mathcal{P}_0$, Eq.(7.68), for the ideal case without damping. Assuming $\hat{\boldsymbol{\xi}} = [1/2,\, 15,\, 15,\, 50]$, the following value of the critical load is obtained

$$\mathcal{P}_d^*(0,0,0,\hat{\boldsymbol{\xi}}) = \frac{24902}{479} \approx 51.9875 \,<\, 76.2073,$$

which is lower than the corresponding value for the undamped system, so that the Ziegler's destabilization paradox again occurs. Eq.(7.64) leads to a fifth-order polynomial in the loading parameter $\tilde{p}^{\text{QS}}$ that can be exploited in order to evaluate the analytical divergence load. Also in this case the divergence load as a function of the damping parameter $\tilde{c}_{t,L}$ tends to the ideal case for vanishing viscosity, so that no destabilization paradox for the divergence is observed.

Non-holonomic constraint with rotational damping $\tilde{c}_{r,L}$ ($\tilde{c}_i = \tilde{c}_e = \tilde{c}_{t,L} = 0$). In the presence of only the rotational damping at the non-holonomic constraint $\tilde{c}_{r,L}$, *again the critical flutter load results to be independent of this damping coefficient and never higher than the value obtained for the ideal system without damping.* In particular, Eq.(7.63) leads to

$$\mathcal{P}_d(\tilde{c}_{r,L},\,\boldsymbol{\xi}) = \mathcal{P}_d^*\left(\frac{\pi}{2},0,0,\boldsymbol{\xi}\right) = \frac{2\left(\tilde{d}^2+\tilde{d}\tilde{k}_1+\tilde{d}+2(\tilde{k}_1+2)\tilde{M}_L+1\right)}{\tilde{d}^2+\tilde{d}+4\tilde{M}_L+1}, \tag{7.79}$$

which is independent of $\tilde{c}_{r,L}$ and never higher than the critical load (7.68) of the ideal case without damping. The proof of this statement was obtained using the command `Reduce` of the commercial code Mathematica®. Assuming $\hat{\boldsymbol{\xi}} = [1/2,\, 15,\, 15,\, 50]$, the following value of the critical load for flutter is obtained

$$\mathcal{P}_d^*\left(\frac{\pi}{2},0,0,\hat{\boldsymbol{\xi}}\right) = \frac{12694}{247} \approx 51.3927 \,<\, 76.2073,$$

which is remarkably lower than the value obtained in the undamped case, thus confirming again the Ziegler paradox.

Again the divergence load tends to the value of the ideal undamped system for vanishing viscosity, so that no destabilization paradox for the divergence is observed.

Influence on stability of two damping coefficients

Two examples related to the simultaneous presence of two damping coefficients are presented to highlight the disappearance of the Ziegler paradox when specific directions $\boldsymbol{\varphi}$ are considered. Such condition is strictly related to the specific choice of the vector of parameters $\boldsymbol{\xi}$, for instance it can be achieved with $\hat{\boldsymbol{\xi}} = [1/2,\ 15,\ 15,\ 50]$ but it can not with $\tilde{\boldsymbol{\xi}} = [1/10,\ 1/10,\ 0,\ 1]$.

Combined effect of internal and external damping $\{\tilde{c}_i, \tilde{c}_e\} \neq 0$ $(c_{t,L} = \tilde{c}_{r,L}) = 0$. This case has also been analyzed for the Ziegler's double pendulum in [111, 89]. The two non-null viscosities can be parametrized through $\tilde{c}_e = r\sin\phi_3$, $\tilde{c}_i = r\cos\phi_3$ (so that $r = \sqrt{\tilde{c}_e^2 + \tilde{c}_i^2}$) and the related critical flutter load (reported in the Appendix C.10) can be evaluated through the Routh-Hurwitz criterion. The behaviour of the flutter load, when varying the magnitude r and angle ϕ_3, is shown in Fig.7.9 (left) for $\hat{\boldsymbol{\xi}} = [1/2,\ 15,\ 15,\ 50]$. Its limit value for vanishing both viscosities ($r \to 0$) along any direction ϕ_3 is given by

$$P_d^*\left(\frac{\pi}{2},\ \frac{\pi}{2},\ \phi_3,\ \hat{\boldsymbol{\xi}}\right) = \frac{4}{5}\left(\frac{576\cot\phi_3(57927483\cot\phi_3 + 10504342) + 240974002}{54519984\cot\phi_3 + 2826493} + \right.$$
$$\left. - \frac{3\sqrt{2}(12568\cot\phi_3 + 721)\sqrt{34704\cot\phi_3(11283138\cot\phi_3 - 711833) + 987561353}}{54519984\cot\phi_3 + 2826493}\right), \tag{7.80}$$

whose maximization yields

$$\max_{\phi_3}\left\{P_d^*\left(\frac{\pi}{2},\ \frac{\pi}{2},\ \phi_3,\ \hat{\boldsymbol{\xi}}\right)\right\} \equiv P_d^*\left(\frac{\pi}{2},\ \frac{\pi}{2},\ \phi_3 \approx 0.995,\ \hat{\boldsymbol{\xi}}\right) \equiv P_0\left(\hat{\boldsymbol{\xi}}\right), \tag{7.81}$$

namely, the maximum value of the critical flutter load is coincident with that of ideal case of null viscosity (further details can be found in the Appendix C.10).

The combined effect of translational and rotational damping for non-holonomic constraints $\{\tilde{c}_{t,L}, \tilde{c}_{r,L}\} \neq 0$ $(\tilde{c}_i = \tilde{c}_e = 0)$. The parametrization

of the two non-null viscosity parameters as $\tilde{c}_{r,L} = r\sin\phi_1$, $\tilde{c}_{t,L} = r\cos\phi_1$ (so that $r = \sqrt{\tilde{c}_{r,L}^2 + \tilde{c}_{t,L}^2}$) leads to the critical flutter load. For the sake of conciseness, the related expression is reported in the Appendix C.10.

The behaviour of the flutter load, when varying the magnitude r and angle ϕ_1, is shown in Fig.7.9 (right) for $\hat{\boldsymbol{\xi}} = [1/2,\, 15,\, 15,\, 50]$. Its limit value for vanishing both viscosities ($r \to 0$) along any direction ϕ_1 is given by

$$\mathcal{P}_d^*\left(\phi_1,\, 0,\, 0,\, \hat{\boldsymbol{\xi}}\right) = \frac{440805\cos(2\phi_1) - 3(8854828\sin(2\phi_1) + 6098513)}{6534\cos(2\phi_1) - 288272\sin(2\phi_1) - 234538} + \\ + \frac{(250\sin\phi_1 + 241\cos\phi_1)\sqrt{632330074 - 423120376\sin(2\phi_1) - 12220470\cos(2\phi_1)}}{6534\cos(2\phi_1) - 288272\sin(2\phi_1) - 234538}, \tag{7.82}$$

whose maximization provides, similarly to the previous case,

$$\max_{\phi_1}\left\{\mathcal{P}_d^*\left(\phi_1,\, 0,\, 0,\, \hat{\boldsymbol{\xi}}\right)\right\} \equiv \mathcal{P}_d^*\left(\phi_1 \approx 0.771,\, 0,\, 0,\, \hat{\boldsymbol{\xi}}\right) \equiv P_0\left(\hat{\boldsymbol{\xi}}\right). \tag{7.83}$$

Further details are available in the Appendix C.10.

Note in Fig.7.9 (right) the two red lines showing an example of the 'viscosity-independent Ziegler paradox', namely the critical load is constant for every modulus r when $\phi_1 = 0$ ($\tilde{c}_{r,L} = 0$) or when $\phi_1 = \pi/2$ ($\tilde{c}_{t,L} = 0$).

7.5 Post-critical behaviour and limit cycles

The linearized eigenvalue analysis so far developed shows that the straight configuration of the visco-elastic double pendulum is always stable (unstable) for loads smaller (higher) than the critical value for flutter, but nothing can be said about stability *at* the critical load and also on the stability of the post-critical dynamics involving large displacements.

The post-critical behaviour has been analyzed numerically to show that, in the presence of dissipation, limit cycles can be attained only through application of a dead load F (condition B), while loading with the external elastic device (condition A) always realizes a decaying motion. The latter behaviour is shown in Fig.7.10 through the integration of the non-linear equations of motion for a triple visco-elastic pendulum. The elastic column is loaded through a linear spring compressed beyond the flutter load, while the initial conditions $\Theta_i(0) = 10^{-7}$ and $\dot{\Theta}_i(0) = 0$ ($i = 1, 2, 3$) have been imposed for the bars' rotation and

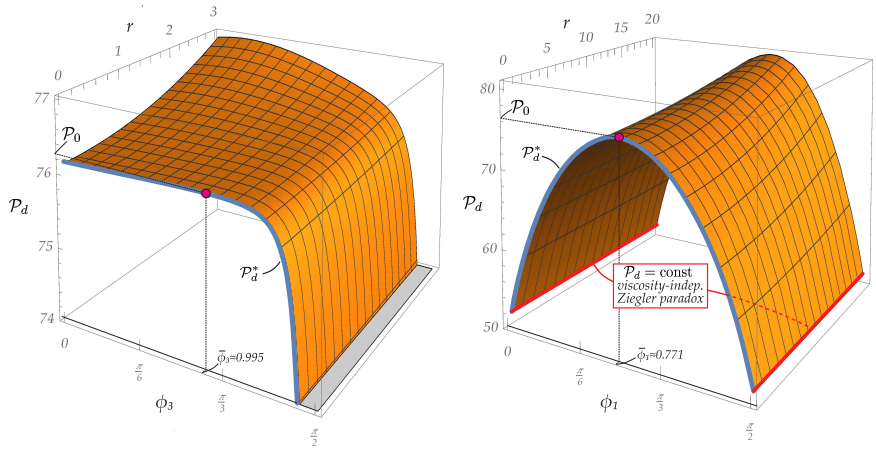

Figure 7.9: (Left) Critical load $\mathcal{P}_d$ for flutter instability in a double visco-elastic pendulum with internal $\tilde{c}_i = r\cos\phi_3$ and external $\tilde{c}_e = r\sin\phi_3$ viscosities (but $c_{t,L} = \tilde{c}_{r,L} = 0$), as a function of the modulus $r = \sqrt{\tilde{c}_i^2 + \tilde{c}_e^2}$ and of the angular parameter ϕ_3 ($\phi_1 = \phi_2 = 0$). The ideal critical load $\mathcal{P}_0$ is recovered in the limit of vanishing viscosity only for $\bar{\phi}_3 \approx 0.995$. (Right) As for the left part, but with translational $\tilde{c}_{t,L} = r\cos\phi_1$ and rotational $\tilde{c}_{r,L} = r\sin\phi_1$ viscosities (while $\tilde{c}_i = \tilde{c}_e = 0$), $r = \sqrt{\tilde{c}_{t,L}^2 + \tilde{c}_{r,L}^2}$ and angular parameter ϕ_1. The ideal critical load $\mathcal{P}_0$ is recovered in the limit of vanishing viscosity only for $\bar{\phi}_1 \approx 0.771$. The 'viscosity-independent Ziegler paradox' is highlighted by red lines, corresponding to a constant flutter load.

velocity, respectively. The structure is defined by $\bar{\boldsymbol{\xi}} = [1/2,\ 1,\ 0,\ 10]$, $\tilde{K} = 40$, $\tilde{\Delta} = 0.2$ and $\tilde{c}_i = 0.2$.

It is clear from Fig.7.10 that the motion following instability is an oscillation which initially increases to relieve the compression in the spring, but later decreases and decays to zero as a consequence of the effect of dissipation. Note also the sharp corners visible in the trajectory of the skate and typical of the non-holonomic constraint.

In the following, the case of a double pendulum subject to dead loading F is analyzed, where the Hopf theorem in $\mathbb{R}^4$ allows to analyze the stability at the critical point. In particular, it becomes possible to detect the correspondence of the flutter load with a Hopf bifurcation and therefore the existence of limit cycles in the neighbourhood of the critical load. Following Kutznetsov [70] and Marsden and McCracken [80], the first Lyapunov coefficient is evaluated to

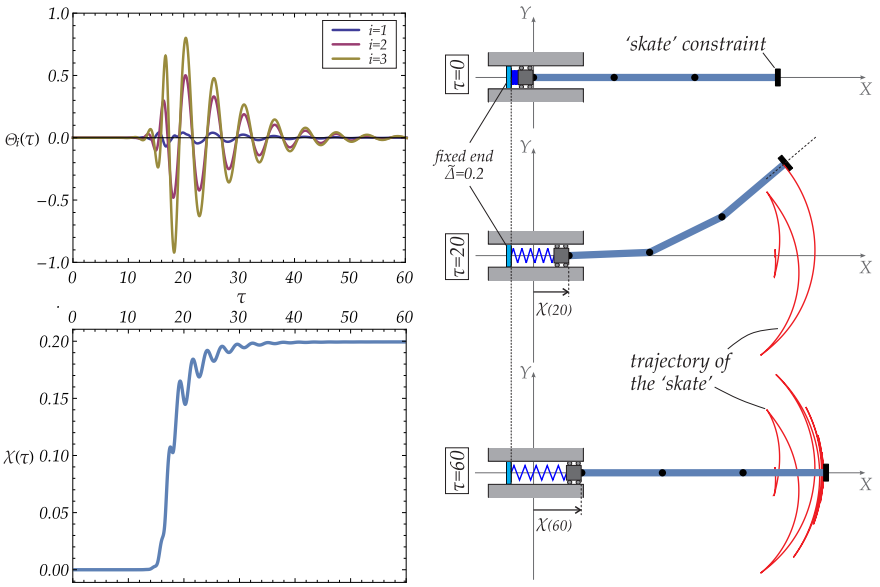

Figure 7.10: Post-critical behaviour (in terms of time evolution of the bars' rotations Θ_i and of the global horizontal displacement χ) for a visco-elastic triple ($N = 3$) pendulum subject to the non-holonomic 'skate' constraint and loaded through a linear elastic device. The dynamic instability occurs as the compressive force exceeds a critical value, thus generating a global horizontal motion χ. Eventually, oscillation decays due to the progressive unloading of the spring, so that periodic motion cannot be achieved. Note the sharp corners evidenced by the trajectory of the end of the structure, typical of the non-holonomic constraint.

discriminate between supercritical (positive coefficient) and subcritical (negative coefficient) Hopf bifurcation, respectively corresponding to the existence of stable or unstable periodic orbits in the neighbourhood of the bifurcation point.

Hopf bifurcations are investigated by expressing the governing equations through the Hamiltonian formalism. Moreover, although the following equations are referred for simplicity to the double pendulum only, the approach remains valid for an N–link column. The Lagrangian equations of motion (7.49) are independent of $\chi = X_0/L$, but depend on its derivatives $\dot{\chi}$ and $\ddot{\chi}$, so that it is possible to rewrite them by explicitly substituting such derivatives through the non-holonomic constraint, Eq.(7.49d). On the other hand, Eq.(7.49c) can be solved in the reaction force p, which can be substituted in Eqs.(7.49a) and

(7.49b) to provide a system of two non-linear equations in the two unknown rotations Θ_1 and Θ_2. The obtained system can be expressed via Hamiltonian formalism as

$$\dot{\mathbf{x}} = \mathbf{f}(\mathbf{x}, \tilde{F}), \qquad \mathbf{x} = \left[\Theta_1, \Theta_2, \dot{\Theta}_1, \dot{\Theta}_2\right] \in \mathbb{R}^4, \tag{7.84}$$

where $\tilde{F}$ is the dimensionless dead load, playing now the role of a bifurcation parameter, and $\mathbf{f} : \mathbb{R}^4 \times \mathbb{R} \to \mathbb{R}^4$ is an analytic and smooth function of $\mathbf{x}$ and $\tilde{F}$.

By considering an equilibrium point $\mathbf{x}_0$ such that

$$\mathbf{f}(\mathbf{x}_0, \tilde{F}) = \mathbf{0}, \tag{7.85}$$

a Hopf bifurcation occurs [50, 70, 80] at a critical value of the bifurcation parameter $\tilde{F} = \tilde{F}_{\rm cr}$ when both the following conditions hold:

(i.) the Jacobian matrix $\mathbf{J}$ of the function $\mathbf{f}$ at the equilibrium point $\mathbf{x}_0$ and load $\tilde{F}_{\rm cr}$ has a pair of pure complex conjugate eigenvalues $\lambda_{1,2} = \pm i\,\omega_0$ ($\omega_0 > 0$), while the remaining two eigenvalues have negative real part;

(ii.) the imaginary eigenvalues λ_1 and λ_2 of the Jacobian matrix $\mathbf{J}(\mathbf{x}_0, \tilde{F}_{cr})$ cross the imaginary axis at a non-null 'speed' (*crossing condition*)

$$\left.\frac{\partial\, \mathrm{Re}\left[\lambda_{1,2}\right]}{\partial \tilde{F}}\right|_{\tilde{F}=\tilde{F}_{\rm cr}} \neq 0. \tag{7.86}$$

From the above discussion, the fulfilment of the two conditions (i.) and (ii.) guarantees the existence of periodic orbits in the neighbourhood of the equilibrium point $\mathbf{x}_0$. It may also be concluded that Hopf bifurcations are excluded for null dissipations, because the real part of the eigenvalues is always zero until the critical flutter load is reached.

In the following, calculations are referred to the case of perfectly-aligned non-holonomic constraint $\beta_0 = 0$, so that the only possible equilibrium state for systems subject to both 'skate' or 'violin bow' constraints is the trivial configuration, $\mathbf{x}_0 = \mathbf{0}$.

In order to evaluate the stability condition for the Hopf bifurcation, the equations of motion (7.84) are expanded up to the third order around the equilibrium configuration $\mathbf{x}_0 = 0$ at a fixed value of the dead load $\tilde{F} = \tilde{F}_{\rm cr}$

$$\dot{\mathbf{x}} = \mathbf{J}\mathbf{x} + \frac{1}{2}\mathbf{B}(\mathbf{x}, \mathbf{x}) + \frac{1}{6}\mathbf{C}(\mathbf{x}, \mathbf{x}, \mathbf{x}) + O\left(||\mathbf{x}||^4\right), \tag{7.87}$$

where $\mathbf{B}$ and $\mathbf{C}$ are symmetric multilinear vector functions of $\mathbf{x} \in \mathbb{R}^4$. The stability of the Hopf bifurcation point has been assessed by exploiting two different but equivalent procedures, the first described by Kutsnetsov [70] and the second by Marsden and McCracken [80]:

- the right $\boldsymbol{q}$ and left $\boldsymbol{p}$ eigenvectors of the Jacobian matrix $\mathbf{J}$ are obtained as

$$\mathbf{J}\boldsymbol{q} = i\omega_0\,\boldsymbol{q}, \qquad \mathbf{J}^{\intercal}\boldsymbol{p} = -i\omega_0\,\boldsymbol{p}, \tag{7.88}$$

  and respectively correspond to the eigenvalues $i\omega_0$ and $-i\omega_0$. A normalization of the eigenvectors $\boldsymbol{q}$ and $\boldsymbol{p}$ is introduced, so that $\langle \boldsymbol{p}, \boldsymbol{q} \rangle = 1$ and $\langle \boldsymbol{q}, \bar{\boldsymbol{q}} \rangle = 0$, where $\langle \boldsymbol{a}, \boldsymbol{b} \rangle = \bar{a}_1 b_1 + ... + \bar{a}_n b_n$ denotes the scalar product in $\mathbb{C}^n$ while $\bar{\boldsymbol{a}}$ denotes the conjugate vector of $\boldsymbol{a}$. The (real) so-called *first Lyapunov coefficient* $l_1(0)$ [70] can be finally evaluated as

$$\begin{aligned} l_1(0) = \frac{1}{2\omega_0}\mathrm{Re}\Big[&\langle \boldsymbol{p}, \mathbf{C}(\boldsymbol{q}, \boldsymbol{q}, \bar{\boldsymbol{q}}) \rangle - 2\left\langle \boldsymbol{p}, \mathbf{B}(\boldsymbol{q}, \mathbf{J}^{-1}\mathbf{B}(\boldsymbol{q}, \bar{\boldsymbol{q}})) \right\rangle + \\ &+ \left\langle \boldsymbol{p}, \mathbf{B}(\bar{\boldsymbol{q}}, (2i\omega_0\mathbf{I} - \mathbf{J})^{-1}\mathbf{B}(\boldsymbol{q}, \boldsymbol{q})) \right\rangle \Big], \end{aligned} \tag{7.89}$$

  where the sign of $l_1(0)$ provides the stability property of the critical point.

- the third order Eq.(7.87) is transformed through a linear invertible change of basis $\mathbf{x} = \mathbf{A}\mathbf{y}$ defined in a way that the transformed Jacobian matrix assumes the following canonical real Jordan form

$$\tilde{\mathbf{J}} = \mathbf{A}^{-1}\mathbf{J}\mathbf{A} = \begin{bmatrix} 0 & \omega_0 & 0 & 0 \\ -\omega_0 & 0 & 0 & 0 \\ 0 & 0 & \lambda_3 & 0 \\ 0 & 0 & 0 & \lambda_4 \end{bmatrix}, \tag{7.90}$$

  as the eigenvalues λ_3 and λ_4 have a negative real part. One can demonstrate (see proof in Appendix C.7) that the matrix $\mathbf{A}$ can be written in terms of the eigenvector $\boldsymbol{q}$ defined in Eqs.(7.88) and the right eigenvectors $\mathbf{v}_3^{\mathrm{r}}$ and $\mathbf{v}_4^{\mathrm{r}}$ related to λ_3 and λ_4 as

$$\mathbf{A} = \left[\mathrm{Re}\left[\boldsymbol{q}\right], \mathrm{Im}\left[\boldsymbol{q}\right], \mathbf{v}_3^{\mathrm{r}}, \mathbf{v}_4^{\mathrm{r}} \right]. \tag{7.91}$$

  At this stage the center manifold theorem is exploited to 'isolate' the two variables $[y_1, y_2]$ considered responsible for the instability, namely by

imposing $[y_3, y_4] = \mathbf{h}(y_1, y_2)$ in the neighbourhood of the bifurcation point, where $\mathbf{h} = [h_1, h_2]$ is a vector of quadratic forms in the variables $[y_1,\, y_2]$. Finally, differentiations of the right-hand sides of the equations governing $[y_1,\, y_2]$

$$\begin{bmatrix} \dot{y}_1 \\ \dot{y}_2 \end{bmatrix} = \begin{bmatrix} 0 & \omega_0 \\ -\omega_0 & 0 \end{bmatrix} \begin{bmatrix} y_1 \\ y_2 \end{bmatrix} + \boldsymbol{F}(y_1,\, y_2,\, \mathbf{h}(y_1,\, y_2)), \tag{7.92}$$

where $\boldsymbol{F}$ is a smooth function containing all the non-linear terms, lead to the expression for the real term called $V'''(0)$ by Marsden and McCracken (Eq.(4.2) at page 126 of [80]), whose sign provides the stability property of the critical point.

In summary, a Hopf bifurcation occurs at a critical point once the two conditions (i.) and (ii.) for the validity of the Hopf theorem are satisfied. The stability of the periodic orbits in the neighbourhood of such critical point can be classified on the basis of the sign of the first Lyapunov coefficient $l_1(0)$ (Eq.(7.89)) or, equivalently, through that of $V'''(0)$ as

$$l_1(0) \text{ or } V'''(0) \begin{cases} < 0 & \rightarrow \text{ supercritical Hopf bif. (stable orbits),} \\ = 0 & \rightarrow \text{ critical case,} \\ > 0 & \rightarrow \text{ subcritical Hopf bif. (unstable orbits).} \end{cases} \tag{7.93}$$

7.5.1 Limit cycles by applying a dead load F

The conditions obtained in the previous section are now used together with numerical integration to analyze the post-critical dynamics of a visco-elastic double pendulum $N = 2$ subject to non-holonomic constraints. Two numerical simulations are presented in Fig.7.11 referred to the same initial conditions ($\Theta_i(0) = 0$ and $\dot{\Theta}_i(0) = 10^{-2}$), damping coefficients ($\tilde{c}_i = 1.5$, $\tilde{c}_e = \tilde{c}_{t,L} = \tilde{c}_{r,L} = 0$), input parameters ($\hat{\boldsymbol{\xi}} = [1/2,\, 15,\, 15,\, 50]$) and dead load ($\tilde{F}/\tilde{F}_{cr} = 1.1$ being $\tilde{F}_{cr} \approx 76.338$). Both the 'skate' and 'violin bow' constraints are considered.

The following two pairs of complex conjugate eigenvalues are obtained at the critical point

$$\lambda_{1,2} \approx \pm 1.01923\, i, \qquad \lambda_{3,4} \approx -0.625886 \pm 0.653007\, i,$$

so that criterion (i.) of the Hopf theorem is satisfied, together with the crossing condition (ii.)

$$\left.\frac{\partial \operatorname{Re}[\lambda_{1,2}]}{\partial \tilde{F}}\right|_{\tilde{F}=\tilde{F}_{\mathrm{cr}}} \approx 0.0744935 \neq 0,$$

showing the existence of a Hopf bifurcation at the critical point.

The first Lyapunov coefficient (or equivalently $V'''(0)$ from [80]) calculated at the bifurcation point is negative for both systems, so that a supercritical Hopf bifurcation occurs and the periodic orbits are stable. In fact, calculations performed with the commercial code Mathematica®show that

$$l_1(0) = \frac{V'''(0)}{3\pi} \approx \begin{cases} -2.1838 & \text{for the 'skate' constraint;} \\ -0.900238 & \text{for the 'violin bow' constraint.} \end{cases}$$

Despite the identity of the linearized stability, the two systems based on different non-holonomic constraints display different post-critical behaviours, and consequently different shapes of their limit cycles. However, for the particular choices of viscosities and input parameters, both systems show a supercritical Hopf bifurcation at the critical point and are characterized by periodic stable orbits, which exhibit increasing amplitudes at increasing $\tilde{F}$ (beyond the critical load for flutter, but within a finite interval).

The time evolution of the global horizontal displacement χ is reported in Fig.7.11 (left), showing that the velocity of the rigid block quickly approaches an oscillatory behaviour with a constant mean value. Meanwhile, the mechanical system achieves a limit cycle, shown in the phase portraits in Fig.7.11 (right), which, according to the Hopf theorem, is stable at least in a neighbourhood of the critical load for flutter.

The stability of the critical points can be evaluated by expressing the first Lyapunov coefficient in Eq.(7.89) as a function of the damping parameters, so that the domain of stability of the Hopf bifurcations, given by the sign of $l_1(0)$, can be directly expressed in terms of the magnitude of the damping parameters acting on the system. This calculation was possible only by fixing the values of $\boldsymbol{\xi}$ and by considering only one damping coefficient acting on the system. Two examples of the calculated Lyapunov coefficients (functions of one of the four damping sources assumed of magnitude r), are reported in Fig.7.12, providing a sketch of the qualitative stability behaviour.

Fig.7.12 shows that, depending on the magnitude of dissipation, the sign of the Lyapunov coefficient may or may not change, so that the Hopf bifurcations may be either supercritical ($l_1(0) < 0$) or subcritical ($l_1(0) > 0$). Changes in stability are highlighted in the figure by dashed lines. In the case of the 'skate' constraint with $\hat{\boldsymbol{\xi}} = [1/2,\ 15,\ 15,\ 50]$ (upper left corner) it can be concluded that both damping sources $\tilde{c}_i$ (reported green) and $\tilde{c}_e$ (reported red) can stabilize the bifurcation point if they overcome a certain threshold value (respectively, ≈ 22.07 and ≈ 482.14). On the other hand, no subcritical Hopf bifurcations can

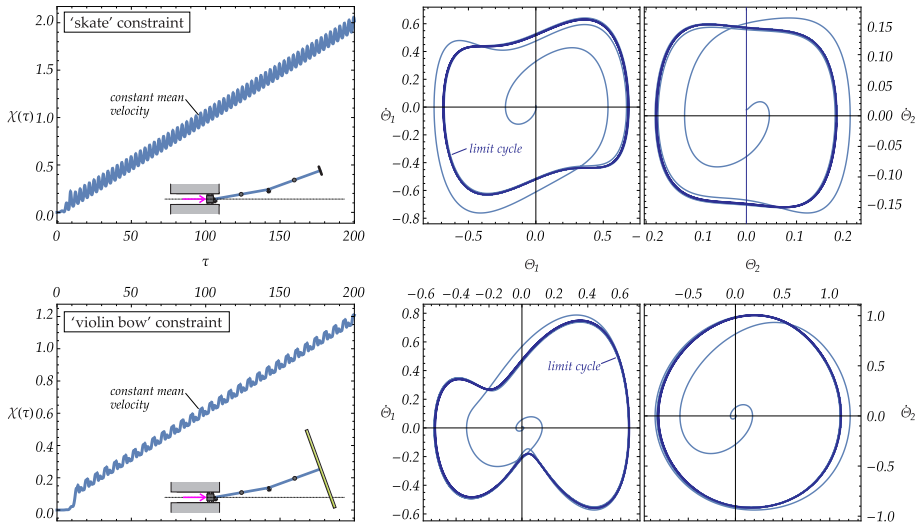

Figure 7.11: Evolution in time of the global horizontal displacement χ (left) and phase portraits $\{\Theta_i, \dot{\Theta}_i\}$ for the rotations of the two rigid bars, (right, with limit cycles highlighted in dark blue), for a double pendulum subject to a 'skate' (upper part) and 'violin bow' (lower part) constraints and loaded through a dead load $\tilde{F} = 1.1\tilde{F}_{cr}$. Note that the post-critical behaviour is different if a 'skate' or a 'violin bow' constraint applies, even though the same initial conditions, viscosities, and input parameters have been imposed and even though the two structures have the same critical flutter load.

be obtained at varying every damping source (acting alone) when the structure with $\hat{\boldsymbol{\xi}}$ ends with the 'violin bow' constraint (lower left part of the figure).

It may be interesting to remark, in closure of this Section, that analyses not reported for conciseness show that structures subject to dead loading reach a limit steady motion with constant *mean* velocity even when only the viscosity of the hinges is present. This situation is in contrast to what happens in the absence of viscosity where the system, subject to a constant force, is subjected to an increasing velocity. In other words, the rotational viscosity of the hinges, taken alone, acts as the ambient viscosity during the falling of a mass in a gravitational field.

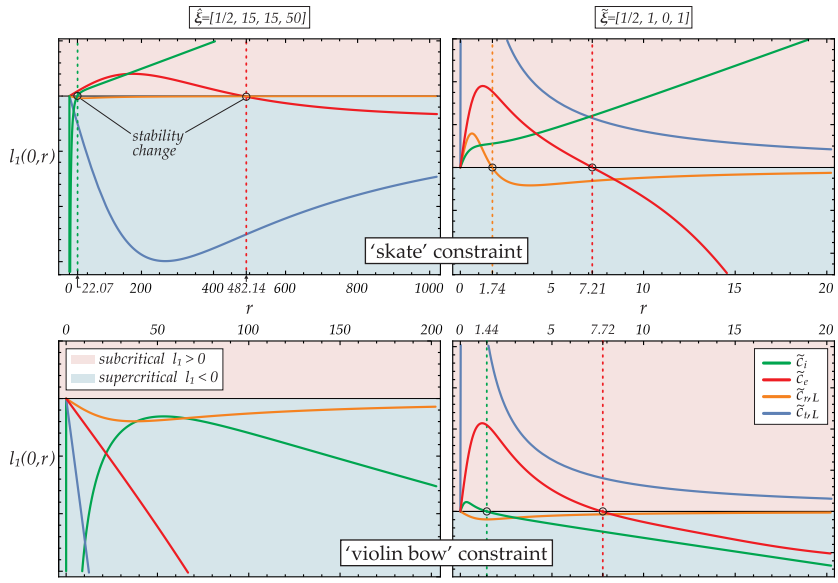

Figure 7.12: First Lyapunov coefficient l_1 (only the sign matters, so that ticks are not reported on the vertical axis) as a function of the magnitude of only one of the four damping parameters (the other three are assumed null) for the 'skate' constraint (upper part) and for the 'violin bow' constraint (lower part). The coefficient discriminates between supercritical and subcritical Hopf bifurcations and was obtained for two sets of coefficients: $\hat{\boldsymbol{\xi}} = [1/2, 15, 15, 50]$ (left part) and $\tilde{\boldsymbol{\xi}} = [1/2, 1, 0, 1]$ (right part). Changes in stability are highlighted by dashed lines and show that subcritical Hopf bifurcations cannot be obtained when the structure with $\hat{\boldsymbol{\xi}} = [1/2, 15, 15, 50]$ ends with the 'violin bow' constraint (lower left corner).

7.5.2 A note on non-aligned constraint ($\beta_0 \neq 0$)

Until now the non-holonomic constraints have always be assumed to be aligned parallel to the last bar, $\beta_0 = 0$. Therefore, it may be interesting to explore the effect of constraint non-alignment. In particular, a case of double pendulum with non-aligned 'violin bow' constraint, $\beta_0 = \pi/100 = 1.8°$, is investigated and the phase portraits of the two bars' rotations is shown in Fig.7.13, reported as green curves, together with the blue curves representing the perfect system ($\beta_0 = 0$, analyzed at a load $\tilde{F} = 80$, beyond the flutter load ≈ 76.338).

A non-trivial equilibrium solution for the double pendulum with $\beta_0 = \pi/100$ is found for $\Theta_1^{\mathrm{QS}} \approx -0.050282$ and $\Theta_2^{\mathrm{QS}} \approx 0.701512$ (shown in Fig.7.13 on the left)

at a load $\tilde{F} = 80$, beyond the flutter load (≈ 78.276). For this configuration, the solutions for the characteristic equation (7.42) (with $m = 4$) consist in two pairs of complex conjugate eigenvalues, where only two eigenvalues have a positive real part, so that the equilibrium configuration is unstable.

The non-trivial equilibrium configuration is used to analyze the unstable dynamics of the system by imposing the initial conditions $\Theta_i(0) = \Theta_i^{\text{QS}}$ and $\dot{\Theta}_i(0) = 10^{-2}$ (the coordinates of the center of the spirals representing the phase portraits in Fig.7.13) and assuming $\tilde{c}_i = 1.5$, $\tilde{c}_e = \tilde{c}_{t,L} = \tilde{c}_{r,L} = 0$ and $\hat{\boldsymbol{\xi}} = [1/2, 15, 15, 50]$. The following observations can be drawn from Fig.7.13:

- The non-trivial equilibrium solution corresponding to a small imperfection $\beta_0 = \pi/100$ exhibits a large deviation from rectilinearity;
- The flutter load for the non-trivial solution (≈ 78.276) is slightly higher than that relative to the trivial solution (≈ 76.338);
- The phase portraits for the imperfect system confirm the existence of periodic orbits in the presence of imperfections, intended now as a misalignment of the non-holonomic constraint;
- When the phase portraits of the perfect and imperfect systems are compared, the former possess a symmetry which is lost in the latter. Moreover, the oscillations of the perfect system exhibit larger amplitudes than the imperfect one.

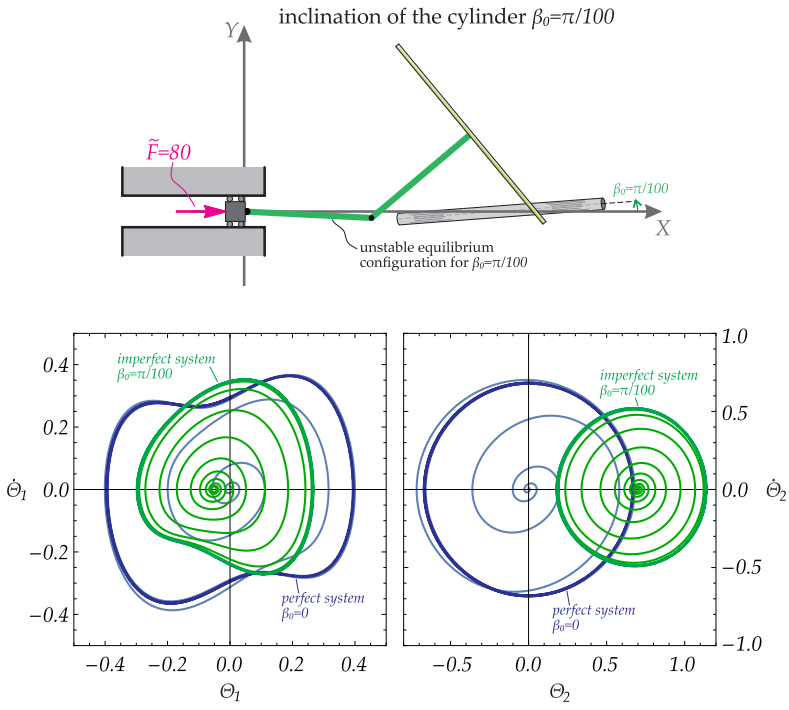

Figure 7.13: Phase portraits (green curves, in terms of bar's rotations Θ_1 on the center, Θ_2 on the right) showing the achievement of a limit cycle for a visco-elastic double pendulum with a misaligned 'violin bow' constraint, $\beta_0 = \pi/100 = 1.8°$ (shown on the left). The phase portrait of the perfect system $\beta_0 = 0$ is also reported for comparison (blue curve). The initial equilibrium configuration for the imperfect system exhibits a large deviation from rectilinearity ($\Theta_1^{\rm QS} \approx -0.050282$, $\Theta_2^{\rm QS} \approx 0.701512$, shown on the left) and is unstable, so that the system starts oscillating with increasing amplitudes towards a stable limit cycle.

7.6 Locomotion and friction

Limbless locomotion. The periodic solutions so far obtained for the analyzed structures can be exploited in the design of limbless locomotion devices. In fact, the time evolution of the rigid bars' rotations exhibiting a generic limit cycle can directly be imposed to the same structures which are left only with the horizontal motion X_0 of the end of the structure as 'free coordinate'. With this set-up, the non-holonomic constraint is capable of converting the imposed

oscillations of the rigid bars into an horizontal displacement, providing the locomotion to the system.

An example of the dimensionless equations of motion of a double pendulum with controlled rotations at both ends and with an appended dead load $\tilde{F}$ at the left end of the structure is given by

$$\begin{aligned}
&\frac{\tilde{c}_e}{8}\Big(8\dot{\chi} - 3\,\dot{\Theta}_1(\tau)\sin\Theta_1(\tau) - \dot{\Theta}_2(\tau)\sin\Theta_2(\tau)\Big) + \\
&+ \frac{\tilde{c}_{t,L}}{2}\Big(2\dot{\chi} - \dot{\Theta}_1(\tau)\sin\Theta_1(\tau) - \dot{\Theta}_2(\tau)\sin\Theta_2(\tau)\Big) + \tilde{M}_X\ddot{\chi} + \\
&+ \frac{1}{4}\Big(4\ddot{\chi} - \tilde{d}\,\ddot{\Theta}_1(\tau)\sin\Theta_1(\tau) - \tilde{d}\,\dot{\Theta}_1^2(\tau)\cos\Theta_1(\tau) - \tilde{d}\,\ddot{\Theta}_2(\tau)\sin\Theta_2(\tau) + \\
&- \tilde{d}\,\dot{\Theta}_2^2(\tau)\cos\Theta_2(\tau) - \ddot{\Theta}_1(\tau)\sin\Theta_2(\tau) - \dot{\Theta}_1(\tau)\dot{\Theta}_2(\tau)\cos\Theta_2(\tau)\Big) + \qquad (7.94a)\\
&+ \frac{\tilde{M}_L}{2}\Big(2\ddot{\chi} - \ddot{\Theta}_1(\tau)\sin\Theta_1(\tau) - \dot{\Theta}_1^2(\tau)\cos\Theta_1(\tau) - \ddot{\Theta}_2(\tau)\sin\Theta_2(\tau) + \\
&- \dot{\Theta}_2^2(\tau)\cos\Theta_2(\tau)\Big) + \tilde{p}\,\tilde{a}_3 + \tilde{F} = 0,
\end{aligned}$$

$$\tilde{a}_1\,\dot{\Theta}_1(\tau) + \tilde{a}_2\,\dot{\Theta}_2(\tau) + \tilde{a}_3\dot{\chi} = 0, \qquad (7.94b)$$

where $\Theta_1(\tau)$ and $\Theta_2(\tau)$ are time-dependent rotations *imposed to* the two rigid bars and representing the periodic solution for the same structure with free and unknown rotations. The coefficients $\tilde{a}_i$ in Eq.(7.94) are expressed by Eqs.(7.51) for the 'skate' and (7.52) for the 'violin bow' non-holonomic constraints.

In conclusion, it is suggested that the rotations $\Theta_1(\tau)$ and $\Theta_2(\tau)$ can be 'borrowed' from the solution for a structure subject to a dead force. Then, such a solution can be exploited as imposed rotations for a similar double-pendulum, but characterized in general by different properties. In this way, because the coefficients $\tilde{a}_i$ in Eq.(7.94b) are independent of the structural parameters, the two systems display the same dimensionless displacement of the left end $\chi(\tau)$, so generating a steady motion with a constant mean velocity. Therefore, the controlled system is capable of moving any dead load by tuning the reaction at the non-holonomic constraint, Eq.(7.94a).

Friction between two solids. Another possible application of the results so far obtained is in the problem of friction between two different solids in contact. In fact, the non-holonomic constraint corresponds to a situation of 'directional

infinite friction', so that motion is impossible in all the analyzed structures (with $\beta_0 = 0$) if instability does not occur. If the non-holonomic constraint is believed to remain valid within a friction cone, instability may decrease the force needed to move the system. In other words, if the structures are regarded as 'black boxes' which are to be displaced through the application of an external force, perceived as the force needed to overcome some friction, then this force can be strongly decreased by the instability. As a conclusion, the results presented in this article can find application in the analysis of microstructural effects at the contact between two solids, to possibly explain 'unexpected drop' in the applied forces to produce relative motion between the two solids.

7.7 Conclusions

It has been shown how flutter instability and Hopf bifurcations can be found in visco-elastic structures under *conservative loads*, when subject to non-holonomic constraints. This finding opens a new perspective in structures suffering instabilities and provides a proof of the mechanical equivalence between non-holonomic conditions and *polygenic* forces, which cannot be derived from any scalar functional (for instance follower loads) [71]. In this context, the reaction force related to a non-holonomic constraint can be seen as the polygenic force applied to the Ziegler or Reut pendulum, but now with possibly varying modulus, such that the kinematic non-holonomic condition is satisfied. Under this circumstance, the work done by the force is always null. The obtained results may find applications in limbless locomotion and as possible explanation of micromechanics leading to instabilities in frictional contact between two solids.

8

Fluttering of elastic rods subject to non-holonomic constraints. Continuous model

8.1 Introduction

The aim of the present chapter is to prove that flutter instabilities can be obtained for a continuous conservative system subject to non-holonomic constraints. In contrast with Chapter 7, calculations are referred to an elastic rod subject to a 'skate' constraint only, while the sliding clamp at the left end of the rod is loaded through the elastic device (condition A).[1] Also in this case, the imposed displacement Δ of the left end of the extensional spring is considered fixed in time, so that the entire system is loaded through a fully-conservative device.

By considering a perfectly-aligned constraint (case $\beta_0 = 0$ as in Chapter 7), such non-holonomic system yields the same critical load, dissipation induced instabilities, including the so-called 'Ziegler paradox', that is found for the Beck column [14], or more in general, for a Pflüger column [20, 21, 87], two cases

[1] The case of loading through a dead force F can be easily developed by simply considering the contribution of its external work within the definition of the total potential energy. Anyhow, according to the findings reported in Chapter 7, the same critical loads for the linearized structure can be found by considering one or the other loading condition at the initial end.

where a follower force is applied to an end of a clamped cantilever. Moreover, according to the findings reported in Chapter 7 in the case of discretized rods, the *Ziegler's viscosity-independent paradox* is found when some external damping forces acting on the 'skate' non-holonomic constraint are introduced, so that the corresponding flutter load is found to be independent of the magnitude of viscosities.

Finally, the flutter load for the continuous non-holonomic system in the presence of internal dissipation is compared with that obtained for a discretized rod at increasing number N of its constituent rigid bars. The comparison shows how the latter critical load tends to the value of the continuous rod, as the number of bars N is increased.

8.1.1 The continuous elastic column with non-holonomic constraint

A planar elastic rod of constant length l is parametrized through a curvilinear coordinate $\mathsf{s} \in [0, l]$. The rod has a distributed mass ρ and bending stiffness B and is constrained at the initial end $\mathsf{s} = 0$ by a rigid block of mass M_X equipped with an extensional horizontal spring of stiffness K. Its final end $\mathsf{s} = l$ is constrained through a 'skate' non-holonomic constraint (realized for instance through a wheel or a knife edge) of mass M_L and rotational inertia $I_{r,L}$, which constraints the local component of the velocity to be parallel to the sliding direction of the skate. Following the same notation adopted for the discrete system, such non-holonomic constraint is rigidly attached to the final end of the rod ($\mathsf{s} = l$), thus forming an angle β_0 with respect to the inclination $\Theta(l, t)$ of the tangent vector at the considered point.

Self-contact phenomena in the rod are disregarded, so that the rod's deformed shape is completely described by the unknown rotation field $\Theta(\mathsf{s}, t)$, measured with respect to the horizontal X axis and by the position $X_0(t)$ of the sliding clamp along the horizontal direction. Moreover, the rod is considered inextensible and shear deformations are neglected.

The same four dissipative effects introduced in Chapter 7 are assumed to be present. In particular, by considering the external damping coefficient c_e and the further coefficients $c_{t,L}$ and $c_{r,L}$ expressing the translational and rotational damping effects on the non-holonomic constraint, the mathematical model describing the continuous system is complemented by the effect of the internal damping, introduced by means of a visco-elastic constitutive law. Following Bigoni [22], a uniaxial constitutive law is assumed relating the internal

longitudinal stress σ to the strain ϵ in the form

$$\sigma = E\,\epsilon + \Lambda\,\dot{\epsilon}\,, \tag{8.1}$$

where E is the Young modulus and Λ a constant viscous term, the internal bending moment is given by

$$M = \int_A [E\,\epsilon\,y + \Lambda\,\dot{\epsilon}\,y]\,\mathrm{d}A. \tag{8.2}$$

Assuming a linearized theory, so that $\epsilon = y\,\Theta'$, one obtains

$$M(\mathsf{s},t) = B\,\Theta'(\mathsf{s},t) + D\,\dot{\Theta}'(\mathsf{s},t)\,, \tag{8.3}$$

where the superimposed ‘ ˙ ’ and ‘ ′ ’ symbols represent the derivatives with respect to time t and to the curvilinear coordinate s, respectively. The constant term $D = \Lambda I$ represents the internal viscous damping coefficient and $B = EI$, where I is the moment of inertia of the cross section. The described mechanical system is shown in Fig.8.1.

Differently from what seen in Chapter 2, the considered rod cannot be represented through the exact solution for the Euler's elastica because of the presence of distributed loads within its span. These forces are strictly related to the dynamic effects involved in the presented model, and in particular are given by the distributed inertia and damping sources. Consequently, the quasi-static configurations can be expressed through the solution for the Euler's elastica and the corresponding load at both ends is given by the unknown reaction force of the non-holonomic constraint (denoted by $p(t)$ in the following Sections). Moreover, the elastica can also model the dynamics of such continuous rods in the case of negligible distributed mass and damping effects along its span, as these effects are supposed to act only at both ends (see Armanini et al. [4, 5]). In the remaining cases, the problem of the dynamics of the rod can be attacked through the numerical integration of the governing PDE's or through a FEM code (see for instance the procedure proposed by Bartels [7]). In the present Chapter, the non-linear dynamics of the continuous rod is not addressed.

8.2 Equations of motion

The exact equations of motion for a continuous system subject to a non-holonomic ‘skate’ constraint are obtained by firstly writing the elastic energy of

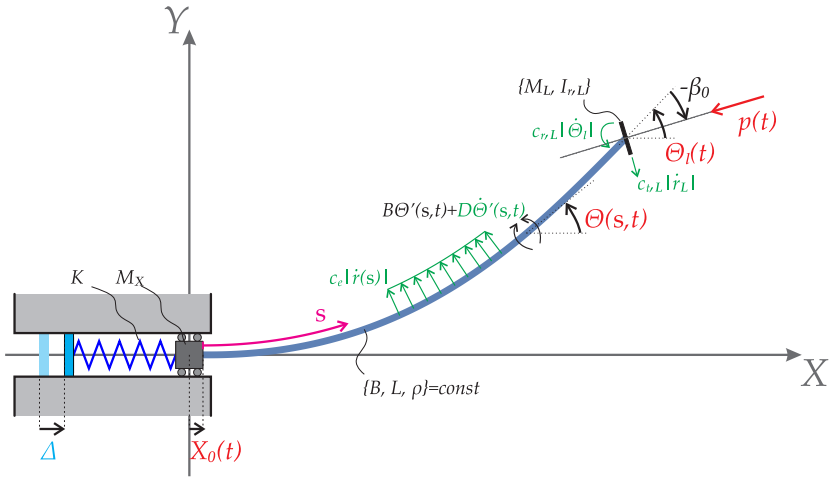

Figure 8.1: Structure of the non-holonomic elastic rod as a function of the unknown rotation field $\Theta(\mathsf{s},t)$ and horizontal displacement $X_0(t)$ of the clamped initial end $\mathsf{s}=0$, which is loaded through an horizontal extensional spring with axial stiffness K. The final end $\mathsf{s}=l$ is constrained by a non-holonomic 'skate' constraint, which is inclined at an angle β_0 taken with respect to the tangent vector of the rod.

the system

$$\mathcal{E}=\frac{1}{2}K(X_0(t)-\Delta)^2+\frac{1}{2}B\int_0^l\Theta'(\mathsf{s},t)^2\mathrm{d}\mathsf{s}, \tag{8.4}$$

while its 'density' along the span of the rod can be simply defined as

$$\mathscr{E}=\frac{K}{2l}(X_0(t)-\Delta)^2+\frac{1}{2}B\Theta'(\mathsf{s},t)^2. \tag{8.5}$$

so that $\mathcal{E}=\int_0^l\mathscr{E}\mathrm{d}\mathsf{s}$. The kinetic energy of the system can be written as

$$\begin{aligned}\mathcal{T}=&\frac{1}{2}M_X\dot{X}_0(t)^2+\frac{1}{2}I_{r,L}\dot{\Theta}(l,t)^2+\frac{1}{2}M_L\left(\dot{X}(l,t)^2+\dot{Y}(l,t)^2\right)+\\&+\frac{1}{2}\rho\int_0^l\left(\dot{X}(\mathsf{s},t)^2+\dot{Y}(\mathsf{s},t)^2\right)\mathrm{d}\mathsf{s},\end{aligned} \tag{8.6}$$

so that its 'density' along the span of the rod is expressed by

$$\mathscr{T}=\tfrac{M_X}{2l}\dot{X}_0(t)^2+\tfrac{I_{r,L}}{2l}\dot{\Theta}(l,t)^2+\tfrac{M_L}{2L}\left(\dot{X}(l,t)^2+\dot{Y}(l,t)^2\right)+\tfrac{\rho}{2}\left(\dot{X}(\mathsf{s},t)^2+\dot{Y}(\mathsf{s},t)^2\right).$$

(8.7)

The horizontal and vertical coordinates X and Y singling out the deformed shape of the rod as functions of the time t and of the curvilinear coordinate s are respectively expressed by

$$X(\mathsf{s},t) = X_0(t) + \int_0^{\mathsf{s}} \cos\Theta(\varsigma,t)\mathrm{d}\varsigma = X_0(t) + \zeta(\mathsf{s},t), \qquad Y(\mathsf{s},t) = \int_0^{\mathsf{s}} \sin\Theta(\varsigma,t)\mathrm{d}\varsigma, \tag{8.8}$$

where $\zeta(\mathsf{s},t)$ denotes the integral introduced in the definition of X and s is defined within the interval $[0,\, l]$.

The inextensibility constraint of the elastic rod and the imposed null rotation $\Theta(0,t) = 0$ at the initial coordinate $\mathsf{s} = 0$ are introduced through the following (holonomic) constraint equations

$$X'(\mathsf{s},t) - \cos\Theta(\mathsf{s},t) = 0, \qquad Y'(\mathsf{s},t) - \sin\Theta(\mathsf{s},t) = 0, \qquad \Theta(0,t) = 0\,. \tag{8.9}$$

The viscous frictional forces are introduced by means of the Rayleigh dissipation function

$$\begin{aligned}\mathcal{F}_d = &\frac{1}{2}c_e \int_0^l (\dot{X}(\mathsf{s},t)^2 + \dot{Y}(\mathsf{s},t)^2)\mathrm{d}\mathsf{s} + \frac{1}{2}c_{t,L}\left(\dot{X}(l,t)^2 + \dot{Y}(l,t)^2\right) + \frac{1}{2}c_{r,L}\dot{\Theta}(l,t)^2 + \\ &+ \frac{1}{2}D\int_0^l \dot{\Theta}'(\mathsf{s},t)^2\mathrm{d}\mathsf{s},\end{aligned} \tag{8.10}$$

or in terms of its 'density' per unit-length by

$$\mathscr{F}_d = \frac{c_e}{2}(\dot{X}(\mathsf{s},t)^2 + \dot{Y}(\mathsf{s},t)^2) + \frac{c_{t,L}}{2l}\left(\dot{X}(l,t)^2 + \dot{Y}(l,t)^2\right) + \frac{c_{r,L}}{2l}\dot{\Theta}(l,t)^2 + \frac{D}{2}\dot{\Theta}'(\mathsf{s},t)^2, \tag{8.11}$$

where D is the internal viscous friction term and the time derivatives of the functions X and Y (see equation (8.8)) can be expressed through the following

integro-differential equations

$$\begin{cases} \dot{X}(\mathsf{s},t) = \dot{X}_0 - \int_0^{\mathsf{s}} \sin\Theta\dot{\Theta}\,\mathrm{d}\varsigma \\ \dot{Y}(\mathsf{s},t) = \int_0^{\mathsf{s}} \cos\Theta\dot{\Theta}\,\mathrm{d}\varsigma \\ \ddot{X}(\mathsf{s},t) = \ddot{X}_0 - \int_0^{\mathsf{s}} \left(\cos\Theta\dot{\Theta}^2 + \sin\Theta\ddot{\Theta}\right)\,\mathrm{d}\varsigma \\ \ddot{Y}(\mathsf{s},t) = \int_0^{\mathsf{s}} \left(-\sin\Theta\dot{\Theta}^2 + \cos\Theta\ddot{\Theta}\right)\,\mathrm{d}\varsigma. \end{cases} \tag{8.12}$$

The Lagrangian function of the system can be written in the following form

$$\begin{aligned} \mathcal{L} = \mathcal{T} - \mathcal{E} + M_0(t)\,\Theta(0,t) + \\ + \int_0^l \left[R_X(\mathsf{s},t)(X' - \cos\Theta) + R_Y(\mathsf{s},t)(Y' - \sin\Theta)\right]\mathrm{d}\mathsf{s}\,, \end{aligned} \tag{8.13}$$

so that the Lagrangian 'density' $\mathscr{L}$ is given by

$$\mathscr{L} = \mathscr{T} - \mathscr{E} + \frac{M_0}{l}\Theta(0) + R_X(X' - \cos\Theta) + R_Y(Y' - \sin\Theta)\,, \tag{8.14}$$

and the introduced functions $R_X(\mathsf{s},t)$, $R_Y(\mathsf{s},t)$ and $M_0(t)$ are the Lagrangian multipliers associated with the constraints (8.9). The vector collecting the fundamental variables of the system is therefore given by

$$\boldsymbol{w} = \{X_0,\, X',\, Y',\, \dot{X},\, \dot{Y},\, \dot{X}(l),\, \dot{Y}(l),\, \dot{X}_0,\, \Theta,\, \Theta',\, \Theta(0),\, \dot{\Theta}(l),\, R_X,\, R_Y,\, M_0\}. \tag{8.15}$$

The Hamilton's action integral can be written as

$$\mathcal{A} = \int_{t_0}^{t_1} \int_0^l \mathscr{L}\mathrm{d}\mathsf{s}\,dt,$$

where all the variations in the fundamental variables of the system (8.15) have to satisfy the imposed boundary conditions at both ends and are null at the extremal points of the time interval, namely

$$\delta\Theta(0) = \delta Y(0) = 0, \quad \delta X(0) = \delta X_0, \quad \delta X(l) = \delta X_0 + \delta\zeta(l), \quad \delta\boldsymbol{w}\big|_{t_0} = \delta\boldsymbol{w}\big|_{t_1} = \mathbf{0}, \tag{8.16}$$

where the parameter ζ is included in the formulation of $X(\mathsf{s},t)$, Eq.(8.8).

Exploiting the Hamilton's principle of least action, one can write

$$\begin{aligned}\delta\mathcal{A} &= \int_{t_0}^{t_1}\int_0^l \delta\mathscr{L}\,\mathrm{d}\mathsf{s}\,dt \\ &= \int_{t_0}^{t_1}\int_0^l \Big\{\mathscr{L}_{\dot{X}}\delta\dot{X} + \mathscr{L}_{\dot{Y}}\delta\dot{Y} + \mathscr{L}_{\dot{X}(l)}\delta\dot{X}(l) + \mathscr{L}_{\dot{Y}(l)}\delta\dot{Y}(l) + \mathscr{L}_{\dot{X}_0}\delta\dot{X}_0 + \\ &\qquad + \mathscr{L}_{\dot{\Theta}(l)}\delta\dot{\Theta}(l) + \mathscr{L}_{\Theta'}\delta\Theta' + \mathscr{L}_{X_0}\delta X_0 + \mathscr{L}_{X'}\delta X' + \mathscr{L}_{Y'}\delta Y' + \\ &\qquad + \mathscr{L}_{\Theta}\delta\Theta + \mathscr{L}_{R_X}\delta R_X + \mathscr{L}_{R_Y}\delta R_Y + \mathscr{L}_{M_0}\delta M_0\Big\}\mathrm{d}\mathsf{s}\,dt,\end{aligned} \tag{8.17}$$

where $\mathscr{L}_\xi = \partial\mathscr{L}/\partial\xi$ denotes the derivative of the 'density' of the Lagrangian function with respect to a generic coordinate ξ. Integrations by parts and the fulfilment of the conditions (8.16) provide the following final form

$$\begin{aligned}\int_0^l \delta\mathscr{L}\,\mathrm{d}\mathsf{s} = \int_0^l \Big\{ &\left(-\frac{d}{dt}(\mathscr{L}_{\dot{X}}) - \frac{d}{d\mathsf{s}}(\mathscr{L}_{X'})\right)\delta X + \left(-\frac{d}{dt}(\mathscr{L}_{\dot{Y}}) - \frac{d}{d\mathsf{s}}(\mathscr{L}_{Y'})\right)\delta Y + \\ &+ \left(\mathscr{L}_{\Theta} - \frac{d}{d\mathsf{s}}(\mathscr{L}_{\Theta'})\right)\delta\Theta + \mathscr{L}_{R_X}\delta R_X + \mathscr{L}_{R_Y}\delta R_Y + \mathscr{L}_{M_0}\delta M_0\Big\}\mathrm{d}\mathsf{s} \\ &+ \left(\mathscr{L}_{Y'}\Big|_l - l\frac{d}{dt}(\mathscr{L}_{\dot{Y}(l)})\right)\delta Y(l) + \left(\mathscr{L}_{X'}\Big|_l - l\frac{d}{dt}(\mathscr{L}_{\dot{X}(l)})\right)\delta\zeta(l) + \\ &+ \left[l\left(\mathscr{L}_{X_0} - \frac{d}{dt}(\mathscr{L}_{\dot{X}_0})\right) + \mathscr{L}_{X'}\Big|_0^l - l\frac{d}{dt}(\mathscr{L}_{\dot{X}(l)})\right]\delta X_0 + \\ &+ \left(\mathscr{L}_{\Theta'}\Big|_l - l\frac{d}{dt}(\mathscr{L}_{\dot{\Theta}(l)})\right)\delta\Theta(l).\end{aligned} \tag{8.18}$$

It is worth to underline that due to the presence of non-holonomic constraints, the variations $\delta\boldsymbol{w}$ in Eq.(8.18) are not independent, so that the equations of motion can not be directly obtained by simply setting the terms in brackets equal to zero. In the following section, as for the Eq.(7.18) for the discretized system, the non-holonomic kinematic condition is introduced by means of the Lagrange multiplier method, leading to a final formulation of the D'Alembert-Lagrange equation for the continuous system.

8.2.1 The 'skate' non-holonomic constraint acting on the continuous system

The formulation of the non-holonomic 'skate' constraint attached to the final end of the rod at the coordinate $\mathsf{s} = l$ can be expressed either in terms of virtual displacements

$$(\delta X_0 + \delta\zeta(l))\cos\vartheta + \delta Y(l)\sin\vartheta = 0\,, \tag{8.19}$$

where $\vartheta = \Theta(l,t) + \beta_0$, or in terms of the true velocities of the system

$$\dot{X}(l)\cos\vartheta + \dot{Y}(l)\sin\vartheta = 0. \tag{8.20}$$

Introducing the non-holonomic constraint (8.19) into the equation (8.18) by means of the Lagrange multiplier method, one obtains

$$\begin{aligned}
&\int_0^l \delta\mathscr{L}\mathrm{d}\mathsf{s} - p(t)\Big[(\delta X_0 + \delta\zeta(l))\cos\vartheta + \delta Y(l)\sin\vartheta\Big] = \\
&\int_0^l \Bigg\{\left(-\frac{d}{dt}(\mathscr{L}_{\dot{X}}) - \frac{d}{d\mathsf{s}}(\mathscr{L}_{X'})\right)\delta X + \left(-\frac{d}{dt}(\mathscr{L}_{\dot{Y}}) - \frac{d}{d\mathsf{s}}(\mathscr{L}_{Y'})\right)\delta Y + \mathscr{L}_{R_X}\delta R_X + \\
&\qquad + \mathscr{L}_{R_Y}\delta R_Y + \mathscr{L}_{M_0}\delta M_0 + \left(\mathscr{L}_{\Theta} - \frac{d}{d\mathsf{s}}(\mathscr{L}_{\Theta'})\right)\delta\Theta\Bigg\}\mathrm{d}\mathsf{s} + \\
&+ \left(\mathscr{L}_{Y'}\Big|_l - l\frac{d}{dt}(\mathscr{L}_{\dot{Y}(l)}) - p\sin\vartheta\right)\delta Y(l) + \left(\mathscr{L}_{X'}\Big|_l - l\frac{d}{dt}(\mathscr{L}_{\dot{X}(l)}) - p\cos\vartheta\right)\delta\zeta(l) + \\
&+ \left[l\left(\mathscr{L}_{X_0} - \frac{d}{dt}(\mathscr{L}_{\dot{X}_0})\right) + \mathscr{L}_{X'}\Big|_0^l - l\frac{d}{dt}(\mathscr{L}_{\dot{X}(l)}) - p\cos\vartheta\right]\delta X_0 + \\
&+ \left(\mathscr{L}_{\Theta'}\Big|_l - l\frac{d}{dt}(\mathscr{L}_{\dot{\Theta}(l)})\right)\delta\Theta(l),
\end{aligned} \tag{8.21}$$

where p is the unknown reaction force (positive in compression) acting on the non-holonomic constraint. The expression (8.21) is therefore a combination of independent variations of the fundamental variables of the system. For this reason, all the equations multiplied by the related variations can be set equal to zero, thus providing the system of the equations of motion for the non-holonomic elastic rod in the ideal case of null damping forces.

The effect of viscosities

Viscosities can be introduced by writing the virtual work of the damping forces. In particular, through the Rayleigh dissipation function (8.10), the following expression is obtained

$$\int_0^l \sum_i \left(\frac{\partial \mathscr{F}_d}{\partial \dot{\xi}_i} \delta \xi_i \right) \mathrm{d}\mathsf{s} = \mathscr{F}_{\dot{\Theta}'} \delta \Theta \Big|_0^l + \int_0^l \left\{ -\frac{d}{d\mathsf{s}} (\mathscr{F}_{\dot{\Theta}'}) \delta \Theta + \mathscr{F}_{\dot{X}} \delta X + \mathscr{F}_{\dot{Y}} \delta Y \right\} \mathrm{d}\mathsf{s} + \\ + l \left(\mathscr{F}_{\dot{Y}(l)} \delta Y(l) + \mathscr{F}_{\dot{\Theta}(l)} \delta \Theta(l) + \mathscr{F}_{\dot{X}(l)} \delta \zeta(l) + \mathscr{F}_{\dot{X}(l)} \delta X_0 \right) , \tag{8.22}$$

where ξ_i denotes a generic i-th variable of the density of dissipation function $\mathscr{F}_d$ (see Eq.(8.11)). The expression for the equations of motion with non-conservative dissipative effects can be obtained by setting the following equation expressing the balance of energy of the system

$$\int_0^l \delta \mathscr{L} \mathrm{d}\mathsf{s} - p(t) \Big[(\delta X_0 + \delta \zeta(l)) \cos \vartheta + \delta Y(l) \sin \vartheta \Big] = \\ \int_0^l \sum_i \left(\frac{\partial \mathscr{F}_d}{\partial \dot{\xi}_i} \delta \xi_i \right) \mathrm{d}\mathsf{s} , \tag{8.23}$$

which represents a generalization of the Eq.(8.21) where dissipation sources are taken into account.

Finally, after invoking the arbitrariness of the independent variations $\delta \boldsymbol{w}$ of the system, one obtains the following equations of motion for the continuous rod subject to a non-holonomic 'skate' constraint (acting on the system through

the unknown reaction force p) and to dissipative effects

$$
\begin{cases}
\dfrac{d}{dt}(\mathscr{L}_{\dot{X}}) + \dfrac{d}{d\mathsf{s}}(\mathscr{L}_{X'}) + \mathscr{F}_{\dot{X}} = 0 & \text{(8.24a)}\\
\dfrac{d}{dt}(\mathscr{L}_{\dot{Y}}) + \dfrac{d}{d\mathsf{s}}(\mathscr{L}_{Y'}) + \mathscr{F}_{\dot{Y}} = 0 & \text{(8.24b)}\\
\mathscr{L}_{\Theta} - \dfrac{d}{d\mathsf{s}}(\mathscr{L}_{\Theta'}) + \dfrac{d}{d\mathsf{s}}(\mathscr{F}_{\dot{\Theta}'}) = 0 & \text{(8.24c)}\\
\mathscr{L}_{R_X} = 0 & \text{(8.24d)}\\
\mathscr{L}_{R_Y} = 0 & \text{(8.24e)}\\
\mathscr{L}_{M_0} = 0 & \text{(8.24f)}\\
l\dfrac{d}{dt}(\mathscr{L}_{\dot{\Theta}(l)}) - \mathscr{L}_{\Theta'}\Big|_l + \mathscr{F}_{\dot{\Theta}'}\Big|_l + l\mathscr{F}_{\dot{\Theta}(l)} = 0 & \text{(8.24g)}\\
l\dfrac{d}{dt}(\mathscr{L}_{\dot{X}(l)}) - \mathscr{L}_{X'}\Big|_l + l\mathscr{F}_{\dot{X}(l)} + p\cos\vartheta = 0 & \text{(8.24h)}\\
l\dfrac{d}{dt}(\mathscr{L}_{\dot{Y}(l)}) - \mathscr{L}_{Y'}\Big|_l + l\mathscr{F}_{\dot{Y}(l)} + p\sin\vartheta = 0 & \text{(8.24i)}\\
l\dfrac{d}{dt}(\mathscr{L}_{\dot{X}}) - l\mathscr{L}_X + l\dfrac{d}{dt}(\mathscr{L}_{\dot{X}(l)}) + l\mathscr{F}_{\dot{X}(l)} - \mathscr{L}_{X'}\Big|_0^l + p\cos\vartheta = 0 & \text{(8.24j)}\\
\dot{X}(l)\cos(\Theta(l)+\beta_0) + \dot{Y}(l)\sin(\Theta(l)+\beta_0) = 0. & \text{(8.24k)}
\end{cases}
$$

The equations above can be made explicit through Eqs.(8.10) and (8.13),

thus obtaining

$$\begin{cases} \rho\ddot{X} + c_e\dot{X} + R'_X = 0 & \text{(8.25a)} \\ \rho\ddot{Y} + c_e\dot{Y} + R'_Y = 0 & \text{(8.25b)} \\ B\Theta'' + D\dot{\Theta}'' + R_X \sin\Theta - R_Y \cos\Theta = 0 & \text{(8.25c)} \\ X' = \cos\Theta & \text{(8.25d)} \\ Y' = \sin\Theta & \text{(8.25e)} \\ \Theta(0,t) = 0 & \text{(8.25f)} \\ I_{r,L}\ddot{\Theta}(l) + c_{r,L}\dot{\Theta}(l) + B\Theta'(l) + D\dot{\Theta}'(l) = 0 & \text{(8.25g)} \\ M_L\ddot{X}(l) + c_{t,L}\dot{X}(l) - R_X(l) + p\cos\left(\Theta(l) + \beta_0\right) = 0 & \text{(8.25h)} \\ M_L\ddot{Y}(l) + c_{t,L}\dot{Y}(l) - R_Y(l) + p\sin\left(\Theta(l) + \beta_0\right) = 0 & \text{(8.25i)} \\ M_X\ddot{X}_0 + K(X_0 - \Delta) + M_L\ddot{X}(l) + c_{t,L}\dot{X}(l) - R_X(l) + R_X(0) + \\ \qquad + p\cos\left(\Theta(l) + \beta_0\right) = 0 & \text{(8.25j)} \\ \dot{X}(l)\cos\left(\Theta(l) + \beta_0\right) + \dot{Y}(l)\sin\left(\Theta(l) + \beta_0\right) = 0. & \text{(8.25k)} \end{cases}$$

The system (8.25) can be rewritten in a more convenient form by firstly integrating the Eqs.(8.25a) and (8.25b), providing the expressions of the Lagrange multipliers $R_X(\mathsf{s},t)$ and $R_Y(\mathsf{s},t)$ along the span of the rod

$$\begin{aligned} R_X &= R_X(l) + \int_{\mathsf{s}}^{l} \left(\rho\ddot{X} + c_e\dot{X}\right) \mathrm{d}\varsigma, \\ R_Y &= R_Y(l) + \int_{\mathsf{s}}^{l} \left(\rho\ddot{Y} + c_e\dot{Y}\right) \mathrm{d}\varsigma, \end{aligned} \tag{8.26}$$

and representing the space evolution of the components of the total internal force projected along the horizontal X and vertical Y directions, respectively. By means of the equations (8.25h) and (8.25i), the terms $R_X(l,t)$ and $R_Y(l,t)$ can be made explicit, so that the final expressions for the internal forces $R_X(\mathsf{s},t)$ and $R_Y(\mathsf{s},t)$ are given by

$$\begin{aligned} R_X &= M_L\ddot{X}(l) + c_{t,L}\dot{X}(l) + p\cos\vartheta + \int_{\mathsf{s}}^{l} \left(\rho\ddot{X} + c_e\dot{X}\right) \mathrm{d}\varsigma, \\ R_Y &= M_L\ddot{Y}(l) + c_{t,L}\dot{Y}(l) + p\sin\vartheta + \int_{\mathsf{s}}^{l} \left(\rho\ddot{Y} + c_e\dot{Y}\right) \mathrm{d}\varsigma. \end{aligned} \tag{8.27}$$

Eqs.(8.27) therefore represent the balance of linear momentum along the X and Y directions for the portion of rod comprised between the coordinates s and l.

The substitution of Eqs.(8.27) into Eqs.(8.25c) and (8.25j) yields the following final expression for the system (8.25)

$$
\begin{cases}
B\Theta'' + D\dot{\Theta}'' + p\sin(\Theta - \vartheta) + \\
\sin\Theta\left(M_L\ddot{X}(l) + c_{t,L}\dot{X}(l) + \displaystyle\int_{\mathsf{s}}^{l}\left(\rho\ddot{X} + c_e\dot{X}\right)\mathrm{d}\varsigma\right) + & (8.28a)\\
-\cos\Theta\left(M_L\ddot{Y}(l) + c_{t,L}\dot{Y}(l) + \displaystyle\int_{\mathsf{s}}^{l}\left(\rho\ddot{Y} + c_e\dot{Y}\right)\mathrm{d}\varsigma\right) = 0 \\
\Theta(0,t) = 0 & (8.28b)\\
I_{r,L}\ddot{\Theta}(l) + c_{r,L}\dot{\Theta}(l) + B\Theta'(l) + D\dot{\Theta}'(l) = 0 & (8.28c)\\
M_X\ddot{X}_0 + K(X_0 - \Delta) + M_L\ddot{X}(l) + c_{t,L}\dot{X}(l) + p\cos\vartheta + \\
\qquad + \displaystyle\int_{0}^{l}\left(\rho\ddot{X} + c_e\dot{X}\right)\mathrm{d}\varsigma = 0 & (8.28d)\\
\dot{X}(l)\cos\left(\Theta(l) + \beta_0\right) + \dot{Y}(l)\sin\left(\Theta(l) + \beta_0\right) = 0 & (8.28e)\\
X' = \cos\Theta & (8.28f)\\
Y' = \sin\Theta. & (8.28g)
\end{cases}
$$

which collects the equations of motion for the mechanical system, expressed in terms of rotation field $\Theta(\mathsf{s}, t)$ and position of the clamp $X_0(t)$ at the rod's initial coordinate $\mathsf{s} = 0$. In fact, equations (8.28f) and (8.28g) can be integrated and expressed through Eqs.(8.8). Therefore, Eqs.(8.28) represent a system of 5 equations in the 5 unknowns $\{\Theta,\, X_0,\, p,\, X,\, Y\}$, complemented by Eqs.(8.28b) and (8.28c) expressing the boundary conditions for Θ. As for the discretized structures, due to the presence of the unknown reaction force p, the non-holonomic constraint's equation (8.28e) has to be introduced within the system of the governing equations.

8.3 Quasi-static solutions: the non-holonomic Euler's elastica

Neglecting the inertial and damping terms in the system (8.25), one obtains the equations for the Euler's elastica subject to a 'skate' non-holonomic constraint. Moreover, mixed Dirichlet and Neumann boundary conditions are given at the ends in virtue of the imposed null rotation at the initial end $\mathsf{s} = 0$ and of the null bending moment at the final one $\mathsf{s} = l$, respectively. The complete set of the governing equations for the quasi-static problem, together with the appropriate boundary conditions, is given by

$$
\begin{cases}
R_X'^{\mathrm{QS}} = 0 \qquad \rightarrow \qquad R_X^{\mathrm{QS}}(\mathsf{s}) = \mathrm{const} & \text{(8.29a)} \\
R_Y'^{\mathrm{QS}} = 0 \qquad \rightarrow \qquad R_Y^{\mathrm{QS}}(\mathsf{s}) = \mathrm{const} & \text{(8.29b)} \\
B\Theta''^{\mathrm{QS}} + R_X^{\mathrm{QS}} \sin\Theta^{\mathrm{QS}} - R_Y^{\mathrm{QS}} \cos\Theta^{\mathrm{QS}} = 0 & \text{(8.29c)} \\
X' = \cos\Theta^{\mathrm{QS}} & \text{(8.29d)} \\
Y' = \sin\Theta^{\mathrm{QS}} & \text{(8.29e)} \\
\Theta^{\mathrm{QS}}(0) = 0 & \text{(8.29f)} \\
B\Theta'^{\mathrm{QS}}(l) = 0 & \text{(8.29g)} \\
R_X^{\mathrm{QS}} = p^{\mathrm{QS}} \cos\vartheta^{\mathrm{QS}} & \text{(8.29h)} \\
R_Y^{\mathrm{QS}} = p^{\mathrm{QS}} \sin\vartheta^{\mathrm{QS}} & \text{(8.29i)} \\
K(X_0^{\mathrm{QS}} - \Delta) + p^{\mathrm{QS}} \cos\vartheta^{\mathrm{QS}} = 0\,, & \text{(8.29j)}
\end{cases}
$$

where the equation for the non-holonomic constraint (8.28e) is automatically satisfied. Therefore, as for the case of the discrete chain, the system (8.29) has a number of unknowns that exceeds the number of the governing equations of a factor 1.

By considering the exact solution for the inflectional elastica reported in Chapter 2 through the Jacobi elliptic functions (see also Cazzolli and Dal Corso [33]), the solution for the Euler's elastica can be obtained by prescribing the following four parameters:

- the left end rotation of the rod $\Theta^{\mathrm{QS}}(0)$, which is prescribed by equation (8.29f);

- the right end rotation of the rod $\Theta^{\text{QS}}(l)$;
- the inclination of the total reaction force at both ends of the rod $\beta = -\vartheta^{\text{QS}} = -\Theta^{\text{QS}}(l) - \beta_0$, which is a function of the end rotation $\Theta^{\text{QS}}(l)$ and of the known inclination of the non-holonomic constraint β_0;
- the characteristic parameter of the elastica η, which can be set equal to $\sin(|\beta_0|/2)$ by properly exploiting the analytical expression for the boundary condition (8.29g) through the Eqs.(2.44) and $(2.39)_2$[2].

Due to the fact that, with reference to the Eqs.(2.15), (2.32) and (2.39), the non-holonomic reaction force $p^{\text{QS}} = |R|$ can be expressed in terms of $\Theta^{\text{QS}}(l)$, such rotation at the final end of the rod $\mathsf{s} = l$ represents the only unknown parameter of the system, while the generalized coordinate X_0^{QS} can be consequently obtained from the equation (8.29j) as a function the known position of the left end of the extensional spring, Δ.

As for the case of the discrete chain, the infinite quasi-static solutions for the system can be parametrized through the only 'free' coordinate of the system (8.29), in this case they are represented by the rotation $\Theta^{\text{QS}}(l)$, which is defined within a *manifold of equilibrium states* (see Neimark and Fufaev [85]). In particular, such domain is given by

$$\mathcal{D} := \left\{ \Theta^{\text{QS}}(l) \in \mathbb{R} \ : \ \left| \frac{\sin\left(\dfrac{\Theta^{\text{QS}}(l) + \beta_0}{2}\right)}{\sin\dfrac{|\beta_0|}{2}} \right| \leq 1 \right\}, \tag{8.30}$$

expressing the condition for the parameter ω_0 in equation $(2.39)_1$ to be real. The domain (8.30) therefore represents the exact expression for the manifold of equilibrium states for the elastica subject to a 'skate' non-holonomic constraint.

An example of multiple solutions for the system (8.29) is shown in Fig.8.2. Five different quasi-static configurations are presented, corresponding to different values of the rotation at the final end $\Theta^{\text{QS}}(l)$ and $X_0^{\text{QS}} = 0$, and therefore to different imposed displacements Δ of the left end of the extensional spring. Solutions are represented with different colors for the particular case $\beta_0 = 0.1\pi$.

[2] In fact, the condition of null curvature at the coordinate $s = 1$ leads to the condition

$$\cos\left\{\arcsin\left[\frac{1}{\eta}\sin\left(\frac{-\beta_0}{2}\right)\right]\right\} = 0, \quad \rightarrow \quad \sqrt{1 - \frac{1}{\eta^2}\sin^2\left(\frac{\beta_0}{2}\right)} = 0$$

so that $\eta = \sin(|\beta_0|/2)$

In particular through Eq.(8.30), the rotation $\Theta^{\text{QS}}(l)$ for an Euler's elastica with $\eta \approx 0.1564$ having a single inflection point at the final end $\mathsf{s} = l$ can be freely chosen within the interval $\Theta^{\text{QS}}(l) \in [0, -0.2\pi]$.

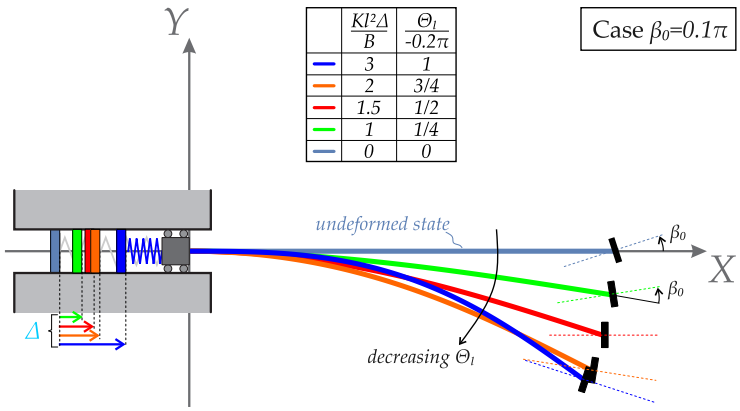

Figure 8.2: Five quasi-static solutions for an Euler's elastica having an inflection point at the final end and $\beta_0 = 0.1\pi$. The solutions are highlighted with different colors (light blue, green, red, orange, blue), differing in the values of the end's rotation $\Theta^{\text{QS}}(l) = -0.2\pi\,[0, 0.25, 0.5, 0.75, 1]$ and corresponding to the dimensionless parameter $Kl^2\,\Delta/B = [0, 1, 1.5, 2, 3]$. Moreover, the displacement of the initial end $\mathsf{s} = 0$ is set to be null $X_0^{\text{QS}} = 0$.

Finally, the exact definition of the characteristic parameter η as a function of the inclination of the non-holonomic constraint β_0

$$\eta = \sin\frac{|\beta_0|}{2}\,,$$

provides a proof of the uniqueness of the trivial solution in the case $\beta_0 = 0$. Indeed, in that case the domain (8.30) reduces to the condition $\Theta^{\text{QS}}(l) = 0$, while the obvious condition $\eta = 0$ implies that the solution is equal to the trivial one ($\Theta^{\text{QS}}(\mathsf{s}) = 0$ for every $\mathsf{s} \in [0, l]$).

8.4 Linearized equations of motion

The linearization of the equations of motion (8.28a) and (8.28d) and of the boundary conditions equations (8.28b) and (8.28c) around the trivial quasi-static solution $\Theta^{\text{QS}} = 0$ is performed by introducing the following perturbations

$$\Theta = \epsilon\,\hat{\Theta}, \qquad X_0 = X_0^{\text{QS}} + \epsilon\,\hat{X}_0, \qquad p = p^{\text{QS}} + \epsilon\,\hat{p}, \tag{8.31}$$

and taking the derivative of the perturbed equations with respect to ϵ around 0. As for the discretized structures in Chapter 7, no perturbations are considered for the imposed displacement Δ.

For the sake of simplicity, the symbol '$\hat{}$' is removed in the following equations and the quantities $\{\Theta,\, X_0,\, p\}$ will therefore denote perturbations of the related scalar fields governing the problem.

With reference to the expressions for the time derivatives of X and Y in Eqs.(8.12), the following linearized version of the equation (8.28a) is obtained

$$\begin{aligned} &B\Theta'' + D\dot{\Theta}'' - M_L \int_0^l \ddot{\Theta}\mathrm{d}\mathsf{s} - c_{t,L}\int_0^l \dot{\Theta}\mathrm{d}\mathsf{s} - \int_{\mathsf{s}}^l \left(\rho\int_0^{\varsigma} \ddot{\Theta}\mathrm{d}\sigma + c_e\int_0^{\varsigma}\dot{\Theta}\mathrm{d}\sigma\right)\mathrm{d}\varsigma + \\ &- p\sin(\beta_0) + p^{\text{QS}}\cos(\beta_0)(\Theta - \Theta(l)) = 0\,, \end{aligned} \tag{8.32}$$

where the reaction force of the non-holonomic constraint is present both in terms of the 'pre-stress' parameter p^{QS} at the equilibrium and in terms of the perturbation field p.

The linearization of the Eq.(8.28g) leads to the following condition

$$Y' = \Theta\,, \tag{8.33}$$

which can be substituted within the equation (8.32) leading to the following expression

$$\begin{aligned} &B\,Y''' + D\,\dot{Y}''' - M_L\int_0^l \ddot{Y}'\mathrm{d}\mathsf{s} - c_{t,L}\int_0^l \dot{Y}'\mathrm{d}\mathsf{s} - \int_{\mathsf{s}}^l \left(\rho\int_0^{\varsigma}\ddot{Y}'\mathrm{d}\sigma + c_e\int_0^{\varsigma}\dot{Y}'\mathrm{d}\sigma\right)\mathrm{d}\varsigma + \\ &- p\sin(\beta_0) + p^{\text{QS}}\cos(\beta_0)\,(Y' - Y'(l)) = 0. \end{aligned} \tag{8.34}$$

In order to simplify the expression (8.34), a derivation with respect to s is performed, leading to the following partial differential equation

$$B\,Y'''' + D\,\dot{Y}'''' + \rho\,\ddot{Y} + c_e\,\dot{Y} + p^{\text{QS}}\cos(\beta_0)\,Y'' = 0\,, \tag{8.35}$$

so that the field $Y(\mathsf{s}, t)$ is still dependent on the value assumed by the reaction force p^{QS} of the non-holonomic constraint at equilibrium.

Due to the presence of fourth order spatial derivatives in the equation (8.35), a further boundary condition has to be introduced. Such condition is obtained by particularising the differential equation (8.34) at the coordinate $\mathsf{s} = l$, thus obtaining

$$B\,Y'''(l) + D\,\dot{Y}'''(l) - M_L\,\ddot{Y}(l) - c_{t,L}\,\dot{Y}(l) - p\,\sin(\beta_0) = 0, \tag{8.36}$$

where the following substitutions in terms of the linearised quantities have been performed (note that $Y(0) = 0$)

$$\ddot{Y}(l) = \int_0^l \ddot{Y}'\mathrm{d}\mathsf{s}, \qquad \dot{Y}(l) = \int_0^l \dot{Y}'\mathrm{d}\mathsf{s}.$$

The linearized formulation of the further boundary conditions' equations is given by

$$B\,Y''(l) + D\,\dot{Y}''(l) + I_{r,L}\,\ddot{Y}'(l) + c_{r,L}\,\dot{Y}'(l) = 0\,, \tag{8.37a}$$

$$Y'(0,t) = 0\,, \tag{8.37b}$$

$$Y(0,t) = 0. \tag{8.37c}$$

where the first two expressions represent the linearized versions of the Eqs.(8.28c) and (8.28b) respectively, and where the latter represents a further Dirichlet boundary condition expressing the condition $Y(0,t) = 0$ imposed at the initial end of the rod $\mathsf{s} = 0$.

Finally, the linearized equations of the non-holonomic constraint (8.28e) and of the Eq.(8.28d) are given by

$$\dot{X}_0\cos\beta_0 + \dot{Y}(l)\sin\beta_0 = 0\,, \tag{8.38}$$

and

$$(M_X + M_L + \rho l)\ddot{X}_0 + (c_{t,L} + c_e l)\dot{X}_0 + K\,X_0 = p^{\mathrm{QS}}\sin\beta_0\,Y'(l) - p\cos\beta_0\,, \tag{8.39}$$

respectively.

In the next Section, all the aforementioned linearized equations are particularized for $\beta_0 = 0$, which represents a perfectly-aligned non-holonomic 'skate' constraint, having a rolling direction perpendicular to the tangent vector at the final end of the rod $\mathsf{s} = l$.

8.4.1 Case of a perfectly-aligned non-holonomic constraint $\beta_0 = 0$

Taking $\beta_0 = 0$ in Eqs.(8.35), (8.36), (8.37) and (8.38), the following system of linearized equations holds

$$\begin{cases} B\,Y'''' + D\,\dot{Y}'''' + \rho\,\ddot{Y} + c_e\,\dot{Y} + p^{\mathrm{QS}}\,Y'' = 0\,, & \text{(8.40a)} \\ B\,Y'''(l) + D\,\dot{Y}'''(l) - M_L\,\ddot{Y}(l) - c_{t,L}\,\dot{Y}(l) = 0\,, & \text{(8.40b)} \\ B\,Y''(l) + D\,\dot{Y}''(l) + I_{r,L}\,\ddot{Y}'(l) + c_{r,L}\,\dot{Y}'(l) = 0\,, & \text{(8.40c)} \\ Y'(0,t) = 0\,, & \text{(8.40d)} \\ Y(0,t) = 0\,, & \text{(8.40e)} \\ \dot{X}_0 = 0 \qquad \rightarrow \qquad X_0 = \mathrm{const}\,, & \text{(8.40f)} \\ (M_X + M_L + \rho l)\ddot{X}_0 + (c_{t,L} + c_e l)\dot{X}_0 + K\,X_0 + p = 0\,, & \text{(8.40g)} \end{cases}$$

which therefore represents the linearized problem of and elastic rod oscillating about its trivial solution and whose final end is constrained to slide perpendicularly to the tangent vector of the rod's final end at any instant of time t.

Moreover, through Eqs.(8.40f) and (8.40g) the perturbation of the reaction force p acting on the system through the non-holonomic constraint is constant and proportional to the perturbation in the parameter X_0

$$p = -K\,X_0 = \mathrm{const}_1. \tag{8.41}$$

Dimensionless formulation

The following dimensionless variables are considered

$$\begin{aligned} &s = \frac{\mathsf{s}}{l}, \quad \tau = \frac{t}{T}, \quad \tilde{Y} = \frac{Y}{l}, \quad \tilde{p}^{\mathrm{QS}} = \frac{p^{\mathrm{QS}} l^2}{B}, \quad \tilde{M}_L = \frac{M_L}{\rho l}, \quad \tilde{I}_{r,L} = \frac{I_{r,L}}{l^3 \rho} \\ &\tilde{c}_e = \frac{c_e l^2}{\sqrt{\rho B}}, \quad \tilde{c}_{t,L} = \frac{c_{t,L} l}{\sqrt{\rho B}}, \quad \tilde{c}_{r,L} = \frac{c_{r,L}}{l\sqrt{\rho B}}, \quad \tilde{D} = \frac{D}{l^2\sqrt{\rho B}}, \end{aligned} \tag{8.42}$$

where $T = l^2\sqrt{\dfrac{\rho}{B}}$ is the characteristic time of the structure expressed in terms of some rod's mechanical parameters. The dimensionless formulation for the

first five equations of the system (8.40) in the displacement $\tilde{Y}(s,\tau)$ is given by

$$\begin{cases} \tilde{Y}'''' + \tilde{D}\,\dot{\tilde{Y}}'''' + \tilde{p}^{\mathrm{QS}}\,\tilde{Y}'' + \ddot{\tilde{Y}} + \tilde{c}_e\dot{\tilde{Y}} = 0\,, & \text{(8.43a)} \\ \tilde{Y}'''(1) + \tilde{D}\,\dot{\tilde{Y}}'''(1) - \tilde{M}_L\,\ddot{\tilde{Y}}(1) - \tilde{c}_{t,L}\,\dot{\tilde{Y}}(1) = 0\,, & \text{(8.43b)} \\ \tilde{Y}''(1) + \tilde{D}\,\dot{\tilde{Y}}''(1) + \tilde{I}_{r,L}\,\ddot{\tilde{Y}}'(1) + \tilde{c}_{r,L}\,\dot{\tilde{Y}}'(1) = 0\,, & \text{(8.43c)} \\ \tilde{Y}'(0,\tau) = 0\,, & \text{(8.43d)} \\ \tilde{Y}(0,\tau) = 0\,, & \text{(8.43e)} \end{cases}$$

where the symbols ' ′ ' and ' ˙ ' represent now derivatives with respect to the dimensionless quantities s and τ.

The exponential solution $\tilde{Y}(s,\tau) = \Psi(s)e^{\Omega\tau}$ is introduced, leading to the following system of equations

$$\begin{cases} (1+\tilde{D}\,\Omega)\,\Psi''''(s) + \tilde{p}^{\mathrm{QS}}\,\Psi''(s) + (\Omega^2 + \tilde{c}_e\,\Omega)\,\Psi(s) = 0\,, & \text{(8.44a)} \\ (1+\tilde{D}\,\Omega)\,\Psi'''(1) = (\tilde{M}_L\,\Omega^2 + \tilde{c}_{t,L}\,\Omega)\,\Psi(1)\,, & \text{(8.44b)} \\ (1+\tilde{D}\,\Omega)\,\Psi''(1) + (\tilde{I}_{r,L}\,\Omega^2 + \tilde{c}_{r,L}\,\Omega)\,\Psi'(1) = 0\,, & \text{(8.44c)} \\ \Psi'(0) = 0\,, & \text{(8.44d)} \\ \Psi(0) = 0\,, & \text{(8.44e)} \end{cases}$$

and where Ω represents the dimensionless eigenvalue of the system.

Absence of buckling loads for $\beta_0 = 0$

Critical loads corresponding to buckling of the elastic rod can be obtained from Eqs.(8.44) by simply imposing $\Omega = 0$, thus obtaining

$$\begin{cases} \Psi''''(s) + \tilde{p}^{\mathrm{QS}}\,\Psi''(s) = 0\,, & \text{(8.45a)} \\ \Psi'''(1) = 0, \quad \Psi''(1) = 0, \quad \Psi'(0) = 0, \quad \Psi(0) = 0\,, & \text{(8.45b)} \end{cases}$$

so that the only solution for Ψ satisfying the imposed boundary conditions is the trivial one. In analogy with Chapter 7, one can therefore conclude that no buckling occurs also for the continuous non-holonomic system in the case of a

perfectly-aligned constraint $\beta_0 = 0$. This statement is in agreement with the conclusions obtained for the quasi-static solutions in Section 8.3, as the unique parameter η holding for $\beta_0 = 0$ is the null one, thus corresponding to the trivial configuration.

Evaluation of the flutter load

The general solution for the differential equation (8.44a) can be written as

$$\Psi(s) = A_1 \sin(\lambda_1 s) + A_2 \cos(\lambda_1 s) + A_3 \sinh(\lambda_2 s) + A_4 \cosh(\lambda_2 s)\,, \quad (8.46)$$

where

$$\begin{aligned} \lambda_1 &= \sqrt{\frac{(\tilde{D}\,\Omega + 1)\sqrt{(\tilde{p}^{\mathrm{QS}})^2 - 4\,\Omega(\tilde{D}\,\Omega + 1)(\tilde{c}_e + \Omega)}}{(\tilde{D}\,\Omega + 1)^2} + \tilde{p}^{\mathrm{QS}}}{2\,\tilde{D}\,\Omega + 2}}\,, \\ \lambda_2 &= \sqrt{\frac{(\tilde{D}\,\Omega + 1)\sqrt{(\tilde{p}^{\mathrm{QS}}) - 4\,\Omega(\tilde{D}\,\Omega + 1)(\tilde{c}_e + \Omega)}}{(\tilde{D}\,\Omega + 1)^2} - \tilde{p}^{\mathrm{QS}}}{2\,\tilde{D}\,\Omega + 2}}\,. \end{aligned} \quad (8.47)$$

The imposition of the boundary conditions (8.44b), (8.44c), (8.44d) and (8.44e) on the general solution (8.46) leads to the following linear system

$$\begin{bmatrix} 0 & 1 & 0 & 1 \\ \lambda_1 & 0 & \lambda_2 & 0 \\ a_{31} & a_{32} & a_{33} & a_{34} \\ a_{41} & a_{42} & a_{43} & a_{44} \end{bmatrix} \begin{bmatrix} A_1 \\ A_2 \\ A_3 \\ A_4 \end{bmatrix} = 0\,, \quad (8.48)$$

where

$$\begin{cases} a_{31} = \lambda_1 \cos\lambda_1 \left(\tilde{c}_{r,L}\Omega + \tilde{I}_{r,L}\Omega^2\right) - \lambda_1^2(\tilde{D}\Omega + 1)\sin\lambda_1, \\ a_{32} = -\lambda_1 \sin\lambda_1 \left(\tilde{c}_{r,L}\Omega + \tilde{I}_{r,L}\Omega^2\right) - \lambda_1^2(\tilde{D}\Omega + 1)\cos\lambda_1, \\ a_{33} = \lambda_2 \cosh\lambda_2 \left(\tilde{c}_{r,L}\Omega + \tilde{I}_{r,L}\Omega^2\right) + \lambda_2^2(\tilde{D}\Omega + 1)\sinh\lambda_2, \\ a_{34} = \lambda_2 \sinh\lambda_2 \left(\tilde{c}_{r,L}\Omega + \tilde{I}_{r,L}\Omega^2\right) + \lambda_2^2(\tilde{D}\Omega + 1)\cosh\lambda_2, \end{cases} \quad (8.49)$$

and

$$\begin{cases} a_{41} = -\sin\lambda_1 \left(\tilde{c}_{t,L}\Omega + \tilde{M}_L\Omega^2\right) - \lambda_1^3(\tilde{D}\Omega + 1)\cos\lambda_1, \\ a_{42} = -\cos\lambda_1 \left(\tilde{c}_{t,L}\Omega + \tilde{M}_L\Omega^2\right) + \lambda_1^3(\tilde{D}\Omega + 1)\sin\lambda_1, \\ a_{43} = -\sinh\lambda_2 \left(\tilde{c}_{t,L}\Omega + \tilde{M}_L\Omega^2\right) + \lambda_2^3(\tilde{D}\Omega + 1)\cosh\lambda_2, \\ a_{44} = -\cosh\lambda_2 \left(\tilde{c}_{t,L}\Omega + \tilde{M}_L\Omega^2\right) + \lambda_2^3(\tilde{D}\Omega + 1)\sinh\lambda_2. \end{cases} \tag{8.50}$$

The system (8.48) admits non-trivial solutions for vanishing determinant of the related matrix, providing the equation for the determination of the eigenvalues Ω as functions of the dimensionless reaction force $\tilde{p}^{\mathrm{QS}}$. Such equation is given by

$$\begin{aligned} &\sinh\lambda_2\Big[(\lambda_1^2 - \lambda_2^2)\sin\lambda_1\left(\lambda_1^2\lambda_2^2C_1^2 - C_2C_3\right) + \lambda_1C_1\left(\lambda_1^2 + \lambda_2^2\right)\cos\lambda_1\left(\lambda_2^2C_2 - C_3\right)\Big] + \\ &+ \lambda_2\cosh\lambda_2\Big[2\lambda_1\cos\lambda_1\left(\lambda_1^2\lambda_2^2C_1^2 - C_2C_3\right) + C_1\left(\lambda_1^2 + \lambda_2^2\right)\sin\lambda_1\left(\lambda_1^2C_2 + C_3\right)\Big] + \\ &+ \lambda_1\lambda_2\Big[C_1^2\left(\lambda_1^4 + \lambda_2^4\right) + 2C_2C_3\Big] = 0\,, \end{aligned} \tag{8.51}$$

where

$$C_1 = 1 + \tilde{D}\,\Omega, \qquad C_2 = \Omega\left(\tilde{c}_{r,L} + \Omega\,\tilde{I}_{r,L}\right), \qquad C_3 = \Omega\left(\tilde{c}_{t,L} + \Omega\,\tilde{M}_L\right).$$

All the critical loads causing flutter instabilities can therefore be obtained from Eq.(8.51) and are represented by values of pre-stress $\tilde{p}^{\mathrm{QS}}$ that cause the real part of the complex conjugate eigenvalues Ω to become positive. Conversely, the divergence load is given by the value of $\tilde{p}^{\mathrm{QS}}$ providing a strictly positive eigenvalue. Moreover, the characteristic equation (8.51) is found to be exactly the same that governs the problem of a non-conservative follower force applied at the final end of an elastic cantilever (Pflüger and Beck columns) and proposed by Detinko [41] and Tommasini et al.[111]. Therefore, in these structures to critical loads are the same when the 'new' parameters of the rotational inertia $\tilde{I}_{r,L}$ and the damping factors $\tilde{c}_{t,L}$ and $\tilde{c}_{r,L}$ at final end of the rod are set equal to zero.

As a final remark, the trivial eigenvalue $\Omega = 0$ is always a solution for Eq.(8.51). As previously seen in Chapter 7, this peculiarity is typical of non-holonomic systems, so that the trivial solution can be simply omitted to evaluate the stability of configurations belonging to the manifold of equilibrium states (see Neimark and Fufaev [85]).

Numerical examples: stability and Ziegler's destabilization paradox

Branches of the real and imaginary parts of the eigenvalues Ω for the non-holonomic continuous rod having a mass ratio $\tilde{M}_L = 1$, a null rotational inertia $\tilde{I}_{r,L} = 0$ at the final end and subject to an internal dissipative effect $\tilde{D} = 0.02$ (while $\tilde{c}_e = \tilde{c}_{t,L} = \tilde{c}_{r,L} = 0$) are reported in Fig.8.3, together with a comparison between the flutter load for the continuous rod, calculated through equation (8.51), and the critical loads obtained for its discretized counterparts (calculated through the methodology proposed in Chapter 7) at increasing number N of rigid bars. The approximated values for the ideal flutter and divergence load at null viscosities 'from the beginning' are also calculated. In agreement with the results obtained for the Pflüger column by Tommasini et al. [111] and according to the definitions (7.67), one obtains $\mathcal{P}_0 \approx 16.212$ and $\mathcal{D}_0 \approx 34.465$, respectively. On the other hand, the approximated value of the flutter and divergence loads for $\tilde{D} = 0.02$ are equal to $\tilde{p}^{\mathrm{QS}}_{\mathrm{flu}} \approx 7.920 < \mathcal{P}_0$ and $\tilde{p}^{\mathrm{QS}}_{\mathrm{div}} \approx 40.646$, respectively.

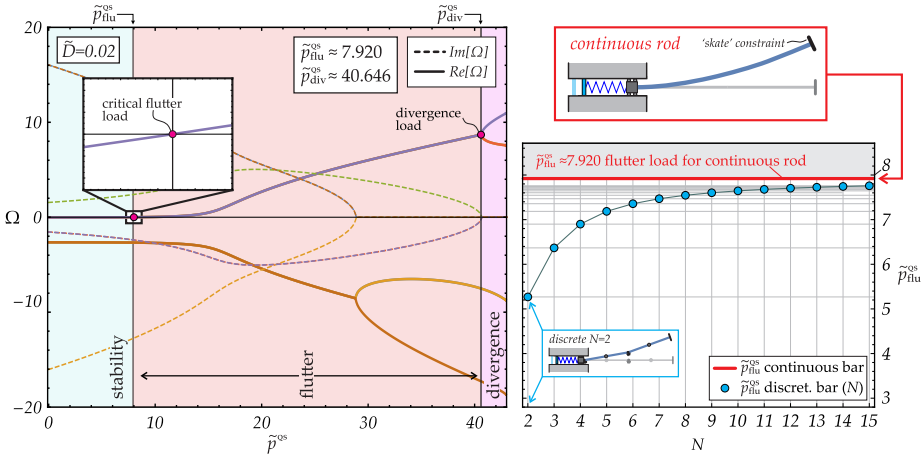

Figure 8.3: (Left) Branching of the real and imaginary parts of the eigenvalues Ω as functions of the dimensionless reaction force $\tilde{p}^{\mathrm{QS}}$ of the non-holonomic 'skate' constraint. Case $\tilde{M}_L = 1$, $\tilde{I}_{r,L} = 0$ and $\tilde{D} = 0.02$. The flutter and divergence loads are approximately equal to $\tilde{p}^{\mathrm{QS}}_{\mathrm{flu}} \approx 7.920$ and $\tilde{p}^{\mathrm{QS}}_{\mathrm{div}} \approx 40.646$, respectively. (Right) Comparison between the critical load of the continuous system and those of the disctretized chains at increasing the number N of rigid bars, showing an asymptotic behaviour towards the critical load of the continuous rod

In order to compare the flutter load obtained for the continuous rod with those of its discretized counterparts, the homogenization of the rotational springs

and of the internal damping is needed. With reference to Domokos [42] and by considering the definitions of damping coefficients and mechanical parameters introduced in Chapter 7 for the visco-elastic chain, the following homogenized quantities are introduced

$$k = \frac{B}{L}N, \qquad c_i = \frac{D}{L}N, \qquad k_1 = 2\,k\,,$$

where the stiffness of the rotational springs is assumed to be the same for all the rigid bars with the exception of the first one $k = k_2 = \cdots = k_N$. Moreover, L is the total length of the discrete system, assumed equal to the length of the continuous rod. As shown in Fig.8.3 (right), the flutter load of the discrete structures at increasing number of rigid bars tends to the flutter load of the non-holonomic continuous column.

Finally, the Ziegler's destabilization paradox in the limit of vanishing viscosities for the particular case $\tilde{M}_L = 1$ and $\tilde{I}_{r,L} = 0$ is demonstrated in the presence of a single damping source.

- **Internal viscosity $\tilde{D} \neq 0$:** by assuming an extremely small viscosity $\tilde{D} = 10^{-10}$, one obtains

  $$\lim_{\tilde{D}\to 10^{-10}} \tilde{p}_{\text{flu}}^{\text{QS}}(\tilde{D}) \approx 7.905 < \mathcal{P}_0\,,$$

  which is lower than the ideal flutter load for the undamped system, so that the Ziegler's destabilization paradox occurs

- **External damping $\tilde{c}_e \neq 0$:** assuming for instance an external damping coefficient equal to $\tilde{c}_e = 0.5$, the critical flutter load is equal to $\tilde{p}_{\text{flu}}^{\text{QS}} \approx 16.124$, which is lower than the ideal load $\mathcal{P}_0$. Moreover, the Ziegler's paradox can be proven by taking the limit for a vanishing damping coefficient, thus obtaining

  $$\lim_{\tilde{c}_e\to 10^{-10}} \tilde{p}_{\text{flu}}^{\text{QS}}(\tilde{c}_e) \approx 16.122 < \mathcal{P}_0\,,$$

- **Translational damping acting on the non-holonomic constraint $\tilde{c}_{t,L} \neq 0$:** consistently with the behaviour of the discretized system introduced in Chapter 7, a *viscosity-independent Ziegler's paradox* also occurs for the continuous rod, as the critical flutter load becomes independent of the value assumed by the damping coefficient $\tilde{c}_{t,L}$ and not higher than the ideal load $\mathcal{P}_0$. In fact, the corresponding critical value is equal to

  $$\tilde{p}_{\text{flu}}^{\text{QS}}(\tilde{c}_{t,L}) = \text{const} \approx 16.052 < \mathcal{P}_0\,,$$

- **Rotational damping acting on the non-holonomic constraint $\tilde{c}_{r,L} \neq 0$:** again the *viscosity-independent Ziegler's paradox* occurs, being the critical flutter load independent of the value assumed by the damping coefficient $\tilde{c}_{r,L}$ and not higher than the ideal load $\mathcal{P}_0$. The corresponding critical value is equal to

$$\tilde{p}_{\text{flu}}^{\text{QS}}(\tilde{c}_{r,L}) = \text{const} \approx 5.219 < \mathcal{P}_0 \,,$$

8.5 Conclusions

The presented analysis shows that a continuous elastic rod subject to a non-holonomic 'skate' constraint and loaded through conservative forces can suffer flutter instabilities.

As for the discrete systems analyzed in Chapter 7, the continuous non-holonomic device shows exactly the same critical loads for flutter and divergence and the same Ziegler paradox that one may obtain from the study of the linearized stability of its non-conservative counterpart, represented in this case by a Pflüger column subject to a follower load. Moreover the rotational and translational viscous friction terms acting on the non-holonomic 'skate' constraint lead to a viscosity-independent destabilization paradox. Such phenomenon therefore represents a new intriguing insight in structural instability and provides a further proof of the mechanical equivalence between non-holonomic conditions and *polygenic* [71] (for instance follower) forces that cannot be derived from any scalar functional.

Finally, the obtained critical loads for a continuous system are also in good agreement with those obtained through a discretized model with homogenized parameters when the number of rigid bars is sufficiently high.

A

Complementary equations for the elastica catastrophe machines

A.1 Complementary equations for the theoretical framework of the *elastica catastrophe machines*

This Section is devoted to further considerations regarding the theoretical framework of the *elastica catastrophe machines*, with emphasis on the reduction of the dependencies of the control parameters on the physical and kinematical coordinates. Moreover, suggested initial values for such control parameters are proposed to initiate the evolution of the deformed shape within the inextensibility set and in the neighbourhood of an (if existing) effective catastrophe locus. Finally, a detailed description of the algorithm for the numerical evaluation of the catastrophe loci is presented.

A.1.1 Reducing the dependencies between coordinates

As discussed in the main document, the generic configuration of the rod can be equivalently described (i.) through the three coordinates $\{X_l, Y_l, \Theta_l\}$ expressing the position of the rod's final end, (ii.) through three primary kinematical

quantities $\{d, \theta_A, \theta_S\}$ or (iii.) through the two control parameters $\{p_1, p_2\}$. The discrepancy in the number of the variables in each of these three representations suggests that the coordinates p_j in the equation

$$p_j = \widetilde{p}_j(X_l, Y_l, \Theta_l, \mathbf{q}), \qquad j = 1, 2, \tag{A.1}$$

can be also expressed as function of only two coordinates of the rod's final end, namely

$$p_j = \widetilde{p}_j(Y_l, \Theta_l, \mathbf{q}) \qquad \text{or} \qquad p_j = \widetilde{p}_j(X_l, \Theta_l, \mathbf{q}), \qquad j = 1, 2, \tag{A.2}$$

so that the substitution into Eq.(6.18) provides one of the two coordinates in terms of the other coordinate and the rotation as

$$X_l = X_l(Y_l, \Theta_l, \mathbf{q}), \qquad \text{or} \qquad Y_l = Y_l(X_l, \Theta_l, \mathbf{q}). \tag{A.3}$$

By considering the two relations (A.3) into Eqs.(6.17) leads to two implicit relations involving the symmetric and antisymmetric angles together with one of the two physical coordinates,

$$\begin{aligned} &G(Y_l, \theta_A, \theta_S, \mathbf{q}) = X_l\left(Y_l, 2\theta_S, \mathbf{q}\right) \tan(\theta_S - \theta_A) - Y_l = 0 \\ &\text{or} \\ &H(X_l, \theta_A, \theta_S, \mathbf{q}) = X_l \tan(\theta_S - \theta_A) - Y_l\left(X_l, 2\theta_S, \mathbf{q}\right) = 0. \end{aligned} \tag{A.4}$$

Assuming further that the kinematic rule (6.18) defined by the machine is such that the implicit function (G or H) has continuous and non-null partial derivative of the implicit function (G or H) with respect to the involved coordinate ($\partial G/\partial Y_l$ or $\partial H/\partial X_l$), such coordinate can be described as a function of the symmetric and antisymmetric angles,

$$Y_l = Y_l(\theta_A, \theta_S, \mathbf{q}) \qquad \text{or} \qquad X_l = X_l(\theta_A, \theta_S, \mathbf{q}). \tag{A.5}$$

From this property it follows that, by considering Eqs.(6.17) and (A.2), the distance d and the control parameters p_j $(j = 1, 2)$ can be expressed in turn as functions of the antisymmetric and symmetric angles only

$$d = d(\theta_A, \theta_S, \mathbf{q}), \qquad p_j = \widehat{p}_j(\theta_A, \theta_S, \mathbf{q}), \qquad j = 1, 2. \tag{A.6}$$

being the latter equation equivalent to

$$p_j = \widehat{p}_j(d, \theta_A, \theta_S, \mathbf{q}), \qquad j = 1, 2, \tag{A.7}$$

but expressed as a function of a lower number of coordinates. In the cases when the function $G(Y_l, \theta_A, \theta_S, \mathbf{q})$ or $H(X_l, \theta_A, \theta_S, \mathbf{q})$ does not satisfy the aforementioned properties, a different pair of primary kinematical quantities can be taken as variable to express the remaining kinematical quantity and the control parameter vector, namely, as

$$\theta_A = \theta_A(d, \theta_S, \mathbf{q}), \qquad p_j = \widehat{p}_j(d, \theta_S, \mathbf{q}), \qquad j = 1, 2, \tag{A.8}$$

or equivalently as

$$\theta_S = \theta_S(d, \theta_A, \mathbf{q}), \qquad p_j = \widehat{p}_j(d, \theta_A, \mathbf{q}), \qquad j = 1, 2. \tag{A.9}$$

It is also worth remarking that, in order to overcome periodicity issues inherent to the trigonometric function arctan, the antisymmetric rotation $\widetilde{\theta}_A$ (as well as the other angular quantities) is evaluated as integration over the time-like parameter t, from an initial and a current state during the controlled ends' history and corresponding to $t = \tau_0$ and $t = \tau$

$$\widetilde{\theta}_A(\tau) = \widetilde{\theta}_A(\tau_0) + \frac{\Theta_l(\tau)}{2} - \int_{\tau_0}^{\tau} \frac{X_l(t)\dot{Y}_l(t) - Y_l(t)\dot{X}_l(t)}{X_l(t)^2 + Y_l(t)^2} \mathrm{d}t, \tag{A.10}$$

where the superimposed dot stands for the derivative with respect to the time-like parameter t.

A.1.2 Suggested initial values for the control parameters

In order to initiate the evolution from a configuration in the 'surroundings' of the (if existing) catastrophe locus, the initial values of control parameters $\mathbf{p}(\tau_0)$ are suggested to be selected satisfying the following initial conditions (IC):

(IC1) the end rotation at the final coordinate is null ($\Theta_l(\tau_0) = 0$), implying a null initial value of the symmetric angle

$$\theta_S(\tau_0) = 0; \tag{A.11}$$

(IC2) the initial deformed configuration displays two inflection points, implying the satisfaction of the modulus restriction for the antisymmetric angle ($|\theta_A(\tau_0)| < \pi$) provided by Eq. (6.23).

Being the symmetric angle θ_S only dependent on Θ_l, Eq.$(6.16)_3$, it follows that imposing the initial condition (IC1) through Eq.(A.11) is equivalent to impose

$$p_2(\tau_0) = p_2^0 = -\upsilon. \tag{A.12}$$

A.1.3 Numerical algorithm for the evaluation of catastrophe sets

The evaluation of the 'catastrophe set' $\mathcal{C}_K$, as the elastica set $\mathcal{E}_K$ intersection with the 'snap-back set' $\mathcal{S}_K$, can be performed only numerically. A specific algorithm was developed in *Mathematica*, whose steps are:

Step 1. to define the discrete set of control parameter vectors $\mathbf{p} \subseteq \mathcal{E}_C$. This is performed as a fine discretization assuming a maximum spacing equal to 10^{-3} for each of the two control parameters;

Step 2. to relate the discrete set of $\mathcal{E}_C$ (introduced at the previous step) to the corresponding projections in the primary kinematical space and the physical plane, as the discretization of the elastica sets $\mathcal{E}_K$ and $\mathcal{E}_P$;

Step 3. to identify the catastrophe set $\mathcal{C}_C$ through the evaluation of the (approximated) critical control parameter vector $\mathbf{p}^{\mathcal{C}}$, belonging to discretization of the elastica set $\mathcal{E}_C$ and numerically found by imposing

$$\mathbf{p}^{\mathcal{C}}: \qquad \left|\theta_S^{sb(\pm)}\left(\overline{d}(\mathbf{p},\mathbf{q}),\overline{\theta}_A(\mathbf{p},\mathbf{q})\right) - \overline{\theta}_S(\mathbf{p},\mathbf{q})\right| < 6\cdot 10^{-4}\,\pi; \quad \text{(A.13)}$$

Step 4. to evaluate catastrophe sets $\{d^{\mathcal{C}}, \theta_A^{\mathcal{C}}, \theta_S^{\mathcal{C}}\}$ and $\{X_l^{\mathcal{C}}, Y_L^{\mathcal{C}}\}$ as the projection of the critical control parameters $\mathbf{p}^{\mathcal{C}}$ (achieved at the previous step) in the kinematical space and in the physical plane.

A.2 Complementary equations and considerations about the proposed *elastica catastrophe machines*

The equations presented in Sect. A.1 are detailed here for both the families of *elastica catastrophe machines*. In particular, the specific cases of rotation centre coincident ($\kappa_R = \lambda_R = 0$) and infinitely far away ($\sqrt{\kappa_R^2 + \lambda_R^2} \to \infty$) from the the origin are analyzed for the ECM-I respectively in Sects. A.2.1 and A.2.1. The limit case of rigid bar with infinite length is developed for ECM-II in Sect. A.2.2.

A.2.1 ECM-I

The description of the primary kinematic quantities $\{d, \theta_A, \theta_S\}$ for ECM-I as functions of the control parameter vector $\mathbf{p}$ follows from Eqs.(6.16) and (6.17) in the main text as

$$\begin{aligned}
\overline{d}(\mathbf{p}, \mathbf{q}^I) &= \sqrt{(\kappa_R + p_1 \cos p_2)^2 + (\lambda_R + p_1 \sin p_2)^2}\, l, \\
\overline{\theta}_A(\mathbf{p}, \mathbf{q}^I) &= \frac{p_2 + \upsilon}{2} - \arctan \frac{\lambda_R + p_1 \sin p_2}{\kappa_R + p_1 \cos p_2}, \\
\overline{\theta}_S(\mathbf{p}, \mathbf{q}^I) &= \frac{p_2 + \upsilon}{2}.
\end{aligned} \tag{A.14}$$

By inverting Eq.(6.35), the control parameters can be expressed as functions of the physical coordinates, in particular the first control parameter is given by

$$\begin{aligned}
\widetilde{p}_1(Y_l, \Theta_l, \mathbf{q}^I) &= \frac{Y_l/l - \lambda_R}{\sin(\Theta_l - \upsilon)}, \qquad \text{for} \quad \Theta_l \neq \upsilon + k\pi,\ k \in \mathbb{Z}, \\
\widetilde{p}_1(X_l, \Theta_l, \mathbf{q}^I) &= \frac{X_l/l - \kappa_R}{\cos(\Theta_l - \upsilon)}, \qquad \text{for} \quad \Theta_l \neq \upsilon + (k + \tfrac{1}{2})\pi,\ k \in \mathbb{Z},
\end{aligned} \tag{A.15}$$

the former equation equivalent to the latter, to be used when the rigid bar is not parallel to the X and Y axis, respectively, while the second control parameter is given by

$$\widetilde{p}_2(\Theta_l, \mathbf{q}^I) = \Theta_l - \upsilon. \tag{A.16}$$

Exploiting the inverse relations (A.15) and (A.16) into Eq.(6.35), one of the two coordinates can be expressed as a function of the other coordinate and the rotation as

$$\begin{aligned}
X_l(Y_l, \Theta_l, \mathbf{q}^I) &= \left[\kappa_R + \frac{\dfrac{Y_l}{l} - \lambda_R}{\tan(\Theta_l - \upsilon)}\right] l, \qquad \text{for} \quad \Theta_l \neq \upsilon + k\pi, \\
Y_l(X_l, \Theta_l, \mathbf{q}^I) &= \left[\lambda_R + \tan(\Theta_l - \upsilon)\left(\tfrac{X_l}{l} - \kappa_R\right)\right] l, \quad \text{for} \quad \Theta_l \neq \upsilon + (k + \tfrac{1}{2})\pi
\end{aligned} \tag{A.17}$$

for any $k \in \mathbb{Z}$. Inverting Eq.(A.14) leads to express the control parameters as functions of two of the primary kinematical quantities. In particular, while the second control parameter is only dependent on the antisymmetric angle

$$\widehat{p}_2(\theta_S, \mathbf{q}^I) = 2\theta_S - \upsilon, \tag{A.18}$$

the first control parameter can be expressed as a function of both the symmetric and antisymmetric angle only when the rotation center of the rigid bar does not lay along the straight line connecting the two rod's ends,

$$\widehat{p}_1(\theta_A, \theta_S, \mathbf{q}^I) = \frac{\kappa_R \tan(\theta_S - \theta_A) - \lambda_R}{\sin(2\theta_S - \upsilon) - \cos(2\theta_S - \upsilon)\tan(\theta_S - \theta_A)}, \qquad \text{for} \quad \theta_S + \theta_A \neq \upsilon + k\pi,\ k \in \mathbb{Z}. \tag{A.19}$$

Differently, in the case when the rotation center of the rigid bar and the two rod's ends are aligned along a straight line, the first control parameter can be expressed as a function of the distance and the symmetric angle as

$$\begin{aligned} &\widehat{p}_1(d, \theta_S, \mathbf{q}^I) = (-1)^k \tfrac{d}{l} - \tfrac{\kappa_R}{\cos 2\theta_S - \upsilon}, \\ &\widehat{p}_1(d, \theta_S, \mathbf{q}^I) = (-1)^k \tfrac{d}{l} - \tfrac{\lambda_R}{\sin 2\theta_S - \upsilon}, \end{aligned} \qquad \text{for} \qquad \theta_S + \theta_A = \upsilon + k\pi,\ k \in \mathbb{Z}. \tag{A.20}$$

Finally, whenever the rigid bar is not parallel to the straight line connecting the rod's ends, the distance d for ECM-I can be described as a function of the symmetric and antisymmetric angles as

$$d(\theta_A, \theta_S, \mathbf{q}^I) = \frac{\kappa_R \tan(2\theta_S - \upsilon) - \lambda_R}{\cos(\theta_S - \theta_A)\tan(2\theta_S - \upsilon) - \sin(\theta_S - \theta_A)} l, \qquad \text{for} \quad \theta_S + \theta_A \neq \upsilon + k\pi,\ k \in \mathbb{Z}, \tag{A.21}$$

differently, when the rigid bar becomes parallel, the distance d becomes a free parameter and the angles are constrained to each other

$$\theta_S(\theta_A, \mathbf{q}^I) = \upsilon + k\pi - \theta_A, \qquad \text{or} \qquad \theta_A(\theta_S, \mathbf{q}^I) = \upsilon + k\pi - \theta_S,\ k \in \mathbb{Z}, \tag{A.22}$$

where the parameter k for these last parametrizations is given by evolution continuity, similarly to Eq.(A.10).

It is also worth noting that a sufficient condition for the connectivity of the inextensibility set $\mathcal{I}_C$ is given by a position of the rotation center R within such a set,

$$\kappa_R{}^2 + \lambda_R{}^2 < 1, \tag{A.23}$$

a property however not fundamental for the realization of an 'effective' *elastica catastrophe machine*. All the cases reported in Figs. 6.7, 6.8 and 6.9 consider a rotation center R of the rigid bar within the inextensibility set, Eq.(A.23). It is observed that when the design parameters are such that an 'effective catastrophe machine' is realized, the rotation center R is never inside the catastrophe locus. It is also worth remarking that the effectiveness of the catastrophe locus does not imply its simple connection in the control parameters plane. This is indeed the case when the rotation center R lays along the catastrophe set $\mathcal{C}_P$ at the physical coordinates corresponding to the junction point of $\mathcal{C}_P^{(+)}$ with $\mathcal{C}_P^{(-)}$. Its projection in the control parameters plane share only the first coordinate $p_1 = 0$ while has two different values in the second coordinate p_2 (as it can be noted in the left column of Fig. 6.7).
Finally, the recommendation for the initial value of the control parameters vector $\mathbf{p}(\tau_0) = \{p_1^0, p_2^0 = -\upsilon\}$ to belong to the inextensibility set $\mathcal{I}_C$ constrains the first control parameter to the range $p_1^0 \in \left[p_{1,\min}^0, p_{1,\max}^0\right]$, with

$$\begin{aligned} p_{1,\min}^0 &= \max\left[0, -\kappa_R\cos\upsilon + \lambda_R\sin\upsilon - \sqrt{1-\kappa_R^2-\lambda_R^2+\left(\kappa_R\cos\upsilon-\lambda_R\sin\upsilon\right)^2}\right], \\ p_{1,\max}^0 &= -\kappa_R\cos\upsilon + \lambda_R\sin\upsilon + \sqrt{1-\kappa_R^2-\lambda_R^2+\left(\kappa_R\cos\upsilon-\lambda_R\sin\upsilon\right)^2}. \end{aligned} \tag{A.24}$$

From imposing the existence of a range inclusive of positive values in the previous equation, the design parameters κ_R and λ_R are constrained to satisfy

$$\begin{cases} \kappa_R^2 + \lambda_R^2 - \left(\kappa_R\cos\upsilon - \lambda_R\sin\upsilon\right)^2 \le 1, \\ -\kappa_R\cos\upsilon + \lambda_R\sin\upsilon + \sqrt{1-\kappa_R^2-\lambda_R^2+\left(\kappa_R\cos\upsilon-\lambda_R\sin\upsilon\right)^2} > 0. \end{cases}$$

ECM-I with rotation centre R coincident with the origin

Null coordinates for the rotation center ($\kappa_R = \lambda_R = 0$) imply that the distance d reduces to a linear function of the first control parameter p_1 and that

the antisymmetric angle θ_A reduces to a linear function of the second control parameter p_2,

$$d = p_1 l, \qquad \theta_A = \frac{\upsilon - p_2}{2} - \left\lfloor \frac{\frac{\upsilon}{\pi} + 1}{2} \right\rfloor 2\pi, \tag{A.25}$$

where the floor operator $\lfloor\ \rfloor$ provides the greatest integer less than or equal to the relevant argument. Under this condition, the elastica set $\mathcal{E}_K$ reduces to the portion of plane

$$\theta_A + \theta_S = \upsilon - \left\lfloor \frac{\frac{\upsilon}{\pi} + 1}{2} \right\rfloor 2\pi, \tag{A.26}$$

under the constraint (6.23). From the analysis of the intersection of such elastica set $\mathcal{E}_K$ and the snap-back surface $\mathcal{S}_K$, it follows that if $\lambda_R = \kappa_R = 0$ then an effective machine is generated only when

$$\left| \upsilon - \left\lfloor \frac{\frac{\upsilon}{\pi} + 1}{2} \right\rfloor 2\pi \right| \lesssim 0.726\pi. \tag{A.27}$$

ECM-I with rotation centre R infinitely far away from the origin

For large values of $\sqrt{\kappa_R^2 + \lambda_R^2}$, the inextensibility domain approaches an ellipse within the control parameter plane $p_1 - p_2$, described by

$$\mathcal{I}_C = \left\{ \mathbf{p} : \left[p_1 - \sqrt{\kappa_R^2 + \lambda_R^2} \right]^2 + \left(\kappa_R^2 + \lambda_R^2\right) \left[p_2 - \pi - \arctan \frac{\lambda_R}{\kappa_R} \right]^2 \leq 1 \right\}. \tag{A.28}$$

In order to satisfy the aforemmentioned inequality, the second control parameter has to assume the approximately constant value $p_2 \simeq \pi + \arctan \lambda_R/\kappa_R$. Therefore, the symmetric angle θ_S takes the approximately constant values

$$\theta_S = \frac{\pi + \upsilon + \arctan \lambda_R/\kappa_R}{2}. \tag{A.29}$$

It follows that the evolution of the final curvilinear coordinate is just a rigid-body translation within the physical plane, at constant end's rotation $\Theta_l = 2\theta_S$. The equation (A.29) implies that a centre of rotation very distant from the origin never makes effective ECM-I. In the particular case when $\theta_S = \Theta_l = 0$, attained for $\upsilon + \arctan \lambda_R/\kappa_R = -\pi$, all the points of the catastrophe set of ECM-I become pitchfork bifurcations [33]. Under these hypotheses, the ECM-I could be exploited as a *elastica pitchfork bifurcation machine* to show the infinite possible pitchfork bifurcations of the system, as shown in Fig. SM A.1.

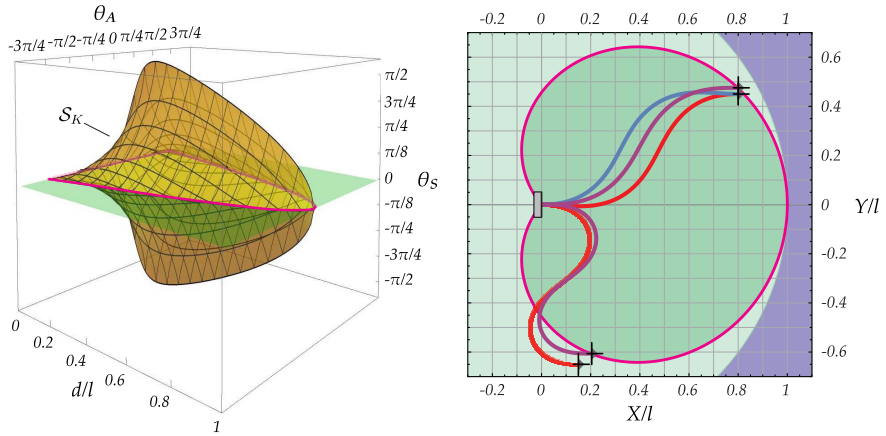

Figure A.1: Projection of the bifurcations set for the *elastica pitchfork bifurcation machine* within the primary kinematical space (left) and the physical plane (right). The elastica pitchfork bifurcation machine can be generated from ECM-I with infinitely far rotation center R ($\kappa_R^2 + \lambda_R^2 \to \infty$) and $\upsilon + \arctan \lambda_R/\kappa_R = -\pi$ or from ECM-IIa and ECM-IIb with rigid bar of infinite length ($\rho \to \infty$) and $\upsilon = -\alpha$ and $\upsilon = -\alpha - \pi$, respectively. Deformed configurations are reported within the physical plane for some end position, with those laying along the bifurcation set that display $m = 3$ inflections points (the mid-point and the two ends, elastica reported in purple). Elastica in red (blue) colour has negative (positive) curvature at the initial coordinate, $\Theta'(s = 0)$.

A.2.2 ECM-II

By considering Eq.(6.39) in Eqs.(6.16) and (6.17), the primary kinematic quantities $\{d, \theta_A, \theta_S\}$ can be expressed for ECM-II as functions of the control parameters vector $\mathbf{p}$ as

$$\begin{aligned}
\overline{d}(\mathbf{p}, \mathbf{q}^{II}) &= \sqrt{(\kappa_D + p_1 \cos\alpha + \rho \cos p_2)^2 + (\lambda_D + p_1 \sin\alpha + \rho \sin p_2)^2}\; l, \\
\overline{\theta}_A(\mathbf{p}, \mathbf{q}^{II}) &= \frac{p_2 + \upsilon}{2} - \arctan \frac{\lambda_D + p_1 \sin\alpha + \rho \sin p_2}{\kappa_D + p_1 \cos\alpha + \rho \cos p_2}, \\
\overline{\theta}_S(\mathbf{p}, \mathbf{q}^{II}) &= \frac{p_2 + \upsilon}{2}.
\end{aligned} \tag{A.30}$$

The first control parameter can be expressed as a function of the physical coordinates by inverting Eq.(6.39) as

$$\widetilde{p_1}(Y_l, \Theta_l, \mathbf{q}^{II}) = \tfrac{Y_l/l - \lambda_D - \rho \sin(\Theta_l - \upsilon)}{\sin\alpha}, \quad \text{for} \quad \alpha \neq k\pi,$$
$$\widetilde{p_1}(X_l, \Theta_l, \mathbf{q}^{II}) = \tfrac{X_l/l - \kappa_D - \rho \cos(\Theta_l - \upsilon)}{\cos\alpha}, \quad \text{for} \quad \alpha \neq \left(k + \tfrac{1}{2}\right)\pi, \tag{A.31}$$

where $k \in \mathbb{Z}$. The previous two equations, equivalent to each other, can be used indifferently except for the case of a designed straight line (where the rigid bar rotation center may move) parallel to the X (Y) axis where only the second (first) equation is feasible.
Relations (A.15) and (A.31) together with Eq.(6.39) provide one of the position coordinates as a function of the two remaining physical coordinates as

$$X_l(Y_l, \Theta_l, \mathbf{q}^{II}) = \frac{Y_l}{\tan\alpha} + l\left[\kappa_D + \rho\cos(\Theta_l - \upsilon) - \frac{\lambda_D + \rho\sin(\Theta_l - \upsilon)}{\tan\alpha}\right], \quad \text{for} \quad \alpha \neq k\pi,$$

$$Y_l(X_l, \Theta_l, \mathbf{q}^{II}) = X_l\tan\alpha + \left[\lambda_D + \rho\sin(\Theta_l - \upsilon) - \tan\alpha\,(\kappa_D + \rho\cos(\Theta_l - \upsilon))\right], \quad \text{for} \quad \alpha \neq (k + \frac{1}{2})\pi. \tag{A.32}$$

The inversion of Eqs.(6.34) and Eq.(A.30) provides the same equation obtained for the ECM-I expressing the second control parameter as a function of the physical rotation and the symmetric angle, respectively

$$\widetilde{p_2}(\Theta_l, \mathbf{q}^{II}) = \Theta_l - \upsilon, \qquad \widehat{p_2}(\theta_S, \mathbf{q}^{II}) = 2\theta_S - \upsilon. \tag{A.33}$$

The inversion of Eq.(A.30) also provides the expression for the first control parameter as function only of the antisymmetric and symmetric angles

$$\widehat{p_1}(\theta_A, \theta_S, \mathbf{q}^{II}) = \frac{(\kappa_D + \rho\cos(2\theta_S - \upsilon))\tan(\theta_S - \theta_A) - \lambda_D - \rho\sin(2\theta_S - \upsilon))}{\sin\alpha - \cos\alpha\tan(\theta_S - \theta_A)}, \quad \text{for} \quad \theta_S - \theta_A \neq \alpha + k\pi \tag{A.34}$$

holding (for $k \in \mathbb{Z}$ and) except when the straight line connecting the two rod's ends is parallel to the designed straight line (where the rigid bar rotation center may move). Differently, under this condition (equivalent to $\alpha + k\pi = \arctan Y_l/X_l$), the first control parameter can be expressed as a function of the distance and symmetric angle as

$$\begin{aligned} \widehat{p}_1(d,\theta_S,\mathbf{q}^{II}) &= (-1)^k \tfrac{d}{l} - \tfrac{\kappa_D+\rho\cos(2\theta_S-\upsilon)}{\cos\alpha}, \\ \widehat{p}_1(d,\theta_S,\mathbf{q}^{II}) &= (-1)^k \tfrac{d}{l} - \tfrac{\lambda_D+\rho\sin(2\theta_S-\upsilon)}{\sin\alpha}, \end{aligned} \quad \text{for} \quad \theta_S-\theta_A = \alpha+k\pi,\ k\in\mathbb{Z}. \tag{A.35}$$

Lastly, one of the three primary kinematical quantities can be expressed as a function of the other two. The distance d for ECM-II can be described as a function of the symmetric and antisymmetric angles as

$$d(\theta_A,\theta_S,\mathbf{q}^{II}) = \frac{\kappa_D+\rho\cos(2\theta_S-\upsilon)\tan\alpha-(\lambda_D+\rho\sin(2\theta_S-\upsilon))}{\cos(\theta_S-\theta_A)\tan\alpha-\sin(\theta_S-\theta_A)}l. \tag{A.36}$$

$$\text{for} \quad \theta_S-\theta_A \neq \alpha+k\pi.$$

As the straight line connecting the two rod's ends is parallel to the designed straight line, the aforementioned equation can not be used and one of the angles θ_A or θ_S can be expressed as a function of the other one (leaving the distance d as free variable)

$$\theta_S(\theta_A,\mathbf{q}^{II}) = \alpha+k\pi+\theta_A, \quad \text{or} \quad \theta_A(\theta_S,\mathbf{q}^{II}) = \theta_S-\alpha-k\pi,\ k\in\mathbb{Z}. \tag{A.37}$$

Finally, it is worth remarking that the initial value of the control parameter vector is constrained by Eq.(A.12) and the condition of belonging to the inextensibility set $\mathcal{I}_C$. The latter condition constrains the first control parameter within the range $p_1^0 \in \left[p_{1,\min}^0, p_{1,\max}^0\right]$ with

$$p_{1,\min}^0 = -\kappa_D\cos\alpha-\lambda_D\sin\alpha-\rho\cos(\alpha+\upsilon)- \sqrt{(\lambda_D\sin\alpha+\rho\cos(\alpha+\upsilon)+\kappa_D\cos\alpha)^2-\left(\kappa_D{}^2+\lambda_D{}^2+\rho^2-2\rho(\lambda_D\sin\upsilon-\kappa_D\cos\upsilon)-1\right)},$$

$$p_{1,\max}^0 = -\kappa_D\cos\alpha-\lambda_D\sin\alpha-\rho\cos(\alpha+\upsilon)+ \sqrt{(\lambda_D\sin\alpha+\rho\cos(\alpha+\upsilon)+\kappa_D\cos\alpha)^2-\left(\kappa_D{}^2+\lambda_D{}^2+\rho^2-2\rho(\lambda_D\sin\upsilon-\kappa_D\cos\upsilon)-1\right)},$$

where, in order to have a non-null set for the possible initial vector $\mathbf{p}^0$, the design parameters κ_D, λ_D, α, ρ, and υ have to satisfy the following inequality

$$1+(\lambda_D \sin\alpha+\rho\cos(\alpha+\upsilon)+\kappa_D \cos\alpha)^2 \geq {\kappa_D}^2+{\lambda_D}^2+\rho^2-2\rho(\lambda_D \sin\upsilon-\kappa_D \cos\upsilon). \tag{A.38}$$

ECM-II with the rigid bar of infinite length

In the case of ECM-II with very large values of rigid bar length ($\rho \to \infty$), the inextensibility domain can be approximated by two ellipses within the control parameter plane $p_1 - p_2$. The ellipse for ECM-IIa is defined by

$$\mathcal{I}_C^{IIa} = \left\{ \mathbf{p} : \left[p_1 + \left(\rho + \kappa_D \cos\alpha + \lambda_D \sin\alpha - \frac{(\kappa_D \sin\alpha - \lambda_D \cos\alpha)^2}{2\rho} \right) \right]^2 + \rho^2 \left[p_2^{(a)} - \alpha - \frac{\kappa_D \sin\alpha - \lambda_D \cos\alpha}{\rho} \right]^2 < 1 \right\}. \tag{A.39}$$

while that for ECM-IIb by

$$\mathcal{I}_C^{IIb} = \left\{ \mathbf{p} : \left[p_1 - \left(\rho - \kappa_D \cos\alpha - \lambda_D \sin\alpha - \frac{(\kappa_D \sin\alpha - \lambda_D \cos\alpha)^2}{2\rho} \right) \right]^2 + \rho^2 \left[p_2^{(b)} - \alpha - \pi + \frac{\kappa_D \sin\alpha - \lambda_D \cos\alpha}{\rho} \right]^2 < 1 \right\}. \tag{A.40}$$

These two inextensibility domains imply an approximately constant value for the second control parameter, $p_2^{(a)} \simeq \alpha$ and $p_2^{(b)} \simeq \alpha + \pi$, so that the symmetric angle θ_S is also constant

$$\theta_S^{(a)} = \frac{\alpha + \upsilon}{2} \qquad \theta_S^{(b)} = \frac{\alpha + \pi + \upsilon}{2}. \tag{A.41}$$

Similarly to ECM-I with rotation center infinitely far away from the origin, ECM-II with infinitely long rigid bars is never an effective catastrophe machine and in some special case ($\upsilon = -\alpha$ for ECM-IIa or $\upsilon = -\alpha - \pi$ for ECM-IIb) displays pitchfork bifurcation points as catastrophe set. The projections of this bifurcation set within the primary kinematical space and within the

physical plane are coincident with the special cases of ECM-I and reported in Fig. SM A.1.
Finally, although the realization of an 'effective' ECM-II is not strictly related to this property, it is noted that the connectivity of its inextensibility domain $\mathcal{I}_C$, Eq.(6.41), is attained when

$$|\kappa_D \sin\alpha - \lambda_D \cos\alpha| + \rho < 1. \tag{A.42}$$

A.3 Additional experimental results

Similar to the experimental results shown in Figs. 6.2 and 6.18 of the main text, photos taken at specific stages are reported here for ECM-IIb with $\kappa_D = \lambda_D = \alpha = 0$, $\rho = 1$ and $\upsilon = \pi$. In particular, all the stable equilibrium configurations are reported at three stages for in Fig. A.2. The clamp position moves from inside the bistable region (left photo) to inside the monostable region (right photo), by crossing the catastrophe locus (central photo) region (from left to right in Figs. 16 and 17). The evolution of the clamp position is ruled by varying the control parameter p_2 at fixed value of p_1. Moreover, the

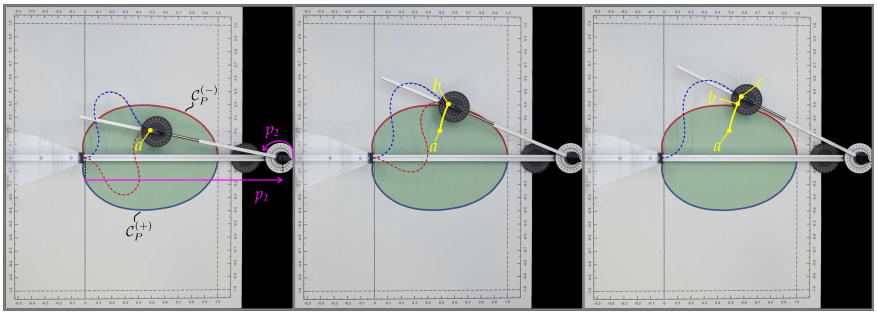

Figure A.2: As for Fig. 6.18 but for ECM-IIb (with $\kappa_D = \lambda_D = \alpha = 0$, $\rho = 1$ and $\upsilon = \pi$), involving a different definition of the control parameters $\{p_1, p_2\}$ (left).

transition of the deformed configuration during a continuous evolution can be also appreciated in Fig. A.3 where the fast motion at snapping is shown in the central photo (each two consecutive snapshots are referred to a time interval of approximately 0.15 sec).

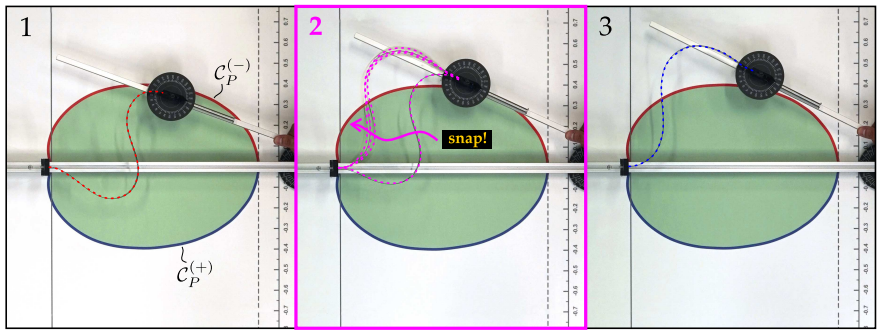

Figure A.3: As for Fig. 6.2, but for ECM-IIb (with $\kappa_D = \lambda_D = \alpha = 0$, $\rho = 1$, $\upsilon = \pi$) with increasing the second control parameter p_2 (rotation angle) and fixed value of p_1. Snapping for a configuration with negative curvature at the two ends (highlighted with a red dashed line) is shown at crossing the part $\mathcal{C}_P^-$ (red line) of catastrophe locus. Due to the symmetry, snapping is not reported for crossing the part $\mathcal{C}_P^+$ (blue line) of catastrophe locus.

B

Equations of motion of the non-holonomic dicrete system in quasi-coordinates

In this Appendix, the alternative formulation of the equations of motion for a non-holonomic system in *quasi-coordinates* is shown. Such equations represent the link between the classical form of the Lagrange equations and the equations of motion of non-holonomic systems, while their main advantage is represented by the fact that the reaction forces on the non-holonomic constraints can be disregarded.

In the first Section, the governing equations expressed in quasi-coordinates, also known in literature as the *Boltzmann-Hamel equations* [52], are firstly obtained for a system described through n generalized coordinates. The exact formulation, which is in general valid also for holonomic systems, is obtained following Greenwood [52] and Neimark and Fufaev [85]. The equations are then specified for the case of non-holonomic systems.

With reference to Chapter 7, in the second Section the general equations are specified for the discretized non-holonomic system made up of N rigid bars. A numerical integration of the governing equations also shows an almost perfect match between the results obtained through the 'classical' form of the Lagrange equations given by (7.20) and those of the proposed formulation

in quasi-coordinates.

B.1 The Boltzmann-Hamel equations

The equations of motion in quasi-coordinates are obtained by considering the set of generalized 'true' coordinates $\mathbf{q} = \{q_1, q_2, \ldots, q_n\}$ and of quasi-coordinates $\boldsymbol{\pi} = \{\pi_1, \pi_2, \ldots, \pi_n\}$, whose derivatives are connected to the generalized velocities $\dot{\mathbf{q}}$ by the following linear equations

$$\dot{\pi}_s = A_{sk}(\mathbf{q})\dot{q}_k, \qquad \dot{q}_k = B_{kl}(\mathbf{q})\dot{\pi}_l, \quad s,k,l = 1,2,\ldots,n \tag{B.1}$$

and where the matrices $\mathbf{A}$ and $\mathbf{B} = \mathbf{A}^{-1}$ depend only on the generalized coordinates $\mathbf{q}$. It is worth to underline that the transformation (B.1$_1$) is completely arbitrary, although the matrix $\mathbf{A}$ has necessarily to be non-singular.

The following properties hold

$$\frac{\partial \dot{q}_s}{\partial \dot{\pi}_k} = \frac{\partial q_s}{\partial \pi_k} = B_{sk}, \qquad \delta q_s = B_{sk}\delta\pi_k \tag{B.2}$$

where δq_s and $\delta\pi_k$ denote variations in the generalized 'true' and quasi-coordinates, so that the D'Alembert-Lagrange equations can be written as

$$\sum_{s=1}^{n}\left(\frac{d}{dt}\frac{\partial \mathcal{T}}{\partial \dot{q}_s} - \frac{\partial \mathcal{T}}{\partial q_s} - Q_s\right) B_{sk}\delta\pi_k = 0, \tag{B.3}$$

where $\mathcal{T}$ is the kinetic energy and Q_s is the s-th generalized force. Moreover, the variations $\delta\pi_k$ are independent, so that one obtains the following system of n equations

$$\left(\frac{d}{dt}\frac{\partial \mathcal{T}}{\partial \dot{q}_s} - \frac{\partial \mathcal{T}}{\partial q_s} - Q_s\right) B_{sk} = 0, \qquad k = 1,2,\ldots,n. \tag{B.4}$$

The function $\mathcal{T}^*$ is introduced by substituting the transformation (B.1) into the kinetic energy $\mathcal{T}$. The first component of the k-th equation in (B.4) can be therefore rewritten as follows

$$\begin{aligned} B_{sk}\frac{d}{dt}\frac{\partial \mathcal{T}}{\partial \dot{q}_s} &= \frac{d}{dt}\left(B_{sk}\frac{\partial \mathcal{T}}{\partial \dot{q}_s}\right) - \frac{\partial \mathcal{T}}{\partial \dot{q}_s}\frac{\partial B_{sk}}{\partial q_l}\dot{q}_l \\ &= \frac{d}{dt}\left(B_{sk}\frac{\partial \mathcal{T}^*}{\partial \dot{\pi}_i}\frac{\partial \dot{\pi}_i}{\partial \dot{q}_s}\right) - \frac{\partial \mathcal{T}^*}{\partial \dot{\pi}_i}\frac{\partial \dot{\pi}_i}{\partial \dot{q}_s}\frac{\partial B_{sk}}{\partial q_l}\dot{q}_l \end{aligned} \tag{B.5}$$

where $\partial\dot{\pi}_i/\partial\dot{q}_s = A_{is}$ and $A_{is}B_{sk} = \delta_{ik}$, so that

$$\begin{aligned} B_{sk}\frac{d}{dt}\frac{\partial\mathcal{T}}{\partial\dot{q}_s} &= \frac{d}{dt}\frac{\partial\mathcal{T}^*}{\partial\dot{\pi}_k} - \frac{\partial\mathcal{T}^*}{\partial\dot{\pi}_i}A_{is}\frac{\partial B_{sk}}{\partial q_l}B_{lj}\dot{\pi}_j \\ &= \frac{d}{dt}\frac{\partial\mathcal{T}^*}{\partial\dot{\pi}_k} + \frac{\partial\mathcal{T}^*}{\partial\dot{\pi}_i}\dot{\pi}_j B_{sk}B_{lj}\frac{\partial A_{is}}{\partial q_l} \end{aligned} \tag{B.6}$$

Using a similar procedure, the second term in (B.4) becomes

$$\begin{aligned} B_{sk}\frac{\partial\mathcal{T}}{\partial q_s} &= \frac{\partial\mathcal{T}^*}{\partial q_s}B_{sk} + \frac{\partial\mathcal{T}^*}{\partial\dot{\pi}_i}\frac{\partial\dot{\pi}_i}{\partial q_s}B_{sk} \\ &= \frac{\partial\mathcal{T}^*}{\partial\pi_i}\delta_{ik} + \frac{\partial\mathcal{T}^*}{\partial\dot{\pi}_i}B_{sk}\frac{\partial A_{il}}{\partial q_s}\dot{q}_l = \frac{\partial\mathcal{T}^*}{\partial\pi_k} + \frac{\partial\mathcal{T}^*}{\partial\dot{\pi}_i}\frac{\partial A_{il}}{\partial q_s}B_{sk}B_{lj}\dot{\pi}_j \end{aligned} \tag{B.7}$$

while the generalized forces can be rewritten as

$$\Pi_k = B_{sk}Q_s \tag{B.8}$$

Finally, merging of the terms (B.6), (B.7) and (B.8) into Eqs.(B.4) leads to the following set of equations

$$\frac{d}{dt}\frac{\partial\mathcal{T}^*}{\partial\dot{\pi}_k} - \frac{\partial\mathcal{T}^*}{\partial\pi_k} + \frac{\partial\mathcal{T}^*}{\partial\dot{\pi}_i}\dot{\pi}_j B_{sk}B_{lj}\left(\frac{\partial A_{is}}{\partial q_l} - \frac{\partial A_{il}}{\partial q_s}\right) = \Pi_k \tag{B.9}$$

where the following terms are introduced

$$\gamma_{kij} = B_{sk}B_{lj}\left(\frac{\partial A_{is}}{\partial q_l} - \frac{\partial A_{il}}{\partial q_s}\right), \tag{B.10}$$

which are known as *Hamel coefficients*. Moreover, such coefficients in Eq.(B.10) represent a skew-symmetric matrix at fixed indices i, thus

$$\gamma_{kij} = -\gamma_{jik}. \tag{B.11}$$

The Eqs.(B.9) therefore assume the final form of the Boltzmann-Hamel equations

$$\frac{d}{dt}\frac{\partial\mathcal{T}^*}{\partial\dot{\pi}_k} - \frac{\partial\mathcal{T}^*}{\partial\pi_k} + \gamma_{kij}\frac{\partial\mathcal{T}^*}{\partial\dot{\pi}_i}\dot{\pi}_j = \Pi_k. \tag{B.12}$$

which represent a set of n equations in the $2n$ unknowns given by the 'true' and quasi-coordinates $\mathbf{q}$ and $\boldsymbol{\pi}$. The system (B.12) needs therefore to be complemented by n further equations, which are represented by the linear transformation in Eqs.(B.1_1).

B.1.1 Formulation with non-holonomic constraints

Following Neimark and Fufaev [85], by considering a mechanical system subject to m non-holonomic constraints in the form

$$a_{pi}\dot{q}_i = 0, \qquad p = 1, 2, \ldots, m;\ i = 1, 2, \ldots, n \tag{B.13}$$

one may conveniently set the transformation (B.1_1) through a (non-singular) matrix $\mathbf{A}$ such that

$$A_{n-m+p,i}\,\dot{q}_i = \dot{\pi}_{n-m+p} = 0 \quad p = 1, 2, \ldots, m;\ i = 1, 2, \ldots, n. \tag{B.14}$$

where $A_{n-m+p,i} = a_{pi}$, so that the non-holonomic constraints (B.13) can be introduced within the presented mathematical formulation by simply imposing the last m components of vector $\dot{\boldsymbol{\pi}}$ to vanish, namely $\dot{\pi}_{n-m+p} = 0$.

The Boltzmann-Hamel equations for a discrete system subject to m non-holonomic constraints therefore reduces to

$$\begin{cases} \dfrac{d}{dt}\dfrac{\partial \mathcal{T}^*}{\partial \dot{\pi}_k} - \dfrac{\partial \mathcal{T}^*}{\partial \pi_k} + \gamma_{kij}\dfrac{\partial \mathcal{T}^*}{\partial \dot{\pi}_i}\dot{\pi}_j = \Pi_k, & k, j = 1, 2, \ldots, n-m;\ i = 1, 2, \ldots, n \\ A_{k,i}\dot{q}_i = \dot{\pi}_k & k = 1, 2, \ldots, n-m;\ i = 1, 2, \ldots, n \\ A_{n-m+p,i}\dot{q}_i = 0 & p = 1, 2, \ldots, m;\ i = 1, 2, \ldots, n. \end{cases} \tag{B.15}$$

thus representing a system of $2n - m$ equations in $2n - m$ unknowns, namely the n 'true' generalized coordinates $\dot{\mathbf{q}}$ and the first $n - m$ quasi-coordinates $\{\pi_1, \pi_2, \ldots, \pi_{n-m}\}$, and where the non-holonomic constraints (B.14) are specified by the last m equations.

B.2 The governing equations for the discretized non-holonomic column

With reference to Chapter 7, the vector of the 'true' generalized coordinates of the system made up of N rigid bars is specified by the following $N + 1$ components

$$\mathbf{q} = [\Theta_1, ..., \Theta_i, ..., \Theta_N, X_0] \tag{B.16}$$

where Θ_i is the rotation of the generic i-th rigid bar with respect to the horizontal and where X_0 is the horizontal displacement of the rigid block at the initial end of the column.

The $(N+1 \times N+1)$ transformation matrix $\mathbf{A}$ in Eq.(B.1_1) can be therefore chosen in the following manner

$$\mathbf{A} = \left[\begin{array}{c|c} \mathbf{I}^{(N)} & \mathbf{0} \\ \hline \{a_1(\mathbf{q},\beta_0),\ldots,a_N(\mathbf{q},\beta_0)\} & a_{N+1}(\mathbf{q},\beta_0) \end{array}\right], \tag{B.17}$$

where $\mathbf{I}^{(N)}$ is the $N \times N$ identity matrix and the coefficients a_i represent the components of the vector of the non-holonomic constraint $\mathbf{a}(\mathbf{q},\beta_0)$, which is specified by Eqs.(7.7) and (7.12) for the 'skate' and 'violin bow' constraints, respectively. Moreover, the determinant of the matrix (B.17) is respectively equal to $\cos(\Theta_N+\beta_0)$ and $\cos(\beta_0)$, being therefore different from zero for every $\beta_0 \neq \pm\pi/2$ (the latter representing the 'pathological' condition for the 'violin bow' constraint).

Due to the well-known properties of the inverse matrices, the matrix $\mathbf{B}$ is therefore given by

$$\mathbf{B} = \left[\begin{array}{c|c} \mathbf{I}^{(N)} & \mathbf{0} \\ \hline -\dfrac{1}{a_{N+1}(\mathbf{q},\beta_0)}\{a_1(\mathbf{q},\beta_0),\ldots,a_N(\mathbf{q},\beta_0)\} & \dfrac{1}{a_{N+1}(\mathbf{q},\beta_0)} \end{array}\right]. \tag{B.18}$$

The fundamental operators for the definition of Eqs.(B.15) are now obtained in the case of a non-holonomic double-pendulum subject to a 'skate' constraint. Moreover, a perfectly-aligned constraint is assumed, so that $\beta_0 = 0$.

B.3 The double-pendulum subject to a 'skate' constraint in quasi-coordinates

The general equations are particularized for a double-pendulum $N = 2$ subject to a 'skate' non-holonomic constraint which is perfectly-aligned with the rod's final rigid bar (thus $\beta_0 = 0$) and loaded through a dead load (loading condition B). A dimensionless analysis is introduced through the change of variables (7.48), while the matrix (B.17) is evaluated through the dimensionless expression for the vector (7.7) holding for the 'skate' constraint, thus obtaining

$$\mathbf{A} = \begin{bmatrix} 1 & 0 & 0 \\ 0 & 1 & 0 \\ -\frac{1}{2}\sin(\Theta_1 - \Theta_2) & 0 & \cos\Theta_2 \end{bmatrix}, \tag{B.19}$$

so that the 'true' and quasi-velocities are connected by the following linear equations

$$\begin{bmatrix} \dot{\pi}_1 \\ \dot{\pi}_2 \\ \dot{\pi}_3 \end{bmatrix} = \begin{bmatrix} 1 & 0 & 0 \\ 0 & 1 & 0 \\ -\frac{1}{2}\sin(\Theta_1 - \Theta_2) & 0 & \cos\Theta_2 \end{bmatrix} \begin{bmatrix} \dot{\Theta}_1 \\ \dot{\Theta}_2 \\ \dot{\chi} \end{bmatrix} \tag{B.20}$$

where the fulfilment of the non-holonomic constraint (7.6) can be simply imposed by setting, according to Eqs.(B.14), $\dot{\pi}_3 = 0$.

The Hamel coefficients at fixed $k = 1, 2, 3$ can be collected into the following matrices

$$\boldsymbol{\gamma}_1 = \begin{bmatrix} 0 & 0 & 0 \\ 0 & 0 & 0 \\ 0 & \frac{1}{2}\cos\Theta_1 \sec\Theta_2 & 0 \end{bmatrix}, \quad \boldsymbol{\gamma}_2 = \begin{bmatrix} 0 & 0 & 0 \\ 0 & 0 & 0 \\ -\frac{1}{2}\cos\Theta_1 \sec\Theta_2 & 0 & \tan\Theta_2 \end{bmatrix}$$
$$\boldsymbol{\gamma}_3 = \begin{bmatrix} 0 & 0 & 0 \\ 0 & 0 & 0 \\ 0 & -\tan\Theta_2 & 0 \end{bmatrix} \tag{B.21}$$

thus verifying the property (B.11), while the function $\mathcal{T}^*$ is given by

$$\begin{aligned} &\mathcal{T}^*(\Theta_1, \Theta_2, \dot{\pi}_1, \dot{\pi}_2) = \\ &\frac{1}{16}\Big\{\dot{\pi}_2^2\left(\tilde{d}^2 + 8\tilde{I}_{r,L} + 2\tilde{M}_L\right) + \dot{\pi}_1^2\Big[\tilde{d}^2 - \sec^2\Theta_2 \sin(\Theta_1 - \Theta_2)\Big(2(\tilde{d} - \tilde{M}_X + \\ &+ \tilde{M}_L - 1)\sin\Theta_1 \cos\Theta_2 + 2(\tilde{M}_X + \tilde{M}_L + 1)\cos\Theta_1 \sin\Theta_2 + \sin(2\Theta_2)\Big) + \\ &+ 2\tilde{M}_L + 1\Big] + 2(\tilde{d} + 2\tilde{M}_L)\dot{\pi}_1\dot{\pi}_2 \cos\Theta_1 \sec\Theta_2\Big\} \end{aligned} \tag{B.22}$$

which is independent on the horizontal displacement χ and where the condition $\dot{\pi}_3 = 0$ has been imposed. The complete set of the Boltzmann-Hamel equations

(B.15) can be therefore easily obtained by operating the terms (B.6), (B.7) and (B.8), where, from the operational point of view, the derivative of $\mathcal{T}^*$ with respect to the quasi-coordinates is given by

$$\frac{\partial \mathcal{T}^*}{\partial \pi_k} = B_{sk} \frac{\partial \mathcal{T}^*}{\partial q_s}. \tag{B.23}$$

For the sake of brevity, the extended equations are not reported.

The comparison between the solutions obtained through the Lagrange equations of motion (7.20) and the Boltzmann-Hamel equations in quasi-coordinates (B.15) for a non-holonomic double-pendulum subject to a 'skate' constraint and loaded through dead load is shown in Fig.B.1. The system is characterized by the parameters $[\tilde{d},\, \tilde{M}_L,\, \tilde{I}_{r,L},\, \tilde{k}_1]$ equal to $\tilde{\boldsymbol{\xi}} = [1/2,\, 1,\, 0,\, 1]$, $\beta_0 = 0$ and by a dimensionless external damping coefficient $\tilde{c}_e = 15$ (while $\tilde{c}_i = \tilde{c}_{t,L} = \tilde{c}_{r,L} = 0$), whose critical point for flutter corresponds (according to Fig.7.12, upper-right corner, red curve) to a supercritical Hopf bifurcation, and therefore to the existence of stable orbits in the neighbourhood of the critical point. Moreover, the system is loaded through a dead load $\tilde{F} \approx 1.15\tilde{F}_{cr}$, where $\tilde{F}_{cr} \approx 6.09$ is the critical flutter load, and the imposed initial conditions are $\Theta_i(0) = 0$ and $\dot{\Theta}_i(0) = \dot{\pi}_i(0) = 1/100$ for $i = 1, 2$. The comparison shows an almost perfect agreement between the numerical solutions for the two systems of equations.

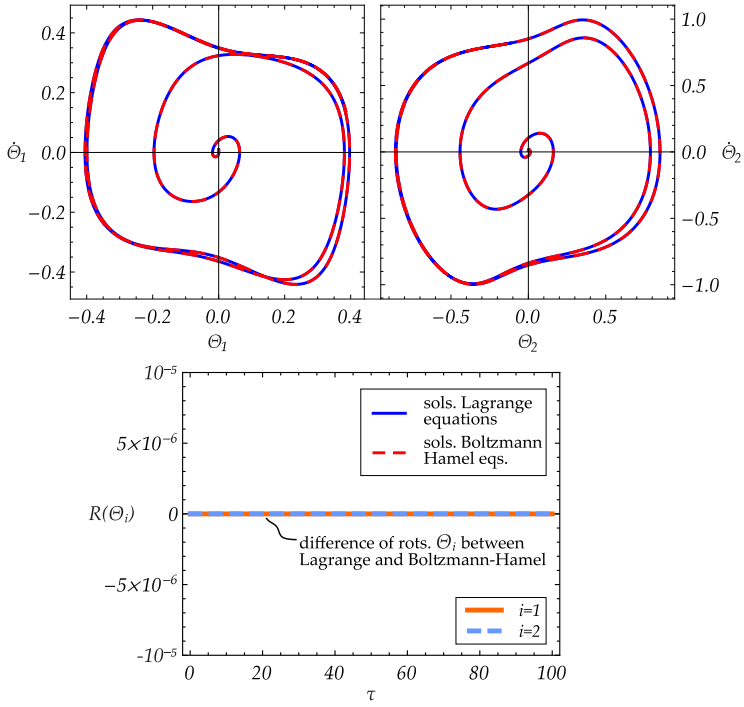

Figure B.1: (Upper part) Comparison between the solutions obtained through the Lagrange equations (blue lines) and the Boltzmann-Hamel formulation in quasi-coordinates (red-dashed lines) for a double-pendulum subject to a perfect ($\beta_0 = 0$) 'skate' non-holonomic constraint for the same external load, machanical parameters, damping coefficients and initial conditions, showing an almost perfect superposition of the obtained orbits (which finally reach a periodic solution). (Lower part) Residual $\Theta_i^{BH} - \Theta_i^L$ as a function of the dimensionless time τ between the solutions obtained by solving the Boltzmann-Hamel and Lagrange equations and showing an almost constant null value along the whole simulation.

C

Complementary equations for the non-holonomic dicrete system

C.1 Determinant of the stiffness matrix $\mathbb{K}^{(N)}$

The determinant of the matrix (7.24) can be obtained through a recursive procedure. The three different cases $N = 1$, $N = 2$ and $N > 2$ are treated separately.

- **Case** $N = 1$: the determinant of the stiffness matrix corresponds to the stiffness k_1 of the first rotational spring

$$\det \mathbb{K}^{(1)} = k_1. \tag{C.1}$$

- **Case** $N = 2$: the determinant of the stiffness matrix is

$$\det \mathbb{K}^{(2)} = \det \begin{bmatrix} k_1 + k_2 & -k_2 \\ -k_2 & k_2 \end{bmatrix} = k_1 k_2. \tag{C.2}$$

- **Case** $N > 2$: the j-th determinant D_j of the $j \times j$ matrix $\mathbb{K}^{(j)}$, defined as the upper-left-corner matrix of $\mathbb{K}^{(N)}$ (so that $D_N = \det \mathbb{K}^{(N)}$), is given

by

$$\begin{aligned} D_1 &= k_1 + k_2 \\ D_2 &= k_1 k_2 + k_1 k_3 + k_2 k_3 \\ D_j &= (k_j + k_{j+1}) D_{j-1} - k_j^2 D_{j-2}, \qquad 2 < j < N, \end{aligned} \tag{C.3}$$

where D_j is a function of the determinants of the two upper-left-corner matrices (of $j-1$ and $j-2$ rank) forming the $j \times j$ matrix $\mathbb{K}^{(j)}$. Note that the sum $(k_j + k_{j+1})$ represents the diagonal element $\mathbb{K}^{(N)}_{jj}$. The determinant of the whole $N \times N$ matrix (7.24) can be rewritten as

$$\det \mathbb{K}^{(N)} = k_N D_{N-1} - k_N^2 D_{N-2}. \tag{C.4}$$

In the case $N = 3$, the condition (C.4) already provides the final expression for the determinant condition

$$\det \mathbb{K}^{(3)} = k_3 D_2 - k_3^2 D_1 = k_1 k_2 k_3. \tag{C.5}$$

In the case $N > 3$, the substitution of the determinants D_{N-1} and D_{N-2} in Eq.(C.4) through Eq.(C.3) can be recursively performed at decreasing values of the index j until the value 3 is reached, thus obtaining the following equation

$$\det \mathbb{K}^{(N)} = (k_3\, D_2 - k_3^2 D_1) \prod_{i=0}^{N-4} k_{N-i}, \tag{C.6}$$

from which Eq.(7.25) can be easily derived.

C.2 Uniqueness of the trivial equilibrium solution for $\beta_0 = 0$

The proof of the uniqueness of the trivial quasi-static solution for both the considered non-holonomic constraints in the case $\beta_0 = 0$ is given for a column made up of an arbitrary number N of rigid elements.

Non-holonomic 'skate' constraint with $\beta_0 = 0$. The N-th term of the vector of non-holonomic coefficients a_k in Eq.(7.7) is always zero $a_N(\mathbf{q}^{\mathrm{QS}}, 0) =$

$l_N \sin 0 = 0$, so that the N-th equation of system (7.22) is always given by an identity between the two last rotations of the N–th and $(N-1)$–th bars

$$\theta_N^{\text{QS}} = \theta_{N-1}^{\text{QS}},$$

thus causing the $(N-1)$–th coefficient of the non-holonomic constraint (see Eq.(7.7)) being zero

$$a_{N-1}(\mathbf{q}^{\text{QS}}, 0) = l_{N-1} \sin\left(\theta_N^{\text{QS}} - \theta_{N-1}^{\text{QS}}\right) = 0. \tag{C.7}$$

Condition (C.7) can be substituted in the $(N-1)$-th equation of system (7.22) thus obtaining the identity between the rotations of the $(N-2)$-th and $(N-1)$-th rigid bars in the form $\theta_{N-2}^{\text{QS}} = \theta_{N-1}^{\text{QS}}$. The system can be therefore solved in a recursive way, finally obtaining all the rotations of the rigid bars being equal the one of the first bar

$$\theta_k^{\text{QS}} = \theta_1^{\text{QS}} \quad \forall\, k = 2, 3, ..., N$$

being the latter equal to zero by means of the first equation of the system (7.22).

Non-holonomic 'violin bow' constraint with $\beta_0 = 0$. The N equations of system (7.22) can be summed up obtaining a null value for the rotation of the first rigid bar $\theta_1^{\text{QS}} = 0$. This condition can be substituted in the expression for the first coefficient of the non-holonomic constraint given in Eq.(7.12), thus obtaining

$$a_1(\mathbf{q}^{\text{QS}}, 0) = -l_1 \sin 0 = 0$$

so that the first equation of the system (7.22) leads to the annihilation of the rotation of the second rigid bar $\theta_2^{\text{QS}} = 0$. Recursive substitutions within the remaining equations of the system (7.22) lead to a vanishing value for all the bars' rotations, completing the proof.

C.3 Proof of the Eq.(7.35)

The proof of the Eq.(7.35) for every $\beta_0 \neq 0$ can be obtained by firstly considering that

$$\det\left(\mathbb{K}^{(N)} + p^{\text{QS}}\mathbb{G}^{(N)}\right) = \det\mathbb{K}^{(N)} \det\left[\mathbf{I} + p^{\text{QS}}\left(\mathbb{K}^{(N)}\right)^{-1}\mathbb{G}^{(N)}\right], \tag{C.8}$$

or equivalently, because the determinant of a matrix coincides with the determinant of the transpose of the matrix,

$$\det\left(\mathbb{K}^{(N)}+p^{\text{QS}}\mathbb{G}^{(N)}\right)=\det\mathbb{K}^{(N)}\det\left[\mathbf{I}+p^{\text{QS}}\left(\mathbb{K}^{(N)}\right)^{-1}\left(\mathbb{G}^{(N)}\right)^{\mathsf{T}}\right] \quad \text{(C.9)}$$

where the stiffness matrix $\mathbb{K}^{(N)}$ (see Eq.(7.24)) is symmetric and positive-definite. The inverse of the stiffness matrix $\left(\mathbb{K}^{(N)}\right)^{-1}$ can be written as a particular case of the representation given by Meurant [81] in the form (the components are denoted by u_i, with $i=1,...,N$)

$$\left(\mathbb{K}^{(N)}\right)^{-1}=\begin{bmatrix} u_1 & u_1 & u_1 & \dots & u_1 \\ u_1 & u_2 & u_2 & \dots & u_2 \\ u_1 & u_2 & u_3 & \dots & u_3 \\ \vdots & \vdots & \vdots & \ddots & \vdots \\ u_1 & u_2 & u_3 & \dots & u_N \end{bmatrix}. \quad \text{(C.10)}$$

For 'skate' ('violin bow') constraint, matrix $\mathbb{G}_S^{(N)\,\mathsf{T}}$ (matrix $\mathbb{G}_V^{(N)}$) has a non-vanishing last row and vanishing last column, see Eq.(7.34). The matrix $\mathbf{N}$ is introduced, expressing the matrix product between the inverse of the stiffness matrix (C.10) and the geometric stiffness matrix $\mathbb{G}^{(N)}$, such that

- for 'skate' constraint using the Eq.(C.9)

$$\mathbf{N}=\left(\mathbb{K}^{(N)}\right)^{-1}\mathbb{G}_S^{(N)\,\mathsf{T}}; \quad \text{(C.11)}$$

- for 'violin bow' constraint using the Eq.(C.8)

$$\mathbf{N}=\left(\mathbb{K}^{(N)}\right)^{-1}\mathbb{G}_V^{(N)}. \quad \text{(C.12)}$$

By considering the expression for the inverse of the stiffness matrix (C.10) and the expressions of the geometrical stiffness matrices for both constraints (7.34), the matrix $\mathbf{N}$ can be evaluated through the Eqs.(C.11) and (C.12) leading to the following expression

$$\mathbf{N}=\begin{bmatrix} 0 & 0 & 0 & \dots & 0 \\ \gamma_1(u_2-u_1) & 0 & 0 & \dots & 0 \\ \gamma_1(u_3-u_1) & \gamma_2(u_3-u_2) & \ddots & & \vdots \\ \vdots & \vdots & & 0 & \vdots \\ \gamma_1(u_N-u_1) & \gamma_2(u_N-u_2) & \dots & \gamma_{N-1}(u_N-u_{N-1}) & 0 \end{bmatrix}, \quad \text{(C.13)}$$

valid for both the 'skate' and 'violin bow' constraints, where γ_i can be interpreted as the i-th parameter $\gamma_{S,i}$ or $\gamma_{V,i}$ in Eq.(7.34). The strictly upper triangular matrix $\mathbf{N}$ is therefore a nilpotent matrix of index N having its N-th power equal to the null matrix, $\mathbf{N}^N = 0$. Due to well-known properties of nilpotent matrices, the following determinant condition holds

$$\det\left[\mathbf{I} + p^{\text{QS}}\mathbf{N}\right] = 1, \tag{C.14}$$

for every choice of the non-holonomic constraint, such that

$$\det\left(\mathbb{K}^{(N)} + p^{\text{QS}}\mathbb{G}^{(N)}\right) = \det\mathbb{K}^{(N)}, \tag{C.15}$$

and also leading to the following condition

$$\left(\mathbb{K}^{(N)} + p^{\text{QS}}\mathbb{G}^{(N)}\right)^{-1} = \left(\mathbb{K}^{(N)}\right)^{-1} \sum_{j=0}^{N-1} (-\mathbf{N})^j, \tag{C.16}$$

where $(-\mathbf{N})^0 = \mathbf{I}$.

The obtained equations hold for every value of the angle β_0 and are valid for both the non-holonomic constraints and the loading conditions at the initial end.

C.4 Considerations on the buckling condition $\rho_m = 0$ for $\beta_0 \neq 0$

Due to the multiplicity of quasi-static configurations in the case $\beta_0 \neq 0$, buckling conditions along generic equilibrium paths are theoretically achievable. Therefore, the equation $\rho_m = 0$ is particularized for all the considered non-holonomic constraints and loading conditions at the initial end. In particular, no buckling conditions can be achieved for the 'violin bow' constraint when subject to the loading condition B (dead load) even in the case $\beta_0 \neq 0$, while critical loads seem to be theoretically achievable for all the remaining systems.

Buckling for the loading condition A: elastic device. According to Eq.(7.30), the term $\partial^2\Xi(\mathbf{q})/\partial X^2 = K$ is different from zero; the expressions of the stiffness matrices (7.30) and (7.32) and the condition (C.15) can be used to rewrite equation $\rho_m = 0$ for the the two cases of 'skate' and 'violin bow' types of constraint as follows.

- **'Skate' constraint**: Eqs.(7.32) and (7.38) lead to the following expression for the buckling condition

$$K\,\mathbf{w}^{(N)\intercal}\left(\mathbb{K}^{(N)}+p^{\text{QS}}\mathbb{G}^{(N)}\right)^{-1}\mathbf{w}^{(N)}+w_{N+1}\Big(w_{N+1}+ \\ -\mathbf{g}\left(\mathbb{K}^{(N)}+p^{\text{QS}}\mathbb{G}^{(N)}\right)^{-1}\mathbf{w}^{(N)}\Big)=0, \tag{C.17}$$

  where vector $\mathbf{g}\neq 0$ denotes the presence of the 'skate' constraint.

- **'Violin bow' constraint**: Eqs.(7.33) show that the analytical expression for the buckling condition can be simply obtained by setting $\mathbf{g}=0$ to yield

$$K\,\mathbf{w}^{(N)\intercal}\left(\mathbb{K}^{(N)}+p^{\text{QS}}\mathbb{G}^{(N)}\right)^{-1}\mathbf{w}^{(N)}+w_{N+1}^2=0. \tag{C.18}$$

Buckling for the loading condition B: dead load. Now $K=0$, so that the equation governing buckling can be obtained as a particular case of Eqs.(C.17) and (C.18).

- **'Skate' constraint**: setting $K=0$ in Eq.(C.17) one obtains

$$w_{N+1}^2-w_{N+1}\mathbf{g}\left(\mathbb{K}^{(N)}+p^{\text{QS}}\mathbb{G}^{(N)}\right)^{-1}\mathbf{w}^{(N)}=0. \tag{C.19}$$

- **'Violin bow' type constraint**: the condition $\mathbf{g}=0$ in the Eq.(C.19), or alternatively $K=0$ in Eq.(C.18), leads to the following solution for buckling

$$w_{N+1}^2=0 \quad\rightarrow\quad \beta_0=\pi/2+k\pi, \qquad k=1,2,3,... \tag{C.20}$$

  proving the absence of buckling loads for the 'violin bow' constraint even in the case $\beta_0\neq 0$. In fact, the case $\beta_0=\pi/2+k\pi$ represents a pathological condition providing a null bucking load, as the system undergoes a lability along the horizontal direction.

C.5 Determinant of the sum of 2×2 matrices

The Cayley-Hamilton theorem writes for a square 2×2 matrix as

$$p(\mathbf{A})=\mathbf{A}^2-\operatorname{tr}\mathbf{A}\,\mathbf{A}+\det\mathbf{A}\,\mathbf{I}_2=0. \tag{C.21}$$

Applying the trace operator to Eq.(C.21), the following equation for the determinant of $\mathbf{A}$ is obtained

$$\det \mathbf{A} = \frac{(\operatorname{tr} \mathbf{A})^2 - \operatorname{tr} \mathbf{A}^2}{2}, \tag{C.22}$$

which can be extended to the case when the determinant is the sum of a generic number of 2×2 matrices

$$\det \left(\sum_{i=1}^{M} \mathbf{A}_i \right) = \sum_{i=1}^{M} \left[\det \mathbf{A}_i + \sum_{j=i+1}^{M} \left(\operatorname{tr} \mathbf{A}_i \ \operatorname{tr} \mathbf{A}_j - \operatorname{tr} \left[\mathbf{A}_i \, \mathbf{A}_j \right] \right) \right], \tag{C.23}$$

where $M \geq 1$ is the number of matrices. For $M = 3$ Eq.(C.23) particularizes to

$$\begin{aligned} \det \left[\mathbf{A}_1 \zeta^2 + \mathbf{A}_2 \zeta + \mathbf{A}_3 \right] = \det \mathbf{A}_1 \zeta^4 + \left(\operatorname{tr} \mathbf{A}_1 \ \operatorname{tr} \mathbf{A}_2 - \operatorname{tr} \left[\mathbf{A}_1 \, \mathbf{A}_2 \right] \right) \zeta^3 + \det \mathbf{A}_3 + \\ + \left(\det \mathbf{A}_2 + \left(\operatorname{tr} \mathbf{A}_1 \ \operatorname{tr} \mathbf{A}_3 - \operatorname{tr} \left[\mathbf{A}_1 \, \mathbf{A}_3 \right] \right) \right) \zeta^2 + \left(\operatorname{tr} \mathbf{A}_2 \ \operatorname{tr} \mathbf{A}_3 - \operatorname{tr} \left[\mathbf{A}_2 \, \mathbf{A}_3 \right] \right) \zeta \end{aligned} \tag{C.24}$$

where $\zeta \in \mathbb{C}$ is a generic scalar quantity.

C.6 Exact solution for a quartic polynomial

The exact solutions for a quartic in the form:

$$p_0 \, x^4 + p_1 \, x^3 + p_2 \, x^2 + p_3 \, x + p_4 = 0$$

can be expressed in the following form

$$x = -\frac{p_1}{4 \, p_0} \pm_1 H \pm_2 \frac{1}{2} \sqrt{-4 \, H^2 - 2 \, \xi \mp_1 \frac{\zeta}{H}}$$

where

$$\xi = \frac{8 \, p_0 \, p_2 - 3 \, p_1^2}{8 \, p_0^2}, \quad \zeta = \frac{p_1^3 - 4 \, p_0 \, p_1 \, p_2 + 8 \, p_0^2 \, p_3}{8 \, p_0^3},$$

$$H = \frac{1}{2} \sqrt{-\frac{2}{3} \xi + \frac{1}{3 \, p_0} \left(J + \frac{\Delta_0}{J} \right)}$$

and where

$$J = \sqrt[3]{\frac{\Delta_1 + \sqrt{\Delta_1^2 - 4\,\Delta_0^3}}{2}}, \quad \Delta_0 = p_2^2 - 3\,p_1\,p_3 + 12\,p_0\,p_4,$$
$$\Delta_1 = 27\left(p_1^2\,p_4 + p_0\,p_3^2\right) - 9\,p_2\,(8\,p_0\,p_4 + p_1\,p_3) + 2\,p_2^3$$

and bifurcations in the real part of the roots x occur when $\Delta_1^2 - 4\,\Delta_0^3 = 0$, a condition leading to Eq.(7.64).

C.7 Considerations on the transformed matrix (7.90)

For the given 4×4 real matrix $\tilde{\mathbf{J}}$ in the form (7.90) with two complex conjugate eigenvalues $\lambda_{1,2} = \pm i\omega_0$ ($\omega_0 > 0$) and two additional eigenvalues λ_3 and λ_4 with negative real part, its spectral representation in dual (complex) bases is

$$\tilde{\mathbf{J}} = \omega_0 i\,\mathbf{e}_1^{\mathrm{r}} \otimes \mathbf{e}_1^{\mathrm{l}} - \omega_0 i\,\mathbf{e}_2^{\mathrm{r}} \otimes \mathbf{e}_2^{\mathrm{l}} + \lambda_3\,\mathbf{e}_3 \otimes \mathbf{e}_3 + \lambda_4\,\mathbf{e}_4 \otimes \mathbf{e}_4, \tag{C.25}$$

where $\mathbf{e}_i^{\mathrm{r}}$ and $\mathbf{e}_j^{\mathrm{l}}$ denote the right and left eigenvectors of $\tilde{\mathbf{J}}$ related to the i-th and j-th eigenvalue, respectively. The following property holds true

$$\left\langle \mathbf{e}_i^{\mathrm{r}},\, \bar{\mathbf{e}}_j^{\mathrm{l}} \right\rangle = \delta_{ij}, \tag{C.26}$$

where δ_{ij} is the Kronecker delta and $\langle \boldsymbol{a}, \boldsymbol{b} \rangle = \bar{a}_1 b_1 + ... + \bar{a}_4 b_4$ denotes the scalar product in $\mathbb{C}^4$, while $\bar{\boldsymbol{a}}$ the conjugate of $\boldsymbol{a}$. More specifically, the particular form (7.90) of the matrix $\tilde{\mathbf{J}}$ leads to the following set of eigenvectors satisfying the condition (C.26)

$$\mathbf{e}_1^{\mathrm{r}} = \bar{\mathbf{e}}_2^{\mathrm{r}} = \begin{bmatrix} 1 \\ i \\ 0 \\ 0 \end{bmatrix}, \quad \mathbf{e}_1^{\mathrm{l}} = \bar{\mathbf{e}}_2^{\mathrm{l}} = \frac{1}{2}\begin{bmatrix} 1 \\ -i \\ 0 \\ 0 \end{bmatrix}, \qquad \mathbf{e}_3 = \begin{bmatrix} 0 \\ 0 \\ 1 \\ 0 \end{bmatrix}, \qquad \mathbf{e}_4 = \begin{bmatrix} 0 \\ 0 \\ 0 \\ 1 \end{bmatrix}. \tag{C.27}$$

The real transformation matrix $\mathbf{A}$ is introduced, such that the original matrix $\mathbf{J}$ can be represented as

$$\begin{aligned}\mathbf{J} =& \mathbf{A}\tilde{\mathbf{J}}\mathbf{A}^{-1} \\ =& \omega_0\,i\,\mathbf{A}\mathbf{e}_1^{\mathrm{r}} \otimes \mathbf{A}^{-\intercal}\mathbf{e}_1^{\mathrm{l}} - \omega_0\,i\,\mathbf{A}\mathbf{e}_2^{\mathrm{r}} \otimes \mathbf{A}^{-\intercal}\mathbf{e}_2^{\mathrm{l}} + \lambda_3\,\mathbf{A}\mathbf{e}_3 \otimes \mathbf{A}^{-\intercal}\mathbf{e}_3 + \lambda_4\,\mathbf{A}\mathbf{e}_4 \otimes \mathbf{A}^{-\intercal}\mathbf{e}_4,\end{aligned}$$

or equivalently through eigenvectors (7.88)

$$\mathbf{J} = \omega_0\, i\, \boldsymbol{q} \otimes \bar{\boldsymbol{p}} - \omega_0\, i\, \bar{\boldsymbol{q}} \otimes \boldsymbol{p} + \lambda_3\, \mathbf{v}_3^{\mathrm{r}} \otimes \mathbf{v}_3^{\mathrm{l}} + \lambda_4\, \mathbf{v}_4^{\mathrm{r}} \otimes \mathbf{v}_4^{\mathrm{r}}. \tag{C.28}$$

The above expression holds because the left eigenvector $\boldsymbol{q}^{\mathrm{l}}$ of $\mathbf{J}$ corresponding to the eigenvalue $i\,\omega_0$ and the eigenvector $\boldsymbol{p}$ can be obtained as

$$\mathbf{J}^{\intercal}\boldsymbol{q}^{\mathrm{l}} = i\,\omega_0 \boldsymbol{q}^{\mathrm{l}}, \qquad \mathbf{J}^{\intercal}\boldsymbol{p} = -i\,\omega_0 \boldsymbol{p},$$

so that $\boldsymbol{q}^{\mathrm{l}} = \bar{\boldsymbol{p}}$. A similar expression holds for $\boldsymbol{p}^{\mathrm{r}}$ and $\bar{\boldsymbol{q}}$.

An analysis of the eigenvectors (C.27) of matrix $\tilde{\mathbf{J}}$ reveals that the conditions

$$\boldsymbol{q} = \mathbf{A}\mathbf{e}_1^{\mathrm{r}}, \qquad \mathbf{v}_3^{\mathrm{r}} = \mathbf{A}\mathbf{e}_3, \qquad \mathbf{v}_4^{\mathrm{r}} = \mathbf{A}\mathbf{e}_4, \tag{C.29}$$

hold true if the matrix $\mathbf{A}$ is taken as in Eq.(7.91), thus completing the proof.

C.8 Explicit expression for the coefficients ρ_i of the characteristic polynomial for the non-holonomic double pendulum

From Eqs.(58), the explicit expressions for the coefficients ρ_i $(i = 0, ..., 4)$ can be obtained as

$$\rho_0 = \frac{1}{4}\left(\tilde{I}_{r,L}\,\tilde{M}_L + \frac{1}{16}\tilde{d}^4 + \frac{1}{2}\tilde{d}^2\,\tilde{I}_{r,L} + \frac{1}{4}\tilde{d}^2\,\tilde{M}_L - \frac{1}{4}\tilde{d}\,\tilde{M}_L + \frac{1}{2}\tilde{I}_{r,L} + \frac{1}{8}\tilde{M}_L\right), \tag{C.30}$$

$$\begin{aligned}\rho_1 = {} & \frac{1}{64}\left(\frac{5}{3}\tilde{c}_e\,\tilde{d}^2 - \tilde{c}_e\,\tilde{d} + \frac{1}{3}\tilde{c}_e\right) + \frac{1}{16}\left(\frac{1}{3}\tilde{c}_e\tilde{M}_L + \tilde{c}_{t,L}\,\tilde{d}^2 - \tilde{c}_{t,L}\,\tilde{d} + \frac{1}{2}\tilde{c}_{t,L}\right) + \\ & + \frac{1}{8}\Big(\tilde{c}_{r,L}\,\tilde{d}^2 + \tilde{c}_{r,L} + 2\tilde{c}_{r,L}\,\tilde{M}_L + 2\tilde{c}_{t,L}\,\tilde{I}_{r,L} + 3\,\tilde{c}_i\,\tilde{d}^2 + 2\tilde{c}_i\,\tilde{d} + \tilde{c}_i + 10\,\tilde{c}_i\tilde{M}_L\Big) + \\ & + 2\,\tilde{c}_i\,\tilde{I}_{r,L} + \frac{1}{6}\tilde{c}_e\,\tilde{I}_{r,L},\end{aligned} \tag{C.31}$$

$$\begin{aligned}\rho_2 = {} & \frac{1}{16}\left(\frac{1}{3}\tilde{c}_e\,\tilde{c}_{t,L} - \tilde{d}^2\tilde{p}^{\mathrm{QS}} - \tilde{d}\,\tilde{p}^{\mathrm{QS}}\right) + \frac{1}{8}\left((2+\tilde{k}_1)\,\tilde{d}^2 + 3\,\tilde{c}_e\,\tilde{c}_i + 1\right) + \\ & \frac{1}{4}\Big(\tilde{c}_{r,L}\,\tilde{c}_{t,L} + 5\,\tilde{c}_{t,L}\,\tilde{c}_i + \tilde{d} - \tilde{p}^{\mathrm{QS}}\tilde{M}_L + (4+\tilde{k}_1)\tilde{M}_L\Big) + \frac{7}{2304}\tilde{c}_e^2 + \\ & \frac{1}{6}\tilde{c}_e\,\tilde{c}_{r,L} - \frac{1}{2}\tilde{I}_{r,L}\,\tilde{p}^{\mathrm{QS}} + 2\,\tilde{c}_{r,L}\,\tilde{c}_i + \tilde{c}_i^2 + (1+\tilde{k}_1)\,\tilde{I}_{r,L},\end{aligned} \tag{C.32}$$

$$\begin{aligned}\rho_3 = {} & -\frac{5}{96}\tilde{c}_e\,\tilde{p}^{\mathrm{QS}} + \frac{8+\tilde{k}_1}{24}\tilde{c}_e + \frac{1}{4}\left((4+\tilde{k}_1)\,\tilde{c}_{t,L} - \tilde{c}_{t,L}\,\tilde{p}^{\mathrm{QS}}\right) - \frac{1}{2}\tilde{c}_{r,L}\,\tilde{p}^{\mathrm{QS}} + \\ & (1+\tilde{k}_1)\,(\tilde{c}_i + \tilde{c}_{r,L}),\end{aligned} \tag{C.33}$$

$$\rho_4 = \tilde{k}_1. \tag{C.34}$$

C.9 Critical flutter load with a single source of viscosity

C.9.1 Presence of internal damping $\tilde{c}_i$

The critical load for flutter in the presence of only the internal damping $\tilde{c}_i = r$ is given by

$$\mathcal{P}_d\left(\tilde{c}_i, \boldsymbol{\xi}\right) = \mathcal{P}_d\left(r, \frac{\pi}{2}, \frac{\pi}{2}, 0, \boldsymbol{\xi}\right) =$$
$$2\Bigg(\frac{\tilde{d}^4(2(\tilde{k}_1-1)\tilde{k}_1+5)+\tilde{d}^2\left(16\tilde{I}_{r,L}(\tilde{k}_1(2\tilde{k}_1-1)+3)+\tilde{k}_1^2+4(\tilde{k}_1(3\tilde{k}_1-2)+10)\tilde{M}_L+9\right)}{(\tilde{k}_1+1)\left(\tilde{d}^2+\tilde{d}+8\tilde{I}_{r,L}+4\tilde{M}_L\right)(\tilde{d}(3\tilde{d}+2)+16\tilde{I}_{r,L}+10\tilde{M}_L+1)}+$$
$$+\frac{4\tilde{d}\left(4\tilde{I}_{r,L}\left(\tilde{k}_1^2+3\right)+2\left(\tilde{k}_1^2+\tilde{k}_1+5\right)\tilde{M}_L+1\right)+4\left[4\tilde{I}_{r,L}\left(8\tilde{I}_{r,L}\left(\tilde{k}_1^2+1\right)-\tilde{k}_1+1\right)\right]}{(\tilde{k}_1+1)\left(\tilde{d}^2+\tilde{d}+8\tilde{I}_{r,L}+4\tilde{M}_L\right)(\tilde{d}(3\tilde{d}+2)+16\tilde{I}_{r,L}+10\tilde{M}_L+1)}+$$
$$+\frac{2\tilde{d}^3\left(\tilde{k}_1^2+5\right)+\left[\tilde{M}_L(8\tilde{I}_{r,L}(\tilde{k}_1(3\tilde{k}_1-1)+6)-\tilde{k}_1)+5\left(\tilde{k}_1^2+4\right)\tilde{M}_L^2\right]+16\tilde{M}_L+1}{(\tilde{k}_1+1)\left(\tilde{d}^2+\tilde{d}+8\tilde{I}_{r,L}+4\tilde{M}_L\right)(\tilde{d}(3\tilde{d}+2)+16\tilde{I}_{r,L}+10\tilde{M}_L+1)}\Bigg)+$$
$$+\tilde{c}_i^2\frac{16\,(\tilde{k}_1+1)(\tilde{d}(3\tilde{d}+2)+16\tilde{I}_{r,L}+10\tilde{M}_L+1)}{(\tilde{k}_1+1)\left(\tilde{d}^2+\tilde{d}+8\tilde{I}_{r,L}+4\tilde{M}_L\right)(\tilde{d}(3\tilde{d}+2)+16\tilde{I}_{r,L}+10\tilde{M}_L+1)} \tag{C.35}$$

For $\tilde{c}_i \to 0$ (or equivalently $r \to 0$) the limit critical load is given by

$$\mathcal{P}_d^*\left(\frac{\pi}{2}, \frac{\pi}{2}, 0, \boldsymbol{\xi}\right) =$$
$$2\Bigg(\frac{\tilde{d}^4(2(\tilde{k}_1-1)\tilde{k}_1+5)+\tilde{d}^2\left(16\tilde{I}_{r,L}(\tilde{k}_1(2\tilde{k}_1-1)+3)+\tilde{k}_1^2+4(\tilde{k}_1(3\tilde{k}_1-2)+10)\tilde{M}_L+9\right)}{(\tilde{k}_1+1)\left(\tilde{d}^2+\tilde{d}+8\tilde{I}_{r,L}+4\tilde{M}_L\right)(\tilde{d}(3\tilde{d}+2)+16\tilde{I}_{r,L}+10\tilde{M}_L+1)}+$$
$$+\frac{4\tilde{d}\left(4\tilde{I}_{r,L}\left(\tilde{k}_1^2+3\right)+2\left(\tilde{k}_1^2+\tilde{k}_1+5\right)\tilde{M}_L+1\right)+4\left[4\tilde{I}_{r,L}\left(8\tilde{I}_{r,L}\left(\tilde{k}_1^2+1\right)-\tilde{k}_1+1\right)\right]}{(\tilde{k}_1+1)\left(\tilde{d}^2+\tilde{d}+8\tilde{I}_{r,L}+4\tilde{M}_L\right)(\tilde{d}(3\tilde{d}+2)+16\tilde{I}_{r,L}+10\tilde{M}_L+1)}+$$
$$+\frac{2\tilde{d}^3\left(\tilde{k}_1^2+5\right)+\left[\tilde{M}_L(8\tilde{I}_{r,L}(\tilde{k}_1(3\tilde{k}_1-1)+6)-\tilde{k}_1)+5\left(\tilde{k}_1^2+4\right)\tilde{M}_L^2\right]+16\tilde{M}_L+1}{(\tilde{k}_1+1)\left(\tilde{d}^2+\tilde{d}+8\tilde{I}_{r,L}+4\tilde{M}_L\right)(\tilde{d}(3\tilde{d}+2)+16\tilde{I}_{r,L}+10\tilde{M}_L+1)}\Bigg) \tag{C.36}$$

C.9.2 Presence of external damping $\tilde{c}_e$

The critical load for flutter in the presence of only the external damping $\tilde{c}_e = r$ is given by

$$
\begin{aligned}
&\mathcal{P}_d\left(\tilde{c}_e,\, \boldsymbol{\xi}\right) = \mathcal{P}_d\left(r,\, \frac{\pi}{2},\, \frac{\pi}{2},\, \frac{\pi}{2},\, \boldsymbol{\xi}\right) = \\
&\Bigg(140\,\tilde{c}_e^2\tilde{M}_L + 35\,\tilde{c}_e^2 - (\tilde{d}(5\tilde{d}-3) + 32\tilde{I}_{r,L} + 4\tilde{M}_L + 1)\Big[1225\,\tilde{c}_e^4 + \\
&+ 20160\,\tilde{c}_e^2\left(3\tilde{d}^2(\tilde{k}_1-2) - 2\tilde{d}(\tilde{k}_1+3) + 8\tilde{I}_{r,L}(3\tilde{k}_1-11) + 2(\tilde{k}_1-12)\tilde{M}_L + 5\right) + \\
&+ 82944\Big(\tilde{d}^4(\tilde{k}_1(9\tilde{k}_1+64)+36) + \tilde{d}^3(4\tilde{k}_1(17-3\tilde{k}_1)+72) + \\
&+ 2\tilde{d}^2(8\tilde{I}_{r,L}(\tilde{k}_1(9\tilde{k}_1+79)+66) + \tilde{k}_1(6\tilde{k}_1\tilde{M}_L + 2\tilde{k}_1 + 196\tilde{M}_L - 13) + 144\tilde{M}_L - 12) + \\
&+ 4\tilde{d}(-24\tilde{I}_{r,L}((\tilde{k}_1-4)\tilde{k}_1 - 11) + \tilde{k}_1(-2\tilde{k}_1\tilde{M}_L + 38\tilde{M}_L + 5) + 72\tilde{M}_L - 15) + \\
&+ 64\tilde{I}_{r,L}^2(\tilde{k}_1(9\tilde{k}_1+94)+121) + 16\tilde{I}_{r,L}(\tilde{k}_1(6\tilde{k}_1\tilde{M}_L) + \\
&+ 206\tilde{M}_L - 15) + 264\tilde{M}_L - 55 + 4\tilde{M}_L((\tilde{k}_1(\tilde{k}_1+136)+144)\tilde{M}_L - 5(\tilde{k}_1+12)) + 25\Big)\Big]^{\frac{1}{2}} + \\
&+ 175\,\tilde{c}_e^2\tilde{d}^2 - 105\,\tilde{c}_e^2\tilde{d} + 1120\,\tilde{c}_e^2\tilde{I}_{r,L} + 7200\tilde{d}^4\tilde{k}_1 + 14400\tilde{d}^4 - 3168\tilde{d}^3\tilde{k}_1 + 14976\tilde{d}^3 + \\
&+ 122112\tilde{d}^2\tilde{I}_{r,L}\tilde{k}_1 + 297216\tilde{d}^2\tilde{I}_{r,L} + 22464\tilde{d}^2\tilde{k}_1\tilde{M}_L + 288\tilde{d}^2\tilde{k}_1 + 87552\tilde{d}^2\tilde{M}_L - 7776\tilde{d}^2 + \\
&- 29952\tilde{d}\tilde{I}_{r,L}\tilde{k}_1 + 94464\tilde{d}\tilde{I}_{r,L} - 1728\tilde{d}\tilde{k}_1\tilde{M}_L + 576\tilde{d}\tilde{k}_1 + 32256\tilde{d}\tilde{M}_L + \\
&+ 3168\tilde{d} + 516096\tilde{I}_{r,L}^2\tilde{k}_1 + 1548288\tilde{I}_{r,L}^2 + 184320\tilde{I}_{r,L}\tilde{k}_1\tilde{M}_L - 6912\tilde{I}_{r,L}\tilde{k}_1 + \\
&+ 783360\tilde{I}_{r,L}\tilde{M}_L - 89856\tilde{I}_{r,L} + 20736\tilde{k}_1\tilde{M}_L^2 - 576\tilde{k}_1\tilde{M}_L + 119808\tilde{M}_L^2 + \\
&- 10368\tilde{M}_L + 1440\Bigg) \Bigg/ \Bigg(720\Big(5\tilde{d}^4 + 4\tilde{d}^3 + 4\tilde{d}^2(26\tilde{I}_{r,L} + 7\tilde{M}_L - 1) + \\
&+ 2\tilde{d}(8\tilde{I}_{r,L} + 2\tilde{M}_L + 1) + 8\left(30\tilde{I}_{r,L}\tilde{M}_L + \tilde{I}_{r,L}(64\tilde{I}_{r,L} - 3) + 4\tilde{M}_L^2\right) - 2\tilde{M}_L\Big)\Bigg)
\end{aligned}
\tag{C.37}
$$

For $\tilde{c}_e \to 0$ (or equivalently $r \to 0$), the limit critical load is given by

$$
\begin{aligned}
&\mathcal{P}_d^*\left(\frac{\pi}{2}, \frac{\pi}{2}, \frac{\pi}{2}, \boldsymbol{\xi}\right) = \\
&2\Bigg[\tilde{d}^3(52-11\tilde{k}_1)+\tilde{d}^2(8\tilde{I}_{r,L}(53\tilde{k}_1+129)+78\tilde{k}_1\tilde{M}_L+\tilde{k}_1+304\tilde{M}_L-27)+ \\
&+25\tilde{d}^4(\tilde{k}_1+2)++\tilde{d}(8\tilde{I}_{r,L}(41-13\tilde{k}_1)-6\tilde{k}_1\tilde{M}_L+2\tilde{k}_1+112\tilde{M}_L+11)+1792\tilde{I}_{r,L}^2(\tilde{k}_1+3)+ \\
&+8\tilde{I}_{r,L}(80\tilde{k}_1\tilde{M}_L-3\tilde{k}_1+340\tilde{M}_L-39)+8(9\tilde{k}_1+52)\tilde{M}_L^2-2(\tilde{k}_1+18)\tilde{M}_L+5+ \\
&-\left(5\tilde{d}^2-3\tilde{d}+32\tilde{I}_{r,L}+4\tilde{M}_L+1\right)\left\{\tilde{d}^4\left(9\tilde{k}_1^2+64\tilde{k}_1+36\right)+\tilde{d}^3\left(-12\tilde{k}_1^2+68\tilde{k}_1+72\right)+\right. \\
&+2\tilde{d}^2\left(8\tilde{I}_{r,L}\left(9\tilde{k}_1^2+79\tilde{k}_1+66\right)+\tilde{k}_1^2(6\tilde{M}_L+2)+\tilde{k}_1(196\tilde{M}_L-13)+144\tilde{M}_L-12\right)+ \\
&-4\tilde{d}\left(24\tilde{I}_{r,L}\left(\tilde{k}_1^2-4\tilde{k}_1-11\right)+2\tilde{k}_1^2\tilde{M}_L-\tilde{k}_1(38\tilde{M}_L+5)-72\tilde{M}_L+15\right)+ \\
&+64\tilde{I}_{r,L}^2\left(9\tilde{k}_1^2+94\tilde{k}_1+121\right)+16\tilde{I}_{r,L}\left(6\tilde{k}_1^2\tilde{M}_L+\tilde{k}_1(206\tilde{M}_L-15)+264\tilde{M}_L-55\right)+ \\
&\left.+4\tilde{k}_1^2\tilde{M}_L^2+544\tilde{k}_1\tilde{M}_L^2-20\tilde{k}_1\tilde{M}_L+576\tilde{M}_L^2-240\tilde{M}_L+25\right\}^{\frac{1}{2}}\Bigg]\Bigg/\Bigg[5\Big(5\tilde{d}^4+4\tilde{d}^3+ \\
&+4\tilde{d}^2(26\tilde{I}_{r,L}+7\tilde{M}_L-1)+2\tilde{d}(8\tilde{I}_{r,L}+2\tilde{M}_L+1)+512\tilde{I}_{r,L}^2+ \\
&24\tilde{I}_{r,L}(10\tilde{M}_L-1)+2\tilde{M}_L(16\tilde{M}_L-1)\Big)\Bigg]
\end{aligned}
\tag{C.38}
$$

C.10 Critical flutter load with two sources of viscosity

C.10.1 Presence of internal and external damping

For the sake of simplicity, the critical load is particularized for the case $\hat{\boldsymbol{\xi}} = [1/2,\ 15,\ 15,\ 50]$. By setting $\tilde{c}_e = r\sin\phi_3$, $\tilde{c}_i = r\cos\phi_3$ and $r = \sqrt{\tilde{c}_e^2 + \tilde{c}_i^2}$ the critical load is given by

$$
\begin{aligned}
&\mathcal{P}_d\left(r,\ \frac{\pi}{2},\ \frac{\pi}{2},\ \phi_3,\ \hat{\boldsymbol{\xi}}\right) = \\
&\Bigg[25235r^2\sin^2\phi_3 + 3554600r^2\sin\phi_3\cos\phi_3 + 96\big(240r^2\cos^2\phi_3(6284\cot\phi_3 + 2717) + \\
&+ 288\cot\phi_3(57927483\cot\phi_3 + 10504342) + 120487001\big) + \\
&- (12568\cot\phi_3 + 721)\Big\{1225r^4\sin^4\phi_3 + 1152\left(4225r^4\sin^2(2\phi_3) + 35552208708\right) + \\
&+ 132710400r^4\cos^4\phi_3 + 99532800r^4\sin\phi_3\cos^3\phi_3 + \\
&+ 359009280r^2\sin^2\phi_3 - 9953280r^2\cos^2\phi_3(294984\cot\phi_3 + 98747) + \\
&+ 302400r^2\sin\phi_3\cos\phi_3\left(r^2\sin^2\phi_3 + 117036\right) + \\
&+ 1439244288\cot\phi_3(11283138\cot\phi_3 - 711833)\Big\}^{\frac{1}{2}}\Bigg] / \left[60(54519984\cot\phi_3 + 2826493)\right]
\end{aligned}
\tag{C.39}
$$

Moreover, the maximum value of the critical limit load (79) can be obtained by taking the limit of vanishing viscosities along the particular direction

$$
\bar{\phi}_3 = 2\tan^{-1}\left(\frac{\sqrt{1569057166584103530\sqrt{120482} + 26294588465714004524410} - 52150850614 - 150434475\sqrt{120482}}{144389423358}\right)
$$

and corresponding in this case to the critical value for the ideal case without damping $\mathcal{P}_0(\hat{\boldsymbol{\xi}})$, namely

$$
\mathcal{P}_d^*\left(\frac{\pi}{2},\ \frac{\pi}{2},\ \bar{\phi}_3,\ \hat{\boldsymbol{\xi}}\right) = \frac{20}{723}\left(3102 - \sqrt{120482}\right) = \mathcal{P}_0\left(\hat{\boldsymbol{\xi}}\right) \tag{C.40}
$$

C.10.2 Presence of translational and rotational damping for the non-holonomic constraint

For the sake of simplicity, the critical load is particularized to the case $\hat{\boldsymbol{\xi}} = [1/2,\ 15,\ 15,\ 50]$. By setting $\tilde{c}_{r,L} = r\sin\phi_1$, $\tilde{c}_{t,L} = r\cos\phi_1$ and $r = \sqrt{\tilde{c}_{r,L}^2 + \tilde{c}_{t,L}^2}$ the critical load is given by

$$
\begin{aligned}
&\mathcal{P}_d\left(r,\ \phi_1,\ 0,\ 0,\ \hat{\boldsymbol{\xi}}\right) = \\
&\Bigg[-4\sin(2\phi_1)\left(r^2(732\sin(2\phi_1) - 259\cos(2\phi_1)) + 741r^2 + 6641121\right) + \\
&+ 440805\cos(2\phi_1) - 18295539 + 2(250\sin\phi_1 + 241\cos\phi_1)\Big\{64r^4\sin^2\phi_1\cos^4\phi_1 + \\
&+ 2\sin(2\phi_1)\left(8r^2\sin(2\phi_1)\left(2r^2\sin(2\phi_1) + 2823\right) - 52890047\right) \\
&+ \cos^2\phi_1\left(256r^4\sin^4\phi_1 + 155027401\right) + 183984r^2\sin\phi_1\cos^3\phi_1 - 374592r^2\sin^3\phi_1\cos\phi_1 + \\
&+ 161137636\sin^2\phi_1\Big\}^{\frac{1}{2}}\Bigg] / \left[-288272\sin(2\phi_1) + 6534\cos(2\phi_1) - 234538\right]
\end{aligned}
\tag{C.41}
$$

Moreover, the maximum value of the critical flutter load at vanishing viscosity, equation (81), can be obtained as

$$
\bar{\phi}_1 = 2\tan^{-1}\left(\frac{\sqrt{501254456486856076080\sqrt{120482} + 12433474841838756712012219 7} - 315372600\sqrt{120482} - 7947019755154}{7820974511191}\right)
$$

which corresponds to the critical value for the ideal case without damping $\mathcal{P}_0(\hat{\boldsymbol{\xi}})$, namely

$$
\mathcal{P}_d^*\left(\bar{\phi}_1,\ 0,\ 0,\ \hat{\boldsymbol{\xi}}\right) = \frac{20}{723}\left(3102 - \sqrt{120482}\right) = \mathcal{P}_0\left(\hat{\boldsymbol{\xi}}\right) \tag{C.42}
$$

Bibliography

[1] Agostinelli, D., Lucantonio, A., Noselli, G., DeSimone, A. (2019). Nutations in growing plant shoots: The role of elastic deformations due to gravity loading. *Journal of the Mechanics and Physics of Solids*, 103702.

[2] Anderson, N.A., Done, G.T.S. (1971). On the Partial Simulation of a Non-Conservative System by a Conservative System. *International Journal of Solids and Structures*, 7, 183-191.

[3] Ardentov, A.A. (2018). Multiple solutions in Euler's elastic problem. *Aut. Rem. Cont.*, 79(7), 1191-1206.

[4] Armanini, C., Dal Corso, F., Misseroni, D., Bigoni, D. (2017). From the elastica compass to the elastica catapult: an essay on the mechanics of soft robot arm. *Proceedings of the Royal Society A*, 473, 20160870.

[5] Armanini, C., Dal Corso, F., Misseroni, D., Bigoni, D. (2019). Configurational forces and nonlinear structural dynamics. *Journal of the Mechanics and Physics of Solids*, 130, 82-100.

[6] Arnold, V.I. (1984). *Catastrophe Theory*. Springer Berlin Heidelberg.

[7] Bartels S. (2016). A simple scheme for the approximation of elastic vibrations of inextensible curves. *IMA Journal of Numerical Analysis*, 36, 1051-1071.

[8] Bayly, P.V., Dutcher, S.K. (2016). Steady dynein forces induce flutter instability and propagating waves in mathematical models of flagella. *Journal of The Royal Society Interface*, 13, 20160523.

[9] Batista, M. (2013). Large deflections of shear-deformable cantilever beam subject to a tip follower force. *International Journal of Mechanical Sciences*, vol. 75, 388-395.

[10] Batista, M. (2015). On stability of elastic rod planar equilibrium configurations. *International Journal of Solids and Structures*, 72, 144–152.

[11] Batista, M. (2016). A closed-form solution for Reissner planar finite-strain beam using Jacobi elliptic functions. *International Journal of Solids and Structures*, vol. 87, 153-166.

[12] Batista, M. (2018). On Stability of Non-inflectional Elastica.

[13] Bazant, Z.P. and Cedolin, L. (2010). *Stability of Structures: Elastic, Inelastic, Fracture and Damage Theories*. World Scientific.

[14] Beck, M., 1952. Die Knicklast des einseitig eingespannten, tangential gedrückten Stabes. *Z. Angew. Math. Phys.*, 3, 225.

[15] Beharic J., Lucas T. M., Harnett C. K. (2014). Analysis of a Compressed Bistable Buckled Beam on a Flexible Support. *Journal of Applied Mechanics*, 81 / 081011-1

[16] Bertoldi, K., Vitelli, V., Christensen, J., van Hecke, M. (2017). Flexible mechanical metamaterials. *Nature Reviews*, 2:17066.

[17] Bigoni, D., Noselli, G. (2011). Experimental evidence of flutter and divergence instabilities induced by dry friction. *Journal of the Mechanics and Physics of Solids*, 59, 2208-2226.

[18] Bigoni, D. (2012). *Nonlinear solid mechanics: bifurcation theory and material instability*. Cambridge University Press.

[19] Bigoni, D., Bosi, F., Misseroni, D., Dal Corso, F., Noselli, G. (2015). New phenomena in nonlinear elastic structures: from tensile buckling to configurational forces. In CISM Lecture Notes No. 562 *Extremely Deformable Structures* (Ch. 2), edited by D. Bigoni, Springer.

[20] Bigoni, D., Misseroni, D., Tommasini, M., Kirillov, O., Noselli, G. (2018). Detecting singular weak-dissipation limit for flutter onset in reversible systems, *Physical Review E*, 97, 023003.

[21] Bigoni, D., Kirillov, O., Misseroni, D., Noselli, G., Tommasini, M. (2018). Flutter and divergence instability in the Pflüger column: Experimental evidence of the Ziegler destabilization paradox, *Journal of the Mechanics and Physics of Solids*, vol. 116, 99-116.

[22] Bigoni, D. (2019). Flutter from Friction in Solids and Structures. In CISM Lecture Notes No. 586 *Dynamic Stability and Bifurcation in Nonconservative Mechanics* (Ch. 1), edited by D. Bigoni and O.N. Kirillov, Springer.

[23] Bigoni, D., Misseroni, D. (2020). Structures loaded with a force acting along a fixed straight line, or the "Reut's column problem", *Journal of the Mechanics and Physics of Solids*, vol. 134, 103741.

[24] Bolotin, V.V. (1963). *Nonconservative Problems of the Theory of Elastic Stability*, Pergamon Press.

[25] Bolza, O. (1904). *Lectures on the Calculus of Variations*, Chicago University Press, Chicago.

[26] Broman, A. (1970). *Introduction to Partial Differential Equations: From Fourier Series to Boundary-Value Problems.* Addison-Wesley, London.

[27] Byrd, P.F., Friedman, M.D. (1971). *Handbook of Elliptic Integrals for Engineers and Scientists*, Springer Berlin Heidelberg.

[28] Camescasse, B., Fernandes, A., Pouget, J. (2013). Bistable buckled beam: elastica modeling and analysis of static actuation. *International Journal of Solids and Structures*, 50, 2881-2893.

[29] Camescasse, B., Fernandes, A., Pouget, J. (2014). Bistable buckled beam and force actuation: experimental validations. *International Journal of Solids and Structures*, 51, 1750-1757.

[30] Carricato, M., Parenti-Castelli, V., Duffy, J. (2001). Inverse static analysis of a planar system with flexural pivots. *J. Mech. Design* 123, 43-50

[31] Carricato, M., Duffy, J., Parenti-Castelli, V. (2002). Catastrophe analysis of a planar system with flexural pivots. *Mech. Mach. Theory* 37(7), 693-716

[32] Cazottes, P., Fernandes, A., Pouget, J. Hafez, M.(2009). Bistable buckled beam: modeling of actuating force and experimental validations. *J. Mech. Design*, 131, 101001.

[33] Cazzolli, A., Dal Corso, F. (2019). Snapping of elastic strips with controlled ends. *International Journal of Solids and Structures.* 162, 285-303

[34] Cazzolli, A., Misseroni, D., Dal Corso, F. (2019). Elastica catastrophe machine: theory, design and experiments. *Journal of the Mechanics and Physics of Solids*, 103735.

[35] Cazzolli, A., Dal Corso, F., Bigoni, D. (2020). Non-holonomic constraints inducing flutter instability in structures under conservative loadings. *Submitted.*

[36] Chen, J.S., Lin, Y.Z. (2008). Snapping of a planar elastica with fixed end slopes. *ASME J. App. Mech.*, 75, 410241-410246.

[37] Chen, J.S., Lin, W.Z. (2012). Dynamic snapping of a suddenly loaded elastica with fixed end slopes. *Int. J. Non-Linear Mech.*, 47, 489-495.

[38] Cherepanov, G.P., Germanovich, L.N. (1993). An employment of the catastrophe theory in fracture mechanics as applied to brittle strength criteria. *Journal of the Mechanics and Physics of Solids*, 41, 1637-1649.

[39] Cianchetti, M., Calisti, M., Margheri, L., Kuba, M., Laschi, C. (2015). Bioinspired locomotion and grasping in water: the soft eight-arm OCTOPUS robot. *Bioinspiration & Biomimetics*, 10, 035003.

[40] Cohen, T., Givli, S. (2014). Dynamics of a discrete chain of bi-stable elements: A biomimetic shock absorbing mechanism. *Journal of the Mechanics and Physics of Solids*, 64,426-439

[41] Detinko, F.M. (2003). Lumped damping and stability of Beck column with a tip mass. *International Journal of Solids and Structures*, vol 40, 4479-4486

[42] Domokos, G. (2002). The Odd Stability of the Euler Beam. In CISM Lecture Notes No. 436 *Modern Problems of Structural Stability* (Ch. 2), edited by A.P. Seyranian and I. Elishakoff, Springer.

[43] Elishakoff, I. (2005). Controversy associated with the so-called "follower force": critical overview. Appl. Mech. Rev. , 58, 117-142.

[44] Evans, M.E.G. (2009). The jump of the click beetle (Coleoptera, Elateridae)-a preliminary study. *J. Zool.*, 167, 319-336.

[45] Facchini, G., Sekimoto, K., du Pont, S.C. (2017). The rolling suitcase instability: a coupling between translation and rotation. *Proceedings of the Royal Society A*, 473.

[46] Fargette, A., Neukirch, S., Antkowiak, A. (2014). Elastocapillary snapping: Capillarity induces snap-through instabilities in small elastic beams, *Physical Review Letters*, 112, 137802

[47] Fraternali, F., Carpentieri, G. Amendola, A. (2015). On the mechanical modeling of the extreme softening/stiffening response of axially loaded tensegrity prisms. *Journal of the Mechanics and Physics of Solids*, 74, 136–157

[48] Frazier, M.J., Kochmann, D.M. (2017). Band gap transmission in periodic bistable mechanical systems. *J. Sound Vib.*, 388, 315-326

[49] Gilmore, R. (1981). *Catastrophe Theory for Scientists and Engineers*. Dover

[50] Golubitsky, M., Schaeffer, D.G. (1985). *Singularities and Groups in Bifurcation Theory - Volume I*, Springer NY.

[51] Goto, Y., Yoshimitsu, T., Obata, M. (1990). Elliptic integral solutions of plane elastica with axial and shear deformations, *International Journal of Solids and Structures*, vol. 26, 375-390.

[52] Greenwood, D.T. (2003). *Advanced Dynamics*, Cambridge University Press.

[53] Groh, R.M.J., Pirrera, A. (2018). Generalised path-following for well-behaved nonlinear structures. *Computer Methods in Applied Mechanics and Engineering*, 331, 394–426

[54] Harne, R.L., Wang, K.W. (2013). A review of the recent research on vibration energy harvesting via bistable systems. *Smart Mat. Struct.* 22, 023001

[55] Hines, R., Marsh, D., Duffy, J. (1998). Catastrophe Analysis of the Planar Two-Spring Mechanism. *Int. J. Rob. Res.* 17(1), 89-101

[56] Hu, N., Burgueno, R. (2015). Buckling-induced smart applications: recent advances and trends. *Smart Mat. Struct.*, 24 (6), 063001.

[57] Huang, N.C., Nachbar, W., Nemat-Nasser, S. (1967). Willems' Experimental Verification of the Critical Load on Beck's Problem. *J. Appl. Mech.*, 34, 243-245.

[58] Hunt, G.W. (1977). Imperfection-Sensitivity of Semi-Symmetric branching. *Proceedings of the Royal Society A*, 357, 193-211

[59] Jarzebowska, E., McClamroch, N.H. (2000). On nonlinear control of the Ishlinsky system as an example of a non-holonomic non-Chaplygin system. *Proceedings of the 2000 American Control Conference*, 5, 3249-3253.

[60] Jenkins, A. (2013). Self-oscillation. *Physics Reports*, 525, 167-222.

[61] Kim, H., Kim, J-H., Kim, J. (2011). A review of piezoelectric energy harvesting based on vibration. *Int. J. Prec. Eng. Manuf.*, 12, 1129-1141.

[62] Kirillov, O.N. (2005). A theory of the destabilization paradox in non-conservative systems. *Acta Mech.*, 174, 145-166.

[63] Kirillov, O.N. (2013). *Nonconservative Stability Problems of Modern Physics*, De Gruyter.

[64] Kirillov, O.N., Verhulst, F. (2010). Paradoxes of dissipation-induced destabilization or who opened Whitney's umbrella? *ZAMM Z. angew. Math. Mech.*, 90, 462-488.

[65] Kochmann, D., Bertoldi, K. (2017). Exploiting Microstructural Instabilities in Solids andStructures: From Metamaterials to Structural Transitions. *Appl. Mechanics Rev.*, 69, 050801

[66] Koiter, W.T., (1985). Elastic Stability, *Z. Flugwiss. Weltraumforsch.*, 9 4, 205-210.

[67] Koiter, W.T. (1980). Buckling of a flexible shaft under torque loads transmitted by Cardan joints. *Ingenieurs*, 49, 369-373.

[68] Koiter, W.T. (1996). Unrealistic follower forces. *J. Sound and Vibration*, 194, 636-638.

[69] Kuleshov, A.S., Rybin, V.V., (2013). Controllability of the Ishlinsky System. *Proceedings of XLI International Summer School-Conference APM 2013*, 184-190.

[70] Kuznetsov, Y.A. (2004). *Elements of Applied Bifurcation Theory.* Springer New York.

[71] Lanczos, C. (1952). *The Variational Principles of Mechanics.* Oxford University Press.

[72] Laschi, C., Cianchetti, M. (2014). Soft robotics: new perspectives for robot bodyware and control. *Front. Bioeng. Biotechnol.*, 2, 3.

[73] Lengyel, A., You, Z. (2004). Bifurcations of SDOF mechanisms using catastrophe theory. *International Journal of Solids and Structures*, 41, 559-568

[74] Levyakov, S.V. (2001). States of equilibrium and secondary loss of stability of a straight rod loaded by an axial force. *J. App. Mech. and Tech. Phys.*, 42, 321-327.

[75] Levyakov, S.V., Kuznetsov, V.V. (2009). Stability analysis of planar equilibrium configurations of elastic rods subjected to end loads, *Acta Mech*, 211, 73-87.

[76] Levyakov, S.V. (2009). Stability analysis of curvilinear configurations of an inextensible elastic rod with clamped ends. *Mech. Res. Comm.*, 36, 612-617.

[77] Love, A.E.H. (1920). *A treatise on the mathematical theory of elasticity. Third edition*, Cambridge at the university press.

[78] Lu, T., Cheng, S., Li, T., Wang, T., Suo, Z. (2016). Electromechanical Catastrophe. *Int. J. Appl. Mechanics*, 8, 164000

[79] Manning, R.S. (2014). A catalogue of stable equilibria of planar etensible or inextensible elastic rods for all possible Dirichlet boundary conditions. *J. Elasticity*, 115, 105-130.

[80] Marsden, J.E., McCracken, M. (1976). *The Hopf Bifurcation and Its Applications*. Springer New York.

[81] Meurant, G. (1992). A Review on the Inverse of Symmetric Tridiagonal and Block Tridiagonal Matrices. *SIAM Journal on Matrix Analysis and Applications*, vol 13, 707-728.

[82] Mochiyama H., Kinoshita A., Takasu R. (2013). Impulse Force Generator based on Snap-through Buckling of Robotic Closed Elastica: Analysis by Quasi-static Shape Transition Simulation, *IEEE/RSJ International Conference on Intelligent Robots and Systems*, Tokyo, Japan.

[83] Nadkarni, N., Arrieta, A.F., Chong, C., Kochmann, D.M., Daraio, C. (2016). Unidirectional transition waves in bistable lattices. *Physical Review Letters*, 116, 244501.

[84] Nagy, P., Tasnadi, P. (2014). Zeeman catastrophe machines as a toolkit for teaching chaos. *Eur. J. Phys.*, 35, 015018

[85] Neimark, Ju.I., Fufaev, N.A. (1972). *Dynamics of non-holonomic Systems*, American Mathematical Society.

[86] O'Carroll, M.J. (1976). Fold and cusp catastrophes for critical flow in hydraulics. *Appl. Math. Modelling*, 1, 108-109

[87] Pflüger, A. (1955). Zur Stabilität des tangential gedrückten Stabes. *Z. Angew. Math. Mech.*, 35 (5), 191.

[88] Phan, H., Shin, D., Heon Jeon, S., Young Kang, T., Han, P., Han Kim, G., Kook Kim, H., Kim, K., Hwang, Y., Won Hong, S. (2017). Aerodynamic and aeroelastic flutters driven triboelectric nanogenerators for harvesting broadband airflow energy. *Nano Energy*, 33, 476-484.

[89] Plaut, R.H. (1972). A New Destabilization Phenomenon in Nonconservative Systems. *Zeitschrift für Angewandte Mathematik und Mechanik*, vol. 51, 319-321.

[90] Plaut, R.H., Taylor, R.P., Dillard, D. (2004). Postbuckling and vibration of a flexible strip clamped at its ends to a hinged substrate. *International Journal of Solids and Structures*, 41, 859-870.

[91] Plaut, R.H., Virgin, L.N. (2009). Vibration and Snap-Through of Bent Elastica Strips Subjected to End Rotations. *Journal of Applied Mechanics*, 76, 041011-1

[92] Polygerinos, P., Galloway, K.C., Savage, E., Herman, M., O'Donnell, K., Walsh, C.J. (2015). Soft Robotic Glove for Hand Rehabilitation and Task Specific Training. *International Conference on Robotics and Automation (ICRA).* Seattle, WA; 2015.

[93] Poston, T., Stewart, I. (1978). *Catastrophe Theory and Its Applications.* Pitman

[94] Qin, S., Jiao, J.J., Wang, S., Long, H. (2001). A nonlinear catastrophe model of instability of planar-slip slope and chaotic dynamical mechanisms of its evolutionary process. *International Journal of Solids and Structures*, 38, 8093-8109

[95] Raney, J.R., Nadkarni, N., Daraio, C., Kochmann, D.M., Lewis, J.A., Bertoldi, K. (2016). Stable propagation of mechanical signals in soft media using stored elastic energy. *Proc. Nat. Acad. Sci.*, 113 (35), 9722-9727.

[96] Reis, P.M. (2015). A Perspective on the Revival of Structural (In) Stability With Novel Opportunities for Function: From Buckliphobia to Buckliphilia. *ASME J. Appl. Mech.*, 82, 111001-1.

[97] Reissner, E. (1972). On one-dimensional finite-strain beam theory: The plane problem. *Zeitschrift für angewandte Mathematik und Physik ZAMP*, vol. 23, 795-804.

[98] Restrepo, D., Mankame, N.D., Zavattieri, P.D. (2015). Phase transforming cellular materials. *Extreme Mech. Lett.*, 4, 52-60.

[99] Reut, V.I. (1939). About the Theory of Elastic Stability. *Proceedings of the Odessa Institute of Civil and Communal Engineering*, No. 1.

[100] Meijaard, J.P., Papadopoulos, J.M., Ruina, A., Schwab, A.L. (2007). Linearized dynamics equations for the balance and steer of a bicycle: a benchmark and review. *Proceedings of the Royal Society A*, vol. 463, 1955-1982.

[101] Rus, D., Tolley, M.T. (2015). Design, fabrication and control of soft robots. *Nature*, vol. 521, 467-475.

[102] Sachkov, Y.L., Levyakov, S.V. (2010). Stability of inflectional elasticae centered at vertices or inflection points. *Proc. Steklov Inst. Math.*, 271, 177-192.

[103] Sano, T.G., Wada, H. (2018). Snap-buckling in asymmetrically constrained elastic strips, *Physical Review E*, 97, 013002.

[104] Sano, T.G., Wada, H. (2019). Twist-Induced Snapping in a Bent Elastic Rod and Ribbon, *Phys. Rev. Lett.*, 122, 114301.

[105] Schioler, T., Pellegrino, S. (2007). Space Frames with Multiple Stable Configurations. *AIAA Journal*, 45 (7), 1740-1747.

[106] Shepherd, R.F., Ilievski, F., Choi, W., Morin, S.A., Stokes, A.A., Mazzeo, A.D., Chen, X., Wang, M., Whitesides, G.M. (2011). Multigait soft robots. *Proc. Nat. Acad. Sci.*, 108(51), 20,400-20, 403.

[107] Singer, J., Arbocz, J., Weller, T. (1997). *Buckling Experiments*. Wiley, London (Vol. 2, pp. 1-3).

[108] Thom, R. (1969). Topological models in biology. *Topology*, 8(3), 313-335

[109] Thom, R. (1975). *Structural stability and morphogenesis*. W.A. Benjiamin Inc.

[110] Thompson, J.M.T. (1983). On the convection of a cusp in elastic stability. *Journal of the Mechanics and Physics of Solids*, 31 (3), 205-222

[111] Tommasini, M., Kirillov, O.N., Misseroni, D., Bigoni, D. (2016). The destabilizing effect of external damping: Singular flutter boundary for the Pflüger column with vanishing external dissipation. *Journal of the Mechanics and Physics of Solids*, vol. 91, 204-215.

[112] Tsuda, T., Mochiyama, H., Fujimoto, H. (2012). Quick stair-climbing using snap-through buckling of closed elastica. *International Symposium on Micro-NanoMechatronics and Human Science, MHS 2012*, 368-373.

[113] Willems, N. (1966). Experimental Verification of the Dynamic Stability of a Tangentially Loaded Cantilever Column, *J. Appl. Mech.*, 35, 460-461.

[114] Woodcock, A.E.R., Poston, T.A. (1976). A higher catastrophe machine. *Proc. Cambridge Philos. Soc.*, 79, 343-350

[115] Yamada, A., Sugimoto, Y., Mameda, H., Fujimoto, H. (2011). An impulsive force generator based on closed elastica with bending and twisting and its application to quick turning motion of swimming robot. *J. Rob. Soc. Japan*, 29, 0289-1824.

[116] Yang, D., Mosadegh, B., Ainla, A., Lee, B., Khashai, F., Suo, Z., Bertoldi, K., Whitesides, G.M. (2015). Buckling of elastomeric beams enables actuation of soft machines. *Adv. Mater.*, 27, 6323-6327.

[117] Yin, J.P., Marsh, D., Duffy, J. (1998). Catastrophe analysis of planar three-spring mechanism. *Proc. of DETC 98, 1998 ASME Des. Eng. Tech. Conf.*, September 13–16, 1998, Atlanta, GA.

[118] Zeeman, E.C. (1972). A catastrophe machine. In *Towards a Theoretical Biology* (C. H. Waddington, ed.). Edinburgh University Press, Edinburgh. Vol. 4, 276-282.

[119] Zeeman, E.C. (1976). Catastrophe Theory. *Scientific American*, 234, 65-83.

[120] Zeeman, E.C. (1977). *Catastrophe Theory: Selected Papers, 1972-77.* Addison-Wesley Educational Publishers.

[121] Zeeman, E.C. (1976) Euler buckling. In *Structural Stability, the theory of catastrophes, and applications in the sciences* (P. Hilton, ed.). Springer, Berlin, 373-395.

[122] Ziegler, H. (1952). Die Stabilitätskriterien der Elastomechanik. *Ingenieur-Archiv*, vol. 20, 49-56.

[123] Ziegler, H. (1977). *Principles of Structural Stability*, Birkhäuser Basel.

[124] Zhang, A., Chen, G. (2013) A comprehensive elliptic integral solution to the large deflection problems of thin beams in compliant mechanisms. *J. Mech. Rob.*, 5, 021006.

[125] Zunic, J., Rosin, P. L. (2004) A new convexity measure for polygons. *IEEE Transactions on Pattern Analysis and Machine Intelligence*, 26(7), 923-934.